A Synthetic Modelling Study and Assessment of Marine Electromagnetic Data Using Unstructured Tetrahedral Meshes With Applications to Hydrocarbon Exploration in the Flemish Pass Basin, Offshore Newfoundland

by

©Chelsea Lola Woodman Squires

A thesis
presented to the School of Graduate Studies
in fulfillment of the
thesis requirement for the degree of
Master of Science
in
Earth Sciences (Geophysics)

Memorial University

St. John's, Newfoundland and Labrador, Canada
July 2016

I hereby declare that I am the sole author of this thesis. This is a true copy of the thesis, including any required final revisions, as accepted by my examiners.

I understand that my thesis may be made electronically available to the public.

Abstract

Marine controlled-source electromagnetic (CSEM) surveying is a geophysical technique for mapping subsurface electrical resistivity structures in the offshore environment. The method is highly sensitive to resistivity contrasts, which result in interpretable electric field responses. This has caused the method to gain attention in recent years concerning its capabilities as a direct hydrocarbon indicator on a three-dimensional scale. The technique has a significant advantage in being both an independent and complementary method to seismic imaging, allowing for considerable opportunities in joint inversion and interpretation using data that has been previously collected. While raw CSEM data contains rich information about the subsurface, modelling and inversion are required to convert such data into interpretable resistivity estimates. To this end, improvement of modelling tools is integral to the quality and accuracy of interpreted CSEM data.

This study used forward modelling based on the CSEM3DFWD code written by Seyed-Masoud Ansari at Memorial University. The finite-element method is employed over unstructured, tetrahedral meshes that allow irregular geological contacts to be accurately modeled. 1D and 3D models have been built with two main goals: to assess the accuracy of CSEM3DFWD by comparing results to known analytical methods; and to assess the thresholds of detection in 3D models that are complete with bathymetry, horizons of geological contacts, and reservoir geometries that are analogous to those in the Flemish Pass Basin, offshore Newfoundland. Matches of these electric field amplitude and phase results with known semi-analytical methods for 1D models verify the accuracy of the modelling method, allowing an assessment study of detectability of likely reservoirs offshore Newfoundland to be carried out. With this ability to generate accurate synthetic CSEM data for realistic Earth models, more educated decisions can be made concerning marine exploration scenarios: the results of 3D CSEM surveys can be more accurately interpreted and more mindful assessments of risk can be made, increasing the likelihood of reaching successful hydrocarbon plays.

Acknowledgements

This project would not be possible without the assistance (financially, academically and emotionally) of several integral members. I would like to thank my supervisor, Colin Farquharson, for having patience with my neurotic nature and reminding me to stay calm during times of panic. Alison Leitch for her work as second reader. To Brad Bonnell, Mike Livingstone, Eric Albretchsons, and every contributor from Suncor Energy for their use of seismic horizons, reservoir structures, and fried chicken at the Gypsy Tea Room. To Mitacs and the School of Graduate Studies which granted me the resources to not starve nor go homeless during this time. SeyedMasoud Ansari and Peter Lelièvre for giving access and assistance to the programs used throughout this thesis. Keir Hiscock and Darren Smith, whose technical expertiste holds this department together. Michelle Miskell — the size of your heart never ceases to amaze me. You are so fundamental in the success of every student who has walked through this building; if not specifically, then with your unbelievable presence. Last but not least, Griffin Simpson for handing me my first can of India Beer as I finished this thesis.

Dedication

Bert, Joanne, Bailey, Thu & Beau

Table of Contents

List of Tables

List of Figures

Chapter 1

Introduction

1.1 Overview

The marine controlled-source electromagnetic (CSEM) method is a geophysical technique for mapping subsurface electrical resistivity. It has gained attention in recent years as an independent, yet compatible method to seismic acquisition and subsequent interpretation: the integration of the two methods reduces ambiguity of the interpretation of either independent method (e.g. Harris and MacGregor, 2006; Hoversten et al., 2005; Johansen et al., 2007; and Harris et al., 2009). While raw CSEM data contains rich information about the subsurface, modelling and inversion are required to convert raw data into interpretable resistivity estimates. Improvement of modelling tools will assist in closing the present gap between acquisition and interpretation of CSEM data. To this end, the focus of this study is to explore the limits of the latest modelling capabilities within the context of marine EM scenarios.

The study will begin by testing 1D halfspaces and layered Earth models with known

analytical results, to serve as confirmation of the validity of the code used for forward-modelling. The parameters — namely, resistivities — of these models will be dictated by parallel values used in the complex 3D real Earth models that comprise the main focus of this study. These resistivities (ρ; presented in Ωm) may equally be represented as conductivities (σ in S/m), using the relationship $\rho = 1/\sigma$ — both resistivity and conductivity will be used in this study interchangeably. In both the 3D and 1D modelling scenarios in this study, a subsurface structure is designed and discretized using unstructured tetrahedral meshes. The solution of an electric field matrix formulation is calculated via an interative forward solver, CSEM3DFWD, using the unstructured mesh as the basis of the finite-element approach. The comparison between results of simplistic models versus the models complete with bathymetry, stratigraphy, and complex hydrocarbon trap structures will be integral in evaluating the limits of resistivity detection — the principle motivation and aim of this study.

1.2 Historical and Academic Development of CSEM

The historical motivations and methods that were fundamental in the development of the deepwater marine CSEM method used in modern hydrocarbon exploration are described extensively by Constable and Srnka (2007). The technique emerged through work by Charles Cox of the Scripps Institution of Oceanography in the late 1970s (Cox, 1981). The original motivation for these CSEM experiments was to study the shallow and resistive parts of the oceanic lithosphere by replacing the relatively high frequency energy lost during magnetotelluric surveys with energy supplied by a deep-towed, man-made transmitter.

Cox's experimentation over the oceanic lithosphere yielded interesting results: the oceanic lithosphere proved to be remarkably resistive, with the lower crust and upper mantle values approaching 10^5 Ωm. This resistivity, combined with the high apparent conductivity of the ocean (10^4 S) acts to trap horizontal electric currents associated with MT fields or horizontal water flow in the ocean for very large distances — a consequence of the diffusive propagation of electromagnetic signals in the conductive media. The presence of the source at far offset implies propagation through the rocks below the ocean floor, and the variation electric field results are a function of the subsurface resistivities and depth (Cox et al., 1986)

While Cox's work with the oceanic lithosphere was fundamental in the development of the marine CSEM method, alterations had to be made to his method to suit the bias of geologic interest towards features that have undergone tectonic activity and typically had significant bathymetric relief; namely, eliminating the use of the source transmitter on the seabed, as this proved impractical for the rough terrain of the ridge axis. Martin Sinha and his group at the University of Cambridge developed a neutrally buoyant transmitter antenna that allowed the deep-towed transmitter to be carried about 100 m above the seafloor (Sinha et al., 1990). Through trials executed by a collaboration of Cambridge and Scripps on the East Pacific Rise (Evans et al., 1991), the Reykjanes Ridge (MacGregor et al., 1998) and the Valu Fa Ridge (MacGregor et al., 2001), this method was proven to be both an efficient method of circumventing terrain issues, and later, by Exxon in the early 1980s (Srnka, 1986), desirable in the hydrocarbon exploration environment. Unfortunately, a combination of non-ideal water depths, a lack of computational capability, limited digital acquisition capacities, and the growing emphasis on 3D marine seismic technology meant

that this work was before its time in terms of commercial viability.

It was not until the late 1990s when Statoil began examining the use of CSEM that it was concluded that *"if the target is not too small compared with its depth of burial, and the water depth is sufficient to suppress the air wave, then the controlled source signature of the oil-filled layer is detectable, yielding controlled source amplitudes that are a factor of 2 to 10 different than models without the oil layer. The signals are above the noise threshold, and the experimental parameters (frequency, range, antenna length and power) are practicable"* (Westerdahl et al., 2009). With this positive result, Statoil proceeded with field trials in offshore Angola in late 2000 (Ellingsrud et al., 2002).

The high resistivity contrast between hydrocarbon-filled pore space and water-filled pore space allows for the CSEM method to act as a direct hydrocarbon indicator in areas where seismic data can be ambiguous (Johansen et al., 2005; Stefatos et al., 2009; and MacGregor et al., 2007). As evident from EM induction well-logging, this difference in resistivity creates a strongly visible oil-water contact in borehole scenarios, which is a vital indicator in offshore hydrocarbon well development. An attractive advantage of the CSEM method is not only the ability to model the grade and geometry of the hydrocarbon reservoir, but to do this without the need of expensive deep-water drilling.

Hesthammer and Boulaenko (2005) argued that integration of EM methods with conventional seismic and well log data has the potential to greatly improve exploration success rates (e.g. Hansen and Mittet, 2009) and that the application of the CSEM technology in conjunction with traditional prospect evaluation workflows provides the potential to increase the chance of discovering hydrocarbons. As such, as part of a risked value and

cost consideration, the technology offers an opportunity to de-risk and prioritize drilling targets and, most significantly, reduce the risk of drilling dry wells. It is critical to note that resistivity mapping using CSEM data must be mindfully applied to hydrocarbon exploration, as the resistivity contribution is non-unique to hydrocarbons: that is, materials such as salt, volcanics and low-porosity lithologies may cause false positive interpretations (e.g. Gist et al., 2013). These false positives can be avoided through a workflow of forward modelling, inversion, and integrating seismic, well, and regional data.

A recent publication by Hesthammer et al. (2010) provides statistical results from wells on prospects containing CSEM data. Of the 22 calibration surveys acquired over existing surveys, 19 (86%) show a significant CSEM anomaly, categorized by a normalized anomalous amplitude response (NAR) value above 15% for the fundamental frequency. Of the 14 calibration surveys acquired over prospects that are proven dry, 13 (93%) show no significant CSEM anomaly. For exploration wells drilled on a prospect with a significant CSEM anomaly, the success rate is doubled (from 35 to 70%) for wells drilled on prospects without. The NAR value represents the percent difference of the results over a resistively anomalous body to the background trend of a homogeneously resistive region (Figure 1.1). This is analogous to the approach used in this study, where percent difference values are normalized by structurally equivalent reservoirs that are non-hydrocarbon saturated (see Chapter 4 for details).

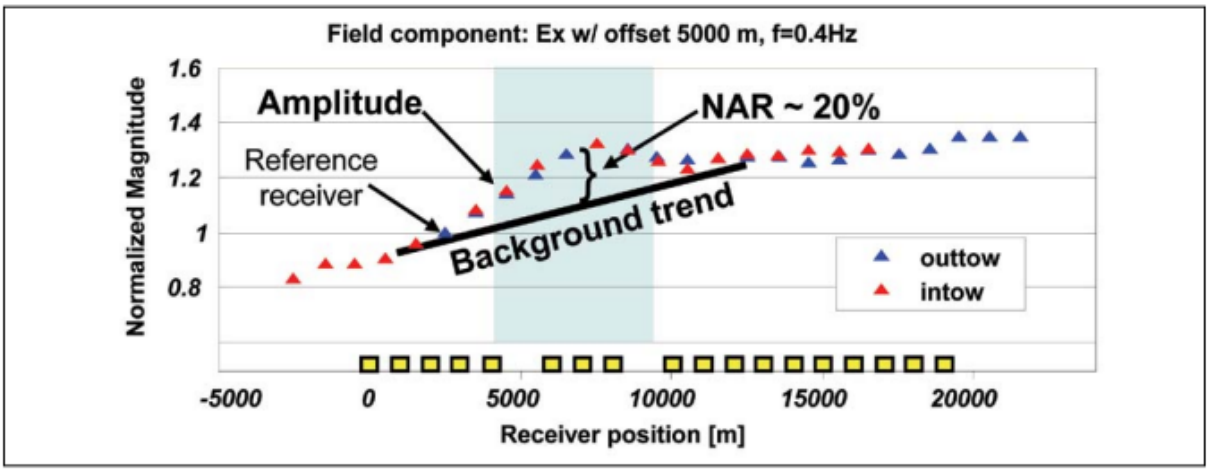

Figure 1.1: A Normalized Amplitude Response plot from the Barents Sea included in Hesthammer et al. (2010) showing a maximum NAR of 20%. The yellow boxes represent the receiver positions for this survey, and the blue highlighted section represents the response to the anomalous region.This technique of reservoir detection is analogous to the normalization method used in this study.

1.3 The CSEM Method

As previously stated, this study will involve the forward modelling of synthetic CSEM data using unstructured meshes. In order to optimize the array configurations and appropriate parameters for synthetic modelling, it is vital to understand the CSEM method and each of its components; namely, how the sources and receivers pertain to marine CSEM scenarios.

Figures 1.2 to 1.4 display the components and preferred configurations of the standard broadband marine CSEM survey. The standard source used in these scenarios is a horizontal electric dipole (HED) which allows the excitement of both vertical and horizontal current flow in the seabed and maximizes resolution for a variety of structures. A vertical magnetic dipole, for example, would excite mainly horizontal current flow (Chave et

al., 1991). The lack of vertical component prevents structures at depth from being penetrated, and thus, being well-resolved. Horizontal magnetic dipoles excite both vertical and horizontal currents, but are less favoured than electric dipoles for operational reasons (Edwards, 2005). Transmitted electric fields are directly proportional to the source dipole moment, A, given by the dipole length times the emission current (in this study is 100 m times 1 A/m). Data for interpretation are normalized by the dipole moment, resulting in a decrease in the system noise floor as A gets larger. This allows wider source-receiver offsets to be recorded and deeper structures to be detected. Dipole lengths are typically 100-300 m (Constable, 2006), as longer lengths would create significant practical challenges when towing transmitter antennae. A short source length can be modelled by an ideal dipole whose moment is equal to the current times the length of the real source. This practice is employed by the semi-analytical method of Key (2009), which is compared to the real Earth models of this study. In practice, a high-voltage AC current is transmitted down a towing cable to a transmitter unit close to the seafloor. Frequencies between 0.1 and 10 Hz may be employed by the HED, with lower frequencies accessing deeper targets, and higher frequencies increasing the resolution of shallow structures (Eidesmo et al., 2002). As the structures in this study are relatively deep, surpassing 3000 m, frequencies between 0.25 and 1.0 Hz have been considered.

As computational technologies allow for more complex models to be examined, the characteristics of CSEM continues to yield several advantages, particularly in marine environments. The highly conductive sea acts as a low pass filter for fluctuating EM fields generated above it either in the ionosphere or magnetosphere, significantly decreasing noise contributions — a significant advantage for the use of CSEM in marine scenarios. The

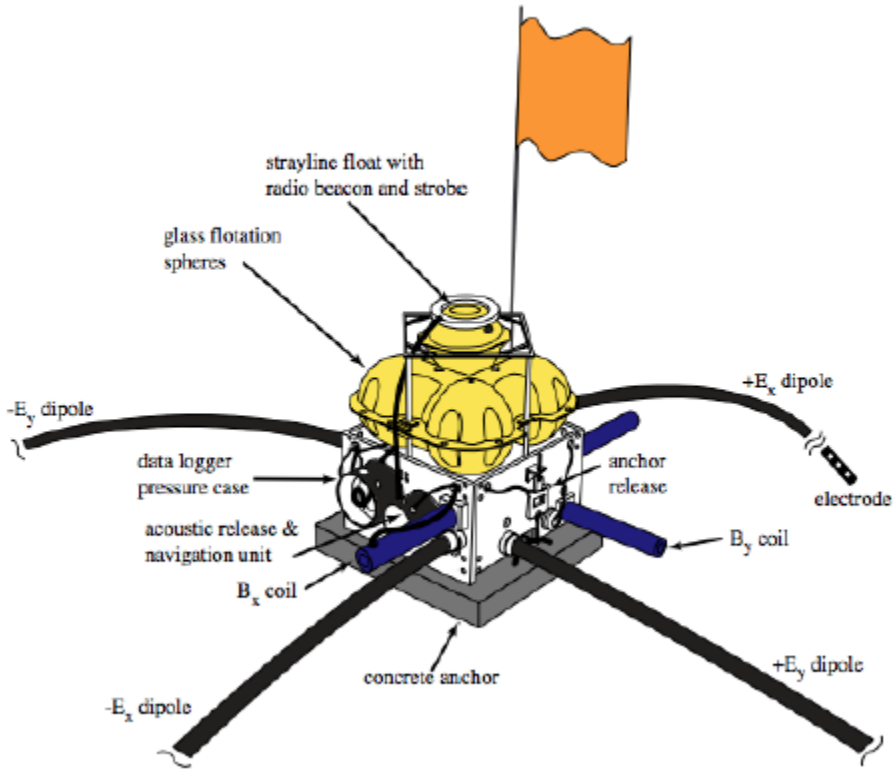

Figure 1.2: Schematic of the typical measurement instrumentation for broadband marine MT. CSEM recievers are very similar (from Key, 2003).

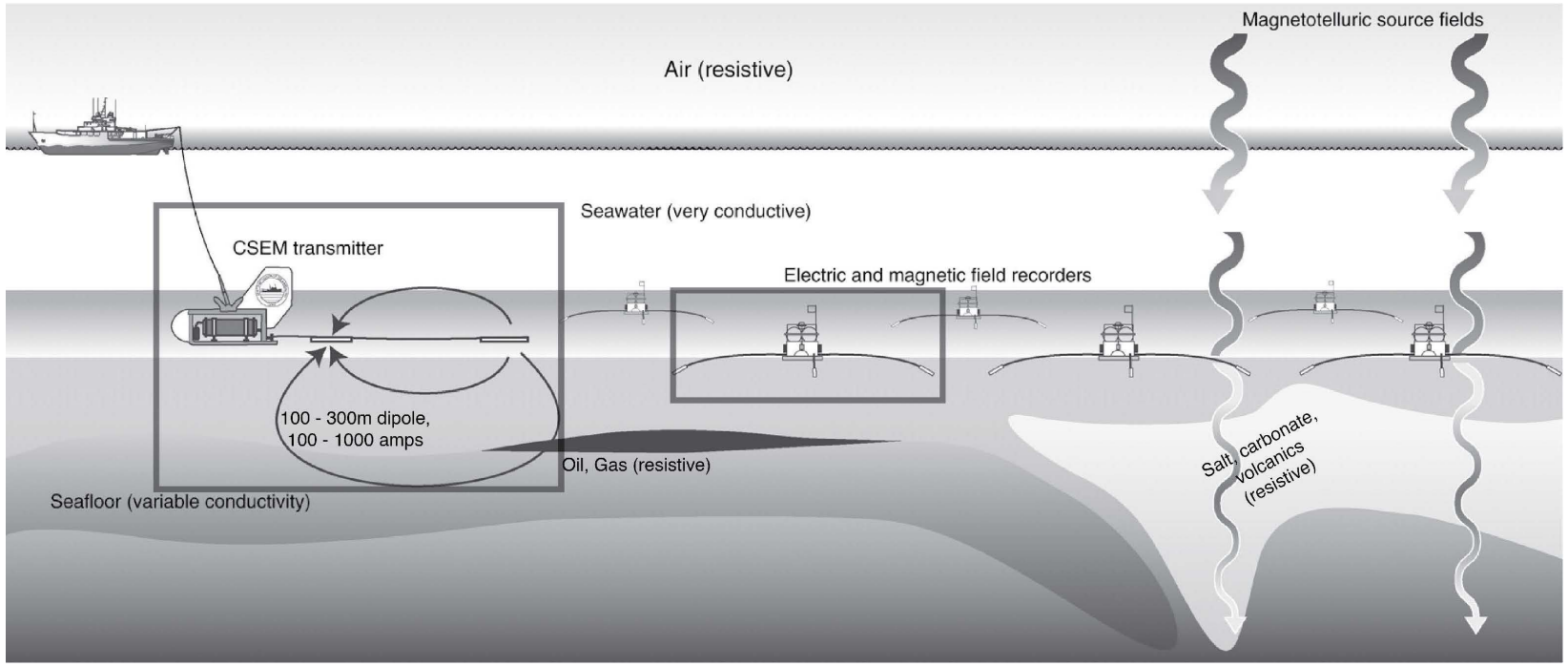

Figure 1.3: Schematic representation of the horizontal electric dipole-dipole marine CSEM method. An electromagnetic transmitter is towed close to the seafloor to maximize the coupling of electric and magnetic fields with seafloor rocks. These fields are recorded by instruments deployed on the seafloor at some distance from the transmitter. Seafloor instruments are also able to record magnetotelluric fields that have propagated downward through the seawater layer. Attention is brought to areas of enlargement for Figure 1.4 (modified from Constable and Srnka, 2007).

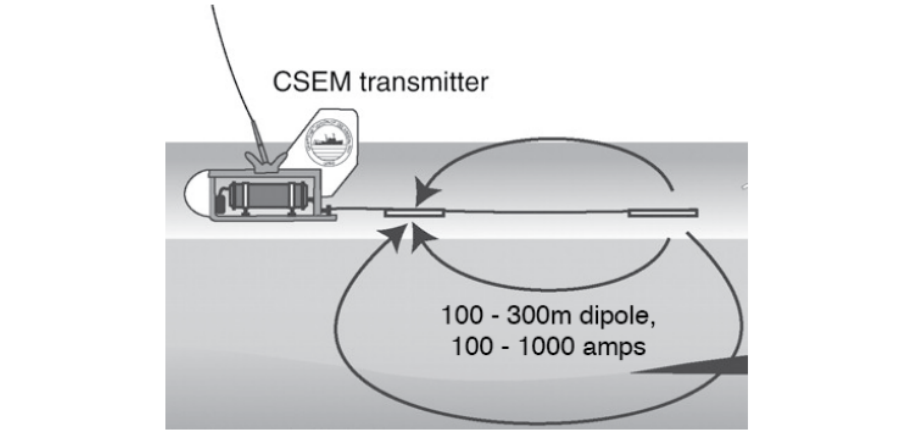

(a)

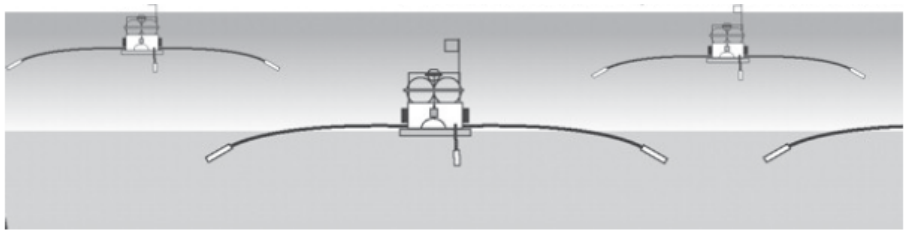

(b)

Figure 1.4: Enlarged view of select equipment from Figure 1.3.

deepwater environment acts to nearly eliminate the effect of above-water EM sources, including the anthropogenic ones. As a result, weak electromagnetic fields that propagate in the underlying sediments from a sea-bottom artificial source are measurable at large transmitter-receiver separations of the order of kilometres. Transmitter currents of 1000 A or more can be passed through seawater with simple electrode systems and reasonable power consumption (of order 100 kW), and transmitter antennae several hundred metres long can be easily towed along their length through the seawater — a strenuous task for similar land surveys. Though high currents are typically used in practice, the data in this

study are synthesized using a 1.0 Am source; results will have the same magnitude as data normalized by the dipole moment of the source.

Measurements are typically taken by the receiver (Figure 1.2) at two orientations: radial electric field, in which the receiver is positioned along the axis of the transmitter and measures a linearly polarized field oriented along this axis; and azimuthal electric fields, in which the linearly polarized field is oriented parallel to the transmitter (Figure 1.5). Studies that have explored the different behaviour of the azimuthal and radial modes in the presence of a thin resistor (e.g., Eidesmo et al., 2002; Constable and Weiss, 2006), have concluded that when the direction inline with the transmitter dipole antenna is considered, the electric field lines are oriented purely radially, and have a significant vertical component (thus, strongly exciting the subsurface vertically, as desired for the CSEM method). This configuration is accurately recorded by radially-oriented receiver. When the associated currents interact with tabular resistors — such as the thin reservoirs investigated — they produce a galvanic distortion that is made visible by an increase in electric field amplitude. In contrast, electric fields in the broadside direction to the transmitter do not produce the galvanic distortion, eliminating the detection of the reservoir. As a result, only the inline transmitter response is synthesized for this study, as it most appropriately models the resistive hydrocarbon reservoir environments considered.

1.4 CSEM Surveys of Offshore Newfoundland

Recent CSEM surveys taken offshore Newfoundland, on the east coast of Canada, have shown considerable application opportunities and relevance for this project. In 2006,

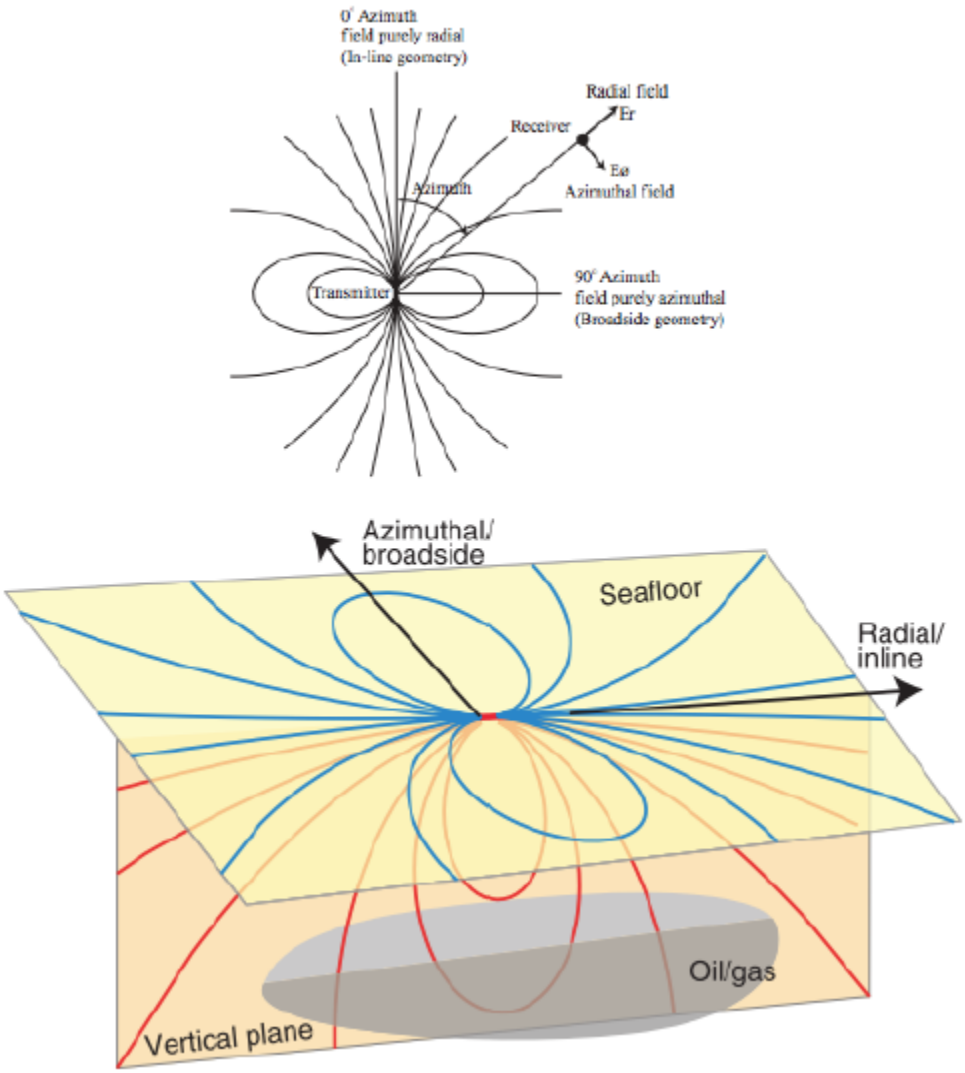

Figure 1.5: The dipole geometry of a near-seafloor transmitter. The maximum vertical electric fields (see red field lines) are below the transmitter in the inline direction. In these lines, fields are of purely radial geometry along the axis of the surface and able to generate galvanic effects when they intersect sub-horizontal, tabular bodies such as oil and gas reservoirs. In the broadside direction, electric fields are purely azimuthal and largely horizontal, producing little interaction with the reservoir (from Constable, 2010, and Constable and Weiss, 2006).

ExxonMobil performed a 3D CSEM survey over the Orphan Basin, located 400 km east of St. John's, Newfoundland, in 2500 m of water on the edge of the continental shelf (Figures 1.6 and 1.7). 3D seismic data displayed a structural high on the base Cretaceous unconformity (Enachescu et al., 2005), and inversion of the CSEM data detected high resistivity along two of the fault blocks in the region, which resulted in a follow-up survey in 2009 (Gist et al., 2013 and Cameron et al., 2015).

Unfortunately, structural complexities in the Orphan Basin led to false positives from the CSEM data (Gist et al., 2013) caused by the high resistivity of the thin-resistive layers. The results of the CSEM survey were accurate in estimating the vertical resistivity around the target horizon, but the target itself had a resistivity more consistent with a more extensive hydrocarbon reservoir than the well outcome suggested. These false positives are exactly the class of conclusions that can be mitigated with additional information, such as acoustic impedance from the seismic indicating alternative reasons for high resistivity.

Most recently, in 2014, EMGS collected a 3D wide-azimuth CSEM and 3D marine MT survey over 1986 km^2 over the North Flemish Pass Basin, approximately 450 km east of St. John's, Newfoundland (Wu, et al., 2015; Figure 1.7). These surveys will allow for calibration over the Mizzen, Harpoon and Bay du Nord discoveries, which have recently attracted attention due to their high production potential (upwards of 600 MMbbl; Wu, et al., 2015).

Discovered in 2010 by Statoil Canada Ltd. and Husky Energy, the main reservoir structure in the Flemish Pass Basin is defined as a fault-bounded, doubly-plunging horst block, with hydrocarbon discoveries in sandstone reservoirs of Upper Jurassic (Tithonian) age

(Haynes et al., 2013). Specific extensions, depths and offset of the hydrocarbon-saturated sand package are inconclusive from current seismic data, allowing opportunity for the construction of various trap structures, as explored in this study. Working from this known area of production, the 3D models in this study will incorporate seismic horizons provided by Suncor for the water bottom, base of Cretaceous and top of Tithonian to represent the bathymetry, resistivity change due to lithology, and stratigraphic trap of the potential reservoir, respectively. As Cretaceous and Tertiary sediments of the Flemish Pass Basin are sedimentary equivalents in the well-studied Jeanne D'Arc Basin (see Figure 1.7), their incorporation opens several venues for potential analogues. The resistivities of the regions used in the 3D modelling sequence of this study have been dictated by Suncor's exploration interest (Figure 1.8). Specific potential structural trap scenarios have also been provided, and have served as the basis of reservoir modelling (Figures 1.9 and 1.10).

Preliminary evaluation of the Flemish Pass Basin suggests that it has the criteria to be a good candidate for a quality CSEM survey. The field is relatively conventional: the primary reservoir interval represents a high net to gross sandstone reservoir, with average porosities greater than 20% and measured permeabilities in the multi-Darcy range. This will create significant resistivity changes in the pore space, optimizing the main advantage of CSEM surveying (Cameron et al., 2015). The potential of this region has been recently highlighted by Electromagnetic Geoservices (EMGS), who in 2016, have entered into a data licensing agreement with an undisclosed company for provision of the 3D CSEM data in the Flemish Pass region (Offshore Energy Today, 2016).

1.5 Thesis Overview

In order to capitalize on the growing interest of local oil and gas companies in the facets of CSEM, this study will use the finite-element method to generate synthetic CSEM data for scenarios that are relevant to the Newfoundland offshore environment. This data, in conjunction with known well log resistivities and seismically-derived horizons and structures, will work in complement with seismic in the region, but most prolifically, will provide quantitative insight into hydrocarbon environments that are well-detected by the CSEM method.

This is achieved by generating a series of scenarios which increase in structural and geological complexity. These models are meshed using an unstructured tetrahedal mesh, which are used to solve the forward EM problem with the finite-element method (described in detail in Chapter 2). These results are verified via known semi-analytical methods.

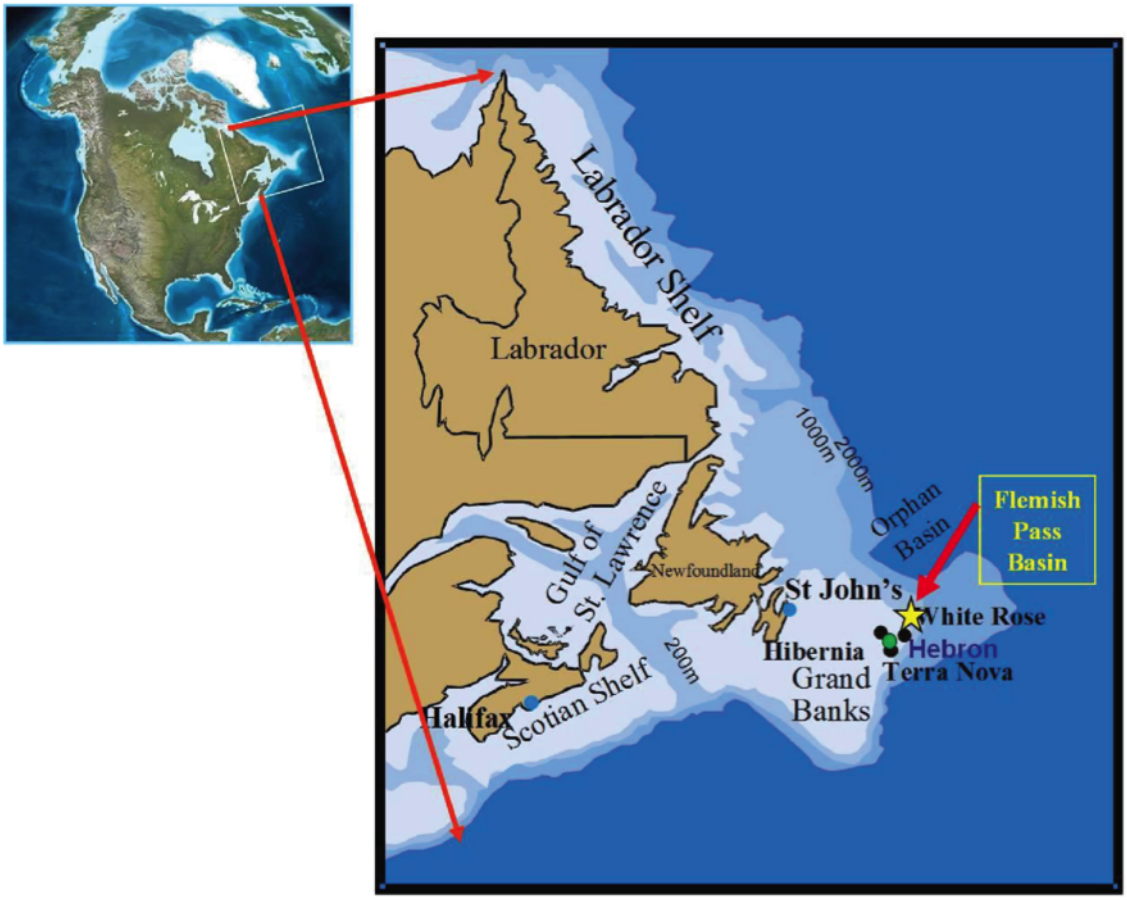

Figure 1.6: Location of Newfoundland and Labrador's major offshore oil fields (black dots) and of the Flemish Pass Basin. Geographically, the basin is located in the bathymetrical saddle between the Grand Banks of Newfoundland and the Flemish Cap (from Enachescu, 2014).

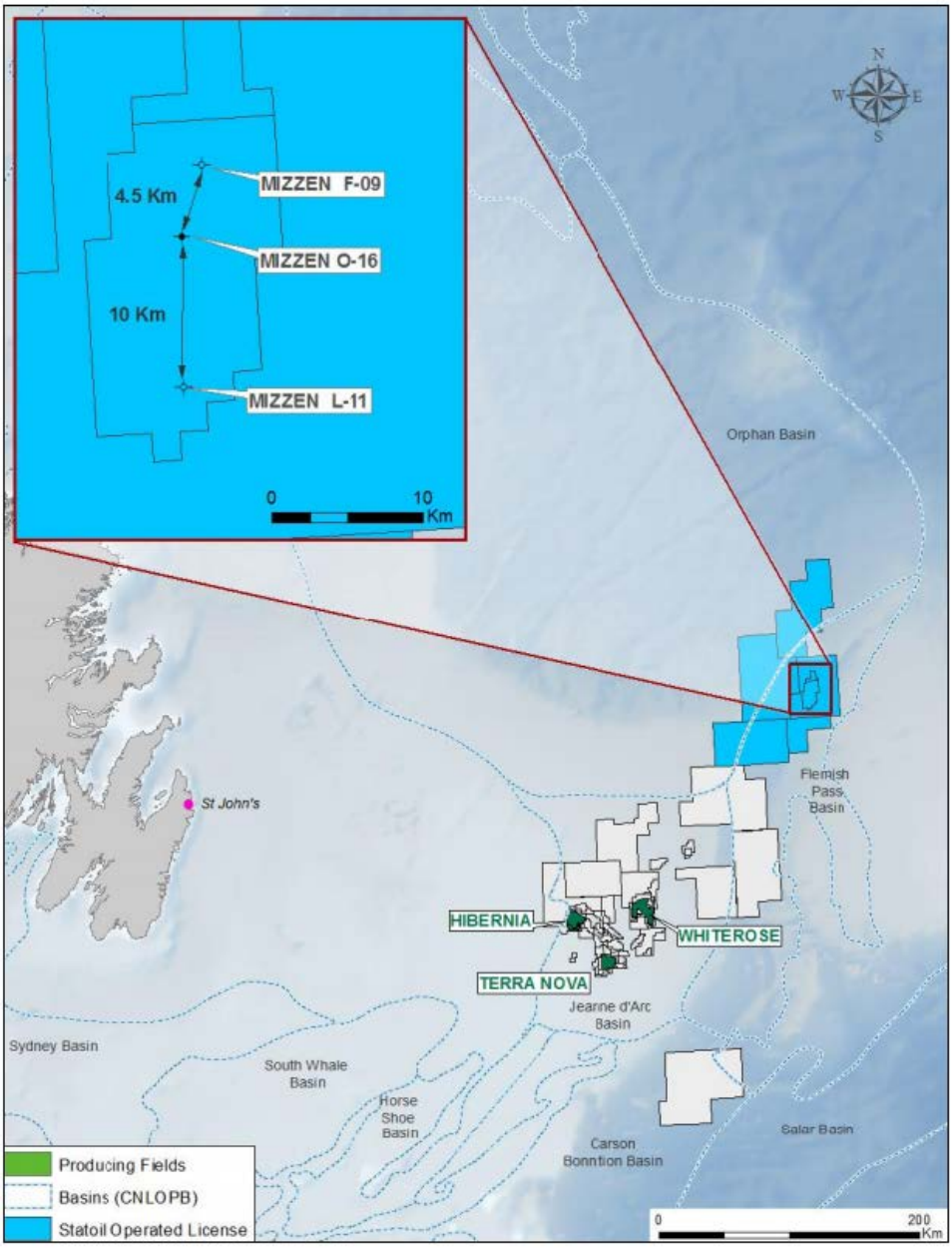

Figure 1.7: Regional map of offshore Newfoundland with license boundaries and generalized basin outlines from the C-NLOPB (from Ainsworth et al., 2015).

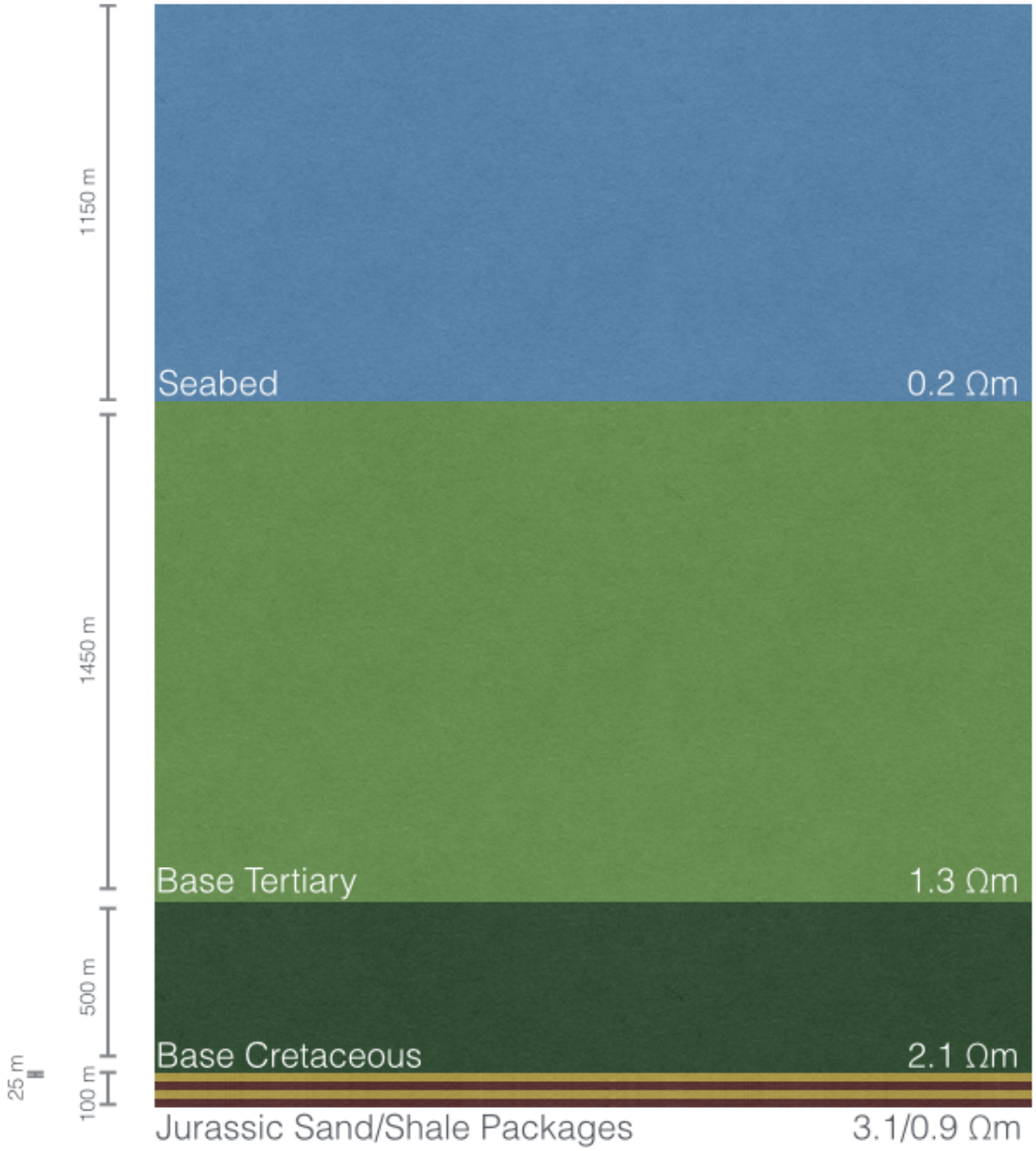

Figure 1.8: Type stratigraphic section of the defining resistivity sections of the survey area. The resistivity values have been provided by Suncor Energy, and are derived by them from well log estimates.

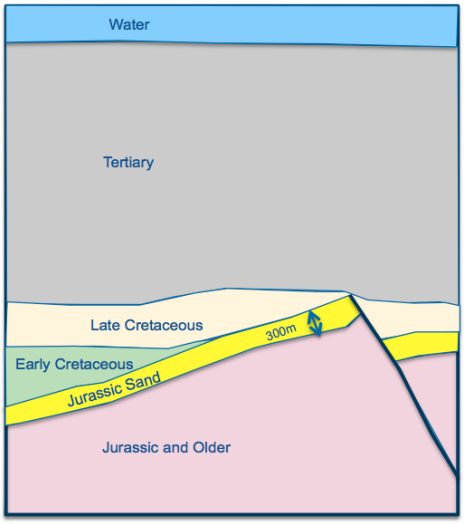

(a)

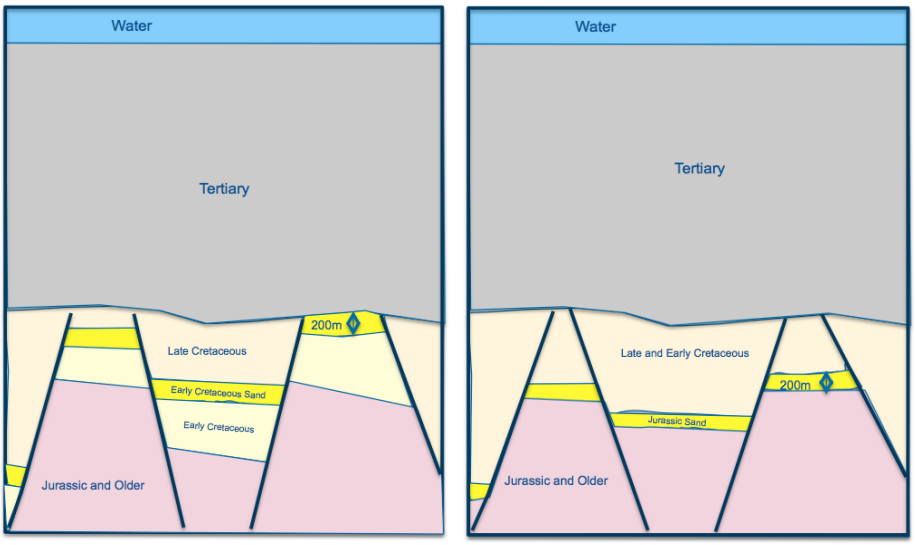

(b) (c)

Figure 1.9: Schematic representations of *Models 1* to *3* (see Section 4.5 for description) of the structural trap scenarios provided by Suncor Energy. These are used as the basis of structural reservoir development for the forward modelling. Blue represents the water layer; grey the region to the Base Tertiary horizon; yellow the late and early Cretaceous regions; yellow the sand package that will represent the reservoir of interest; and pink Jurassic and older sediment. The schematic does not consider the basement region, as it does not represent the entire computational domain to be considered, only the structurally complex reservoir region.

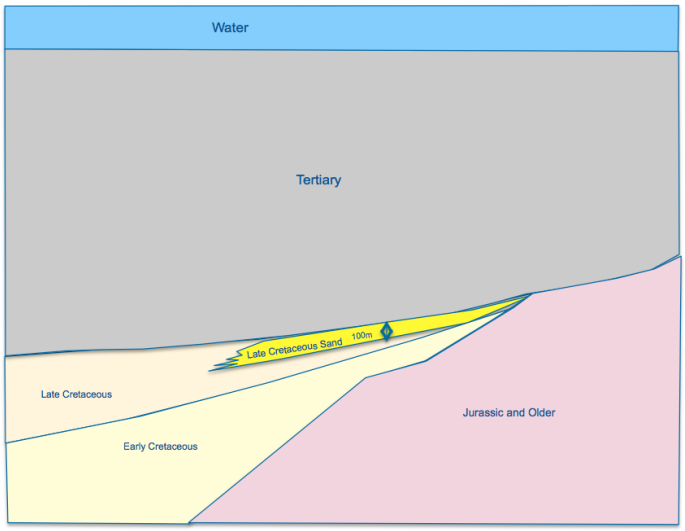

(a)

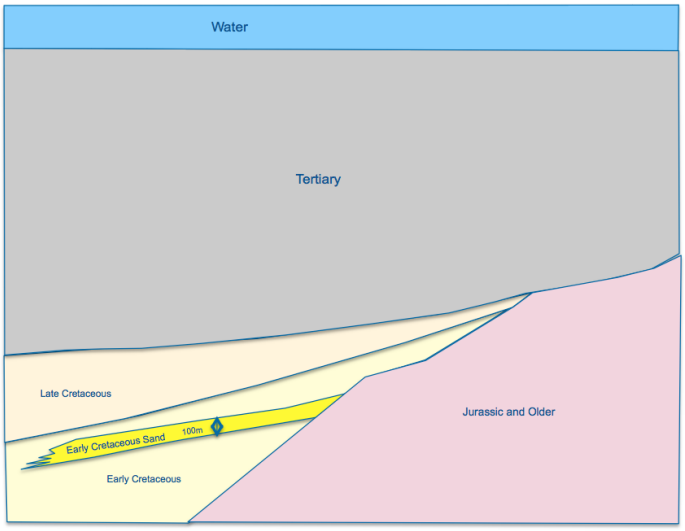

(b)

Figure 1.10: Schematic representations of *Models 4* and *5* (see Section 4.5 for description) of the structural trap scenarios provided by Suncor Energy. These are used as the basis of structural reservoir development for the forward modelling. Blue represents the water layer; grey the region to the Base Tertiary horizon; yellow the late and early Cretaceous regions; yellow the sand package that will represent the reservoir of interest; and pink Jurassic and older sediment. The schematic does not consider the basement region, as it does not represent the entire computational domain to be considered, only the structurally complex reservoir region.

Chapter 2

Synthetic Modelling and Mathematical Methods

2.1 The Finite-Element Method

For three-dimensional geophysical electromagnetic (EM) problems, such as those explored in this study, there is the choice of three approaches for synthesizing data for subsurface resistivity distributions: the integral equation (IE), finite-difference (FD) and finite-element (FE) methods. While each have their specific advantages and disadvantages, it is most important to assess a method's ability to model the specific environment in question. While the IE method has an extensive repertoire historically (e.g. Hohmann, 1975; Lajoie and West, 1976), the approach is most successful for a localized conductivity anomaly in an otherwise simple background model; it is unsuitable for the complex, realistic models

considered in this study. The FD method, likewise, has an extensive body of research behind it (e.g., Wang and Hohmann, 1993; Mackie et al., 1994) and although the models which the FD method is suitable for can be significantly more complex than the IE method, one is limited to a rectilinear formation in meshing. This prevents the FD method from accurately modelling the curves of complex-shaped volumes and irregular geometries in the subsurface, forcing inaccuracies in the resolution of the models. This is particularly significant in the modelling of hydrocarbon systems, as accurate volumes are highly valued when assessing the success of a geologic play whose real Earth geometry (i.e. bathymetry, stratigraphy and fault structure) cannot be modelled by simple planes.

As a result, 3D forward modelling of EM data using the finite-element method (FEM) has received increased attention. The FE solution to the EM problem is given by expanding the approximate EM field in terms of localized basis functions, weighting the residual of the relevant differential equations and integrating over the whole computational domain (Jin, 2002; Monk, 2003). Each of these techniques can be readily applied to unstructured meshes, allowing irregular interfaces to be modelled accurately. This method also gives flexibility in local refinement in regions of interest (e.g. in source and observation points and regions of exceptionally complex geology) and coarsening the mesh close to domain boundaries to reduce the total number of cells required.

The concept of formulation of the finite-element method is the principle of minimization (Coggon, 1971). For EM data, this has been shown to be most accurately achieved by edge-element (vector) basis functions (Nédéléc, 1980) and this continues to be the established FEM approach applied to geophysical EM models. This process involves solving the vector Helmholtz equation. Since solving this PDE for discretized linear basis functions of EM

fields generated by low frequencies (as is the case of this study) is not efficient, the electric field can be decomposed into magnetic vector ($\mathbf{A}$) and electric scalar (ϕ) potentials (Haber et al., 2000; Ansari and Farquharson, 2014). In conjunction with the Coulomb gauge condition, Haber et al. (2000) performed such an $\mathbf{A}$-ϕ decomposition of the electric field to derive a strongly decoupled system of differential equations for a FD solution. This method was historically performed using the FE method for structured rectangular meshes (Mitsuhata and Uchida, 2004; Farquharson and Miensopust, 2011), but was presented by Schwarzbach (2009) on unstructured meshes using a mixed $\mathbf{E}$-V formulation of the Helmholtz equation, which used nodal-elements for the scalar potential V and edge elements for the electric field. With this added scalar term, the rate of convergence for low frequencies improved. The forward modelling component of this study uses the CSEM3DFWD formulation developed by Ansari and Farquharson (2014), with details discussed in Section 2.2. This method was chosen based on its availability to Memorial University and for the full $\mathbf{A}$-ϕ decomposition for unstructured tetrahedral grids that solutions in the environments considered require.

2.2 The Forward Problem

Details of the forward modelling method can be seen in Ansari and Farquharson (2014), where the development of the CSEM3DFWD code is discussed at great length. Through manipulation of Faraday's law of induction and Ampère's law, the E-field Helmholtz equation is obtained:

$$\nabla \times \nabla \times \mathbf{E} + i\omega\mu_0\sigma\mathbf{E} = -i\omega\mu_0\mathbf{J^s} \tag{2.1}$$

where $\mathbf{E}$ is the electric field and $\mathbf{J^s}$ is the current density of the EM source. The equation is also defined by the angular frequency, ω, and magnetic permeability of free space, μ_0. Using the divergence conditions of the electric field and magnetic flux density as well as Faraday's law of induction, we can replace $\mathbf{E}$ with potentials:

$$\mathbf{E} = -i\omega\mathbf{A} - \nabla\phi, \tag{2.2}$$

which gives:

$$\nabla \times \nabla \times \mathbf{A} + i\omega\mu_0\sigma\mathbf{A} + \mu_0\sigma\nabla\phi = \mu_0\mathbf{J^s}, \tag{2.3}$$

where σ represents the conductivity of the region.

While this now gives the complex functions of position and frequency required for the $\mathbf{A}$-ϕ decomposition, the conservation of charge equation is incorporated into an extra equation in order to develop a square system diagonally dominated by the terms from the vector and scalar potentials:

$$i\omega\nabla \cdot (\sigma\mathbf{A}) - \nabla \cdot (\sigma\nabla\phi) = -\nabla \cdot \mathbf{J^s}. \tag{2.4}$$

Solving this system of equations given by Equations 2.3 and 2.4 involves the natural boundary conditions of $\mathbf{A}$ and ϕ (Jin, 2002) as follows:

$$(\mathbf{n} \times \mathbf{A})_\Gamma = 0 \tag{2.5}$$

and

$$\phi_\Gamma = 0, \tag{2.6}$$

where Γ is the outer boundary, and $\mathbf{n}$ is the normal vector for the boundary surfaces of the domain.

This system is now discretized and solved using the FE approach. This solution is based on the method of weighted residuals (Jin, 2002). This method approximates the solution by means of weighting the residual of the differential equation by test functions and seeking to minimize these weighted residuals over the whole domain. The process uses a vector residual formed by approximated vector and scalar potentials ($\tilde{\mathbf{A}}$ and $\tilde{\phi}$, respectively) that are expressed in terms of basis functions and the coefficients of these functions are chosen to minimize weighted residuals. This is presented as a convergence curve, where the value of the residual is expressed as a function of iteration number (e.g. Figure 2.1).

To solve such equations, the computational domain is divided into unstructured tetrahedral elements, as described in Section 2.3. The approximated potentials are expressed in terms of basis functions:

$$\tilde{\mathbf{A}} = \sum_{j=1}^{n_A} \tilde{A}_j \mathbf{N}_j \tag{2.7}$$

and

$$\tilde{\phi} = \sum_{k=1}^{n_\phi} \tilde{\phi}_k N_k, \tag{2.8}$$

where $\mathbf{N}_j$ and N_k are vector and scalar basis functions, respectively. The piecewise linear

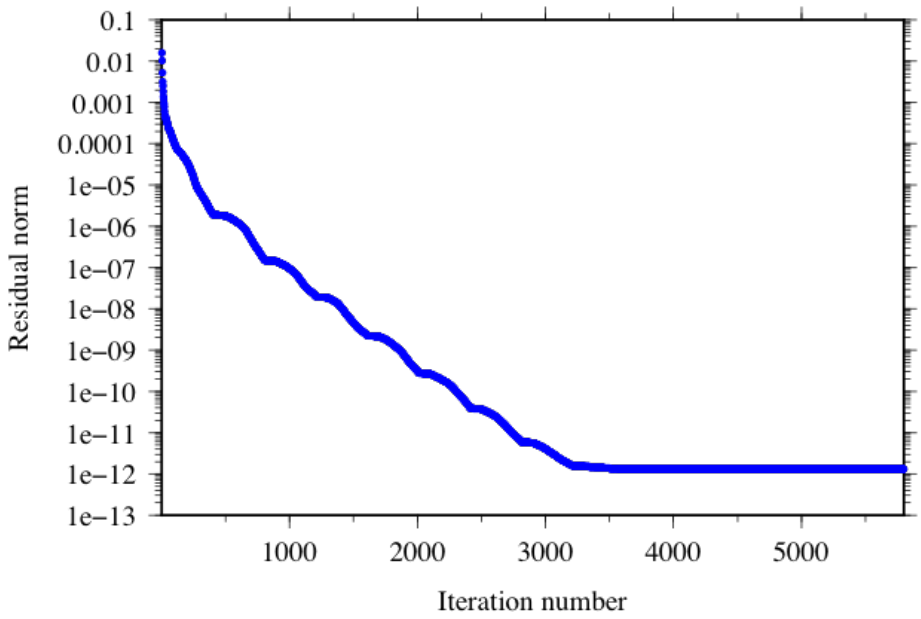

Figure 2.1: Sample of a convergence curve included in this study. The value of the weighted residual, which is minimized through an interative process, is presented as a function of iteration number.

polynomials that are used for these basis functions are based on the number of edges (n_A) and nodes (n_ϕ) in each element; in the case of the tetrahedral element, these values are 6 and 4, respectively. These polynomials develop the nodal-element basis functions for the scalar potential and edge-element basis functions for the vector potential. The tangential components of the vector basis functions, $\mathbf{N_j}$, are continuous from one tetrahedron to the next, and the scalar basis functions, N_j, are continuous to insure that the tangential components of ∇N_j are continuous across interfaces between regions of distinct conductivities. The approximate potentials are separated into their real and imaginary parts, which generates a real-valued matrix form for the system of equations required to solve the forward problem.

In preparation for solving the system of equations described above, homogenous Dirichlet boundary conditions for the vector and scalar potentials are implemented at the mesh boundary (Equations 2.5 and 2.6). The resulting system of equations is solved using the GMRES iterative solver from SPARSKIT (Saad, 1990) and is preconditioned using an incomplete LU decomposition approach (Saad, 2003). Once the system has been solved for real and imaginary parts of the vector and scalar potential, the electric field amplitude is obtained using Equation 2.2.

2.3 Model Building

Modelling marine CSEM systems demands accurate methods that represent highly complex domains and replicate a wide range of scales associated with geological complexities. While previous rectilinear approaches are satisfactory for simplified environments, it is important

that modelling methods — specifically in the meshes used to parameterize Earth models — are more sophisticated when exploring more realistically complex situations. Unstructured tetrahedral meshes enable arbitrary, general geological interfaces and bathymetry to be represented accurately. These meshes can also significantly reduce the problem size involved in forward and inverse calculations in comparison to rectilinear grids: cell volumes are easily increased in particular regions of the subsurface, while avoiding cells with large aspect ratios which can produce modelling challenges for numerical modelling.

As an example of rectilinear versus unstructured tetrahedral meshes, Figure 2.2 displays the representations of a geologically complex area in the Eastern Deeps zone of Voisey's Bay, Labrador, Canada. The first panel shows the wireframe geological model. The second panel shows a geophysical model parameterized in terms of a conventional rectilinear mesh, while the unstructured tetrahedral mesh is shown in the third panel. Rectilinear meshes can be seen to create inaccurate and poorly resolved representations of sharply dipping and conductively contrasting structures. A characteristic "staircase" pattern is seen across the sloping zones of both the ore body and the outcrop. The flexibility of unstructured meshes allows the sloping surfaces to be modelled smoothly, and a more accurate model can be generated.

Unstructured tetrahedral meshes can be created using publicly available software packages. This thesis uses Triangle v.1.6 (Shewchuk, 1996, 2002) to generate triangular 2D meshes, and TetGen v.1.4.3 (Si and Gartner, 2004, 2005; Si, 2007) to generate 3D tetrahedral meshes. 2D mesh generation is required for surface and structural boundaries, whereas 3D mesh generation is required to fill the volumes between the surfaces in the 3D model.

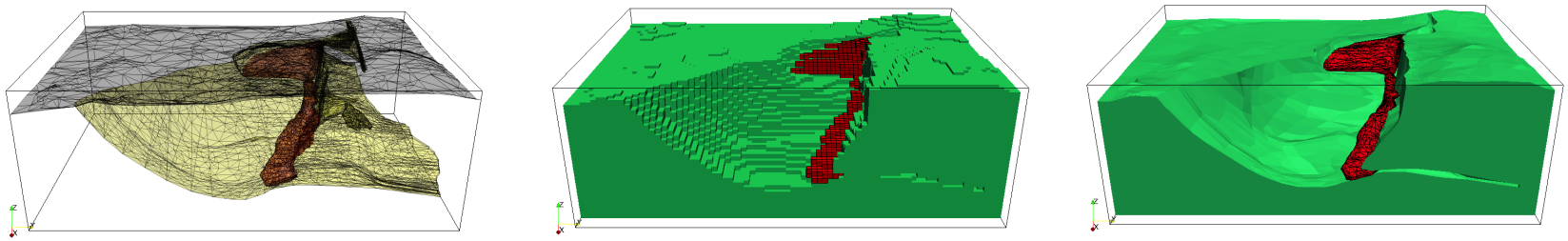

Figure 2.2: Wireframe mesh geological model (left), rectilinear mesh geophysical model (centre), and unstructured tetrahedral mesh geophysical model (right) of the Eastern Deeps zone of Voisey's Bay, Labrador, Canada (from Farquharson et al., 2014.)

In order to parameterize a region using TetGen, the region must be first defined by a set of node-defined, non-intersecting facets. In a simple case, the nodes represent the vertices of a polygon, and the facets represent the faces of this polygon (Figure 2.3). This set of facets is referred to as a piecewise polygonal complex (PPC), and TetGen works to create a volumetric mesh by first subdividing the PPC facets into triangles, then creating tetrahedra from these triangles and extending the tetrahedralization throughout the volume.

TetGen operates by reading *.poly* files where the defining information of the region is stored: this includes a list of the nodes, facets, holes, and regions which constitute the computational domain. In a standard *.poly* file (Figure 2.4), the coordinates of a minimum amount of nodes to define the PPC are listed, and inputted into a facet list to describe how the nodes are connected to create faces. The regional attribute list allows for physical properties to be assigned to each of the regions. Also, the attribute list can be used to restrict cell volume when desired.

Several command switches are employed by TetGen to ensure quality control on the mesh. The $-p$ flag generates the tetrahedral mesh for a PPC and outputs three files: *.node*, *.ele*, and $.face$. The *.node* file contains a list of three-dimensional points in Cartesian coordinates, the *.ele* file the list of tetrahedra, and the $.face$ file list of triangular faces. Using the $-q$ flag applies a minimum radius-edge ratio and the $-a$ flag applies a maximum tetrahedra volume constraint. These constrictions can be very beneficial in ensuring a proper aspect ratio of tetrahedra, and will minimize errors in the resulting EM forward model created by triangular facets with small angles. Volume constraints effectively allow control over the coarseness or refinement of the region. The $-A$ flag assigns the attributes defined in the regional attribute list, and the $-n$ flag is used to produce a *.neigh* file that

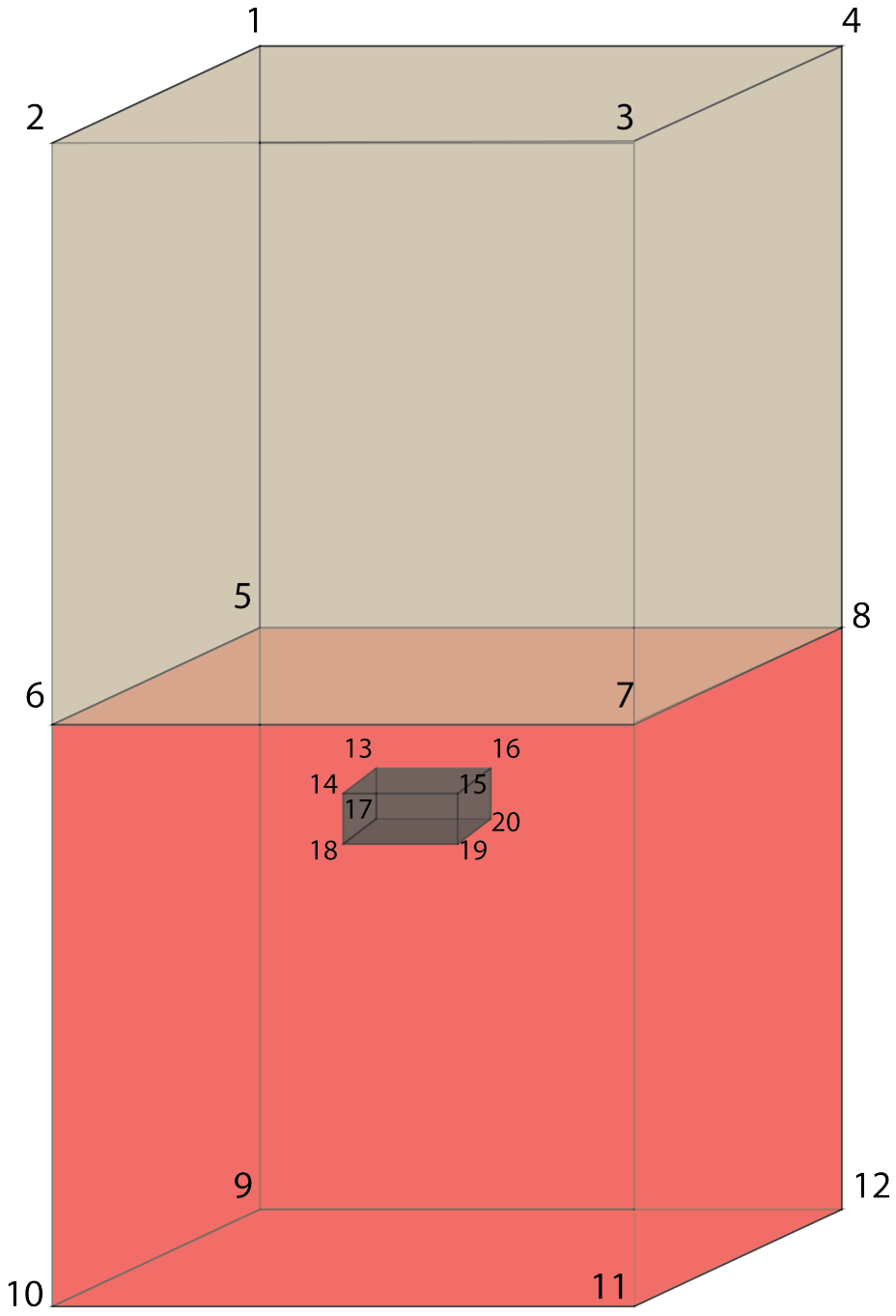

Figure 2.3: Configuration of nodes and facets for the simple block model comprised of a 1000 m × 1000 m × 100 m block in a 40 km × 40 km × 40 km halfspace. Note that the numbering of vertices in this model corresponds to the nodes in the *.poly* file (Figure 2.4).

```
20  3  0  1
 1   -0.200000000000E+05   -0.200000000000E+05   -0.200000000000E+05 1
 2   -0.200000000000E+05    0.200000000000E+05   -0.200000000000E+05 1
 3    0.200000000000E+05    0.200000000000E+05   -0.200000000000E+05 1
 4    0.200000000000E+05   -0.200000000000E+05   -0.200000000000E+05 1
 5   -0.200000000000E+05   -0.200000000000E+05    0.000000000000E+00 0
 6   -0.200000000000E+05    0.200000000000E+05    0.000000000000E+00 1
 7    0.200000000000E+05    0.200000000000E+05    0.000000000000E+00 0
 8    0.200000000000E+05   -0.200000000000E+05    0.000000000000E+00 0
 9   -0.200000000000E+05   -0.200000000000E+05    0.200000000000E+05 0
10   -0.200000000000E+05    0.200000000000E+05    0.200000000000E+05 0
11    0.200000000000E+05    0.200000000000E+05    0.200000000000E+05 0
12    0.200000000000E+05   -0.200000000000E+05    0.200000000000E+05 0
13   -0.500000000000E+03   -0.500000000000E+03    0.100000000000E+04 1
14   -0.500000000000E+03    0.500000000000E+03    0.100000000000E+04 1
15    0.500000000000E+03    0.500000000000E+03    0.100000000000E+04 1
16    0.500000000000E+03   -0.500000000000E+03    0.100000000000E+04 1
17   -0.500000000000E+03   -0.500000000000E+03    0.110000000000E+04 0
18   -0.500000000000E+03    0.500000000000E+03    0.110000000000E+04 0
19    0.500000000000E+03    0.500000000000E+03    0.110000000000E+04 0
20    0.500000000000E+03   -0.500000000000E+03    0.110000000000E+04 0
```

```
      17         1
1 0  1
 4     1     2     3     4
1 0  1
 4     1     2     6     5
1 0  1
 4     2     3     7     6
1 0  1
 4     3     4     8     7
1 0  1
 4     1     4     8     5
1 0  1
 4     5     6     7     8
1 0  0
 4     5     6    10     9
1 0  0
 4     6     7    11    10
1 0  0
 4     7     8    12    11
1 0  0
 4     5     8    12     9
1 0  0
 4     9    10    11    12
1 0  1
 4    13    14    15    16
1 0  0
 4    13    14    18    17
1 0  0
 4    14    15    19    18
1 0  0
 4    15    16    20    19
1 0  0
 4    13    16    20    17
1 0  0
 4    17    18    19    20

0

   3
   1    0.000000000000E+00    0.000000000000E+00   -0.100000000000E+05    1    0.100000000000E+30
   2    0.000000000000E+00    0.000000000000E+00    0.100000000000E+05    2    0.100000000000E+30
   3    0.000000000000E+00    0.000000000000E+00    0.105000000000E+04    3    0.100000000000E+30
```

Figure 2.4: The *.poly* file for the simple block model shown in Figure 2.3. The first section shows the Cartesian cooordinates of the nodes, the second section the connection of the nodes into faces, and the third section the representative position of attribute regions. The last column in the third section reperesents the maximum volume for a tetrahedra in that region.

specifies the neighbours of each cell.

Using TetGen to define simple models is very straight forward. In regions that can be approximated using blocks, each vertex of the block is defined by a node, creating 8 nodes per block. Each facet is then defined by 4 of these nodes, to create 6 faces per block. For more complex regions, this representation becomes cumbersome and the resulting process of model generation is problematic. A suite of programs developed by Peter Lelièvre enable more complex polygonal structures (Lelièvre et al., 2012). For example, the canonical disk model described in Ansari and Farquharson (2014) used the *disk* software created by Lelièvre to define the nodes and facets of a flat, thin, circular cylinder to approximate the hydrocarbon reservoir. This is achieved by approximating the edges of the circles that form the top and bottom of the cylinder as minute segments through the joining of 60 nodes around the circumference. In realistic models with varying bathymetry and irregular contacts, the program FacetModeller can be used — a graphical user interface for creating and editing PPCs developed initially by Gary Blades as part of the High Performance Computing for Geophysical Applications project at Memorial Unviersity, and subsequently revised and extended by Peter Lelièvre. Nodes can be manually added and edited from georeferenced cross-sections in a 2D working window, and combined with sections in the same volume of interest in a 3D viewer window. For this project, the lithological boundaries were meshed using Triangle (as described above), then edited and combined using FacetModeller (Figures 2.5 and 2.6; see details in Chapters 3 and 4).

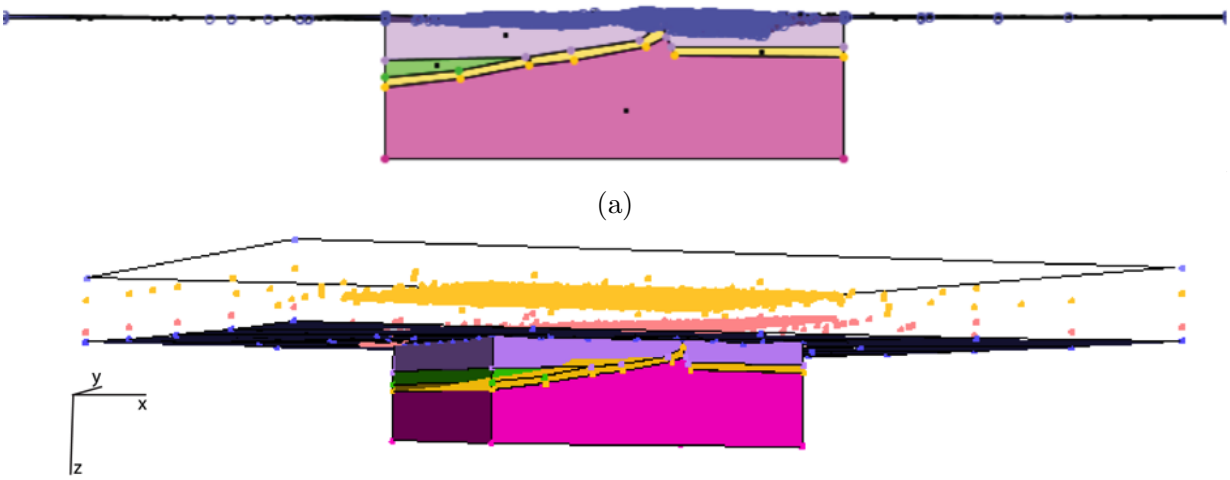

(a)

(b)

Figure 2.5: Panel (a) xz view of FacetModeller at $y = 7500$ m showing the nodes and ajoining facets that comprise a reservoir section (lavender, green, yellow) of *Model 1* (see Section 4.5 for details) with the *Base Cretaceous* layer (purple); panel (b) 3D view of the entire reservoir section in panel (a) including nodes of the *Water Bottom* (gold) and *Base Tertiary* (salmon) horizons

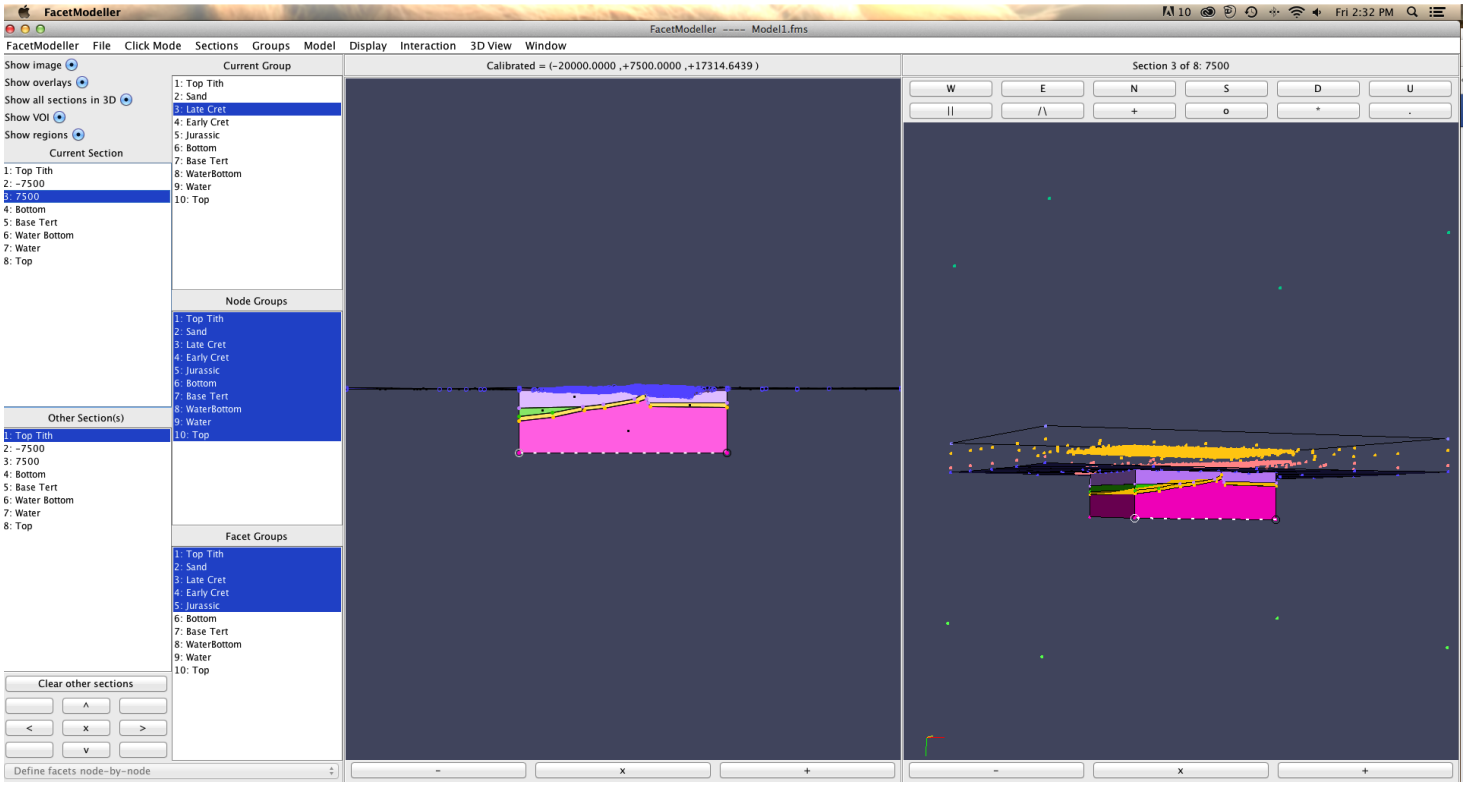

Figure 2.6: Full-screen view of the model in Figure 2.5 including the user interface. Facets are defined by selecting the *Define facets node-by-node* (seen bottom left) option from the *Click Mode* menu (top left), allowing the user to select nodes in the appropriate sequence in which facets are formed. During the process, each defined edge is presented as a white, dashed line (bottom of the pink region), and once the facet is completed by ending the edge selection process on the same node on which the process began, the facet is displayed as the colour of the respected region, as defined by the user.

Chapter 3

Simple Earth Models

3.1 Introduction

In order to ensure validity of all subsequent modelling scenarios and to develop the modelling ability and code familiarity of the user, a series of one-dimensional models were developed and data synthesized using CSEM3DFWD. The computed results were compared to those of the DIPOLE1D forward modelling code of Key (2009), which uses a semi-analytic method that is appropriate for a horizontally layered (i.e. 1D) Earth model only. The modelling scenarios assessed will progressively increase in complexity: from a refinement assessment using homogeneous halfspaces to layered Earths, and then to canonical disk reservoir models and Flemish Pass stratigraphy models.

As previously described, the maximum measurable increase in electric field in the CSEM method will occur in the inline direction, as the purely radial electric field lines strongly

excite the subsurface vertically. As this sensitivity study is mainly concerned with the basic detectability of these resistive reservoirs, only the inline results will be displayed. This represents the typical survey design carried forward in oil and gas exploration (e.g., Eidesmo et al., 2002; Constable and Weiss, 2006; Brad Bonnell and Mike Livingston, Suncor Energy).

The results are equally products of the offset of a target from the source. At the source position (i.e. 0 m offset) electric energy of the source is at its maximum, and thus dominates the electric field amplitude in all scenarios (example, Figure 3.2). As a result, affects of the reservoir on the electric field amplitude will only be visible at an offset distance from the source, when the source energy has dissipated with distance.

In order for an example to successfully run and thus deliver results for a particular model, the memory required must not exceed the maximum amound available. The memory used is proportional to two parameters: the Krylov subspace used in the GMRES solver and the amount of cells in the model. As the Krylov and cell number also dictate the refinement, convergence ability and thus accuracy of the results in question, a balance must be achieved. Each of these models are run on a 48 node, 600-core, 14-GPU hybrid CPU/GPU computer cluster, which are comprised of both 12-core and 16-core nodes with 24 GB and 64 GB of memory, respectively. Despite the memory capacity of the 16-core node, computational issues (i.e. segmentation faults) were experienced for models using over 30 GB of memory.

Simpler models (ie. models discussed in this chapter) can achieve results on a 200 Krylov subspace, using 1 GB of memory on average for a standard running time of 30

minutes. More complex models, incorporating bathymetry, and reservoir geometries require an increase in the Krylov subspace to 400 to reach appropriate convergence, and use upwards of 25 GB of memory for models of approximately 1,500,000 cells. As this memory use approaches the limit of capability for the GPU cluster, it is imperitive to be mindful of minimizing the cell usage of the more complex models.

3.2 Halfspaces

The preliminary stages of model development involved a series of simple halfspace Earth models. The primary purposes of these models were two-fold: (a) comparing this study's results to known analytical results tests the accuracy of or show limitations in this study's methods, and (b) determining the appropriate amount of refinement required about the source and observation locations in the mesh. The models were designed with the intent to balance an adequate amount of refinement to generate quality results with an amount of cells that does not require excessive computer memory.

The following series comprises a homogeneous halfspace of 1.0 S/m representing the conductivity of the sediment, with an overlying layer of 3.2 S/m representing the conductivity of seawater. Each model uses varying levels of refinement: the refinement in a region is achieved by constraining the maximum volume of the cells in that region, with more refinement corresponding to smaller cells in that particular region. Regions of refinement are required around the source, to accurately model the rapid decrease in the electric field close to the source and at the observation locations, specifically, having small tetrahedra close to each observation. This is achieved by placing a thin rectangular prism in appropriate

positions, acting to decrease the cell size via volume constraint in the prism. It would be ideal to surround both the source and observation locations by this restricting volume: this is achievable for the source location, but is limited for the observation locations existing on the water bottom, as adding a region above and below the observations would result in an invalid intersection between the facets of the refinement prism and the facets of the water bottom horizon. The addition is given the same conductivity as the region that it lies in (e.g. the source refinement prism will have a conductivity of 3.2 S/m, as it lies in the water region).

As an example of the importance of refinement, Figure 3.1 shows a 30 km $\times$ 30 km $\times$30 km mesh that has a region of refinement extending from -5 to 5 m in the x- and y-directions respectively, and from 800 to 1000 m in the z-direction, which generates a tetrahedral mesh comprised of 15,261 cells, 2,603 nodes and 145 edges. This region of refinement is selected to refine the area around the line source extending from x = -100 to 0 m. However, the z-distance is considerable from the -100 m source position and seabed observation locations. This resulted in large cells in these areas, which is reflected in the results shown in Figure 3.2. Note that the results follow the pattern of the semi-analytical results, but the large cells at the observation locations generate a stair-stepping pattern — multiple observations are within individual cells — meaning that this refinement is too coarse. The results were generated for a 1 Am, 1 Hz source, using a Krylov subspace dimension of 200 for the GMRES solver. A total of 5800 iterations were used by the GMRES solver, although proper convergence of 10^{-12} was reached after approximately 900 iterations (Figure 3.3).

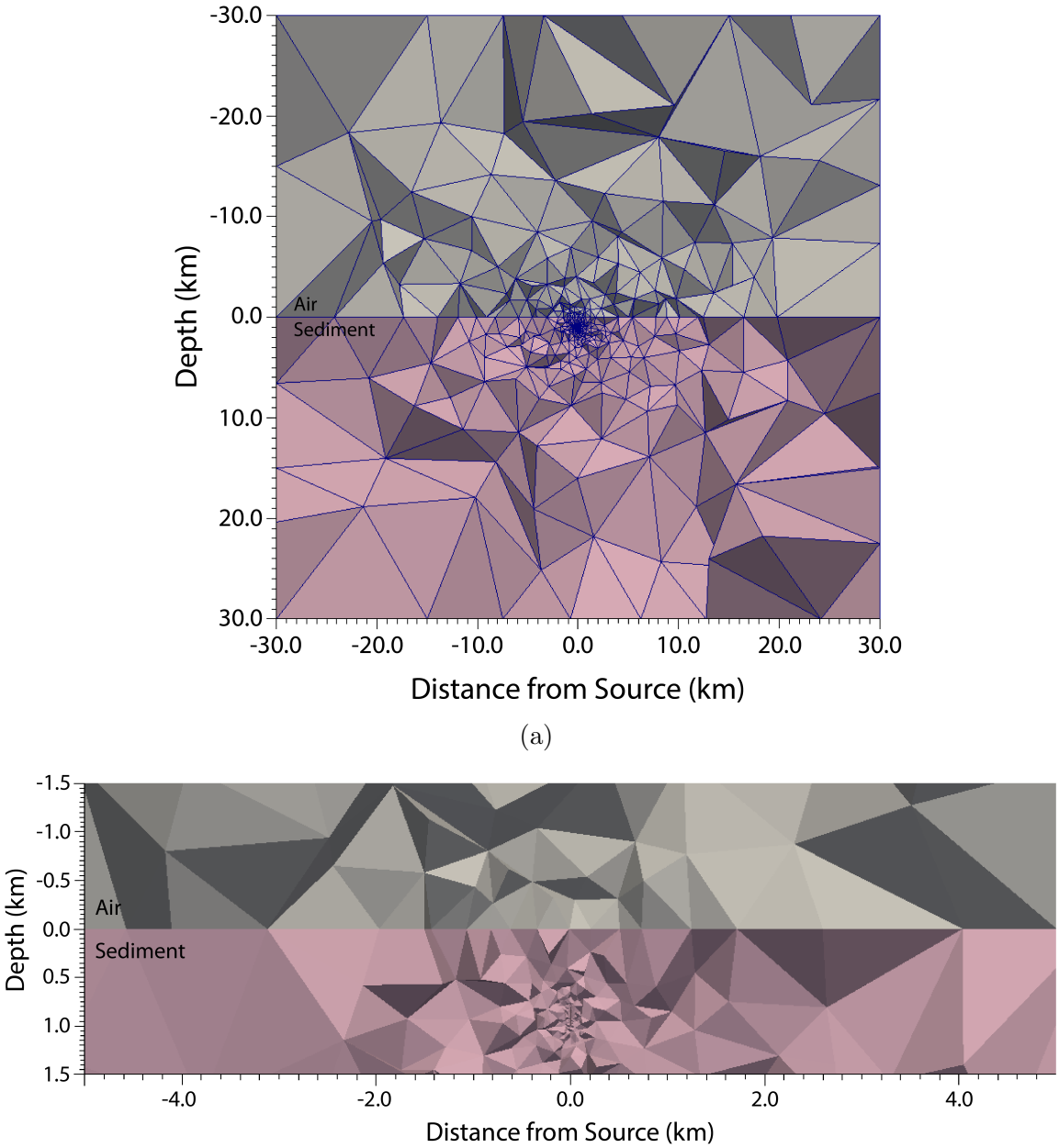

(a)

(b)

Figure 3.1: Cross-sections centered at $y = 0$ m of the halfspace model with *Very Coarse* refinement. Panel (a) full view; panel (b) enhanced view of the refinement. The source is an electric line source, extending from -100 to 0 m in the x-direction. The water layer (grey) has a conductivity of 3.2 S/m, and the sediment layer (pink) has a conductivity of 1.0 S/m.

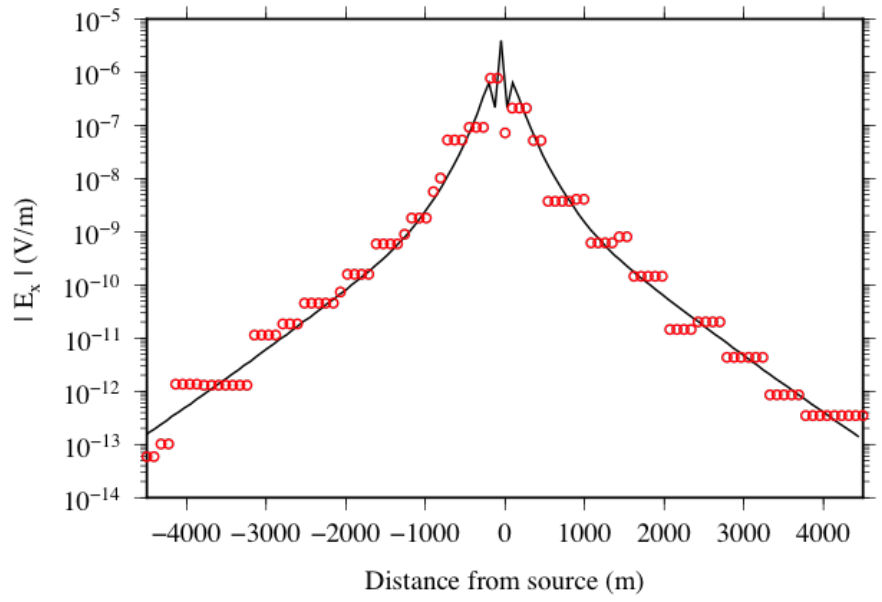

(a)

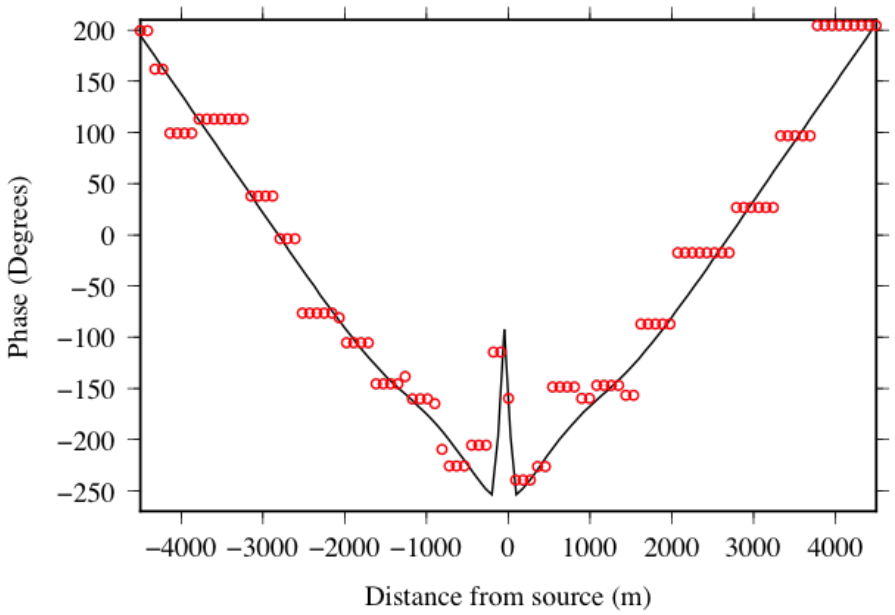

(b)

Figure 3.2: Panel (a) inline electric field amplitude and panel (b) phase results for the *Very Coarse Mesh* (Figure 3.1) using a 1 Am, 1 Hz source. Red circles indicate values computed using the mesh in Figure 3.1; the black lines indicate the semi-analytical results from DIPOLE1D. Steps in the 3D response are a result of the coarse refinement.

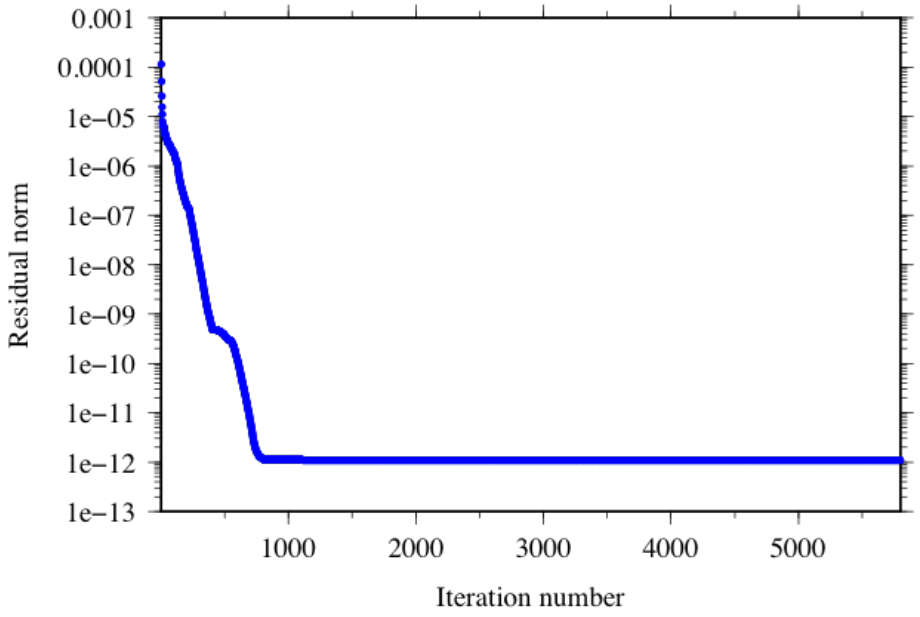

Figure 3.3: Convergence curve for the GMRES iterative solver for the results of the *Very Coarse Mesh* (Figure 3.2).

Figure 3.4 shows the mesh generated with similar dimensions to that in Figure 3.1, but with modified refinement extending similarly in the x- and y-directions, but positioned between 95 and 105 m above the interface of the two media; the region of refinement encompasses the source position. This results in a mesh with 12,678 cells, 2,167 nodes and 87 edges. The source parameters, interative solver inputs and physical properties are the same as in the previous example. The results for this example are shown in Figures 3.5 and 3.6. In relation to the results in Figure 3.2, the results in Figure 3.5 have a slightly more accurate match to the analytical results, with the data having less of a staircasing pattern around the source (i.e. 0 m offset). Notably, the area of refinement in this model is smaller than in the previous case, but is more appropriately positioned to the source region, thus, improving results, particularly surrounding the source region. However, neglecting to create refinement at the observation locations results in cells that are still too large to generate acceptable results, with the stair-casing still evident in Figure 3.5.

Figures 3.7 and 3.8 show a mesh with added refinement at the observation locations, significantly decreasing the cell size for this area of the mesh. The respective refinement regions extend from -101 to 1 m in the x-direction, -1 to 1 m y-directions and 98 to 105 m above the interface in the z-direction for the source, and -4500 to 4500 m in the x-direction, -5 to 5 m in the y-direction and 10 to 20 m below the interface in the z-direction (Figure 3.8). This creates a substantial increase in number of cells, nodes, and edges to 266,152, 43,410, and 3,135, respectively. This acts to generate significantly improved data, which matches accurately the semi-analytical results (Figure 3.9) and reaches appropriate convergence (Figure 3.10). The refinement at the source and observation locations in this example will act as the basis for all refinement in subsequent models.

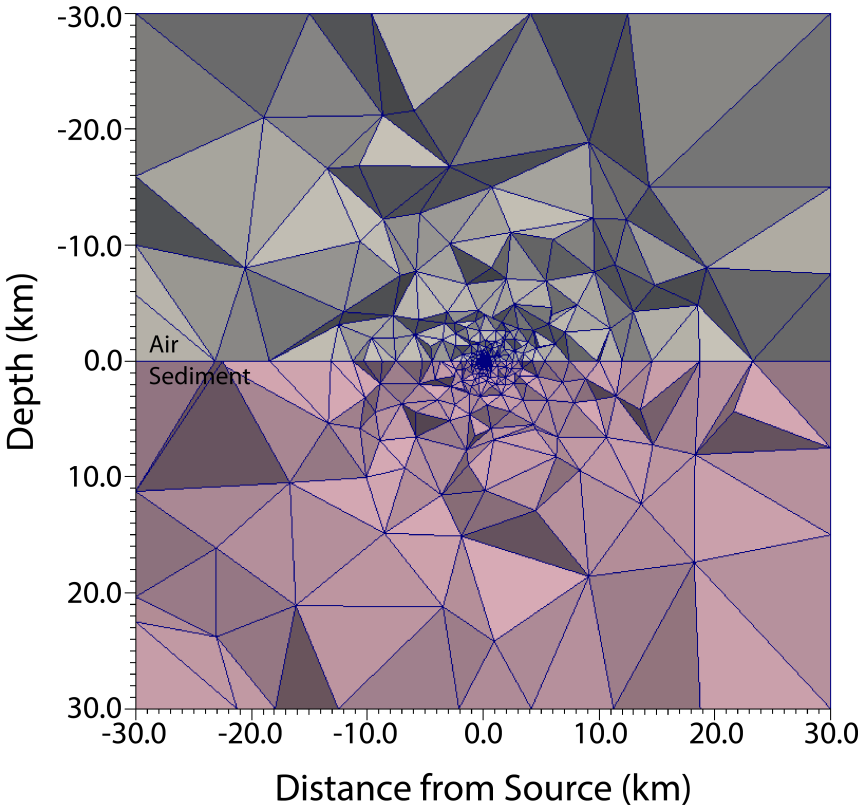

(a)

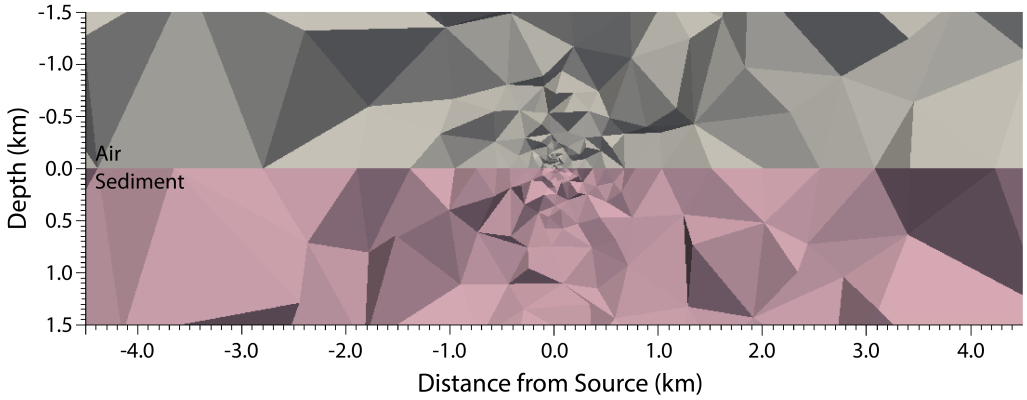

(b)

Figure 3.4: Cross-sections centered at $y = 0$ m of the halfspace model with *Coarse* refinement. Panel (a) full view; panel (b) enhanced view of the refinement. The source is an electric line source, extending from -100 to 0 m in the x-direction. The water layer (grey) has a conductivity of 3.2 S/m, and the sediment layer (pink) has a conductivity of 1.0 S/m

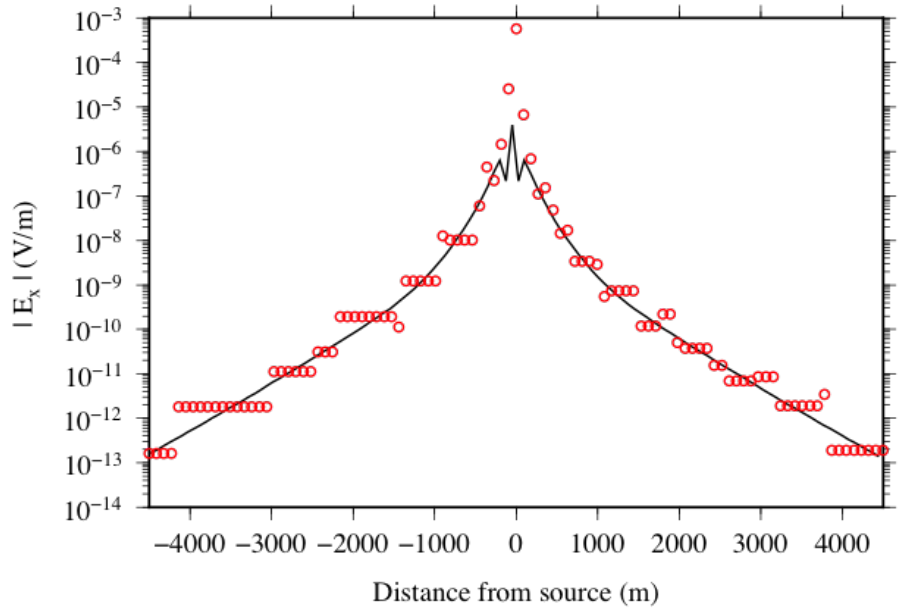

(a)

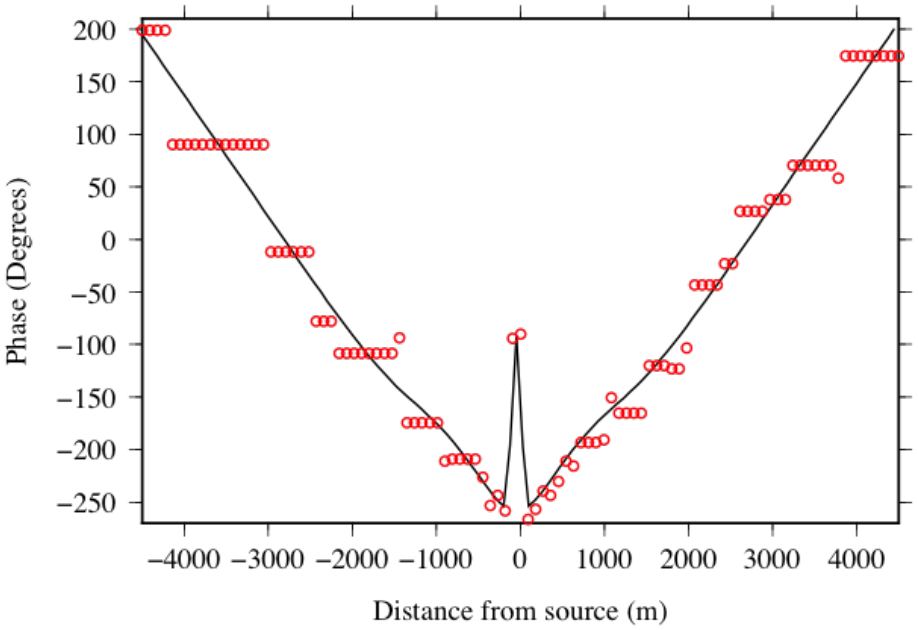

(b)

Figure 3.5: Panel (a) inline electric field amplitude and panel (b) phase results for the *Coarse Mesh* (Figure 3.4) using a 1 Am, 1 Hz source. Red circles indicate values computed using the mesh in Figure 3.4; the black lines indicate the semi-analytical results from DIPOLE1D.

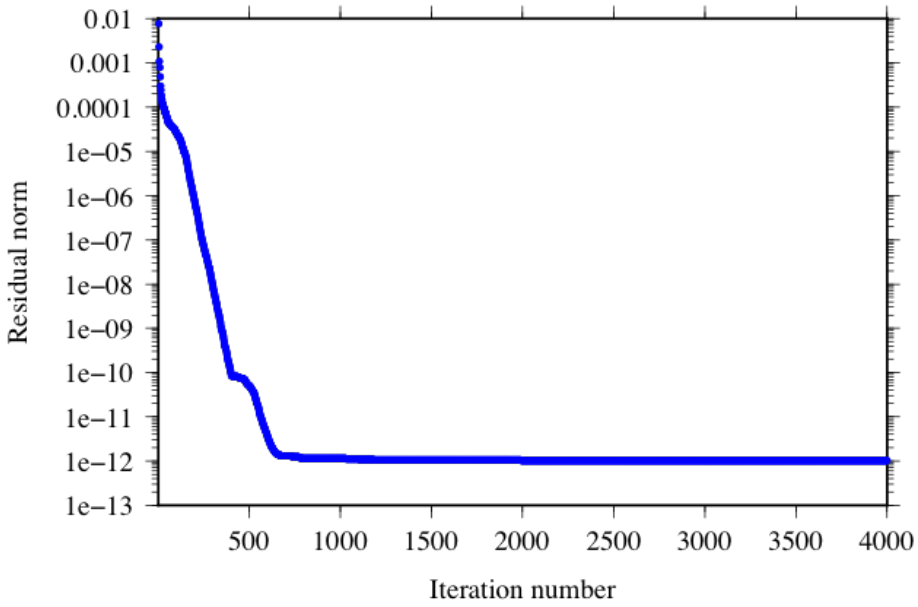

Figure 3.6: Convergence curve for the GMRES iterative solver for the results of the *Coarse Mesh* (Figure 3.4).

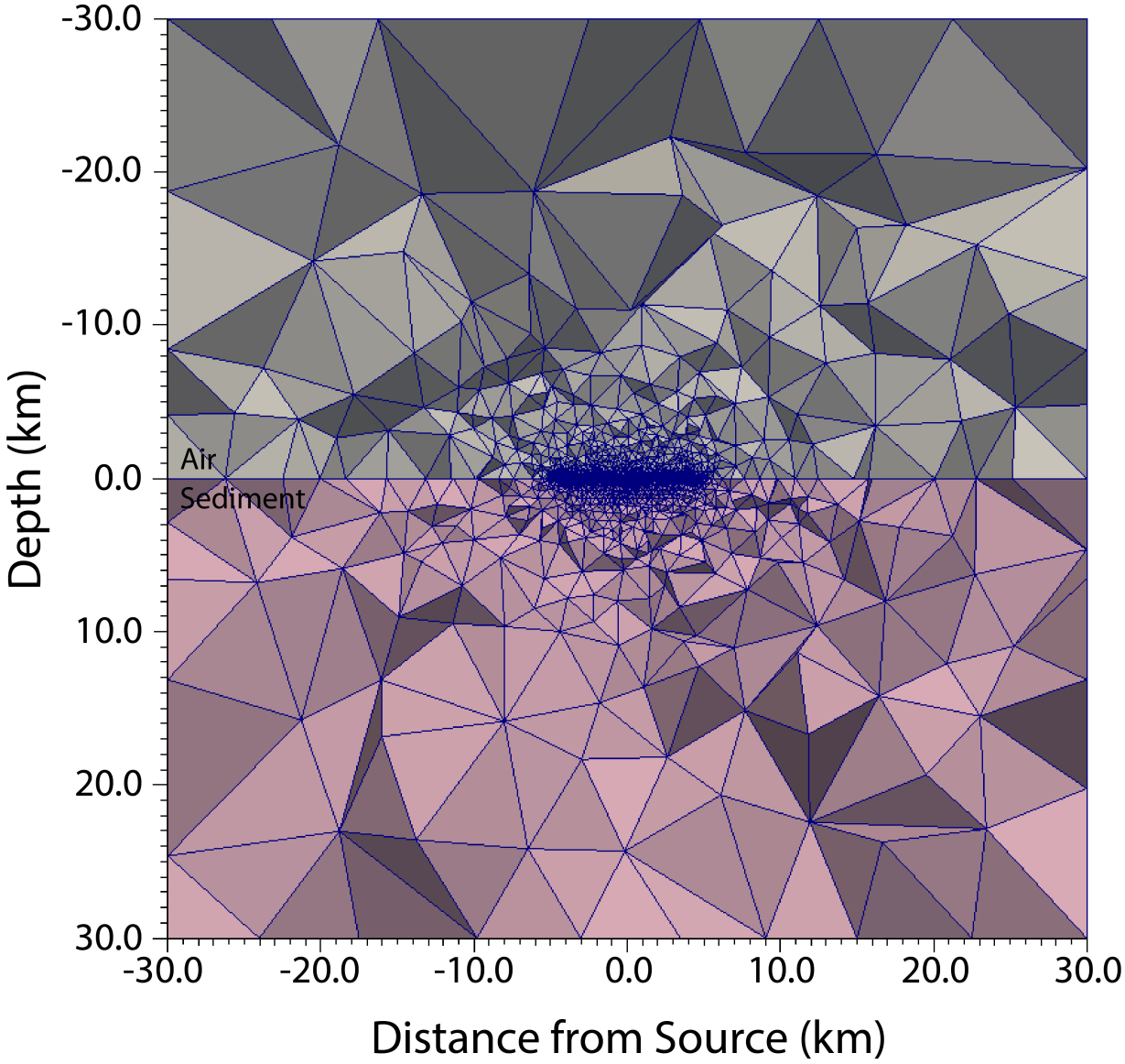

Figure 3.7: Cross-section of the entire computational domain centered at $y = 0$ m of the halfspace model with *Fine* refinement around both source and observation locations. The source is an electric line source, extending from -100 to 0 m in the x-direction. The water layer (grey) has a conductivity of 3.2 S/m, and the sediment layer (pink) has a conductivity of 1.0 S/m.

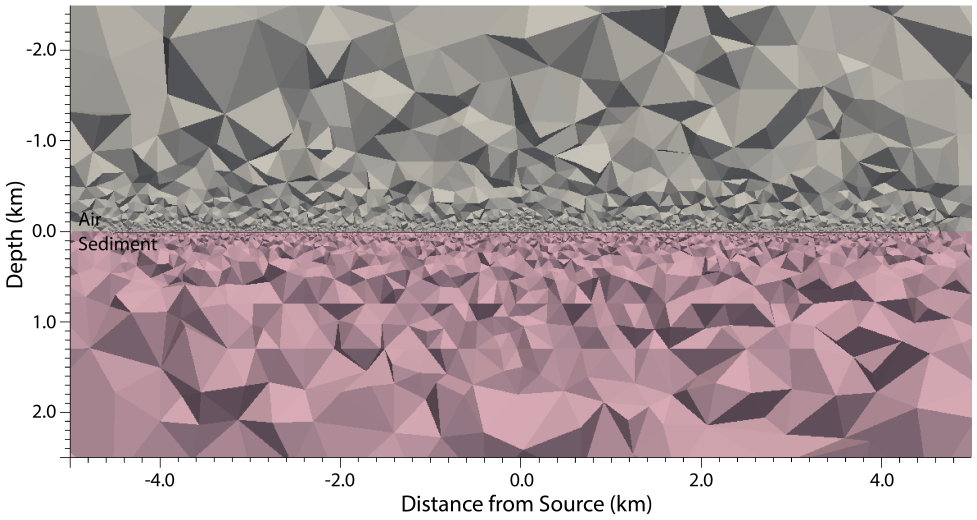

(a)

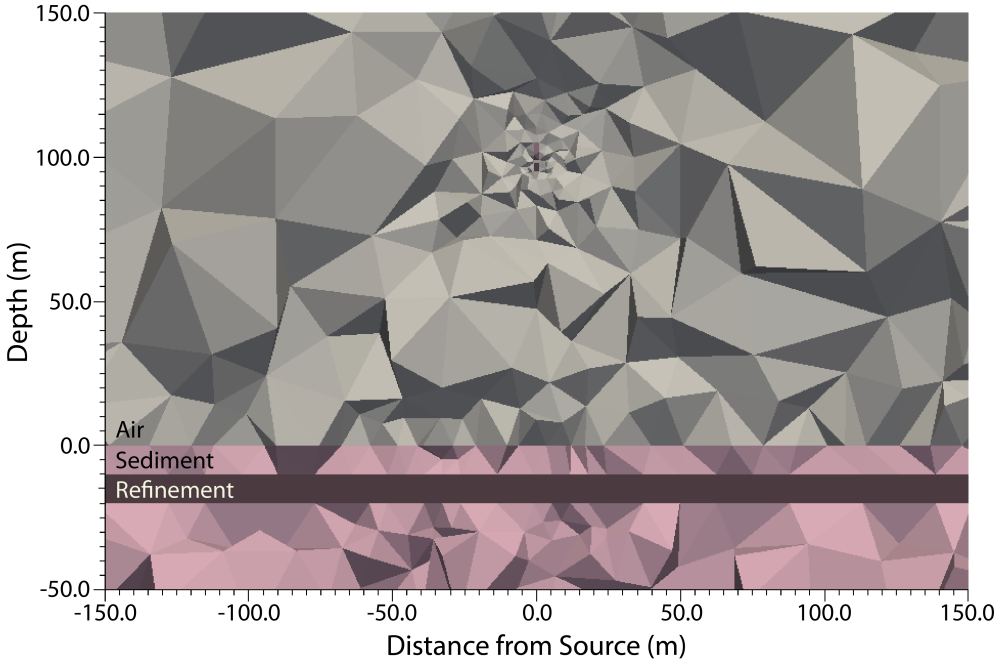

(b)

Figure 3.8: Cross-section centered at $y = 0$ m of the halfspace model with *Fine* refinement around both source and observation locations. Panel (a) enhanced view of observation refinement; panel (b) enhanced view of source refinement. The regions of source and observation refinement (maroon) have the same conductivities as their encompassing regions: 3.2 S/m and 1.0 S/m, respectively.

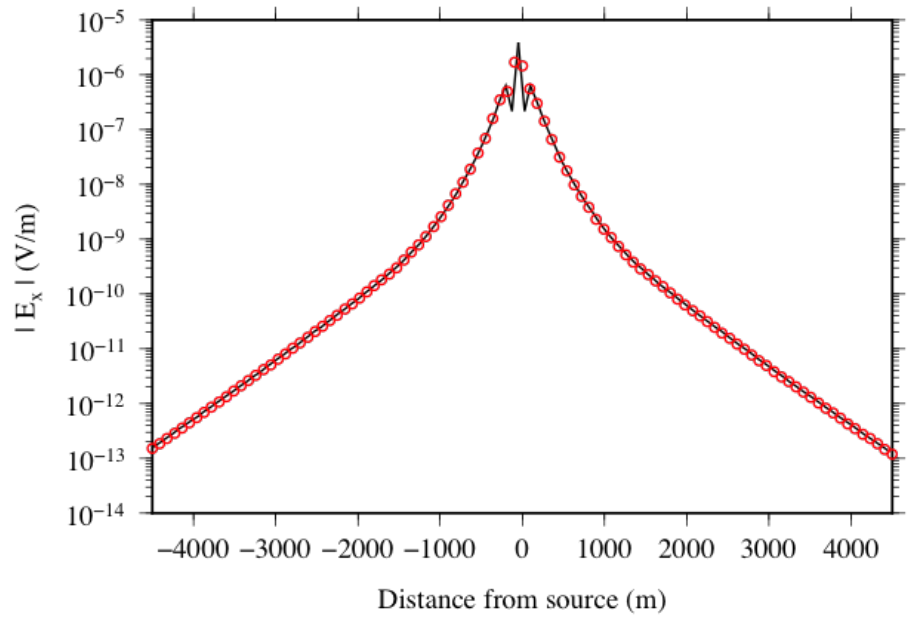

(a)

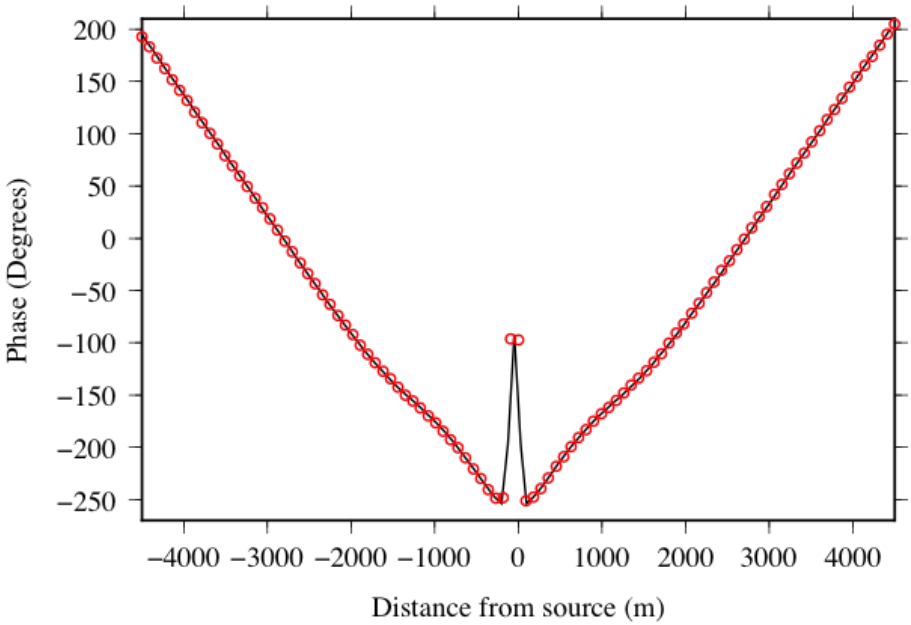

(b)

Figure 3.9: Panel (a) inline electric field amplitude and panel (b) phase results for the *Fine Mesh* (Figure 3.7) using a 1 Am, 1 Hz source.. Red circles indicate values computed using this mesh; the black lines indicate the semi-analytical results from DIPOLE1D.

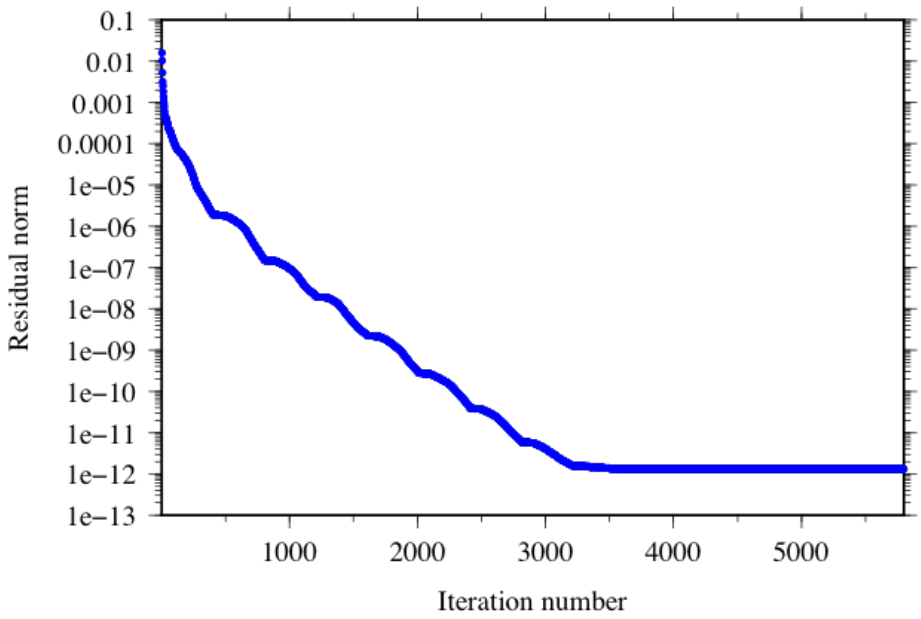

Figure 3.10: Convergence curve for the GMRES iterative solver for the results of the *Fine Mesh* (Figure 3.9).

3.3 Water Depths

As this study focuses on the use of marine CSEM methods, it is imperative to understand the effect of various water depths on electric field results; an investigation of these effects is reported now. For each water depth model, a source of 1 Am at 1 Hz frequency was x-oriented from -100 to 0 m at 100 m above the seabed. The model was comprised of three layers: air (10^{-8} S/m), water (3.2 S/m) and sediment (1.0 S/m) over a 60 km $\times$ 60 km $\times$ 60 km domain. Source refinement was added via a region extending -101 to 1 m in the x-direction and -1 to 1 m in the y-direction and 95 to 105 m above the water-sediment interface in the z-direction, and observation refinement extended from -12000 to 12000 m in the x-direction, -5 to 5 in the y-direction, and 10 to 20 m depth in the z-direction, in the same vein as the refinement in Figure 3.8. Each run uses a Krylov subspace of 200 and is compared to the modified analytical results of Key's DIPOLE1D. Because Key's data used a dipole located at the point (0, 0, -100) m, and in this study a realistic 100 m long electric dipole situated from -100 to 0 m in the x-direction is considered, the amplitude of the semi-analytical results were multiplied by 100 and shifted 50 m in the negative x-direction for comparison. The numbers of cells, nodes, and edges for each mesh are shown in Table 3.1. The increase in water depths leads to a larger region volume and a corresponding decrease in the constriction on the cell size. As a result, the region allowed for larger and thus less, cells in the region and in the computational domain as a whole; for example, increasing the water depth from 300 m to 3000 m decreases the number of cells from 1,072,599 to 277,628. Therefore, an increase in the number of cells and computer memory usage is observed as the water depth decreases. The meshes for three of the six different water depths (300 m,

1150 m, and 3000 m) are shown in Figures 3.11 to 3.14.

Water Depth (m)	Cells	Nodes	Edges
300	1,072,599	174,952	4,343
500	546,588	89,412	3,890
1000	329,394	53,842	3,506
1150	313,960	51,314	3,394
1500	288,427	47,179	3,397
3000	277,628	45,287	3,266

Table 3.1: Numbers of cells, nodes and edges for water depth models.

The most notable difference between the water-sediment halfspace models considered in the previous section and the water depth models here is the effect of air on the electric field amplitude results (see Figure 3.15). At an offset that is comparable to the water depth, the effect of the highly resistive air layer dominates the effect of the water and sediment. As a result, there is a sharp change in the slope of the curve of the electric field amplitude (for example at offset $\approx \pm$ 5200 m in Figure 3.15).

The electric field amplitudes and phases for all the water depths considered are shown in Figures 3.16 and 3.17. The results for the individual meshes, and the comparison with DIPOLE1D results, are displayed in Appendix A. Figures 3.16 and 3.17 also include results for the air-halfspace model (0 m water depth) and water-halfspace model (30000 m water depth), which act as maximum and minimum cases, respectively for electric field amplitude response.

These results appropriately and predictably display the "shallow-water problem" in offshore time-harmonic CSEM exploration: depths less than 300 m pose a significant challenge

for detection of subsurface targets because the weakly attenuated atmospheric response overprints the weaker response of the target.

This effect is particularly evident in the decrease of amplitude directly over the source (at 0 m) between the 0 m and 300 m water depth models. As water depth increases, there is a dampening of the rate of decrease, as the effect of the resistive air layer resides at larger offset (Figure 3.16). A similar pattern is visible in the phase results (Figure 3.17): in shallow water results, the resistive air layer creates a dramatic decrease, and subsequent levelling of the phase value at larger offsets that is absent in deep water results. In an effort to prepare for future 3D models which occur over deepwater reservoirs, a focus was put on water depths greater than 1000 m. Specifically, the 1150 m water depth in these 1D models was chosen as being the most representative of the water depth over the Flemish Pass Basin, which is the main scenario of interest in this thesis.

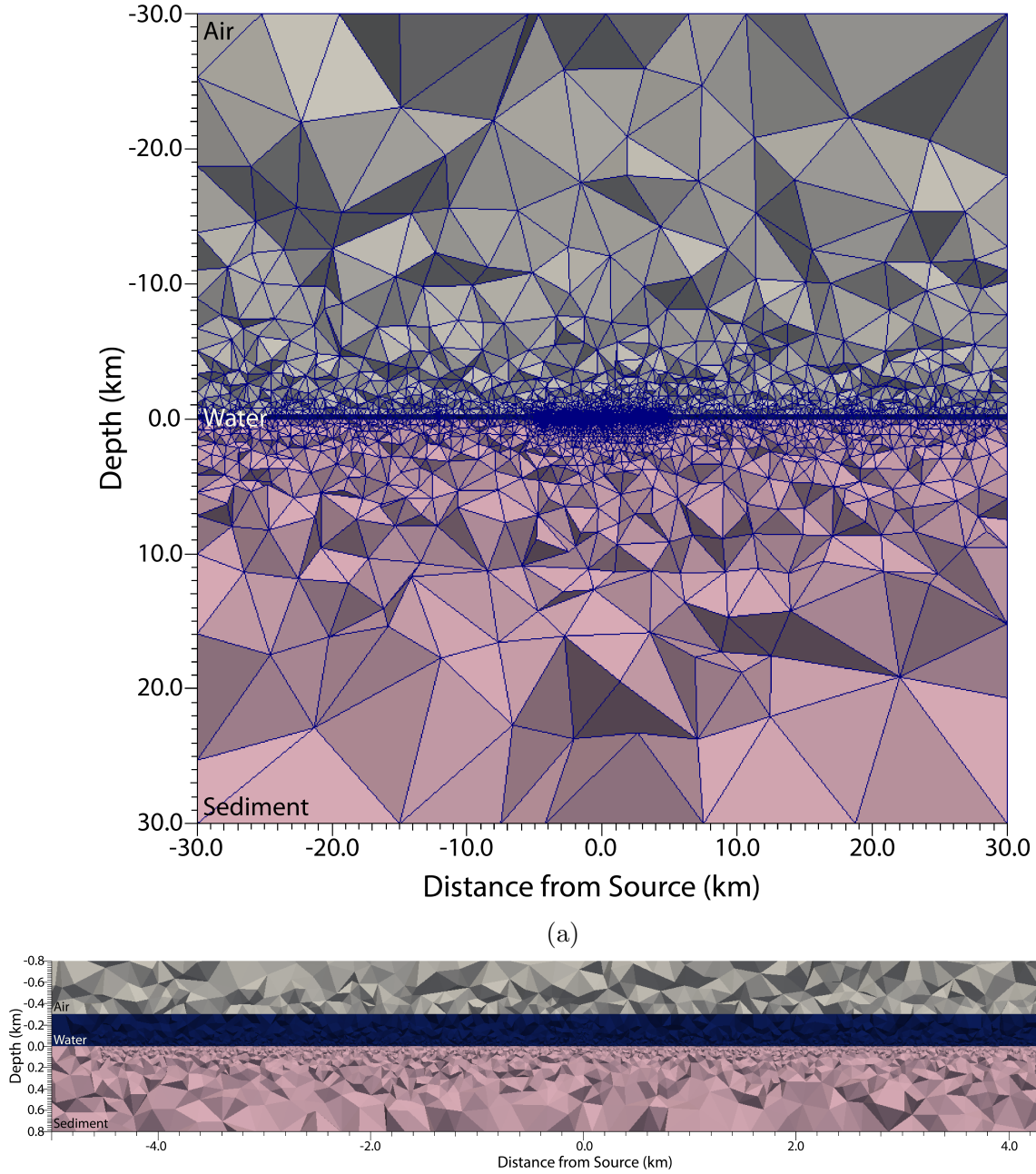

Figure 3.11: Cross-sections centered at $y = 0$ m of the 300 m water depth model. Panel (a) full view; panel (b) enhanced view of the central section of the mesh and water layer. The air layer has a conductivity of 10^{-8} S/m, the water layer (navy) has a conductivity of 3.2 S/m and the sediment layer (pink) has a conductivity of 1.0 S/m.

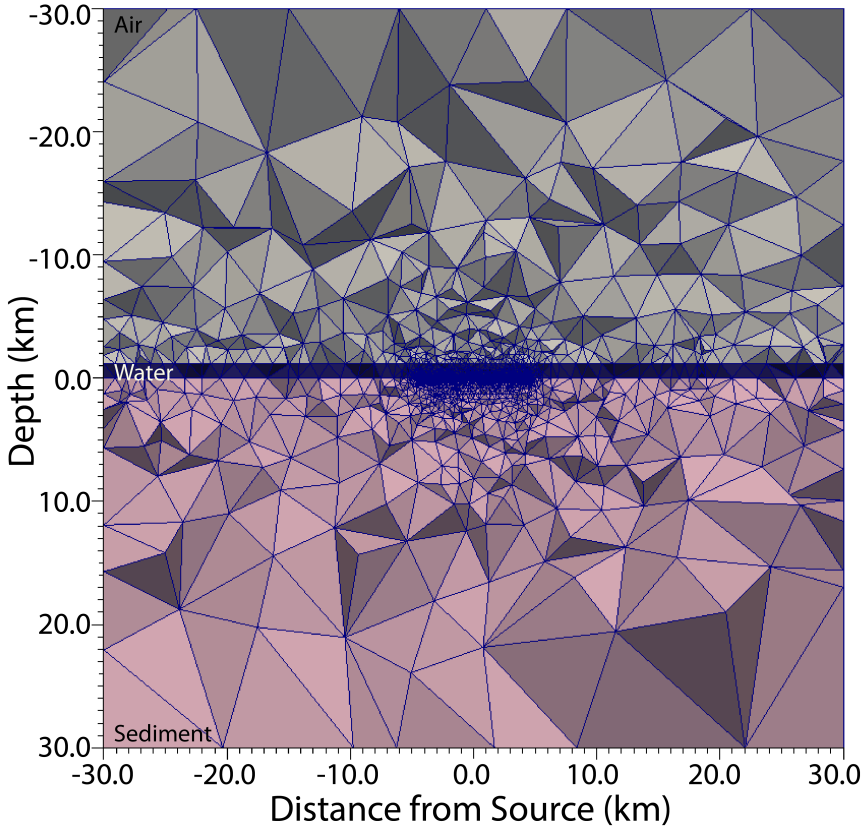

(a)

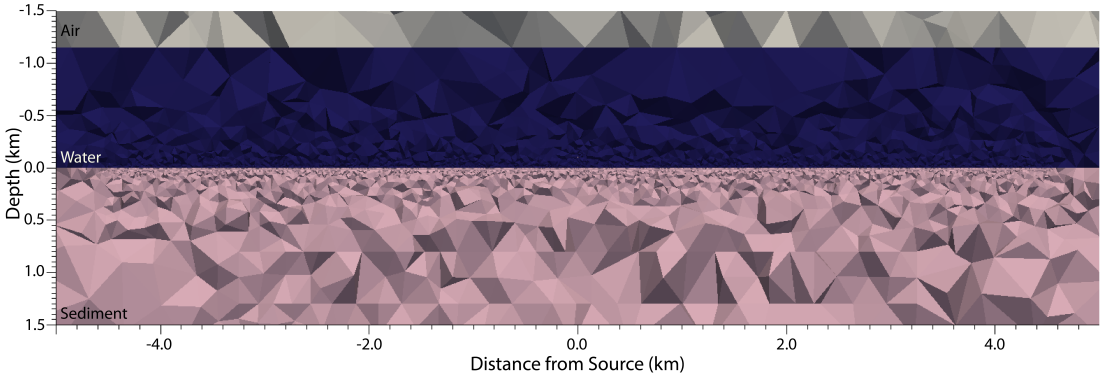

(b)

Figure 3.12: Cross-sections centered at $y = 0$ m of the 1150 m water depth model. Panel (a) full view; panel (b) enhanced view of the central section of the mesh and water layer. The air layer has a conductivity of 10^{-8} S/m, the water layer (navy) has a conductivity of 3.2 S/m and the sediment layer (pink) has a conductivity of 1.0 S/m.

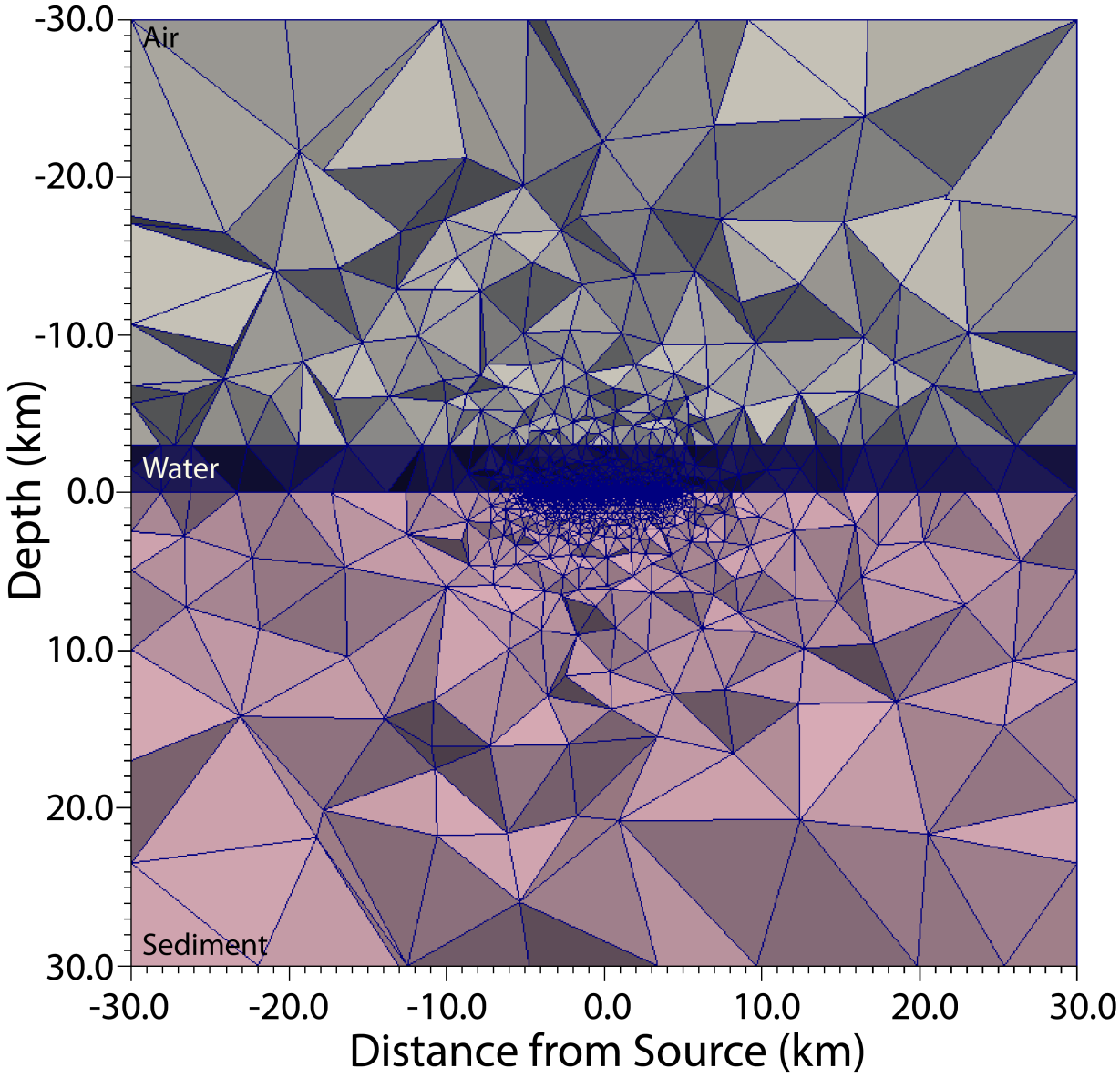

Figure 3.13: Full view cross-section centered at $y = 0$ m of the 3000 m water depth model. The air layer has a conductivity of 10^{-8} S/m, the water layer (navy) has a conductivity of 3.2 S/m and the sediment layer (pink) has a conductivity of 1.0 S/m.

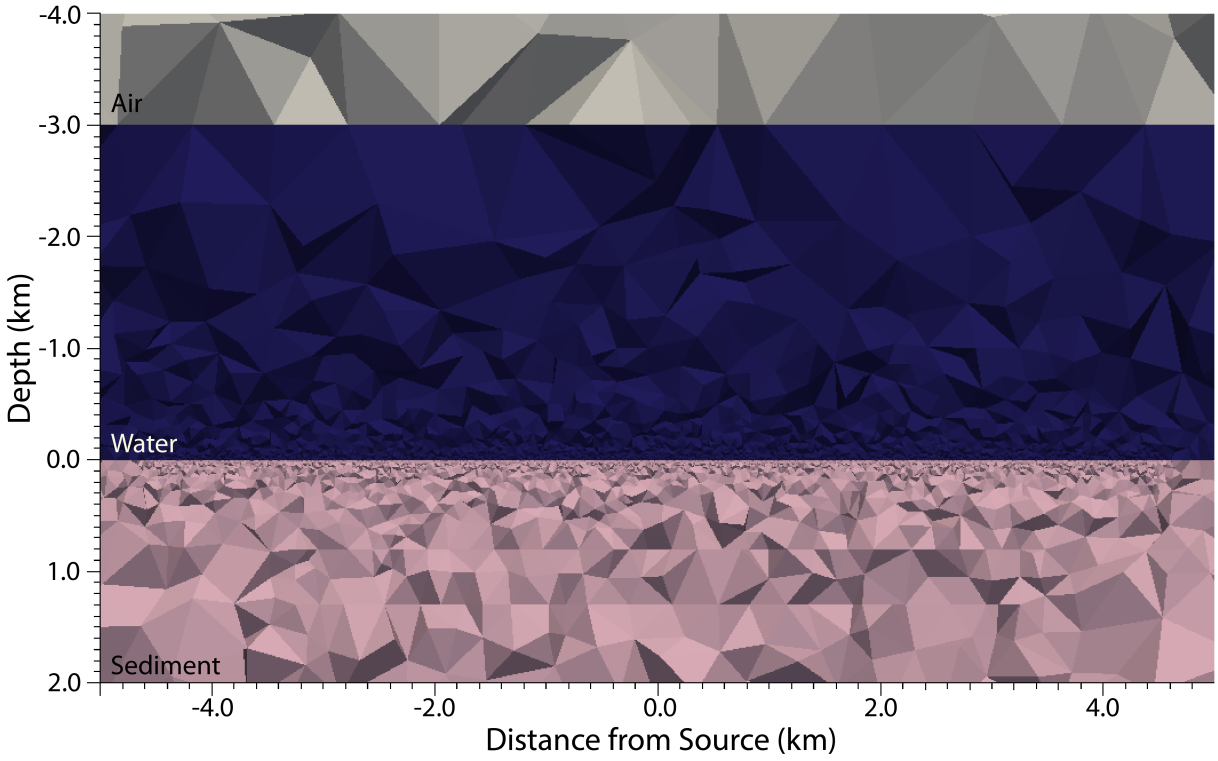

Figure 3.14: Cross-section centered at $y = 0$ m featuring an enhanced view of the central section of the mesh and water layer of the 3000 m water depth model. The air layer has a conductivity of 10^{-8} S/m, the water layer (navy) has a conductivity of 3.2 S/m and the sediment layer (pink) has a conductivity of 1.0 S/m.

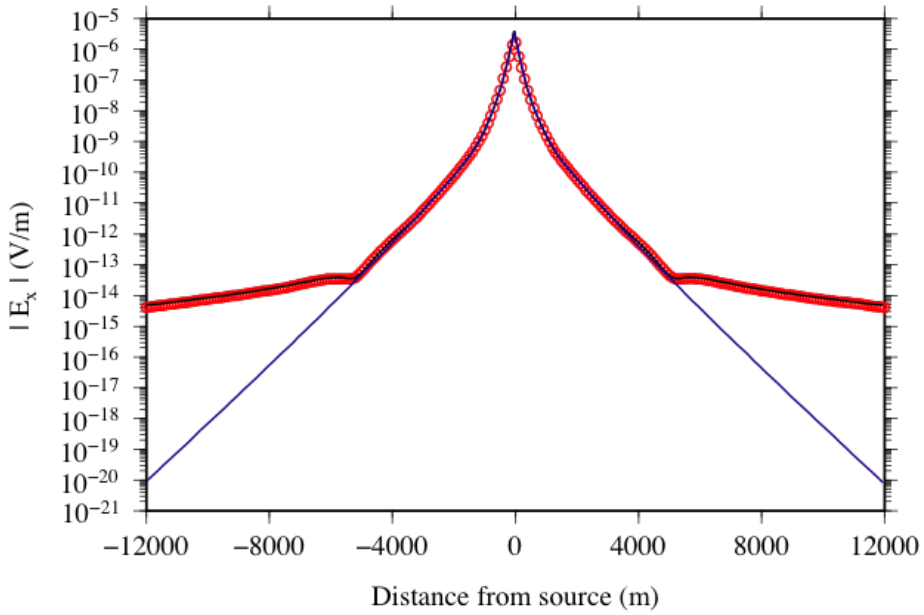

Figure 3.15: Comparison of the inline electric field amplitude for 1000 m water depth model of this study (red circles) and the semi-analytical results from DIPOLE1D (black line), and the water-sediment halfspace model (navy line). Offsets from -12000 to 12000 m were chosen to display the affect of air, which is most significant at large offsets.

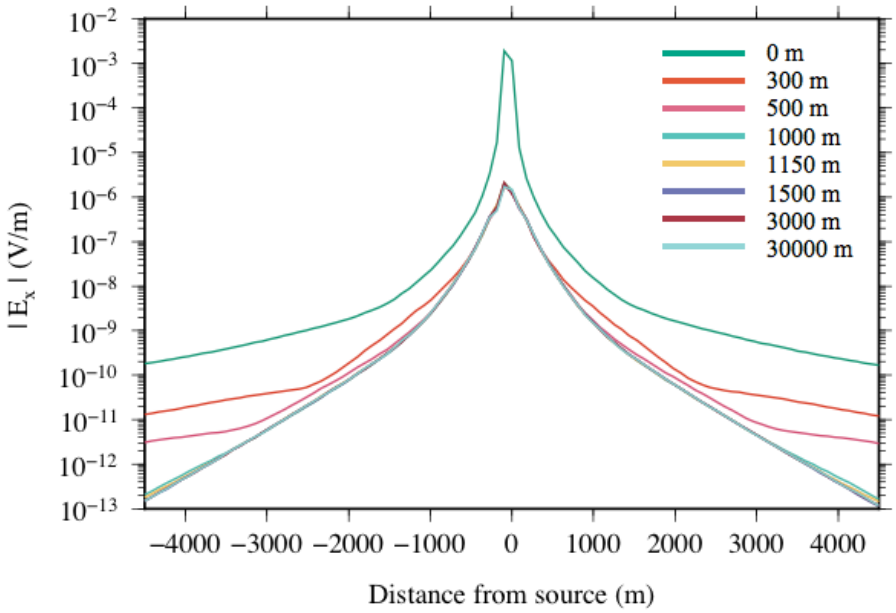

(a)

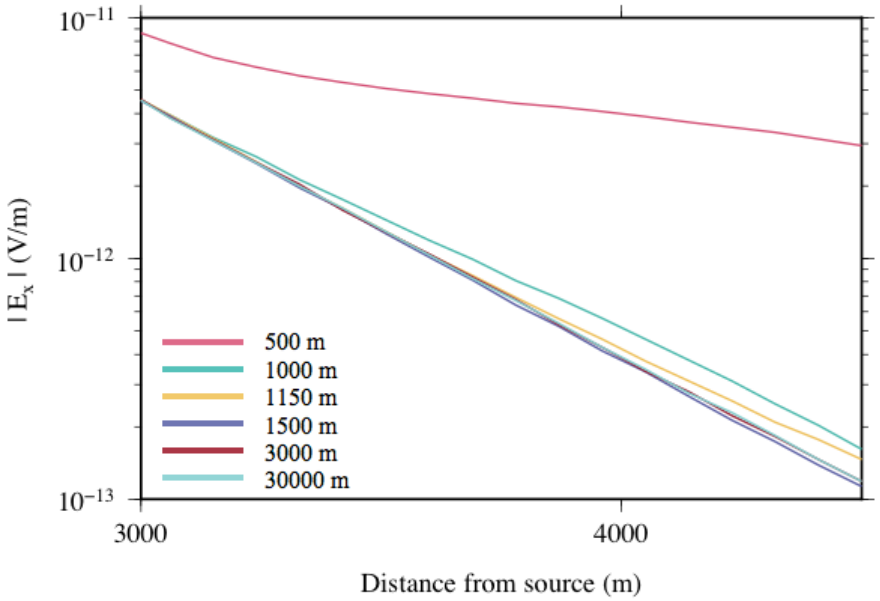

(b)

Figure 3.16: Electric field amplitude results of each of the water depth models. Panel (a) view from -4500 m to 4500 m offset; panel (b) view from 3000 m to 4500 m offset to enhance amplitude difference. Note the absence of the 0 m and 300 m results in panel (b).

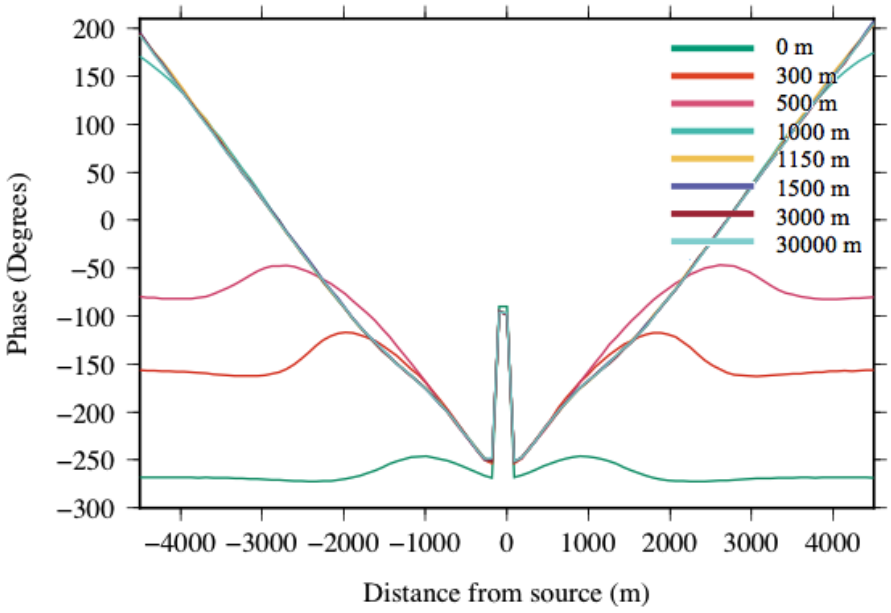

Figure 3.17: Phase results of each of the water depth models. The 0 m and 30000 m depths represent the air and water halfspaces, respectively.

3.4 Canonical Disk Reservoirs

In the literature, the *canonical disk* model — a thin circular resistive reservoir in a homogeneous subsurface — has developed into a standard basic 3D model for marine CSEM hydrocarbon exploration (e.g. Weiss and Constable, 2006). As a means of exploring the capabilities of the CSEM3DFWD modelling code, and for verification against published results, a series of tests were ran for various depths and thicknesses of a disk reservoir.

For each model in the series, the reservoir was centered at $x = 0$ m, $y = 0$ m and had a lateral extent of 2 km (Figures 3.18 and 3.19). The depth for thickness models was maintained at 1000 m, and thickness for depth models was maintained at 100 m. The disk depth position is representative of the z-position of the center of the disk, i.e., a 100 m thick disk positioned at 1000 m depth extended in the z-direction from 950 m to 1050 m depth. The reservoir had a conductivity of 0.01 S/m (reflective of the resistive nature of the oil reservoir), which existed in 1.0 S/m sediment, with 1000 m of 3.2 S/m water overlain by a semi-infinite air layer of 10^{-8} S/m. The model and mesh for the 50 m thick reservoir at 1000 m depth is shown in Figure 3.19; similar figures for the other models are given in Appendix B.

In order to reduce the computation memory required because of the added complexity of the disk relative to the models in previous sections, the computational domain was reduced to 40 km $\times$ 40 km $\times$ 40 km. The mesh parameters for each model are given in Tables 3.2 and 3.3. The larger disks and the associated decreased constriction on cell size, generally allowed for larger, and thus fewer, cells. Note that the 100 m thickness model is equivalent to the 1000 m depth model, and is therefore omitted from the series

of thickness model results. As in the water depth models, the source is an electric line source excited by a 1 Am, 1 Hz current extending from -100 to 0 m in the x-direction and 100 m above the seafloor. Source and observation refinement were added by means of two regions: source refinement extending from -101 to 1 m in the in the x-direction, -2.5 to 2.5 m in the y-direction and 95 to 105 m above the seafloor in the z-direction; and the observation refinement extending from -5 to 5 m and from 10 to 15 m in the y- and z- directions, and from -12000 to 12000 m in the x-direction. This was an increase over that used for the water depth models in order to explore results at farther offsets; as a consequence, cell numbers increased significantly. For each result, quality was ensured by the assessment of the convergence of the GMRES solver, and by confirming that for each example the resisdual decreased a considerable number of orders of magnitude.

The results for all thickness models are shown in Figures 3.20 and 3.21 and the reuslts for the disk depth models are shown in Figures 3.22 and 3.25. The resistive disk creates a distinct increase in electric field amplitude response, as shown in the difference in amplitude between the models including and omitting the reservoir (Figures 3.20 and 3.24). With the increase of depth, there is an associated increase in offset for the detection of the reservoir (Figure 3.24) and the onset of the air layer. With increase in disk thickness, there is an increase in the effect of the resistive reservoir.

Disk Thickness (m)	Cells	Nodes	Edges
50	601,072	98,259	5,779
100	495,363	81,136	5,552
200	463,817	76,029	5,397
500	470,250	77,057	5,396

Table 3.2: Mesh parameters for disk thickness models.

Disk Depth (m)	Cells	Nodes	Edges
500	1,381,200	225,233	16,298
1000	1,398,890	227,757	16,475
2000	1,387,588	226,035	16,308
2500	1,356,281	220,792	16,110
3000	1,688,778	274,666	19,339
4000	1,658,862	269,782	19,207

Table 3.3: Mesh parameters for disk depth models.

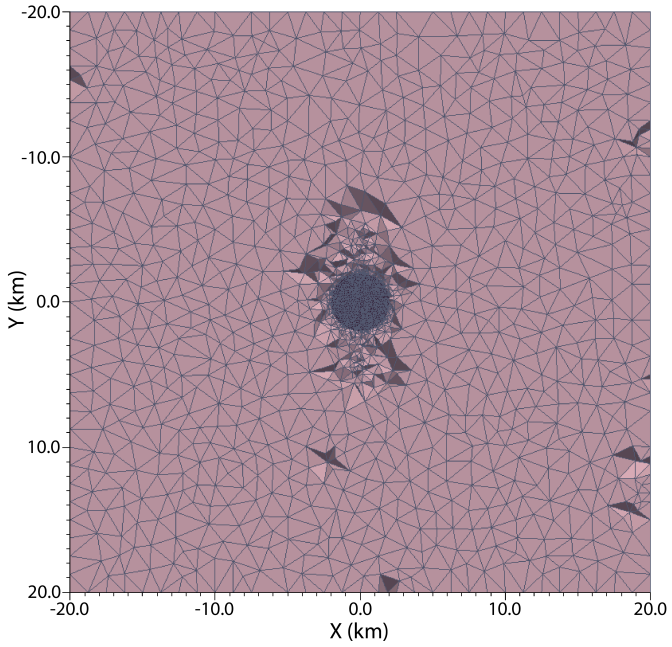

(a)

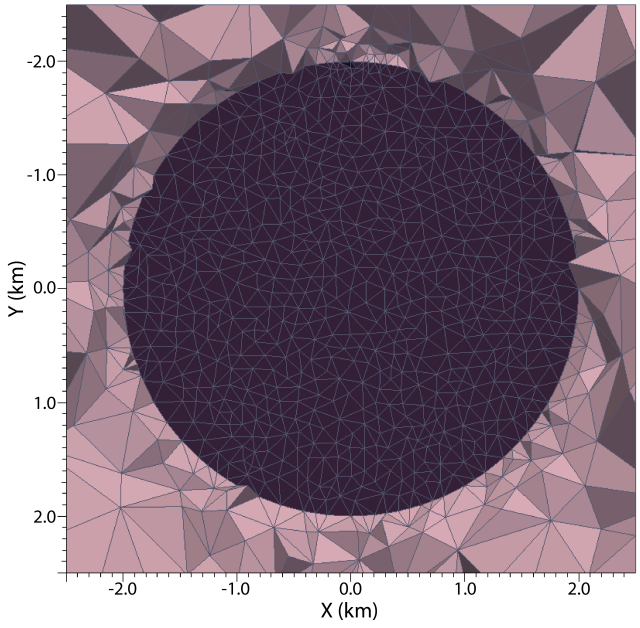

(b)

Figure 3.18: xy slice centered at $z = 1000$ m through the midpoint of the thickness of the disk. The disk has a conductivity of 0.01 S/m and the sediment 1.0 S/m. Panel (a) full view; panel (b) enhanced view of the reservoir.

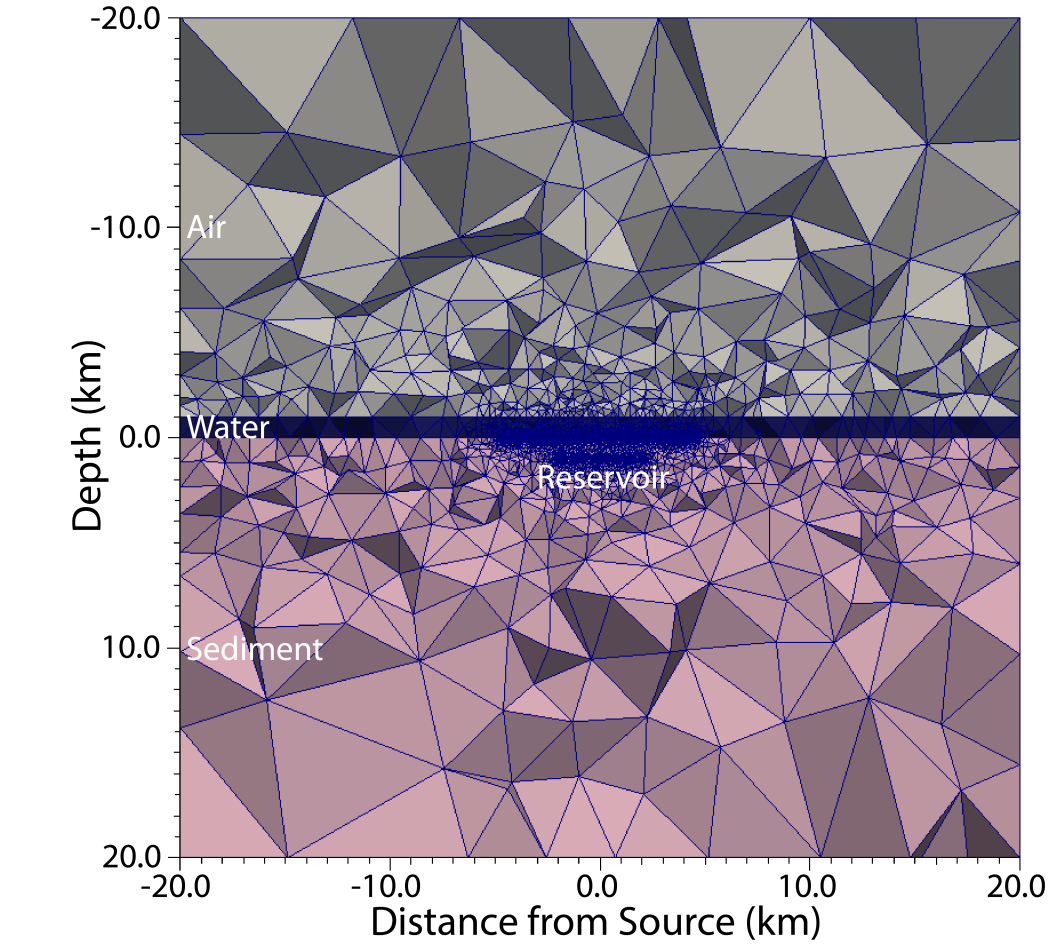

(a)

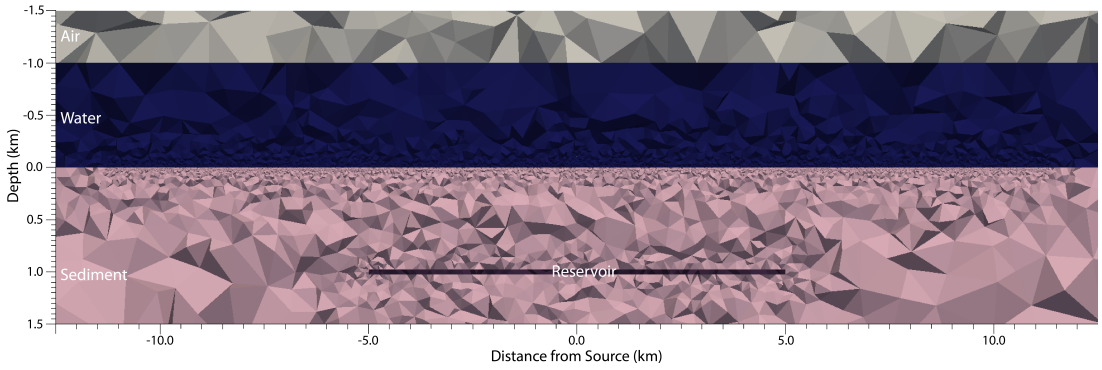

(b)

Figure 3.19: Cross-sections centered at $y = 0$ m of the disk model with a 50 m disk thickness and 1000 m depth. Panel (a) full view; panel (b) enhanced view of the reservoir.

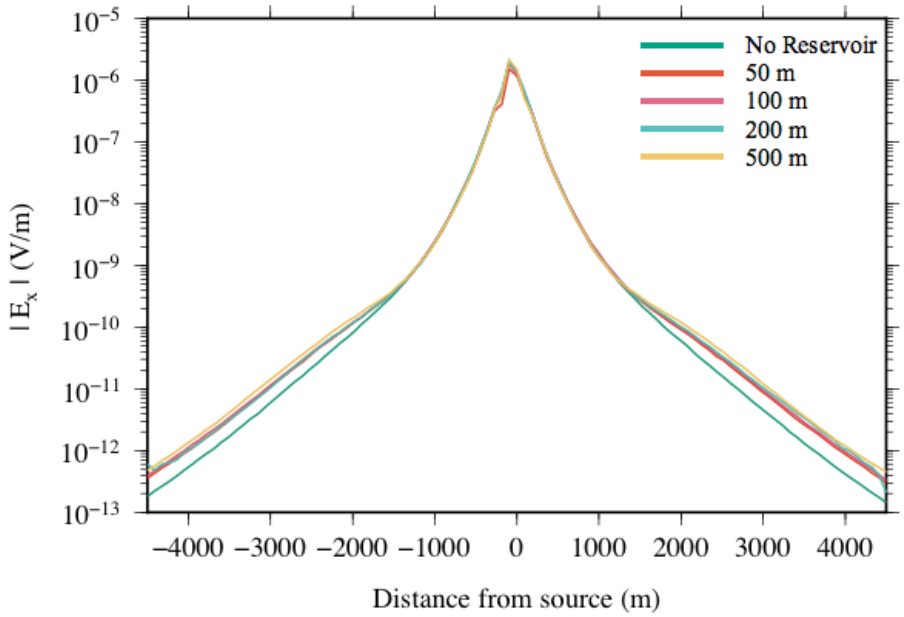

(a)

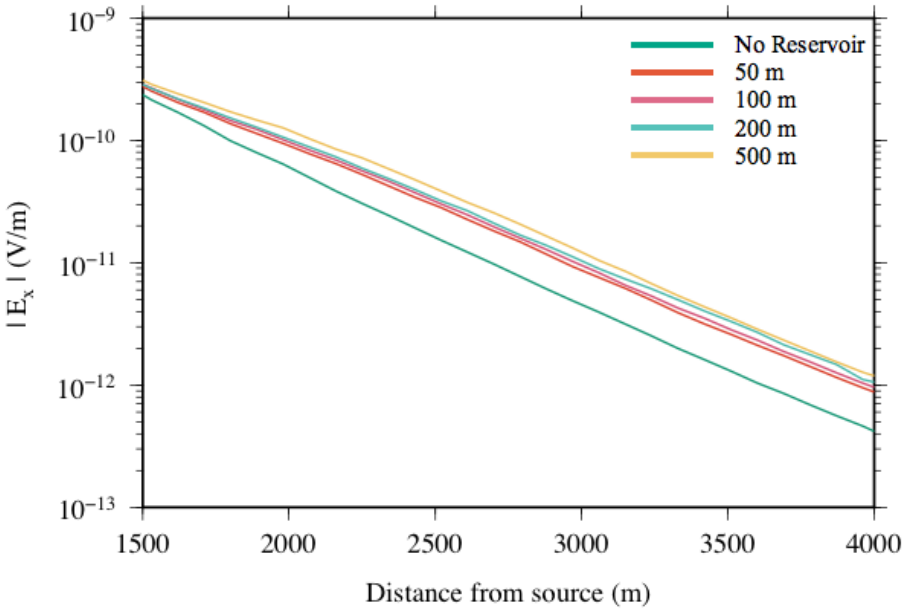

(b)

Figure 3.20: Electric field amplitude results for each of the disk thickness models. Panel (a) view from -4500 to 4500 m offset; panel (b) view from 1500 to 4000 m offset to highlight amplitude difference.

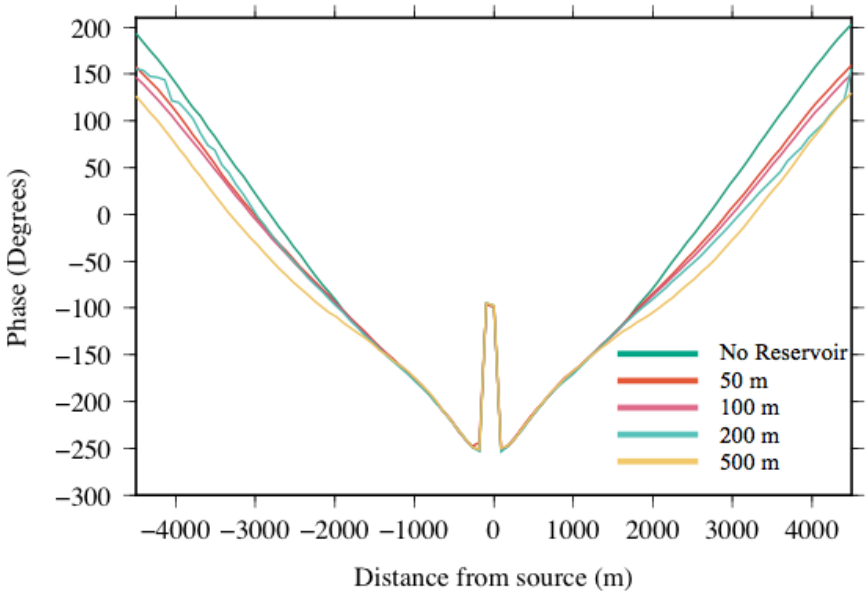

Figure 3.21: Phase results for each of the disk thickness models.

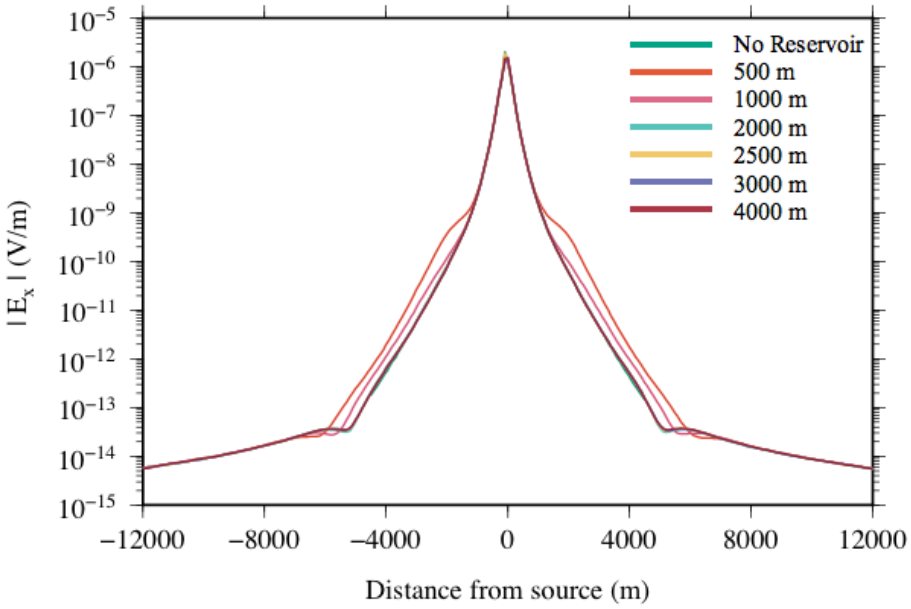

Figure 3.22: Electric field amplitude results for each of the disk depth models showing offset from -12000 to 12000 m to show results including the affects of the overlying air layer.

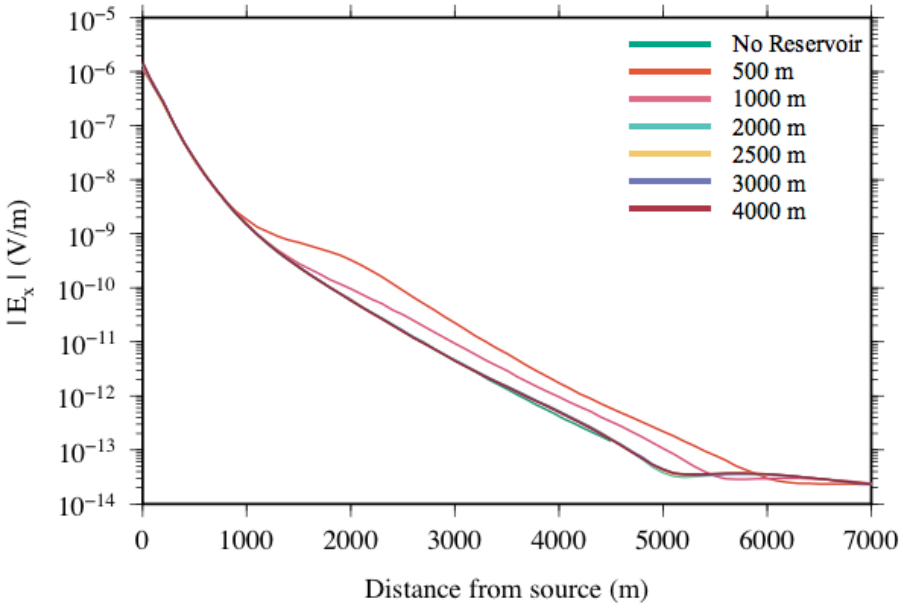

Figure 3.23: Electric field amplitude results for each of the disk depth models showing offset from 0 to 7000 m to emphasize the range of offsets between the source and where the air layer effect begins.

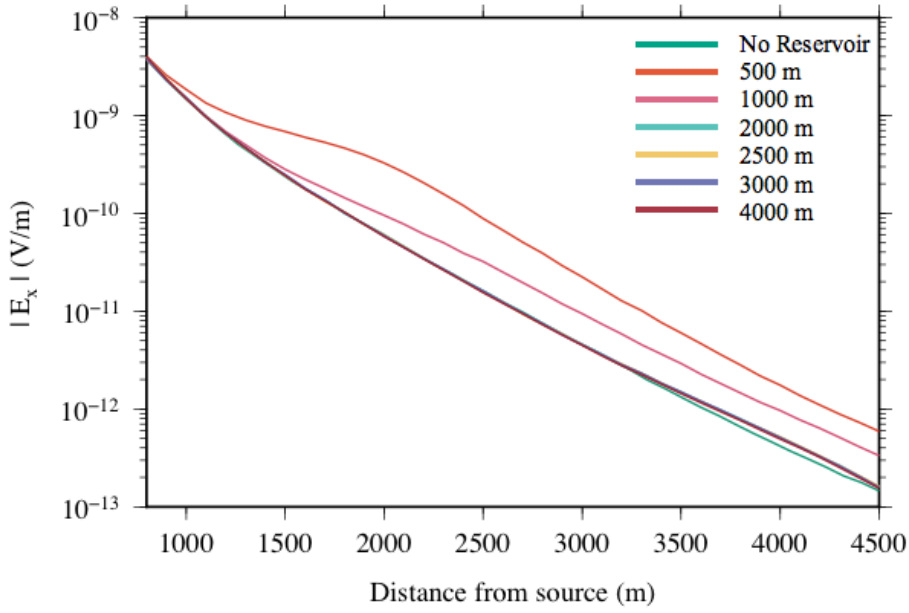

Figure 3.24: Electric field amplitude results of each of the disk depth models showing offsets from 800 to 4500 m to emphasize the affect of the reservoir.

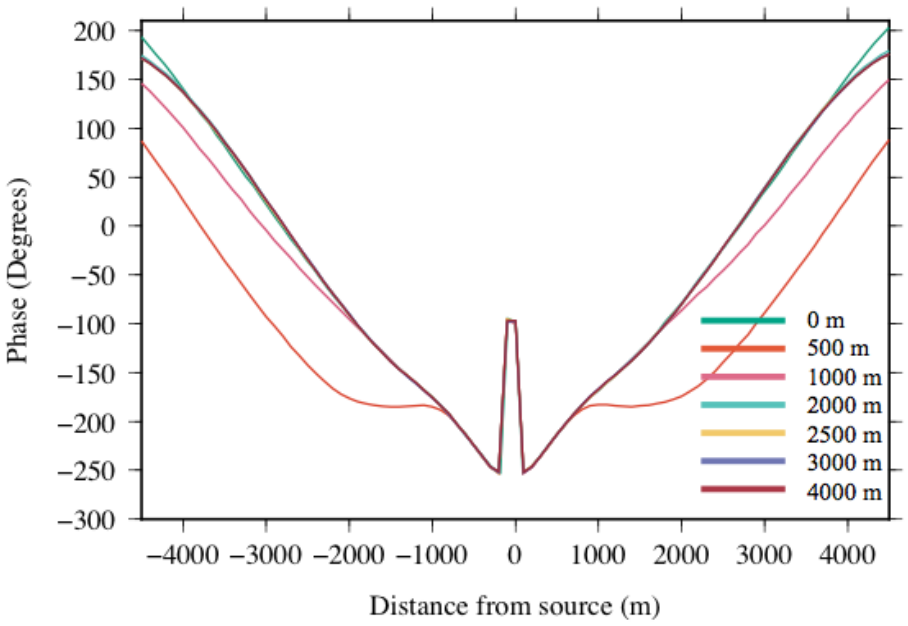

Figure 3.25: Phase results for each of the disk depth models.

3.5 Flemish Pass Stratigraphy Models

Before creating the complex 3D Earth models, it is advantageous to have a thorough understanding of the effects of the overlying lithology on the detection of a resistive hydrocarbon reservoir. Conductivities and thicknesses for these lithologies relevant to the Flemish Pass Basin were provided by Suncor Energy (Brad Bonnell, personal communication; Figure 1.8). The models were composed of an air layer extending the full width of the upper z-boundary (at $z = -20000$ m) with a conductivity of 10^{-8} S/m, and a 1150 m deep water layer at 3.2 S/m. This was underlain by two layers extending to the domain in the x- and y-directions which represent the Cretaceous- and Tertiary-aged strata. The upper layer (from *Water Bottom* to *Base Tertiary*) has a thickness of 1450 m and conductivity of 0.769 S/m, while the lower layer (from *Base Tertiary* to *Base Cretaceous*) has a thickness of 500 m and conductivity of 0.467 S/m (Figure 3.26). The Jurassic reservoir is composed of two 525 m packages representing a sandstone, hydrocarbon-filled reservoir (0.01 S/m) with overlying shale beds (0.111 S/m), respectively. This deviates from the model displayed in Figure 1.8: each of the thin packages were accurately approximated to bulk thicknesses of 525 m each, which were the minimum possible thickness for which meshes and results could be generated. Thinner layers generated substantially more cells in the region, which resulted in memory complications with computation.

The following series of modelling scenarios are be comprised of square reservoir sections of increasing lateral extent and constant thickness to assess the detectability of each size. The reservoir sections are centred at $x = y = 0$, with the lateral extent of each model displayed in Table 3.4.

The entire domain had dimensions 40 km × 40 km × 40 km, and the mesh statistics for each model are displayed in Table 3.4. Two regions were added for the purpose of refinement: source refinement extending from -101 to 1 m in the x-direction, in the y-direction from -2.5 to 2.5 m, and in the z-direction from 99.0 m to 105.0 m above the water-sediment interface, while observation refinement extended from -15000.0 to 15000.0 m in the x-direction, -5 to 5 m in the y-direction and 10 to 15 m below the water-sediment interface — a similar arrangement as the previous examples. The number of cells for each model remained consistent at ∼1.5 million cells, but increased dramatically for the infinite reservoir (Table 3.4). The extension of these layers to the boundary of the computational domain forces the generation of smaller, and thus more, cells at the very boundaries of the model. The models and meshes for three of the reservoir extents are shown here: *No Reservoir* (representing the lowest case of hydrocarbon success, Figure 3.26); 10000 m (representing an intermediate case of hydrocarbon success, Figures 3.27 and C.12); and infinite extension (representing the highest case of hydrocarbon success, Figures 3.28 and C.20).

Each model was electrically excited by a 1.0 Hz, 1.0 Am electric line source. The electric field amplitudes and phases for all extents of the reservoir are shown in Figures 3.29 to 3.31. Two models were used for the sake of comparison: the *No Layers* model (equivalent to Figure 3.12) represents a homogenous halfspace of basement resistivity (1.0 S/m) with a 1150 m water depth, meaning the effects of both the layers and reservoirs can be analyzed; and the *No Reservoir* model (i.e. those shown in Figure 3.26) which allows a comparison to be made that emphasizes the reservoir only. In each result, the addition and extension of the reservoir creates an increase in the electric field amplitude after the effect

of the source has been overcome — at ∼3000 m offset (Figure 3.30). As offset increases, the electric field amplitude for each model follows a similar pattern: once the resistive reservoir is no longer detected, the amplitude dips, and proceeds to approach the results of *No Reservoir*; this dip occurs at greater offsets for larger reservoir extents. The increase in the amplitude of the *No Reservoir* results over the *No Layers* results is generated by the decrease in conductivity of the two lithological layers (0.769 and 0.467 S/m) relative to the basement layer in the *No Layers* model (1.0 S/m). Similar effects are seen with the comparison of phase data (Figure 3.31). The addition of the layers (in comparison to the 1.0 S/m halfspace) dampens the increase in phase at ∼1000 m offset, and the extension of the reservoir increases the offset at which the steady increase in phase is turned over and the phase levels off due to the air layer effect.

Reservoir Extent (m)	Cells	Nodes	Edges
No Reservoir	1,414,116	230,778	17,470
2500	1,445,854	235,836	17,621
5000	1,531,613	249,588	17,330
7500	2,141,679	348,544	22,938
10000	1,658,773	269,989	17,446
12500	1,604,967	261,515	18,589
15000	1,441,716	235,249	17,747
Infinite	2,535,009	412,588	19,505

Table 3.4: Mesh parameters for simple Flemish Pass Basin reservoir models.

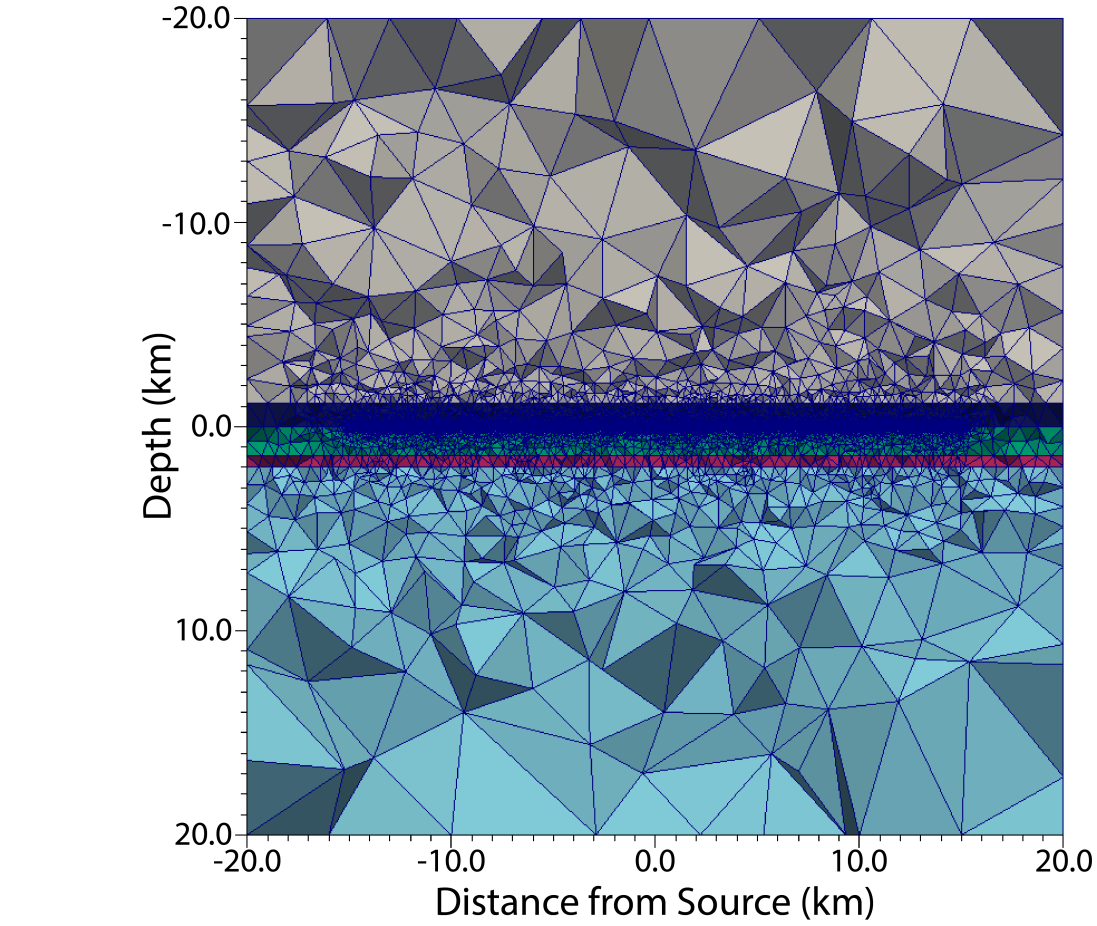

(a)

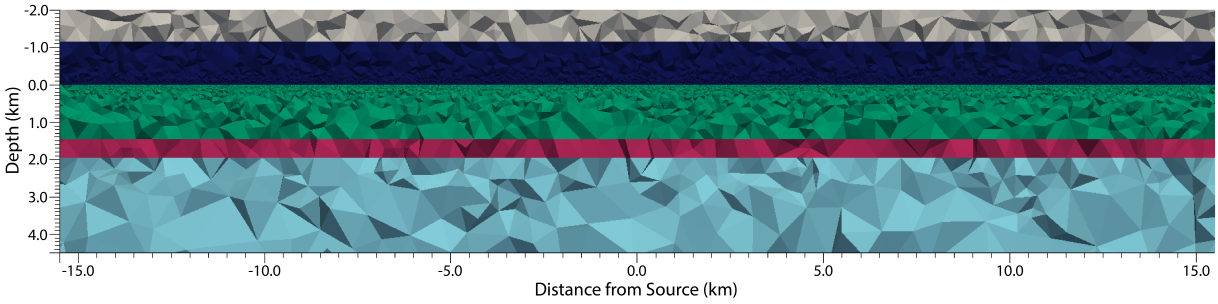

(b)

Figure 3.26: Cross-section centered at $y = 0$ m of the 1D layered Earth model with two infinite subsurface layers. Panel (a) full view; panel (b) enhanced view of the reservoir. The first (green) infinite layer has a conductivity of 0.769 S/m and second (magenta) infinite layer has a conductivity of 0.467 S/m.

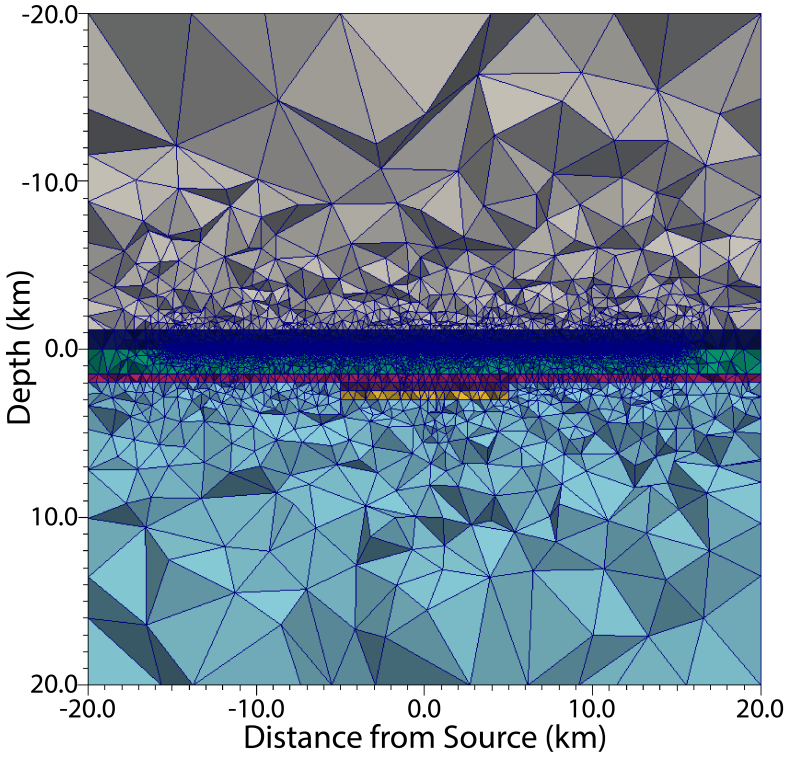

(a)

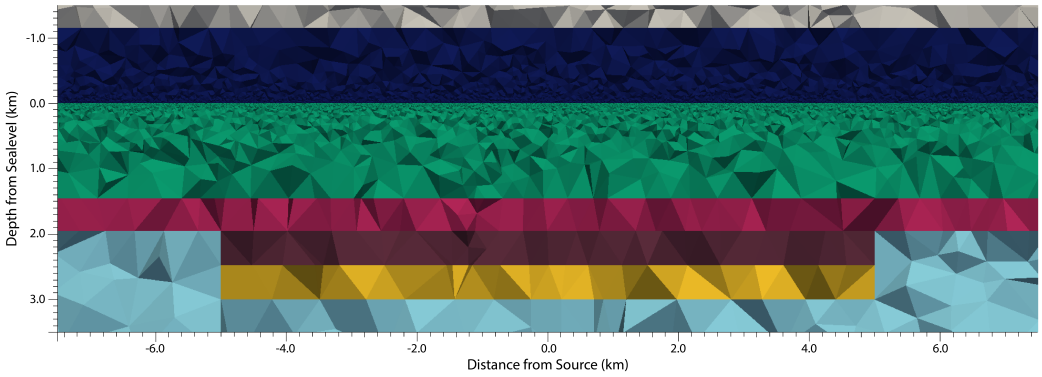

(b)

Figure 3.27: Cross-sections centred at $y = 0$ m of the simple Flemish Pass Basin reservoir model with two infinite subsurface layers and a 10000 m wide reservoir section composed of a shale upper layer (conductivity of 0.111 S/m; brown) and sand reservoir lower layer (conductivity of 0.01 S/m; yellow). Panel (a) full view; panel (b) enhanced view of the reservoir. As in Figure 3.26, the first (green) infinite layer has a conductivity of 0.769 S/m and second (magenta) infinite layer has a conductivity of 0.467 S/m.

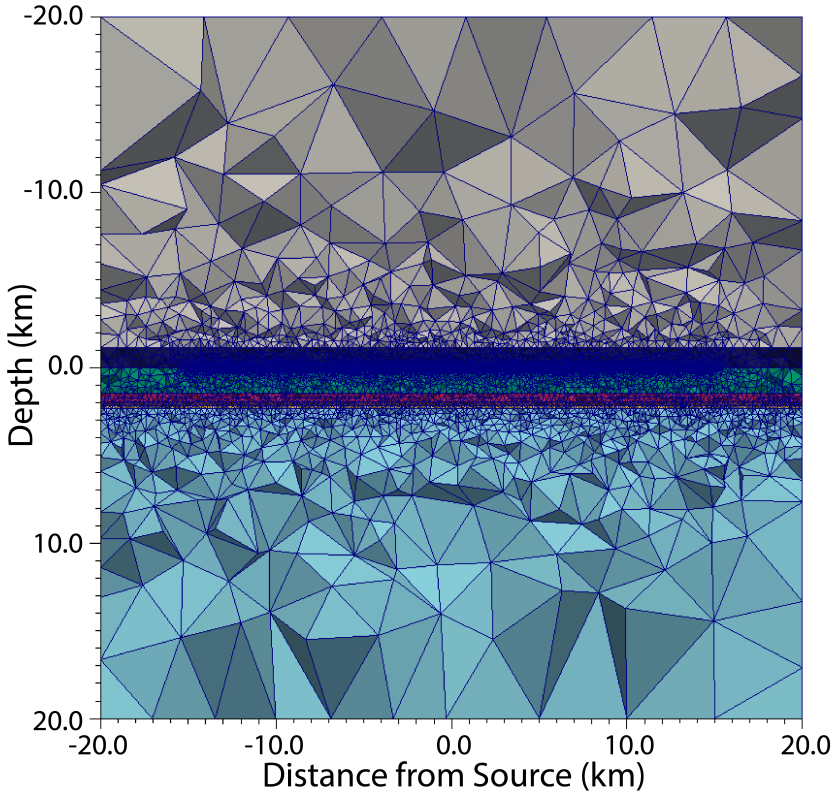

(a)

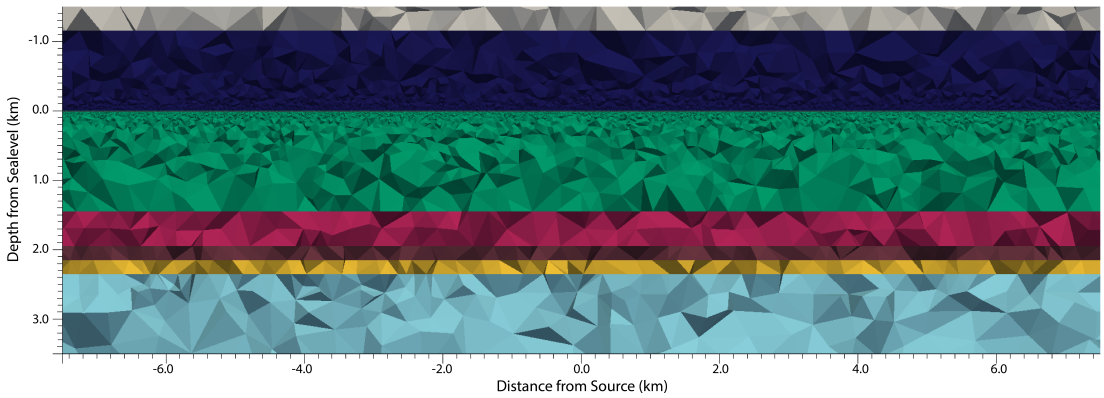

(b)

Figure 3.28: Cross-section centred at $y = 0$ m of the Flemish Pass Basin reservoir model with two infinite subsurface layers and a infinite reservoir section composed of a shale upper layer (conductivity of 0.111 S/m; brown) and sand reservoir lower layer (conductivity of 0.01 S/m; yellow). The first (green) infinite layer has a conductivity of 0.769 S/m and second (magenta) infinite layer has a conductivity of 0.467 S/m.

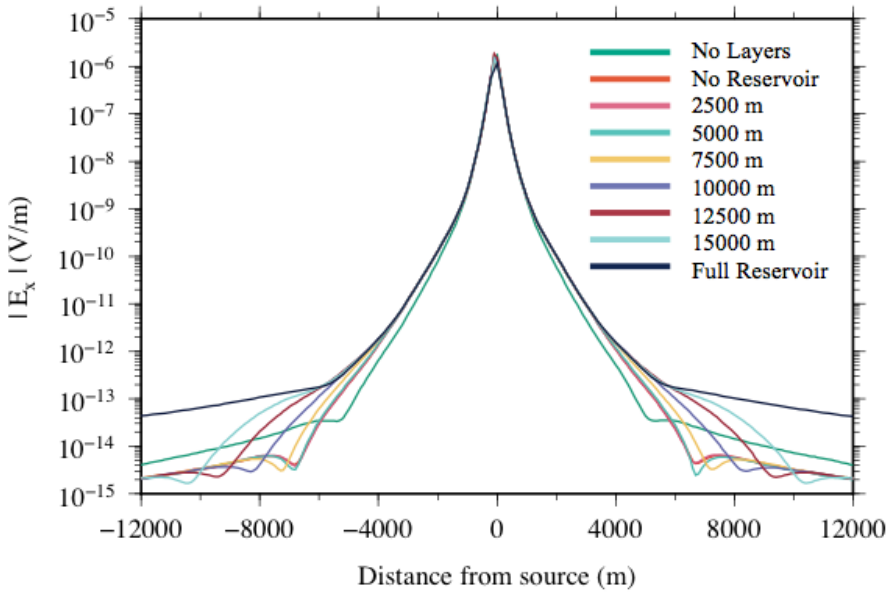

Figure 3.29: Electric field amplitude results for each of the different lateral extents of the simple Flemish Pass Basin reservoir model. The results of the *No Reservoir* model is significantly hidden by the results of the *2500 m* model

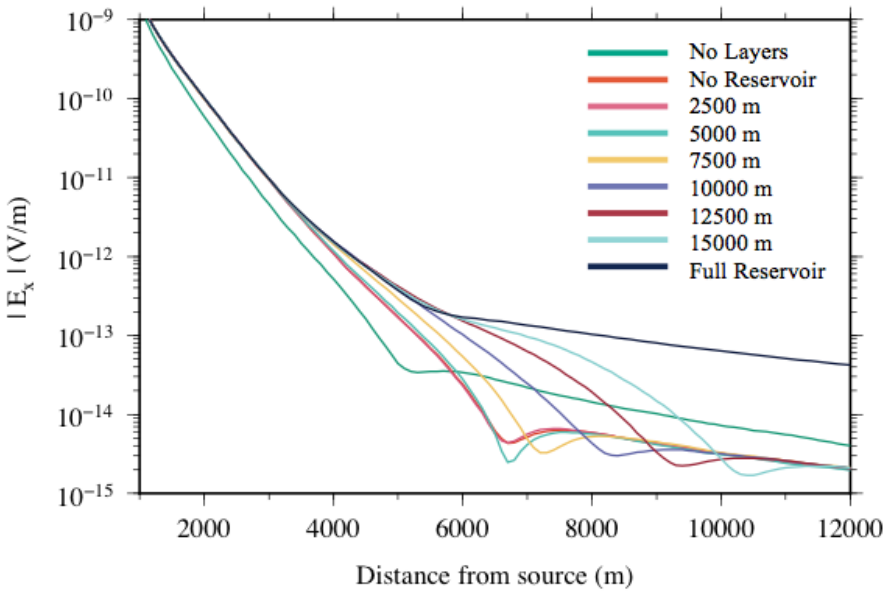

Figure 3.30: Electric field amplitude results for the simple Flemish Pass Basin models showing offsets from 3000 to 12000 m to emphasize the increase in electric field amplitude with reservoir extent.

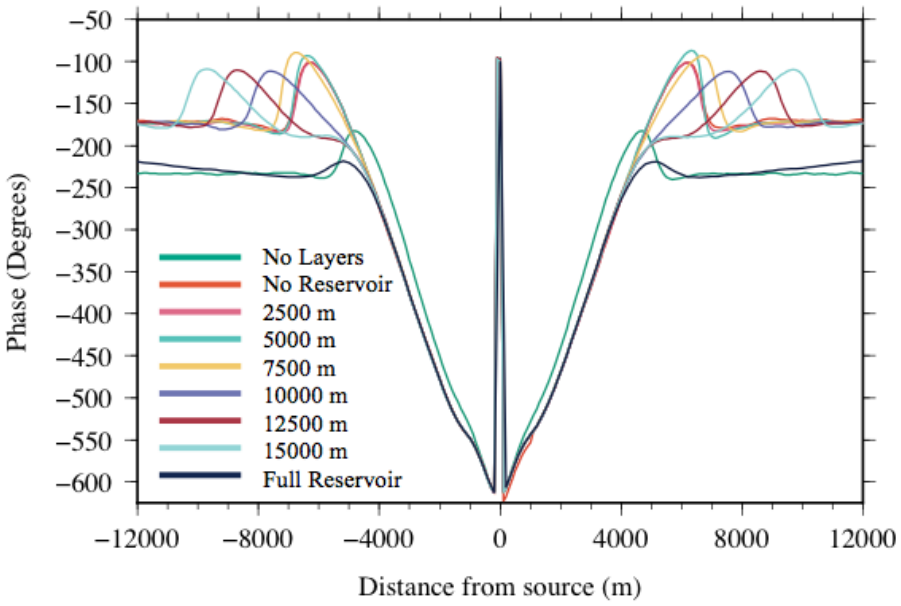

Figure 3.31: Phase results for each of the simple Flemish Pass Basin reservoir models.

Chapter 4

Three-Dimensional Models of the Flemish Pass Basin

4.1 Introduction

The aim of this study, and purpose of previous sections, was to steadily increase the complexity of models to conclude with 3D models that are relevant to offshore scenarios. In order to achieve this, the trade-off between structural accuracy and sizable volume of provided seismic-derived data representing lithological horizons was assessed: the volume of nodes in the original data supplied was far too dense for computational capabilities, but sparse data generates deviations from the real Earth model. Once the horizons were accurately represented into a model and mesh, various reservoir scenarios based on known potential structures from Suncor were explored.

4.2 Incorporating Seismic-Derived Horizon Data

Three horizons were provided by Suncor (Brad Bonnell, personal communication) for the area to represent both bathymetry and lithology for specific formations in the Flemish Pass Basin: 1) the *Water Bottom* horizon; 2) the *Base Tertiary* horizon; and 3) the *Top Tithonian* horizon. Each of these seismically-derived layers were picked by Suncor Energy to represent the fundamental structures and strata of the area.

The horizons were prepared as a series of data points in UTM coordinates, forming approximately 20 km $\times$ 20 km grids, each comprising approximately 130,000 nodes each. Figure 4.1 shows the extreme node density — the lack of node spacing between each black dot creates no negative space in the 2D projection of the horizon, and hence, a blackness of the images. To convert from UTM coordinates to a more convenient local coordinate system, the entire domain was first shifted -840,600 m in the x-direction and -5,323,140 m in the y-direction, along with a rotation 24.0 degrees counterclockwise; this acted to centre the horizon domain about $x = y = 0$ m in the local coordinate system and to align the data perpendicular to the standard modelling domain, preventing tedious position conversions in future models. This transformation was achieved using the *transform* Fortran code developed by Peter Lelièvre.

In order to limit the computation time and memory usage, it was imperative to significantly reduce the number of nodes in each of these horizons. This was achieved by a process of node decimation: a certain node spacing was chosen and nodes were eliminated using the *remove_range* Fortran code developed by Peter Lelièvre.

During the process of node decimation, a series of attempts were made to find a balance

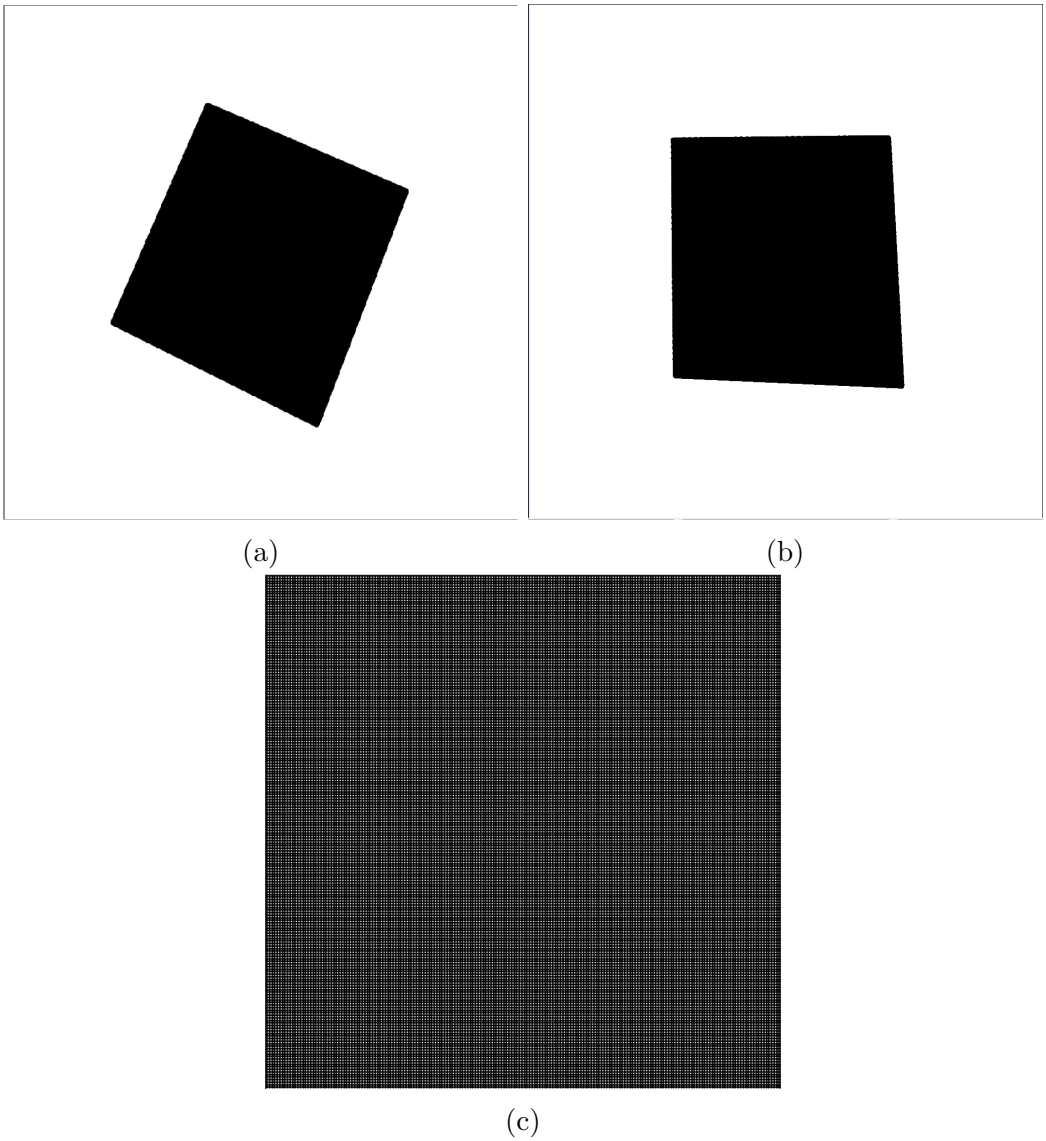

Figure 4.1: Panel (a) a projection of the *Base Tertiary* horizon data onto the plane $z = 0$ m. Each node is a single 1pt black dot, but limited node spacing creates no negative space. The outer boundaries of the select view extend from -20 km to 20 km in both the x- and y-directions; panel (b) shows the rotated *Base Tertiary* horizon and; panel (c) 5 km $\times$ 5 km enlarged view of the data that better indicates the node density.

between sufficiently accurate reproduction of a horizon and the number of nodes and cells in a model. As a dense node spacing generates smaller cells and represents the horizon more accurately, initial attempts used a small node spacing of 500 m. However, despite the decimation, over 13,000 nodes were used for each horizon, and discretizing the model produced over 2,800,000 cells in the mesh, far exceeding the computational capabilities of available computers.

As accurate modelling results require refinement about the source and observation locations, the next attempt maintained dense node spacing in the vicinity of the source and observation locations, but the node spacing was increased to 1000 m in the remaining region (herein referred to as the *Hybrid Configuration*). This was achieved by removing, but saving, all nodes extending from -15000 to 15000 m in the x-direction and -20 to 20 m in the y-direction, decimating the remaining nodes, then combining the nodes of the decimated region with the dense nodes from the removed region, resulting in the configuration seen in Figure 4.2; this was completed for each horizon to maintain structural resolution in the most vital regions. Successful EM modelling results for this configuration could not be achieved: convergence of the GMRES solver did not meet the appropriate criteria of successful convergence, and the corresponding results were visibly poor (Figure 4.3).

The failure of the *Hybrid Configuration* resulted in a series of further node spacing attempts (Figure 4.4 and Table 4.1), while continuously being mindful of the required balance between node elimination and horizon accuracy. A node spacing of 1000 m was finally chosen for each horizon based on these trials. Please note that though Table 4.1 represents the node statistics for the *Water Bottom* horizon, the same node spacing was also used for the other horizons in the model.

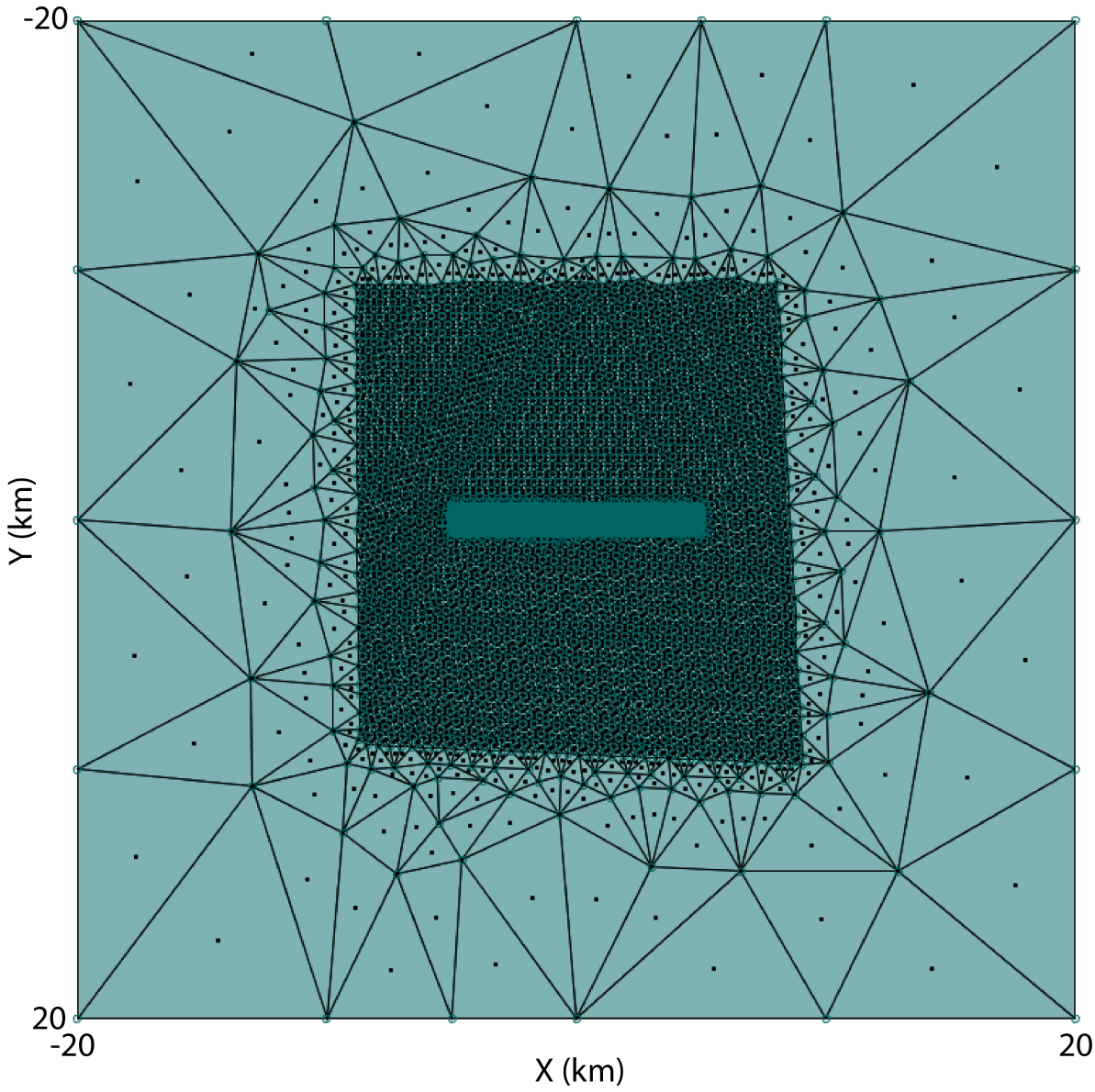

Figure 4.2: Hybrid dense-sparse node spacing configuration of the *Water Bottom* horizon projected onto $z = 0$ m.

Node Spacing (m)	Nodes Remaining	Nodes Removed
0	132,588	0
500	1,341	131,247
750	617	131,971
1000	350	132,238
1250	220	132,368
1500	158	132,430
2000	96	132,492

Table 4.1: Statistics of attempted node-spacing decimation for the *Water Bottom* horizon.

Once the appropriate node configuration had been chosen, an outer boundary was defined for the perimeter of the computational domain. This boundary extended from -20 km to 20 km in the x- and y-directions (Figure 4.5). This dataset was then exported to a *.poly* file and meshed in 2D using Triangle (see Chapter 2) to generate a mesh of each horizon (Figure 4.6). These 2D sections were then converted to 3D using a Fortran interpolation code developed by Peter Lelièvre, which output the *.node* and *.ele* files necessary to input into the 3D option in FacetModeller. FacetModeller was used to join the nodes of the boundaries of each horizon to one another by defining facets between adjacent layers (Figure 4.7). This data was then exported to a *.poly* file and the entire 3D domain was able to be meshed using TetGen (Figure 4.8), as described in Chapter 2.

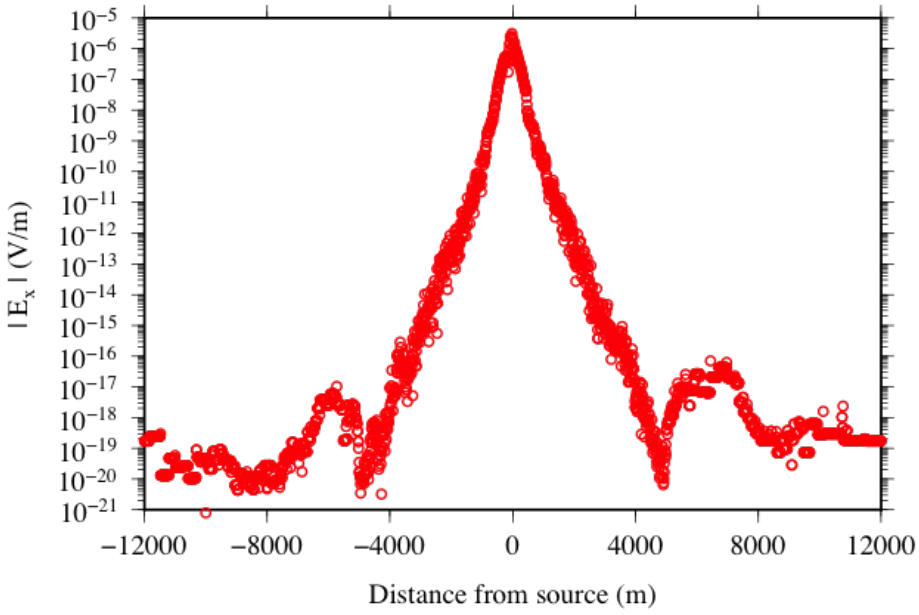

(a)

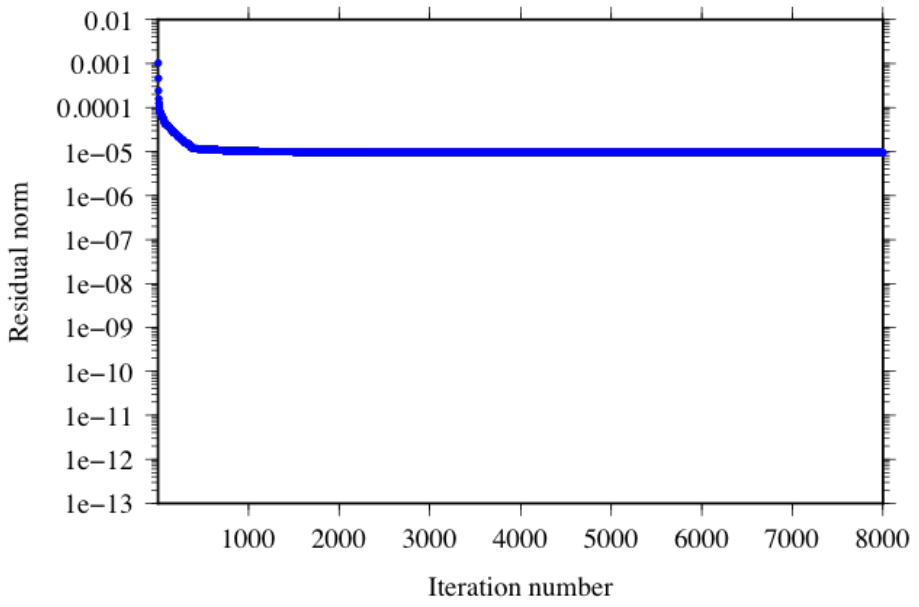

(b)

Figure 4.3: Panel (a) electric field amplitude and panel (b) convergence curve results for the hybrid dense-sparse node configuration.

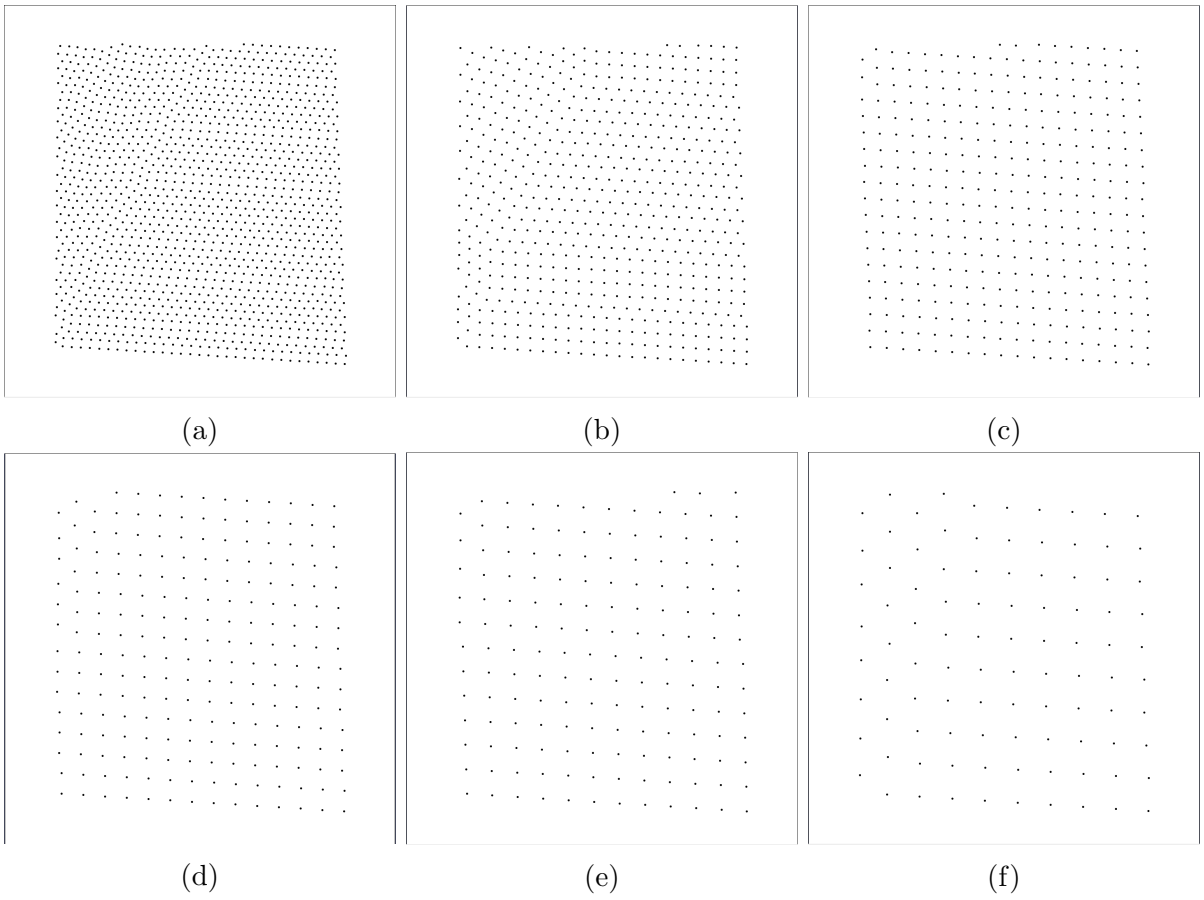

Figure 4.4: Projections of the *Water Bottom* data onto a 12 km × 12 km plane at $z = 0$ m displaying each of the trialled node spacing configurations. Panel (a) 500 m spacing; panel (b) 750 m spacing; (c) 1000 m spacing; (d) 1250 m spacing; (e) 1500 m spacing; (f) 2000 m spacing.

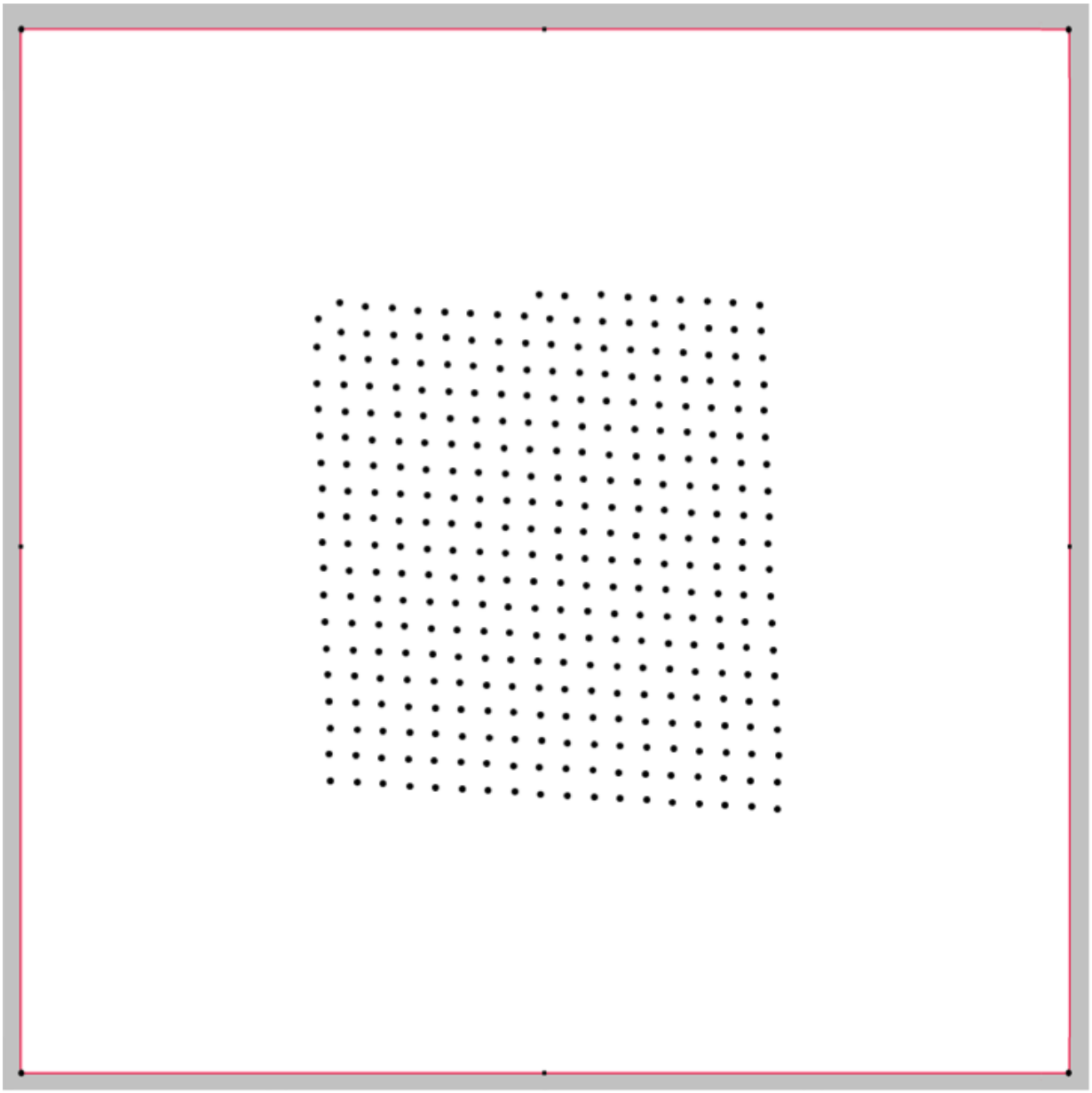

Figure 4.5: A projection of the *Water Depth* data from Figure 4.4c onto the plane $z = 0$ m with the boundary section (white area) extending from -20 to 20 km in the x- and y-directions. The boundary is defined by 2D facets about the perimeter, displayed as red lines.

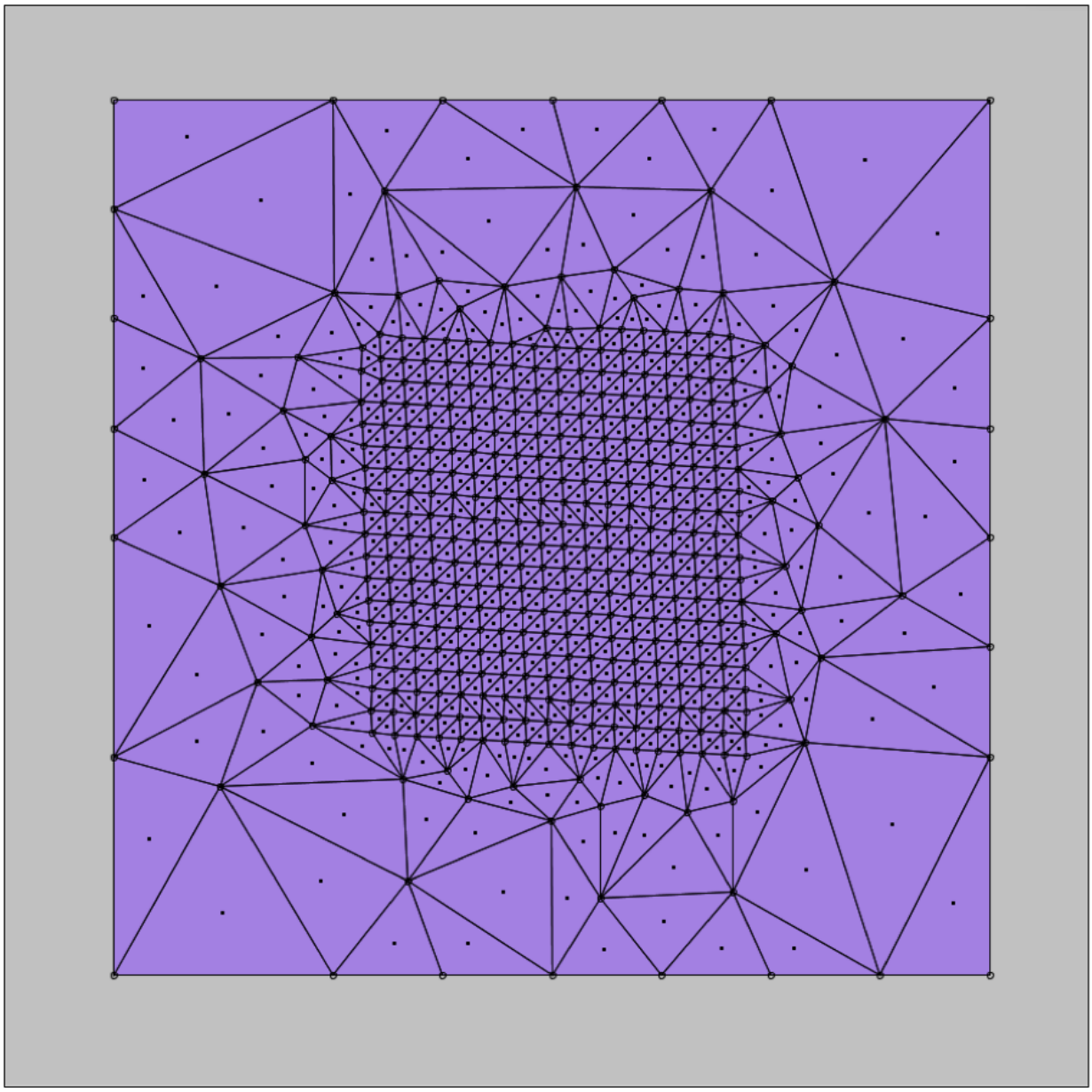

Figure 4.6: A projection of the *Water Depth* data onto the plane $z = 0$ m and extending from -20 to 20 km in the x- and y-directions after a 2D mesh has been generated over the region. Note the addition of nodes along the boundary and in the intermediate area between horizon data and the boundary.

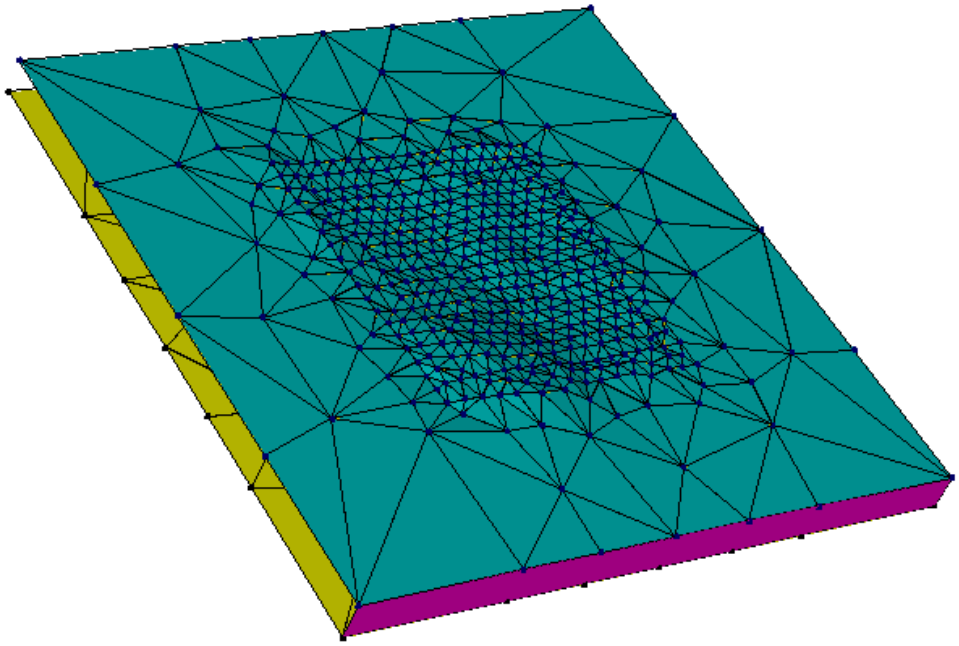

Figure 4.7: The 3D process of joining the 2D horizons by facets. The *Water Bottom* horizon (teal) and *Base Tertiary* (yellow) sections are joined by a facet (pink) by connecting the boundary nodes of each horizon to this facet. While this process is repeated for each face of the region, only one facet is shown here for simplification. Note the topography of the *Water Bottom* horizon that is visible in this perspective view.

It is significant to mention that because of the addition of bathymetry information from the *Water Bottom* horizon, the plane $z = 0$ m now represents sealevel, as opposed to the water-sediment interface of the 1D models in previous sections. As a result, the source — while still extending from -100 to 0 m in the $x-$direction — is now located at $z = 1050$ m, which is 100 m above the water depth average of 1150 m. Because the *Water Bottom* layer is relatively flat — varying only 54 m across the 20 km $\times$ 20 km grid — observation locations were placed along the water depth average, and box-type refinement was used around the source and observation locations (see Figure 3.8). These two refinement regions are based on the experience gained from the modelling sequence covered in Chapter 3, but have been shifted 1050 m in the $+z$-direction to account for the depth change mentioned above; all models discussed in this chapter will follow this refinement pattern unless otherwise stated. While the development of each model followed a similar workflow, the specifics of each are described in their respective sections.

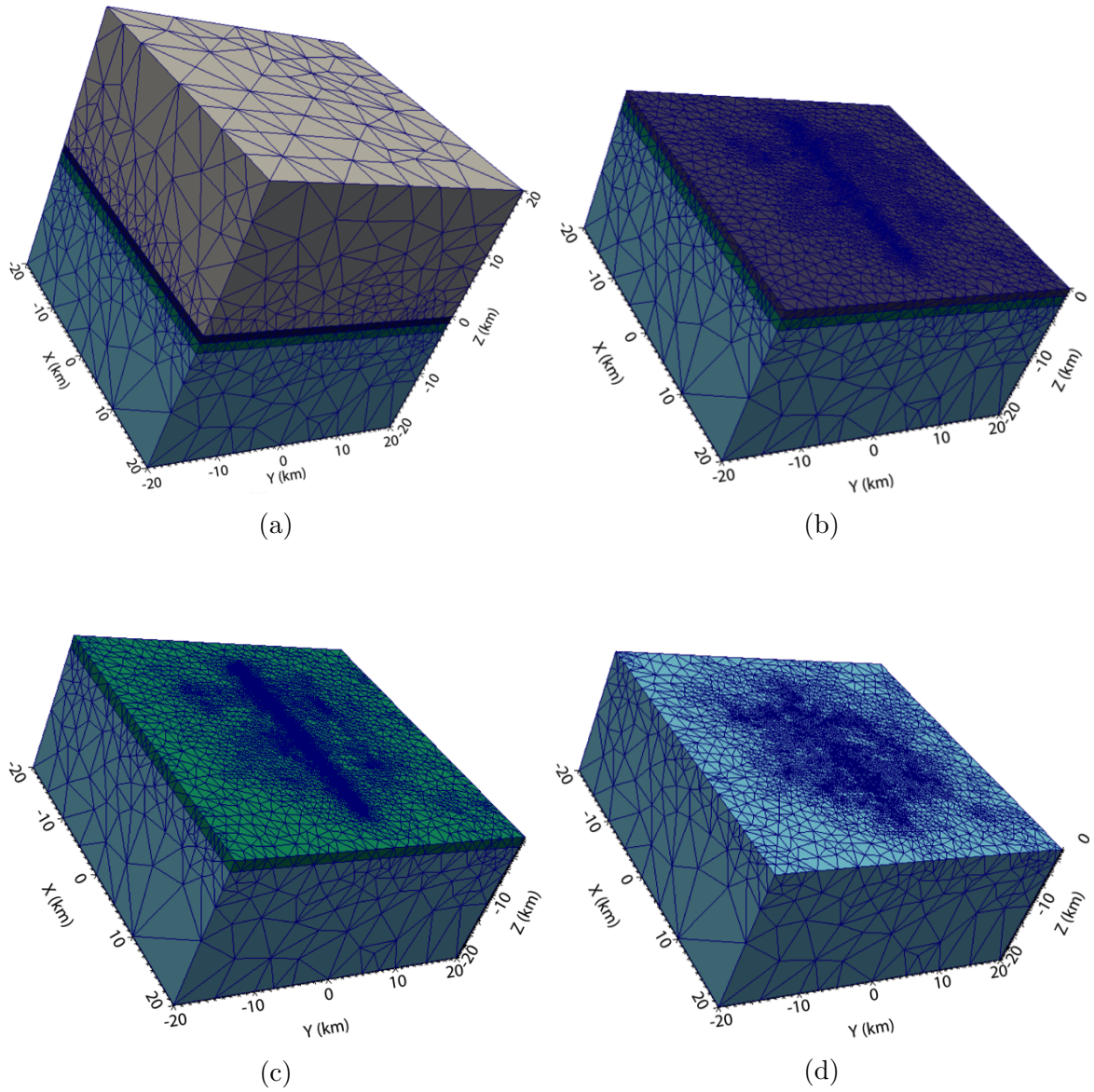

Figure 4.8: A progression of lithology slices displaying each layer of a model with 3D *Water Depth* and *Base Tertiary* horizons added. Grey represents the air layer, navy the water layer, green the *Base Tertiary* section and light blue the basement. Panel (a) displays the entire mesh; panel (b) displays the top of the *Water Bottom* layer (note the change in layer colour to enhance mesh view); panel (c) shows the top of the *Base Tertiary* layer; and panel (d) displays the top of the *Basement* layer.

4.3 Bathymetry

The simplest case in 3D modelling is adding bathymetry to a water-depth model. This is achieved by adding a flat layer at $z = 0$ m, and setting the conductivity of the section between this layer and the *Water Bottom* layer to 3.2 S/m. The region over the flat layer represents an infinite air layer, with a conductivity of 10^{-8} S/m. Two conductivities for the sediment layer were tested to analyse the effect of basement properties on the overall model. One conductivity — 0.769 S/m — represents the properties of the *Tertiary* section (Figures 1.8 to 1.10; Section 3.5), while the other — 1.0 S/m — is representative of standard basement conductivities (e.g. Key, 2009; Chandola et al., 2007; Constable et al., 2009)

The mesh was generated over a 40 km × 40 km × 40 km domain, creating 1,166,642 cells, 190,388 nodes and 14,451 edges (Figure 4.9). The region was electrically excited by a 1.0 Hz, 1 Am, 100 m line source situated at x = -100 to 0 m; this configuration will be used for all subsequent 3D models. Because of the added complexity of the model, the Krylov subspace was increased to 400 in order to decrease the number of iterations required by the GMRES solver to reach convergence (Figure 4.11).

Figure 4.10 displays the results of the bathymetry models. The increase in conductivity of the sediments from 0.769 S/m to 1.0 S/m decreases the electric field amplitude with offset, but results of each converge to the same result once the air layer is detected (beyond ∼7 km offset). The conductivity increase narrows the phase data i.e. the areas of detection happen at shorter offsets for the more conductive sediments. As with the electric field amplitude, the results for each are identical in areas where the source energy (near offset) and air resistivity (far offset) are the dominant contributions.

In order to be accurately compared to real Earth scenarios, the magnitude of noise in raw data and the percent detectability of comparative models must be defined: the noise floor is defined by Constable (2010) as 10^{-15} V/m. For the sake of this study, the threshold of detection of the reservoir is 12.6% percent difference between the hydrocarbon-saturated and dry reservoir models, which is reflective of the maximum uncertainty of CSEM results from Myer et al. (2012).

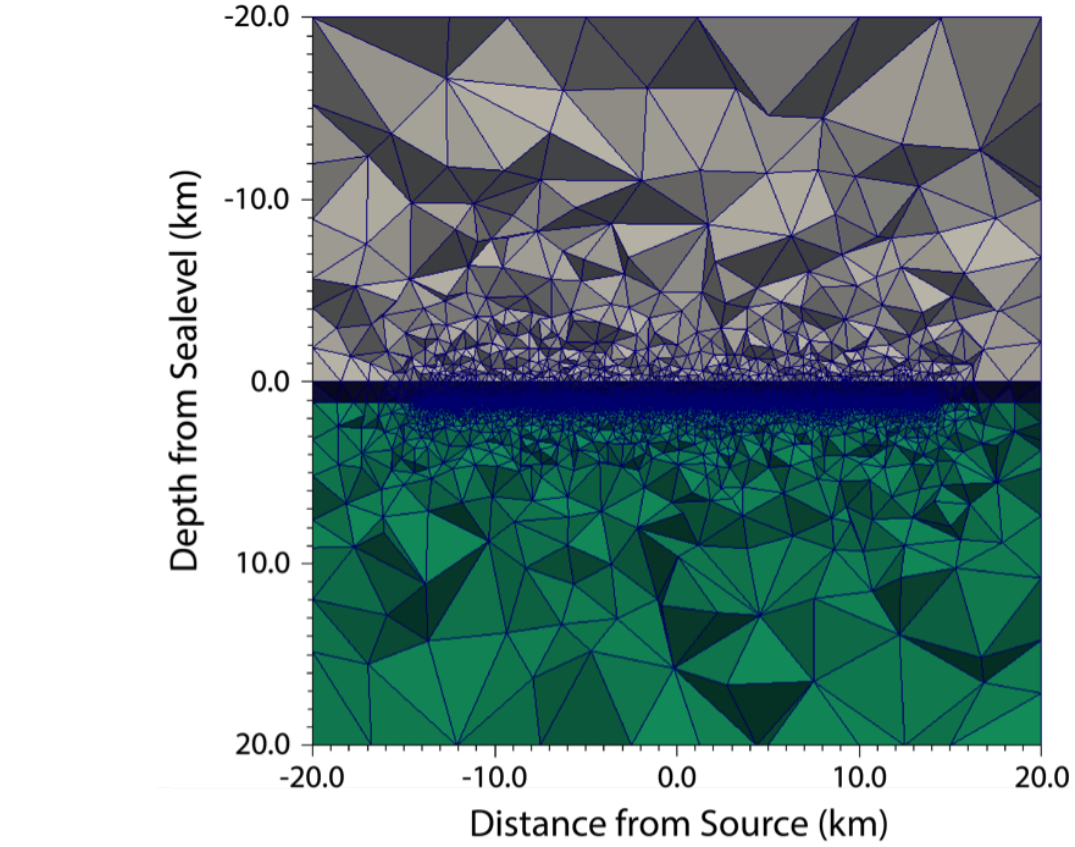

(a)

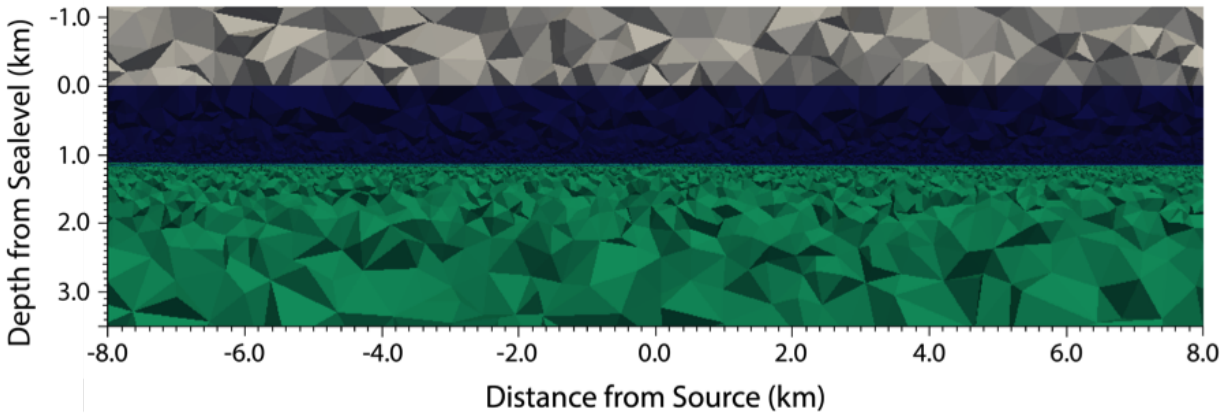

(b)

Figure 4.9: Cross-sections centered at $y = 0$ m of the bathymetry model. Panel (a) full view; panel (b) enhanced view of the bathymetry.

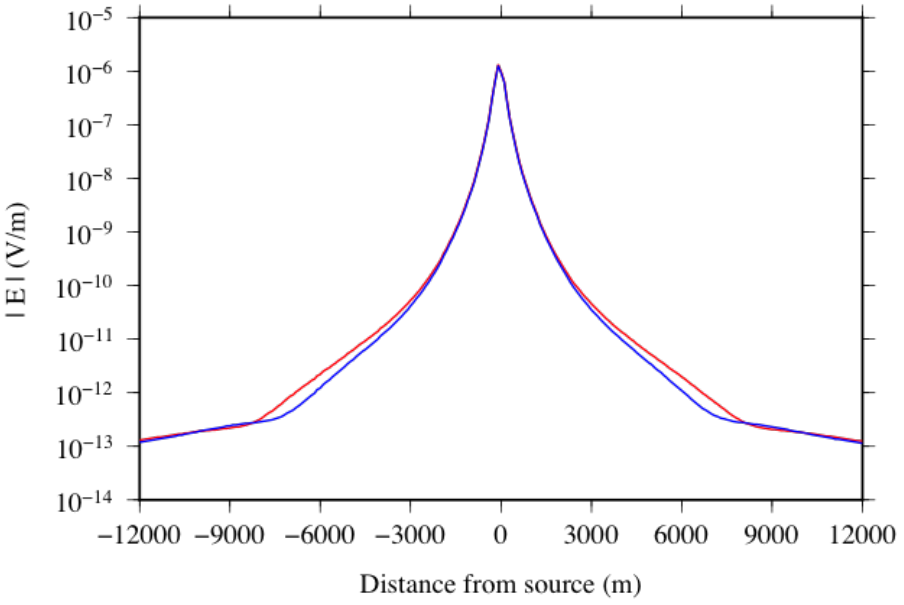

(a)

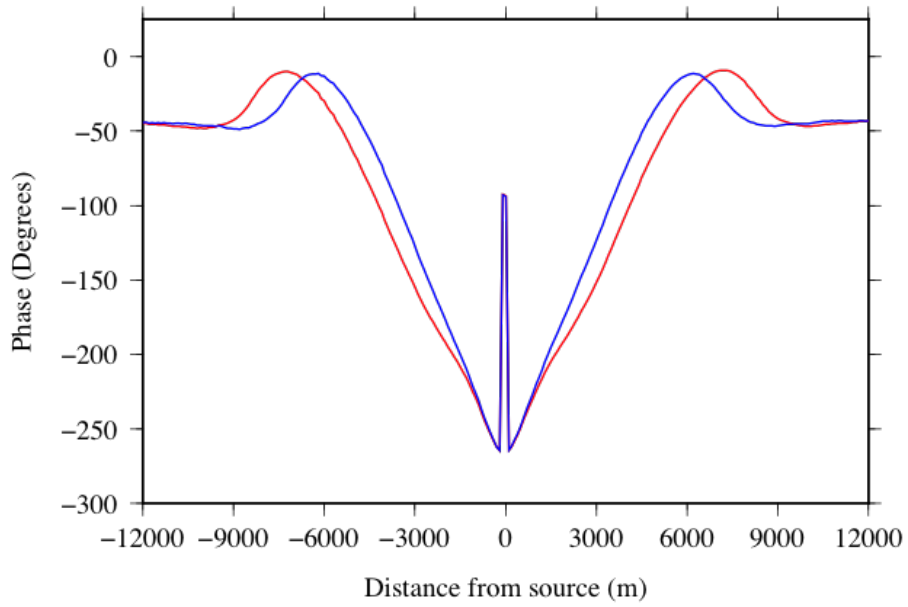

(b)

Figure 4.10: Panel (a) electric field amplitude and panel (b) phase results for the two bathymetry models in Figure 4.9 (*Bathymetry Model*). Red represents the results of sediments having conductivity values of the Tertiary section of the Flemish Pass Basin (0.769 S/m); blue represents the results of sediments with a basement value of 1.0 S/m.

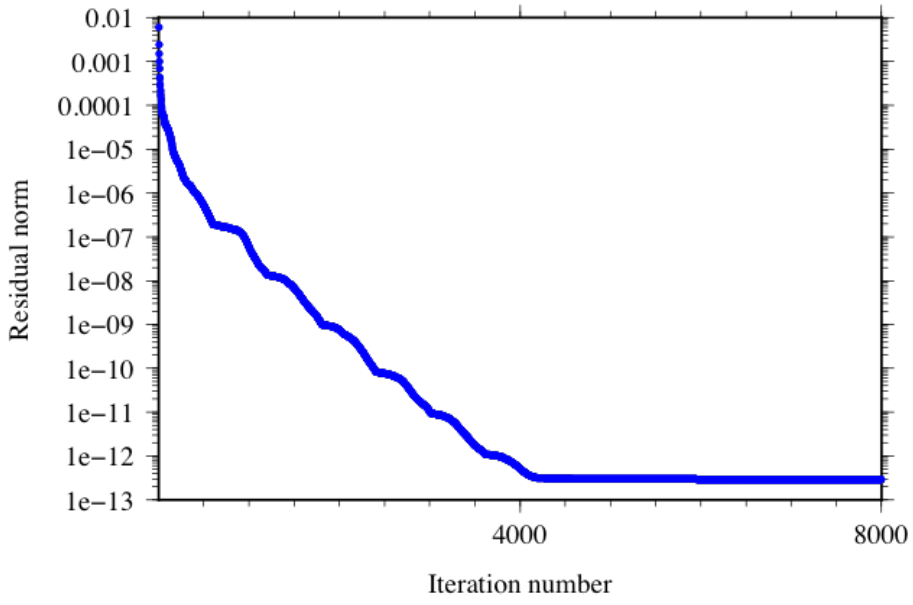

(a)

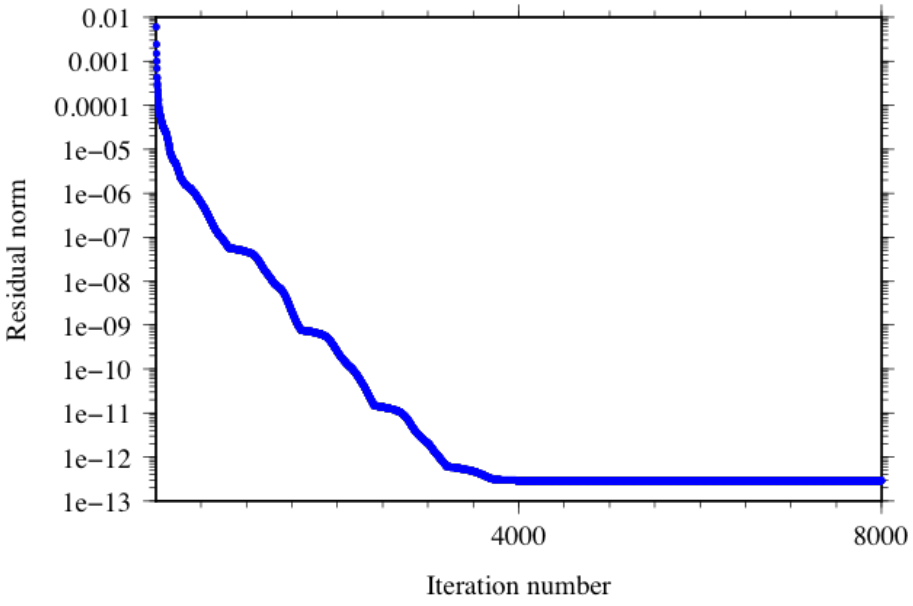

(b)

Figure 4.11: Convergence curves for the GMRES iterative solver for the results of the two bathymetry models (Figure 4.9). Panel (a) using Tertiary conductivity (0.769 S/m) ; panel (b) using 1.0 S/m conductivity.

4.4 Cretaceous and Tertiary Layers with Bathymetry; Background Geological Structure

Proceeding to increasing model complexity, the effect of the additional seismic-derived horizons was explored. The first horizon — representing the *Base Tertiary* — dips very shallowly toward the negative x-direction, representing the north west in UTM coordinates. The layer depth decreases from 3100 m to 2500 m below sealevel in the positive x-direction (Figure 4.12), and decreases from 2800 to 2700 m below sesalevel in the $+y$-direction (Figure 4.13). The addition of this layer to the bathymetry generates 1,223,429 cells, 199,522 nodes, and 17,208 edges across the 40 km $\times$ 40 km $\times$ 40 km computational domain. The region is given a conductivity of 0.769 S/m, as recommended by Suncor Energy, with the basement layer given a conductivity of 1.0 S/m. As with the bathymetry model, the Krylov subspace for the GMRES solver was increased to 400 to ensure proper convergence (Figure 4.17).

The second horizon — representing the *Base Cretaceous* — has a slightly more complex structure: due to the nature of the dip of the overlying *Base Tertiary* horizon and it's unconforming contact, the *Tithonian* layer does not follow the same trend. The horizon remains relatively horizontal at 3600 m depth from sealevel, with the dip of the overlying *Base Tertiary* horizon creating a $\sim$600 m thickening in the positive x-direction, as the contact rises from 3100 m below sealevel to 2500 m (Figure 4.14). The horizon is near-horizontal in the positive y-direction with slight ($\sim$200 m) thickening at the boundaries of the horizon data (Figure 4.15). The addition of this horizon complicates the nature of the mesh, and generates 1,354,151 cells, 221,095 nodes and 23,260 edges. The two horizons

have conductivity values of 0.769 S/m and 0.476 S/m, respectively.

The results for the two models described above are shown in Figure 4.16. As shown from Figure 4.16, the addition of the 0.476 S/m Cretaceous layer does not cause the results to deviate from the single layer model greatly, but the layer is detectable by its slight electric field amplitude increase, which is more noticeable at positive x-offsets (right of the profile) where the Tertiary layer has thinned. There is a comparably minimal effect on phase, slightly delaying the turn-over of the onset of the air layer effect until larger offsets. As the modelled reservoir geometries in further sections are truncated by the *Base Tertiary* unconformity, the *Top Tithonian* horizon is eliminated from future models.

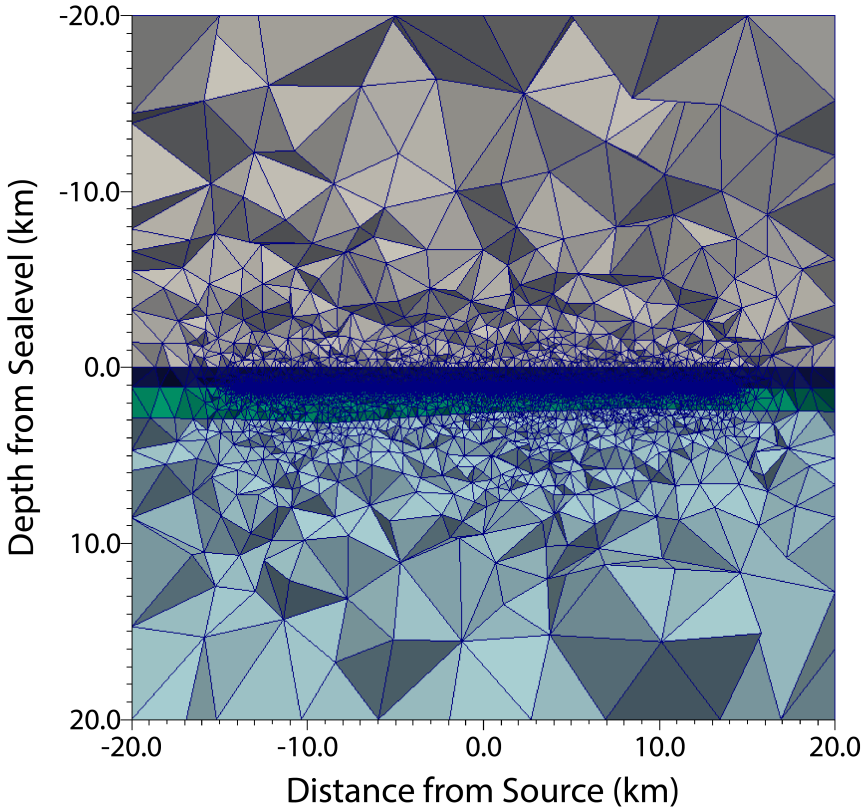

(a)

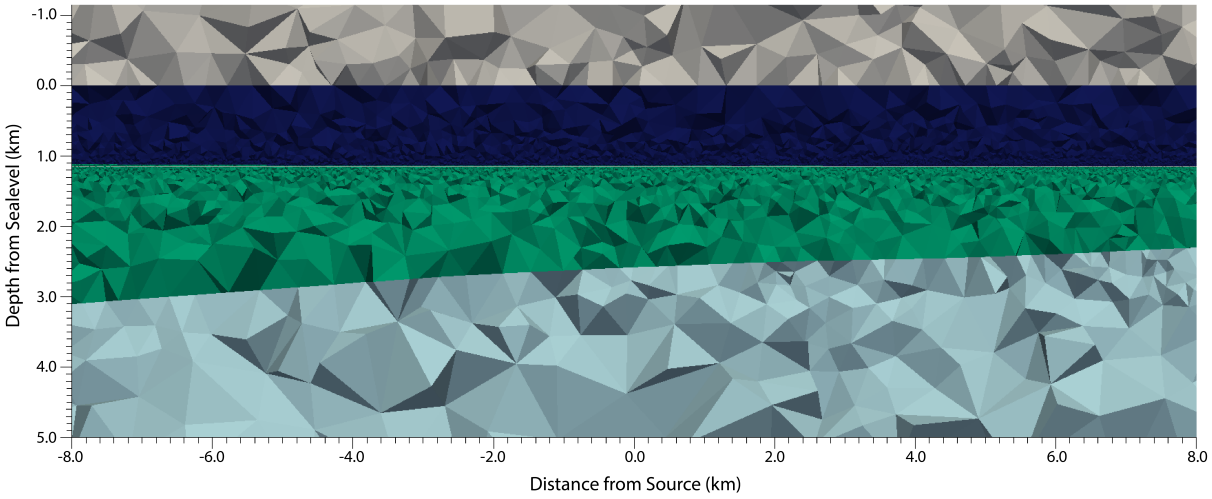

(b)

Figure 4.12: Cross-sections centered at $y = 0$ m of the single-layered (i.e. Tertiary-only) model. Panel (a) full view; panel (b) enhanced view of the layer and bathymetry.

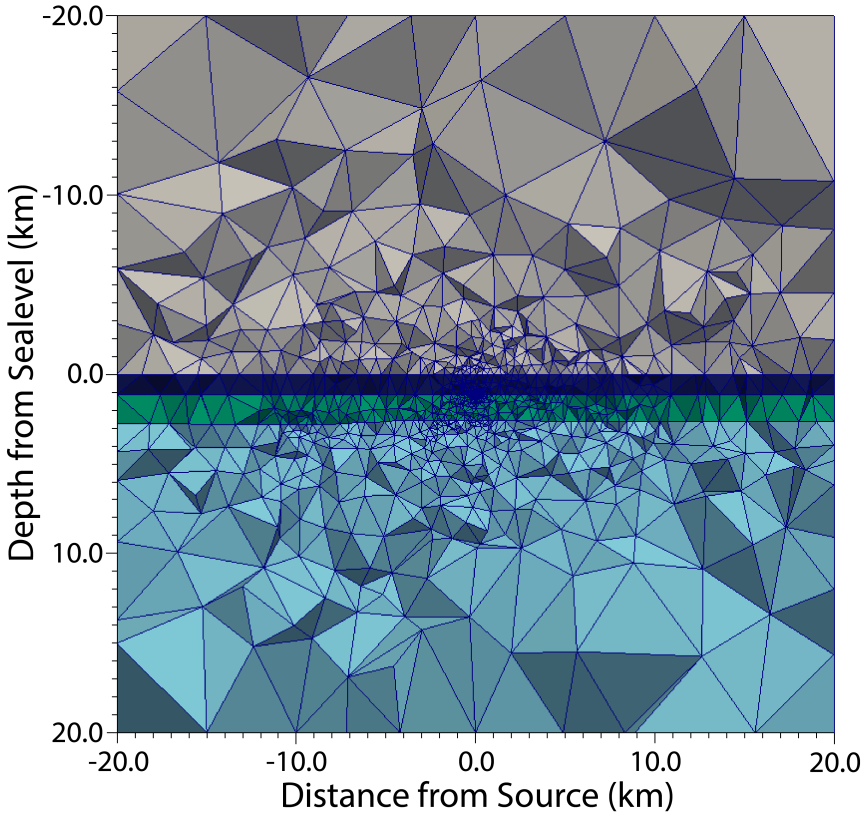

(a)

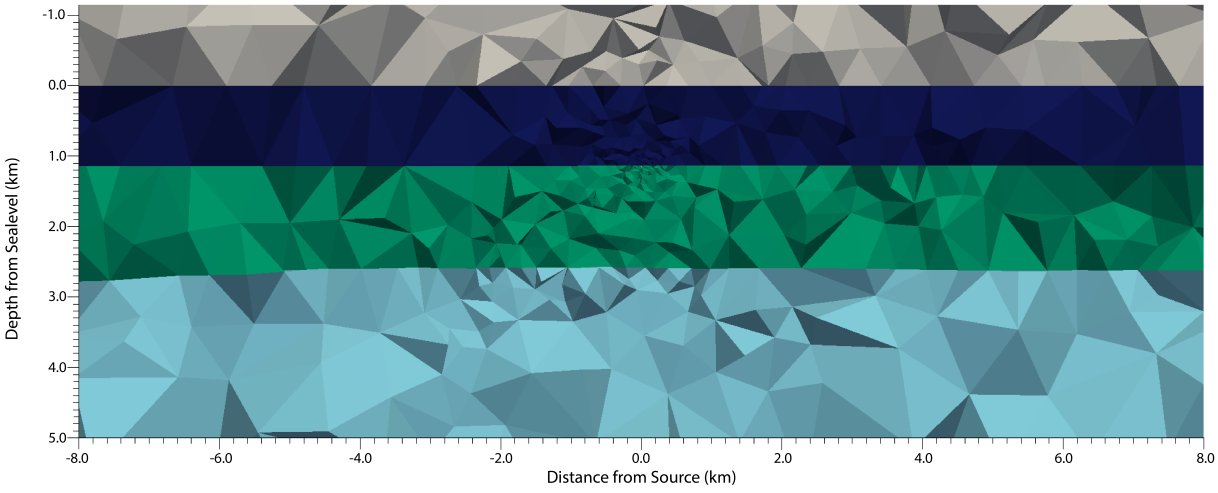

(b)

Figure 4.13: Cross-sections centered at $x = 0$ m of the single-layered (i.e. Tertiary-only) model. Panel (a) full view; panel (b) enhanced view of the layer and bathymetry.

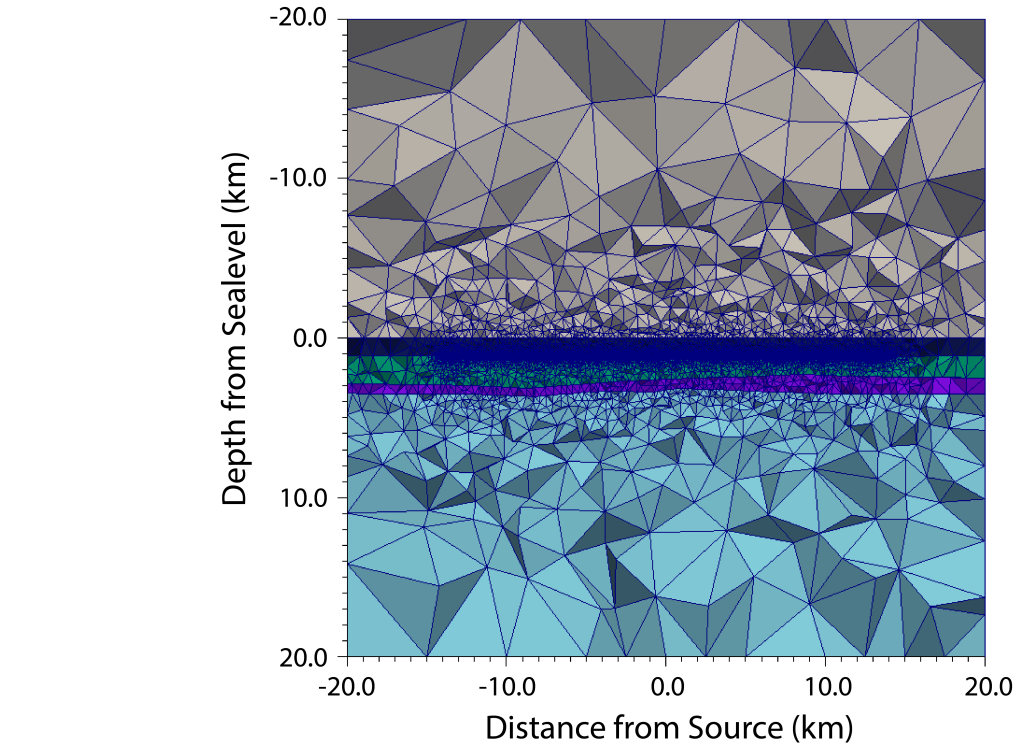

(a)

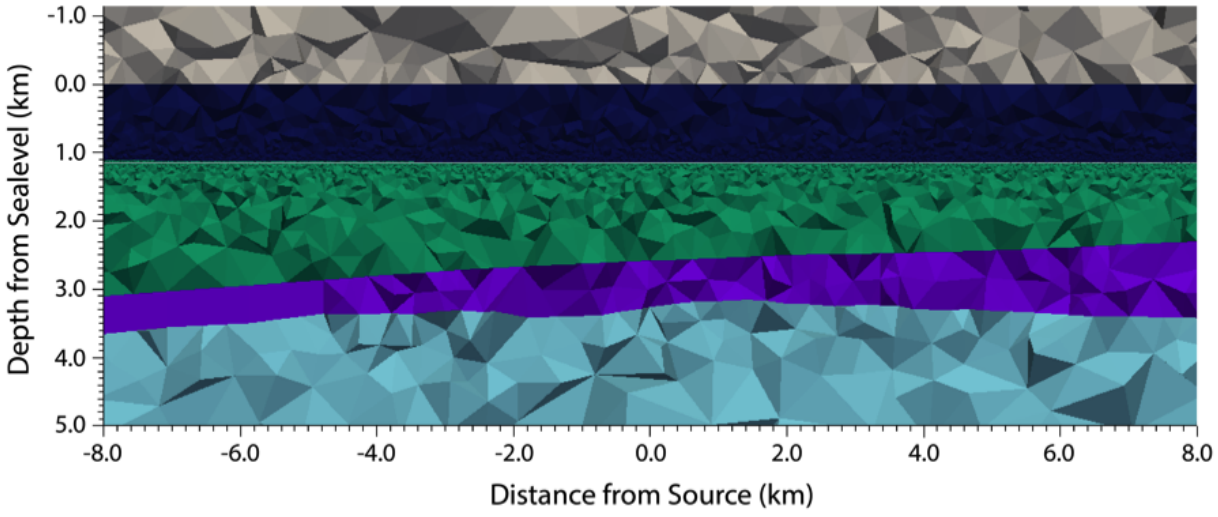

(b)

Figure 4.14: Cross-sections centered at $y = 0$ m of the multi-layered (i.e. Tertiary and Cretaceous) model. Panel (a) full view; panel (b) enhanced view of the layer and bathymetry.

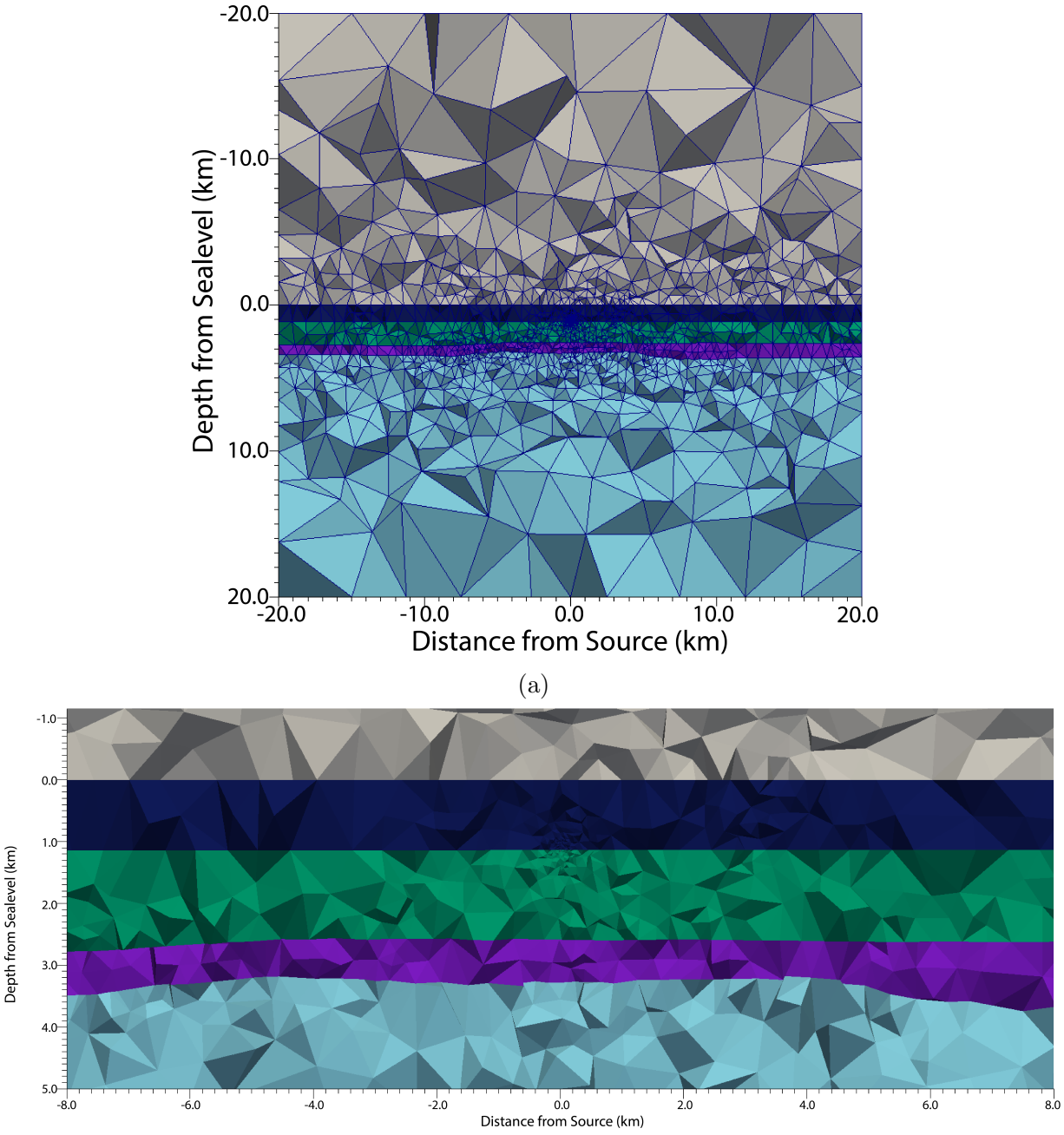

Figure 4.15: Cross-sections centered at $x = 0$ m of the multi-layered (i.e. Tertiary and Cretaceous) model. Panel (a) full view; panel (b) enhanced view of the strata and bathymetry.

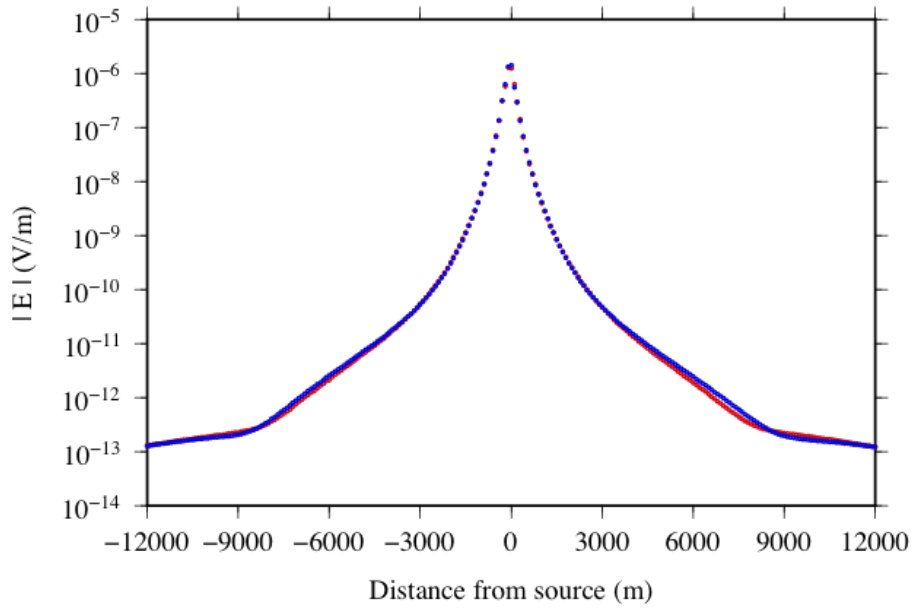

(a)

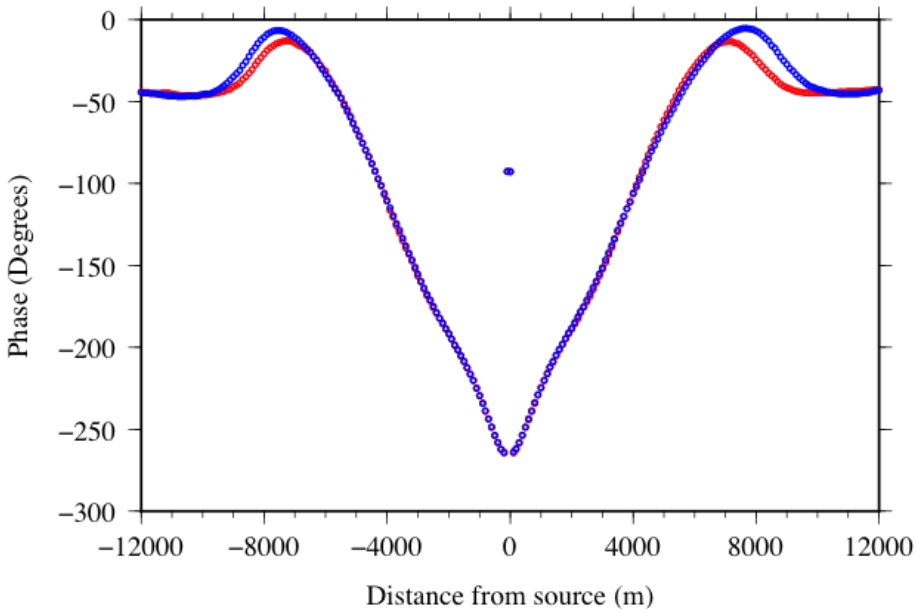

(b)

Figure 4.16: A comparison of the (a) electric field amplitude and (b) phase results of the Tertiary-only (Figures 4.12 and 4.13; red circles) and Tertiary plus Cretaceous (Figures 4.14 and 4.15).

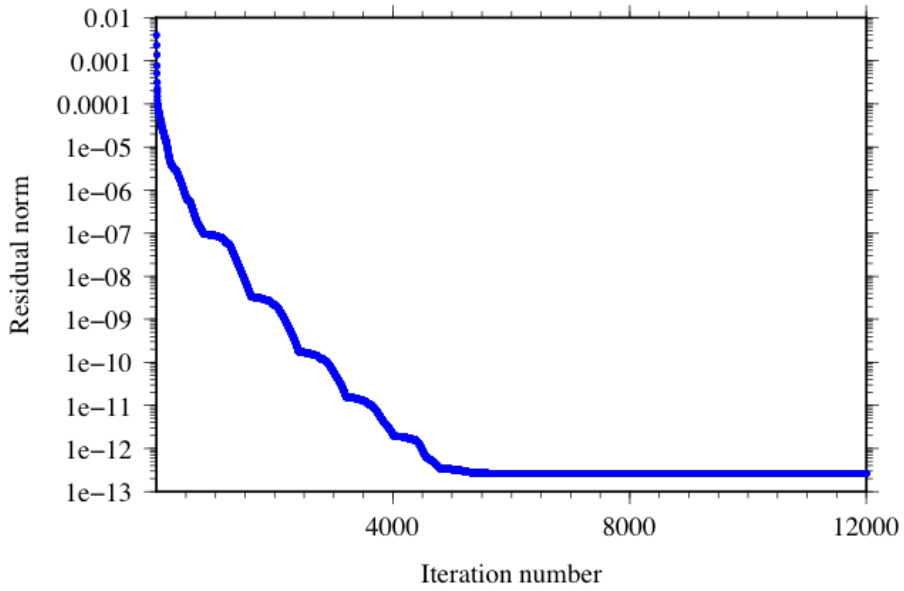

(a)

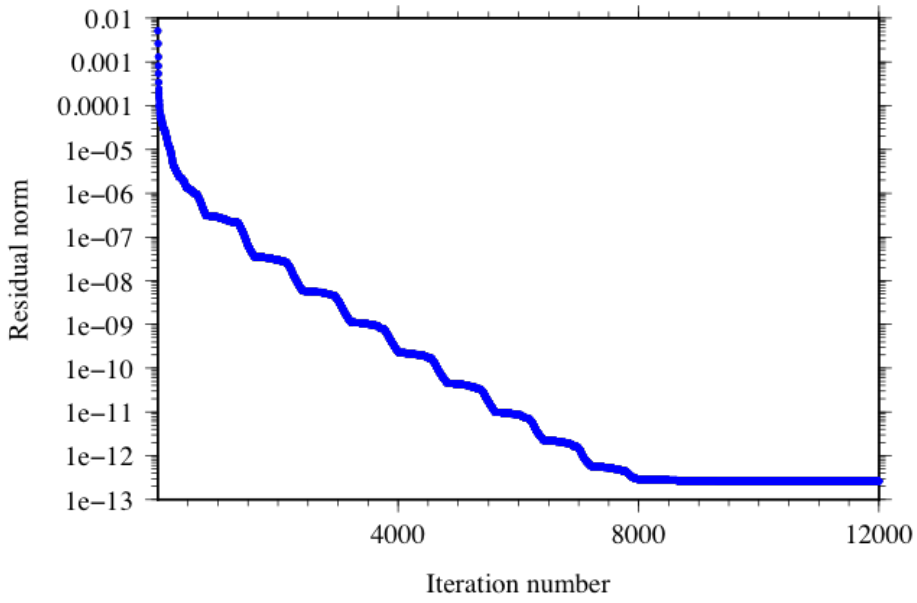

(b)

Figure 4.17: Convergence curves for the GMRES iterative solver for the results of the models in panel (a) Figure 4.12 (*One Layer*) and (b) Figure 4.14 (*Two Layers*).

4.5 Reservoir Geometries

As the main motivation of this study was to explore scenarios that are relevant to real-world offshore environments, the climax for results involves the comparisons of proposed, but as yet unknown, reservoir structures in the subsurface. Through communication with Brad Bonnell of Suncor Energy, a series of schematics of these potential geometries (Figures 1.9 and 1.10) with suggested conductivities (Table 4.2) was developed, without the need of disclosing proprietary information. The resistivities for the water-filled sand package is based on a saline-fluid saturation, hence the higher conductivity of 1.5 S/m. The main aims of this series were to produce a thorough understanding of the CSEM detectability of the reservoir — as in previous models — and to explore results with added reservoir complexities. This includes using various resistivity values to represent the quality of reservoir (typically, reservoir quality is proportional to hydrocarbon resistivity, as the greater volume of hydrocarbons will generate a higher resistivity; Archie, 1942), altering the source position, and incorporating various oil-water contacts representing partially-saturated reservoirs, as is often the case in offshore scenarios (Heasley, et al., 2000). As a consequence, the series of results can be matched to real world CSEM measurements and the most probable reservoir match can be accurately proposed.

The general stratigraphy of the series of reservoir models is shown in Figure 4.18, using *Model 1* as an example: a complex reservoir section — whose age ranges from Jurassic to Late Cretaceous — is truncated by a Tertiary-aged unconformity at ∼3000 m depth (defined by the 3D *Base Tertiary* horizon provided). This Tertiary overburden can be assumed as homogeneous, and extends to the seabed. The reservoir section extends to

Region Colour	Region Age or Characteristic	Region Conductivity (S/m)
	Air	10^{-8}
	Water	3.2
	Water Bottom to Base Tertiary	0.769
	Late Cretaceous	1.1
	Early Cretaceous	0.5
	Hydrocarbon-Filled Sand Package	0.01
	Water-Filled Sand Package	1.5
	Jurassic	0.6
	Basement	1.0

Table 4.2: Characteristics of the regions used in the reservoir geometry models.

7150 m depth for each model but a model-dependent lateral extent is indicated for each respective model.

In preliminary stages of model-building, the reservoir was unattached to the unconformity to explore the general capabilities of constructing such a complex structure (*Model 1*, whose results are discussed in Subsection 4.5.1 is used as an example in Figures 4.19 and 4.20). Attachment of this reservoir to the unconformity is vital in generating an accurate 3D Earth model. Unfortunately, the addition of a 3D contact at the *Base Tertiary* unconformity complicates the task of model-building greatly: imperfect alignment of the horizon's nodes creates an irregular reservoir boundary that would be near-impossible to duplicate for consistent model assessments. This is illustrated in Figures 4.21 to 4.24. Figure 4.21 shows the nodes defining the *Base Tertiary* in the model. Figure 4.22 shows the complex structure of the entire boundary extending from $x = y =$ -7500 to 7500 m. Figure 4.23a displays the great number of irregular cells that would be involved in the process

of attaching the reservoir to this *Base Tertiary* horizon. Figure 4.24a shows all of the nodes that could potentially be incorporated into the boundary attachment. To attach the reservoir to the *Base Tertiary* horizon, the specific facets and nodes which are involved in the attachment process must be duplicated in both the horizon and the reservoir. Having the range of boundary possibilities as indicated in Figures 4.23a and 4.24a would make boundary creation in the reservoir an incredibly painstakingly labourious process.

To simplify this attachment process, nodes were removed from 500 m on either side of the boundary of attachment on the *Base Tertiary* layer (Figure 4.21b), creating a node gap around the boundary, but maintaing nodes inside and outside the boundary. Four nodes were then manually entered at each corner of the boundary at 2500 m depth — the average depth of the horizon. Facets were then introduced, joining these nodes using FacetModeller (Figure 4.21c). The horizon was next exported to a *.poly* file, where it was meshed using the 2D meshing software Triangle (Figure 4.21d; using the process described in Chapter 2). By explicitly defining the reservoir boundary, the reservoir connection process — and thus model generation process — is significantly streamlined. This is visualized by the reduction of boundary possibilities displayed in Figures 4.22b, 4.23b and 4.24b: there is one obvious choice in the straight line boundary directly at $x = 7500$ m. This process was repeated for each of the boundaries in each respective models, for example, at $x = -7500$ m and at $y = -7500$ and 7500 m in *Model 1*.

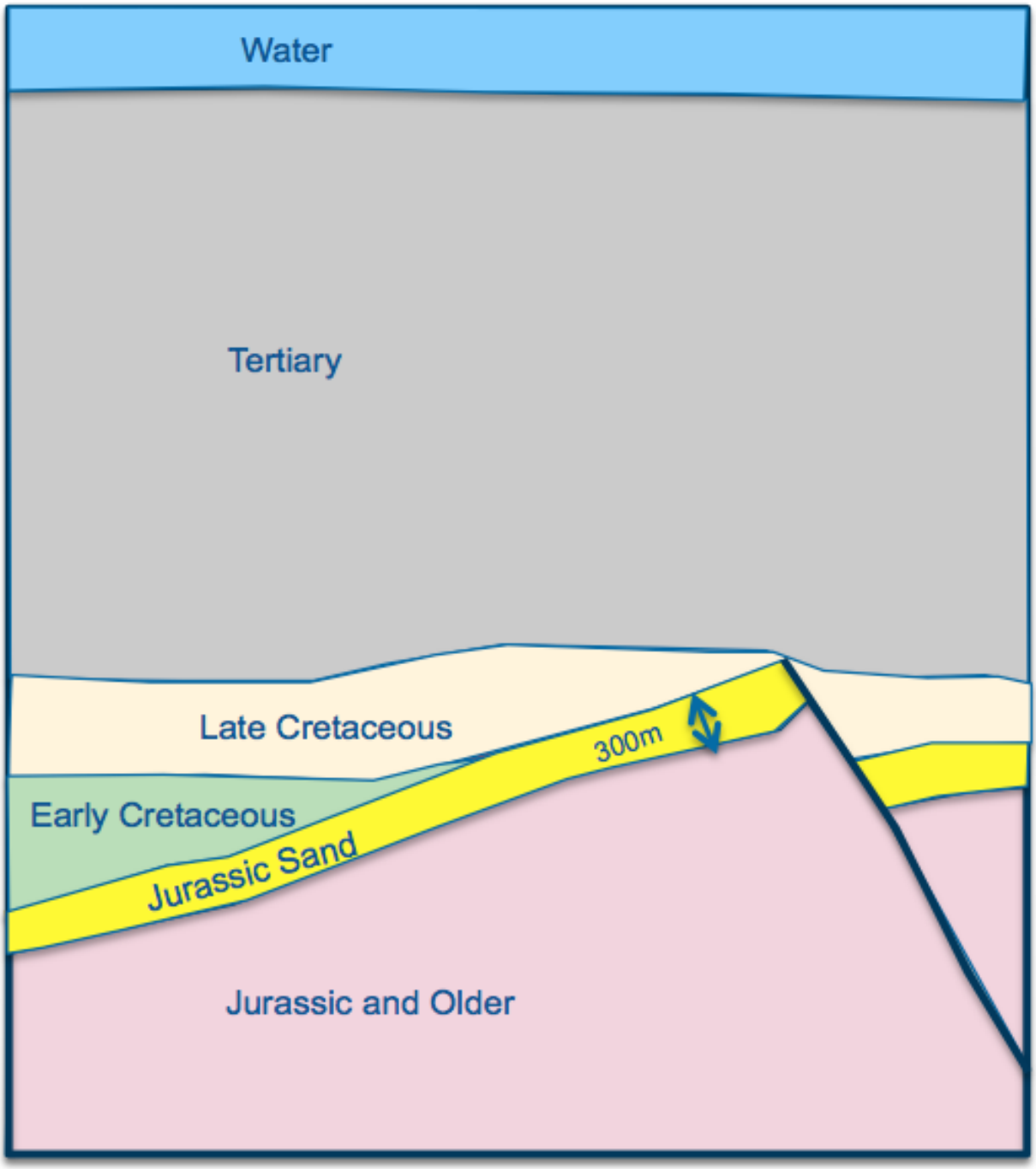

Figure 4.18: Schematic representation of the kind of structural trap scenarios considered in this section (this corresponds to *Model 1*; see Subsection 4.5.1; compliments of Brad Bonnell, Suncor Energy).

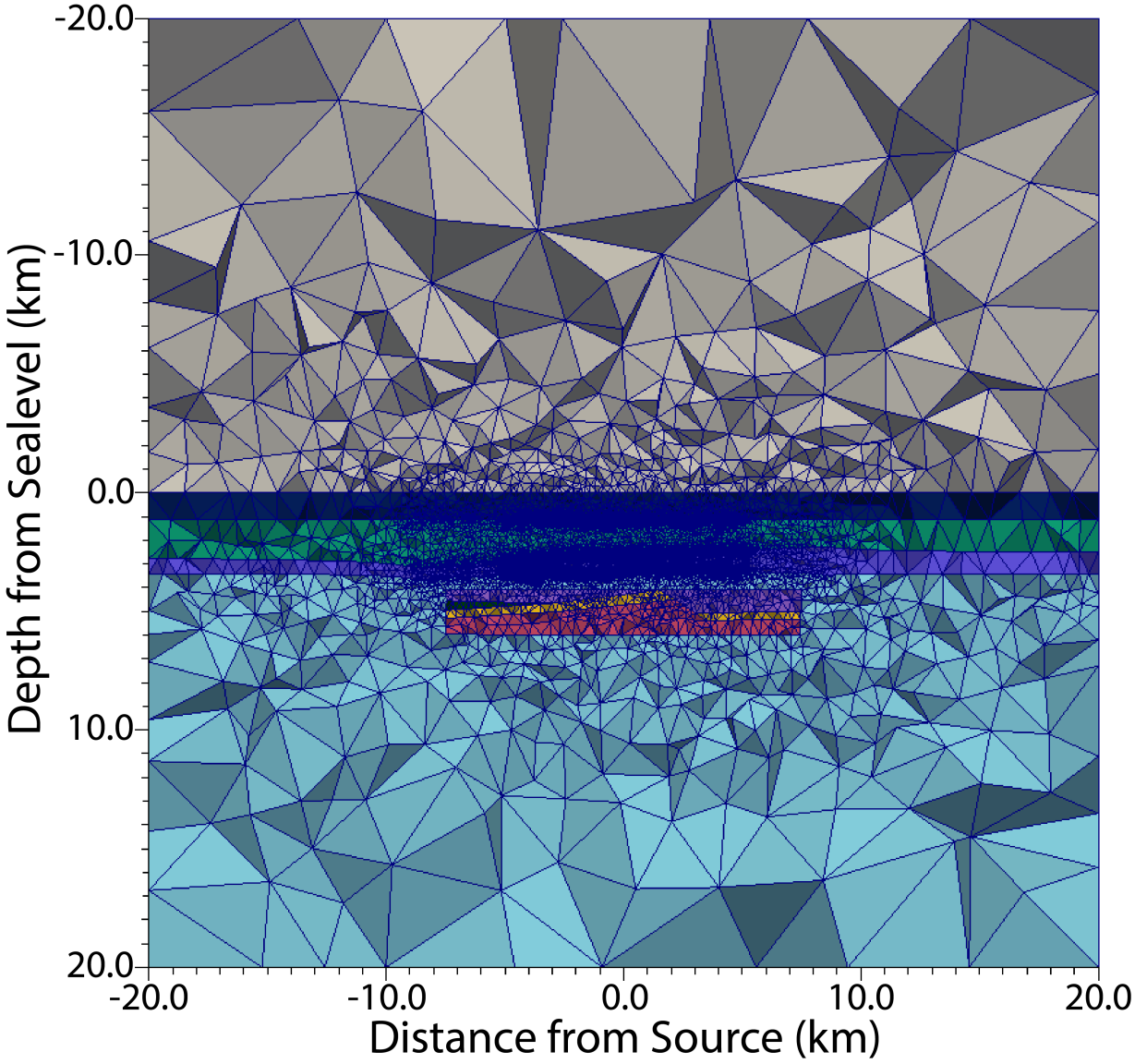

Figure 4.19: Cross-section centered at $y = 0$ m of a preliminary version of *Model 1*. Note the lack of attachment of the reservoir section to the *Base Tertiary* unconformity.

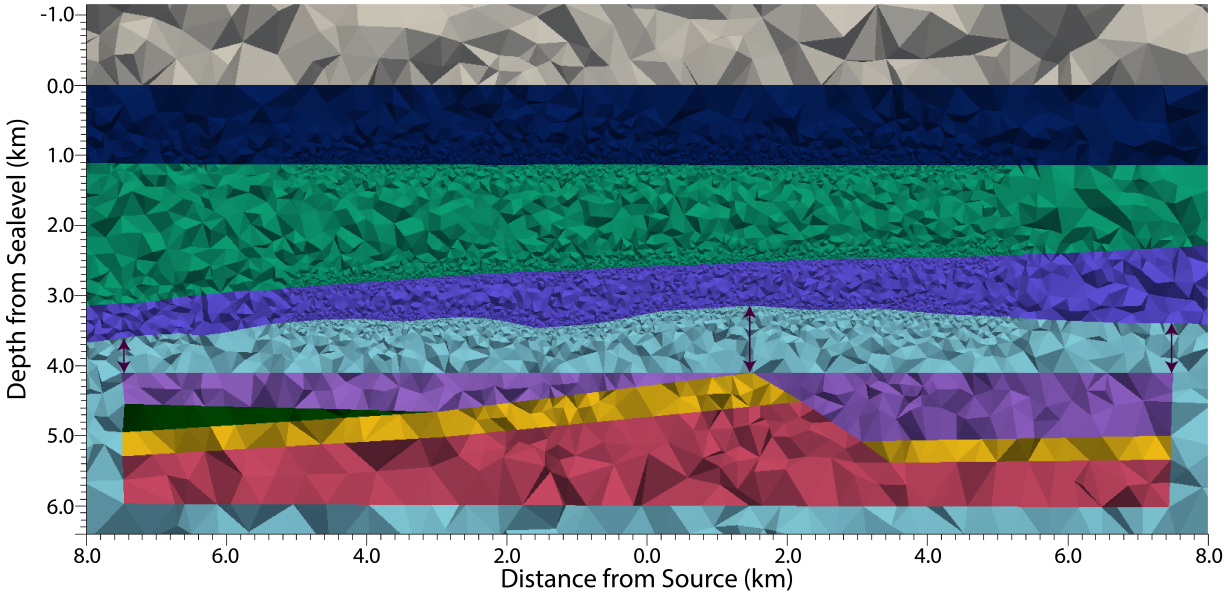

Figure 4.20: Enhanced cross-section centered at $y = 0$ m of the initial attempt of building *Model 1*. Violet arrows indicate areas of detachment from the reservoir boundaries and truncated fault that must be attached to the *Base Tertiary* to accurately represent the structure in the subsurface. Note that this Figure represents a very preliminary stage in the model building process: in finialized models, the *Base Cretaceous* layer (cornflower blue) is removed to more accurately represent timing of deposition, causing cell size and cell density to be significantly altered in subsequent models.

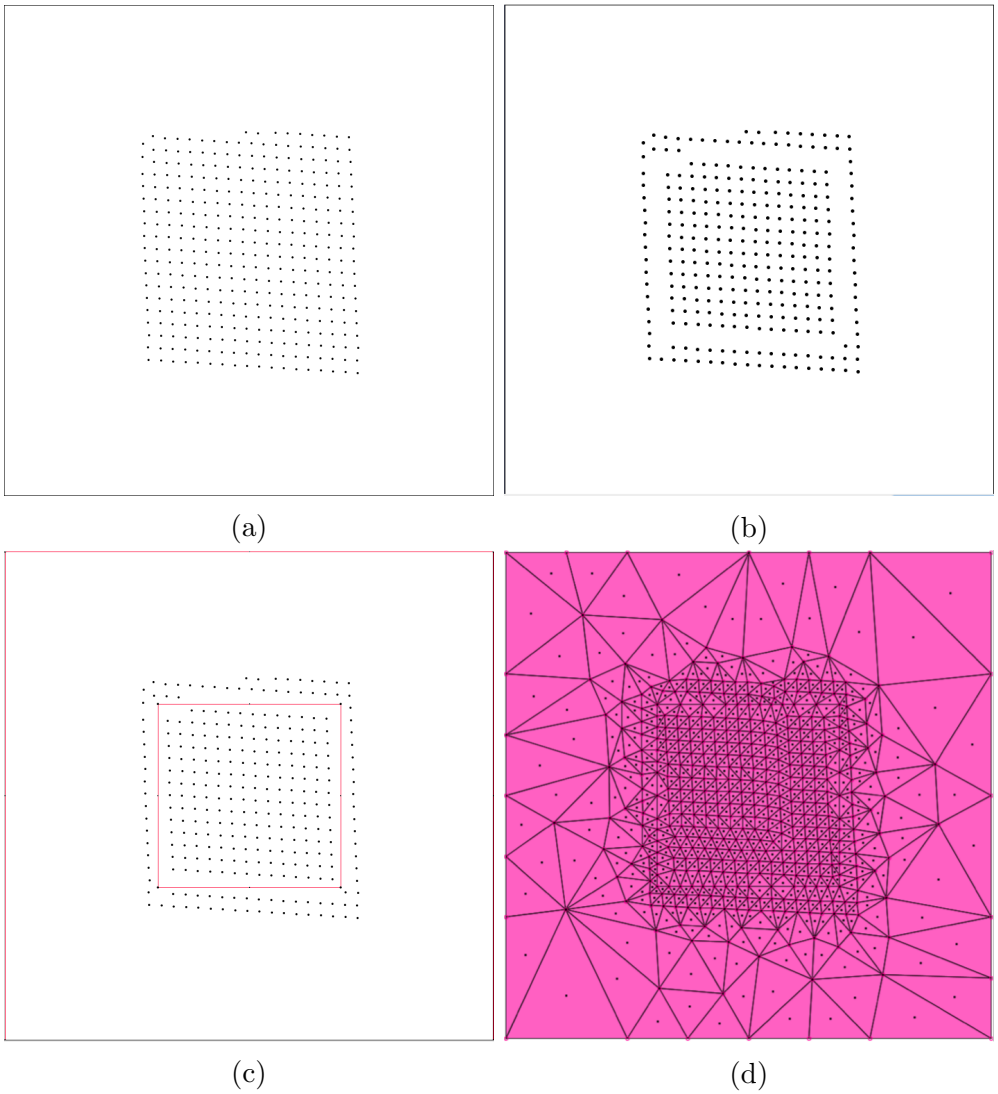

Figure 4.21: 2D projections of the *Base Tertiary* horizon onto the plane $z = 0$ m. Panel (a) nodes of the horizon without reservoir boundary alteration; panel (b) nodes of the horizon after a boundary gap has been created for the connection of the reservoir onto the horizon; panel (c) the horizon including boundary gap, reservoir connection vertices at points (x, y, z) = (-5000, -5000, 2500) m, (-5000, 5000, 2500) m, (5000, -5000, 2500) m, and (5000, 5000, 2500) m, and connecting facets joining these vertices; (d) 2D projection of the final meshed horizon.

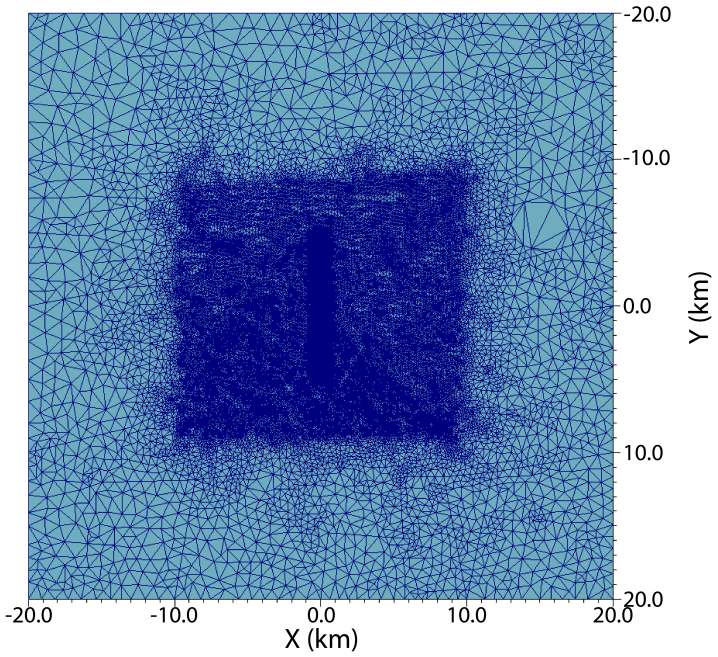

(a)

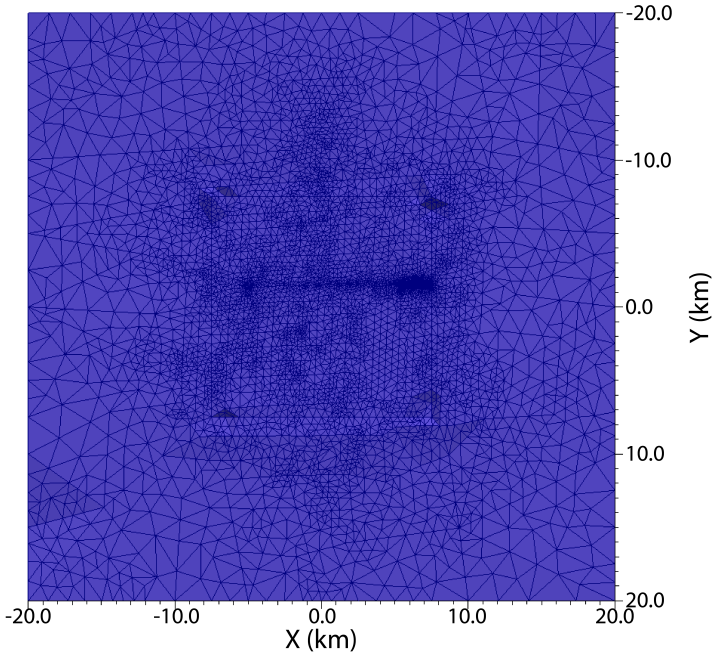

(b)

Figure 4.22: 3D map view visualizations of the *Base Tertiary* unconformity. Panel (a) unaltered horizon; panel (b) horizon with straightened boundary contacts.

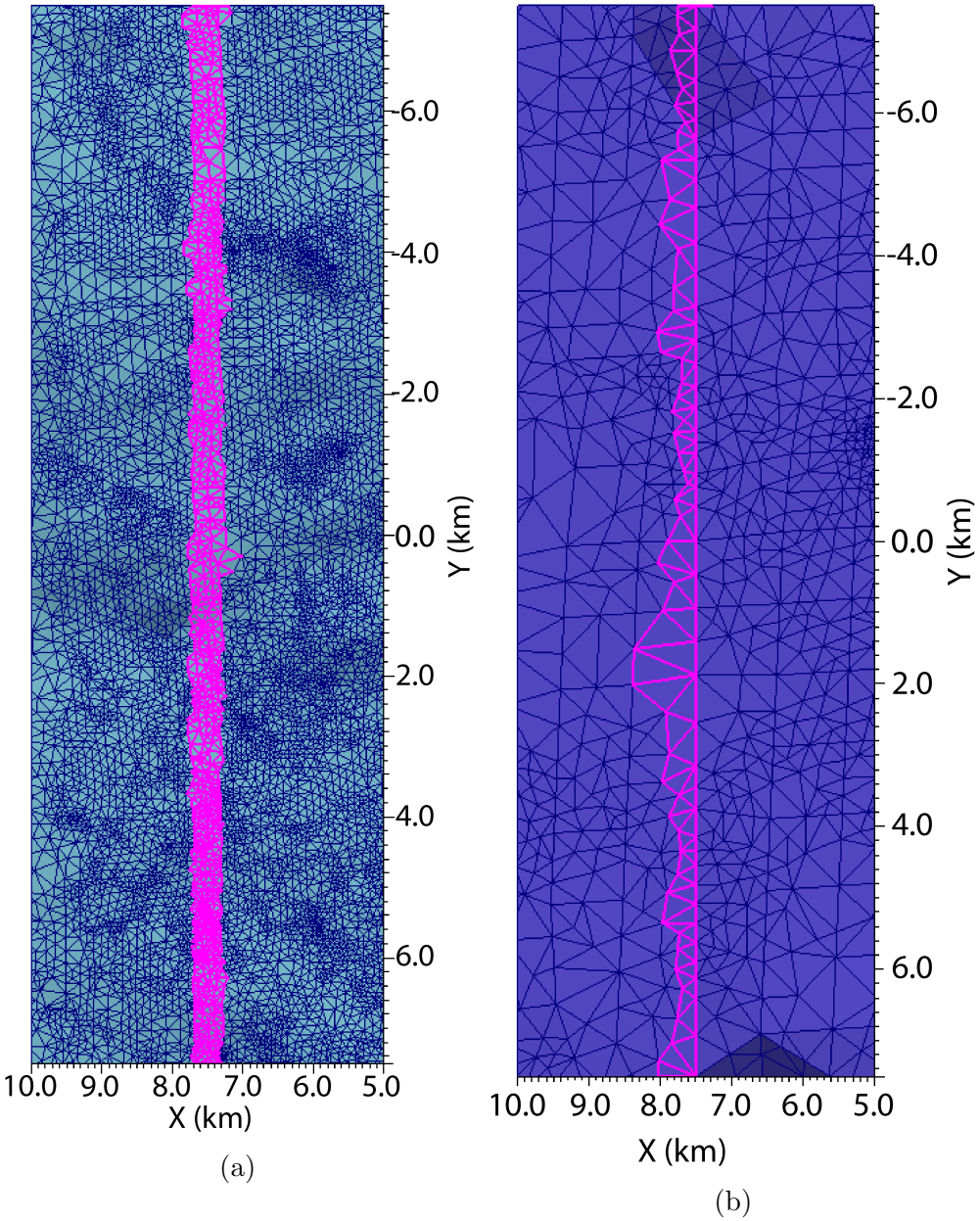

Figure 4.23: Enhanced 3D map view of the facet selection process for the unaltered horizon (panel a) and horizon with straightened boundary contacts (panel b) with highlighted facets (pink) for potential boundary contact of the reservoir with the *Base Tertiary* unconformity. Note the simplification generated by the line precisely at $x = 7500$ m in the straightened case (panel b) against the extreme complexity in the unaltered case (panel a). This process was repeated for each reservoir boundary.

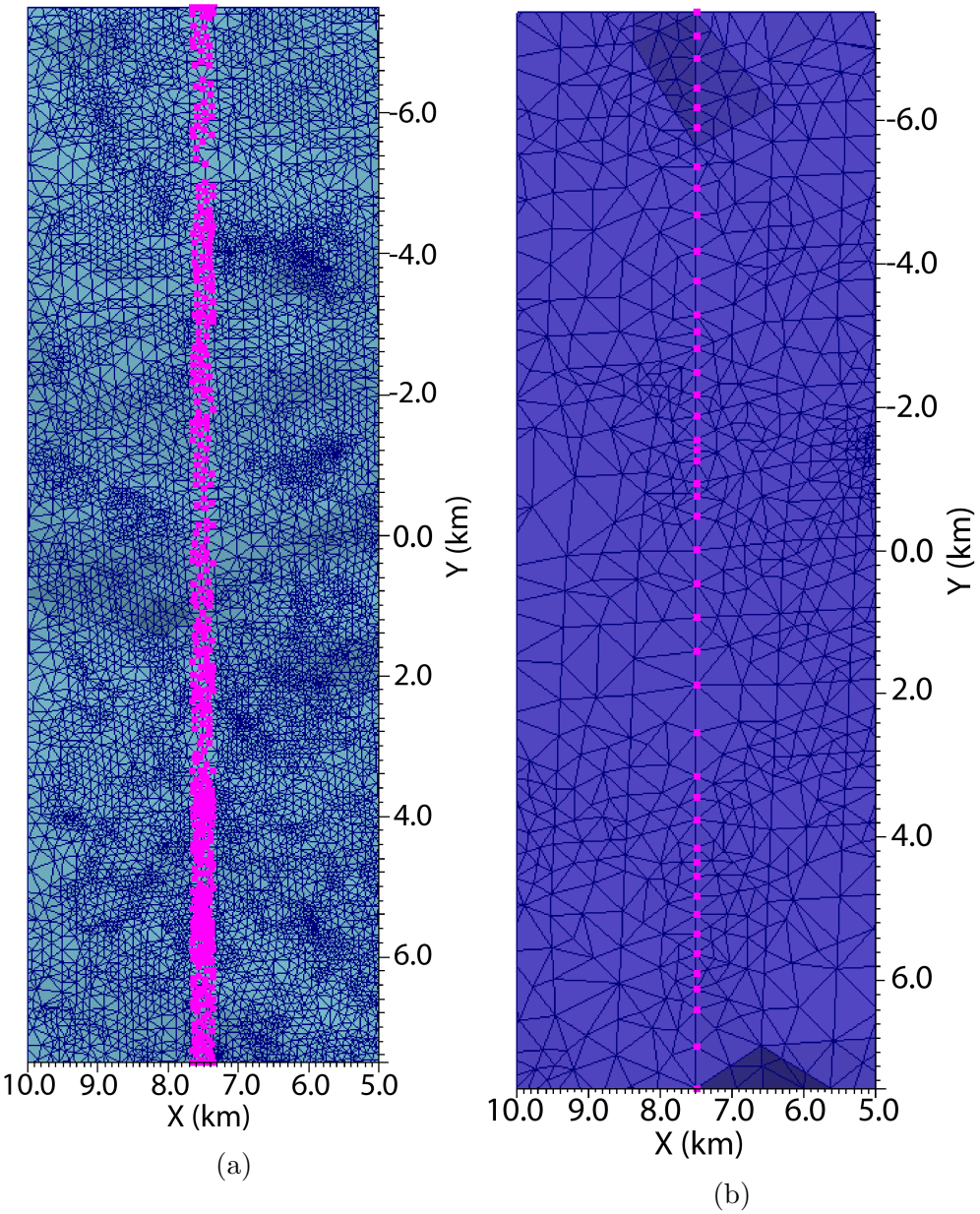

Figure 4.24: Enhanced map view for the unaltered horizon (panel a) and horizon with straightened boundary contacts (panel b). Highlighted nodes (pink) are those that may potentially be joined to make a boundary contact of the reservoir with the *Base Tertiary* unconformity. Note the decreased range and added linearity in the straighted case (panel b). This process was repeated for each reservoir boundary.

Using the schematics suggested by Suncor Energy as a guide, the specific reservoir geometries were created in FacetModeller. The same refinement for source and observation locations as for previous models was added manually. The model was then discretized using TetGen, which provided the neccessary inputs for the CSEM3DFWD modelling code. Once the results of an initial model were deemed accurate, variations were made based on potential reservoir charactersitics and source configuration. The results of each of the scenarios are discussed below, and include absolute and percent difference curves between each reservoir configuration and the results of the *Dry Reservoir* for the resepective scenario. The magnitude of percent difference indicates the detectability of the resistive reservoir, while smooth curves in the absolute difference results suggest the range of offsets that are capable of detecting the reservoir.

4.5.1 Model 1

The first geometry in the suite of potential reservoir configurations is composed of a single fault block system (Figure 4.25) with a lateral extent from -7500 to 7500 m in both the x- and y-directions (herein *Model 1*). The model was built based on the schematic provided by Suncor Energy (Figure 4.18) The reservoir is truncated by the *Base Tertiary* unconformity, as each subsequent model will be. The sand reservoir (yellow) is offset by the normal fault of the block system, and is overlain by a Late Cretaceous layer (purple), which extends across the entire extent of the reservoir. This is complemented by a wedge package in the West (left side of Figure 4.25), representing the Early Cretaceous.

The mesh in Figure 4.25 contains 1,363,926 cells, 222,354 nodes and 19,342 edges. In

order to generate results for this complex model, an increase in computational power was required, which was achieved by an increase in the Krylov subspace to 400 and number of iterations to 8000. Despite these attempts to generate positive results, and with several changes to refinement strategies and physical parameters (specifically, reduction and eventual elimination of conductivity contrast between the Early and Late Cretaceous sections), accurate electric field results could not be achieved, confirmed by a poor convergence curve (Figure 4.26). It was proposed that this issue was due to the creation of cells with a poor aspect ratio by the Early Cretaceous wedge structure. This proposal is supported by the results for the model having the wedge structure removed, but other model specifics maintained (Figures 4.27). Though the mesh statistics have increased slightly — 1,442,887 cells, 235,143 nodes and 19,855 edges — the results are accurate (Figures 4.28 and 4.29) with excellent convergence (Figure 4.30).

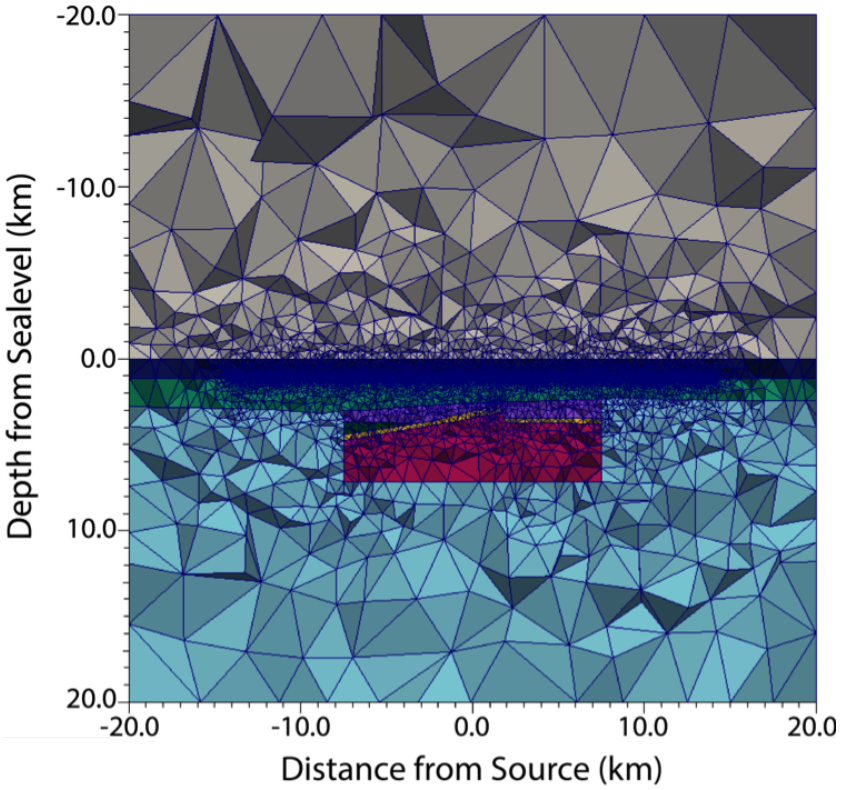

(a)

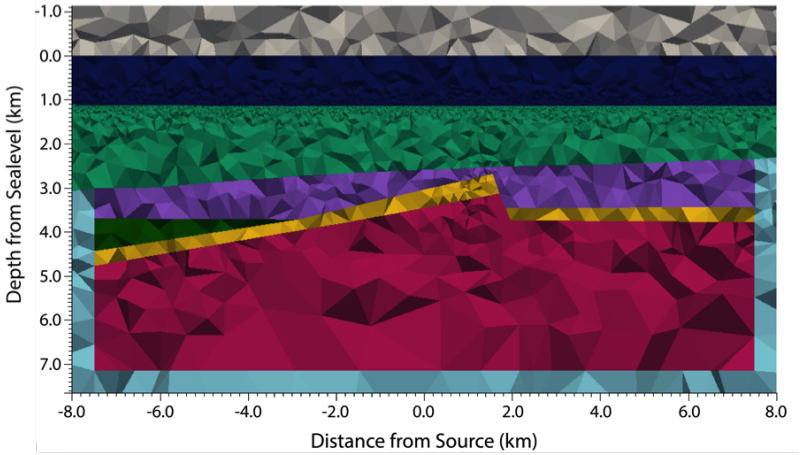

(b)

Figure 4.25: Cross-sections centered at $y = 0$ m of the single fault block system used in *Model 1* including the problematic wedge structure (dark green). Panel (a) full view; panel (b) enhanced view of the reservoir geometry.

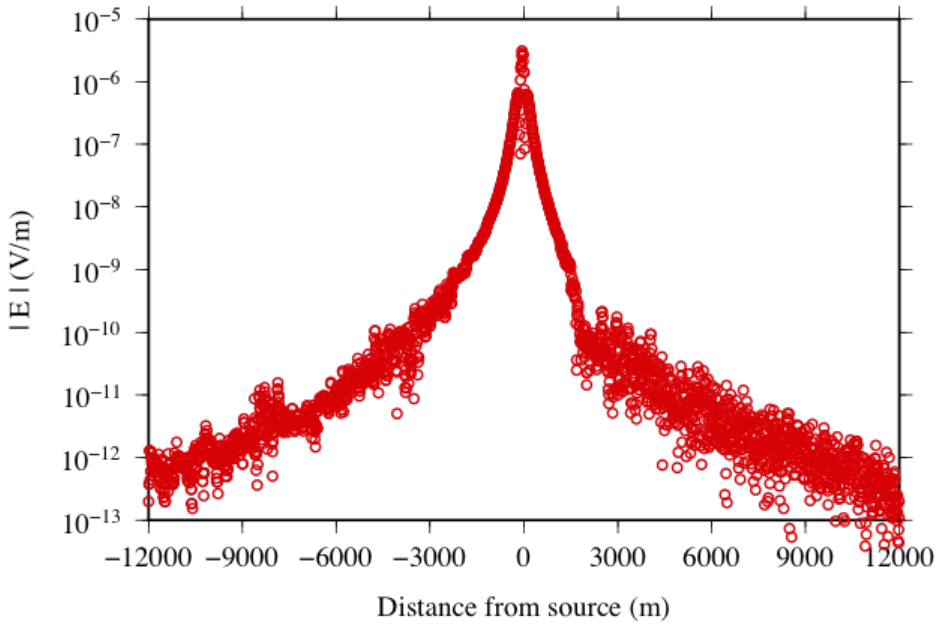

(a)

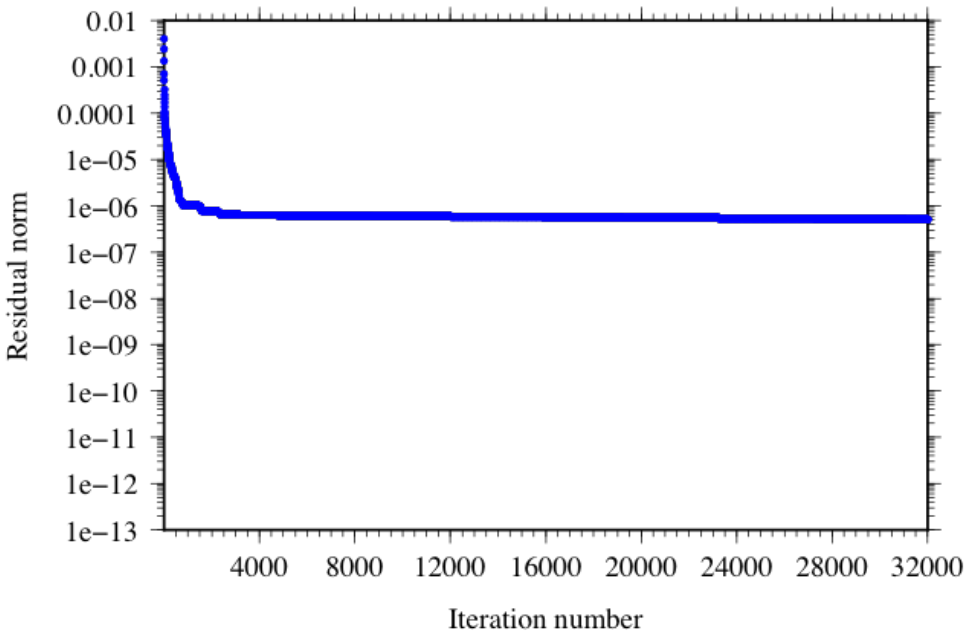

(b)

Figure 4.26: Numerical results for *Model 1 with Wedge* (Figure 4.25). Panel (a) electric field amplitude; panel (b) residual norm.

This accurate base model (i.e. with the wedge model omitted, Figure 4.5.1) allows for changes in reservoir characteristics to be easily generated for comparison purposes. This section will explore different conductivities homogeneously saturating the pore space of the sand reservoir, creating definitive quality standards: 1.0 S/m represents a reservoir containing no fluid in the pore space (herein referred to as *Dry Reservoir*), 0.25 S/m represents a poor reservoir (herein referred to as *Poor Reservoir*), with 0.01 S/m (or 100 Ωm) and 0.001 S/m (or 1000 Ωm) representing variations of reservoir quality. The results for these four scenarios are shown in Figures 4.28 to 4.30.

Deviations of each of the reservoir scenarios from the *Dry Reservoir* result indicate reservoir detection. As a general trend, the electric field amplitude for each of the resistive reservoirs deviates positively from those for the *Dry Reservoir* before the air layer effect causes the slopes of the curves to decrease. The amplitude of the *Poor Reservoir* declines below the *Dry Reservoir* at ∼8000 m offset. This decrease is created by the detection of a resistivity contrast: wider offsets will detect the 1.0 S/m reservoir that lays directly under offsets greater than 7500 m; as the *Poor Reservoir* has a conductivity of 0.25 S/m, its contrast with the basement will be greater than the 1.0 S/m (i.e. *Dry*) reservoir, thus, a more dramatic decrease. This pattern is also visible for the *100 Ωm* and *1000 Ωm Reservoirs*, but their curves cross the *Dry Reservoir* at a wider offset (∼ 9500 m) due to the higher, more detectable resistivity value. The results for the *100 Ωm Reservoir* are very similar to the *1000 Ωm Reservoir*, and are hidden by the curves of the more resistive reservoir in Figures 4.28 and 4.29.

The ability to detect a reservoir and its quality are quantified by the difference in electric field amplitude with the dry reservoir. The absolute difference and percent difference

normalized by the dry reservoir were calculated for the scenarios described above and are plotted in Figure 4.31. As in Figure 4.28, any deviation of the results from the *Dry Reservoir* indicates the possibility of detection. As seen from Figure 4.31, information of the subsurface is lost surrounding the source position, as direct source energy overwhelms the electric field amplitude response. Reservoir detection does not begin until $\sim$ -3000 m for offsets to the left of the source and $\sim$ 4000 m to the right for both *100* Ωm and *1000* Ωm *Reservoirs*, but is relatively unapparent in the *Poor Reservoir* case, with maximum percent difference at $\sim$10% at $\sim$ -8000 and 8000 m offset. Because this percent difference is an absolute value, this is likely reflective of areas where the *Poor Reservoir* had a lower electric field amplitude than the *Dry Reservoir*, and it may be concluded that the *Poor Reservoir* is undetectable in this model. However, the magnitude of percent increase of the highly resistive models (peaking at $\sim$160% and $\sim$245% for negative offsets and $\sim$120% and $\sim$140% for positive offsets of the *100* Ωm and *1000* Ωm *Reservoirs*, respectively) shows great promise of reservoir detection for this model. The slight disparity between results between negative and positive offsets are due to the depth of the reservoir that is detected by these offsets: the reservoir on the hanging wall (positioned under negative offsets) exists at $\sim$3000 m depth, while the reservoir on the footwall (positioned under positive offsets) is positioned at $\sim$4000 m depth.

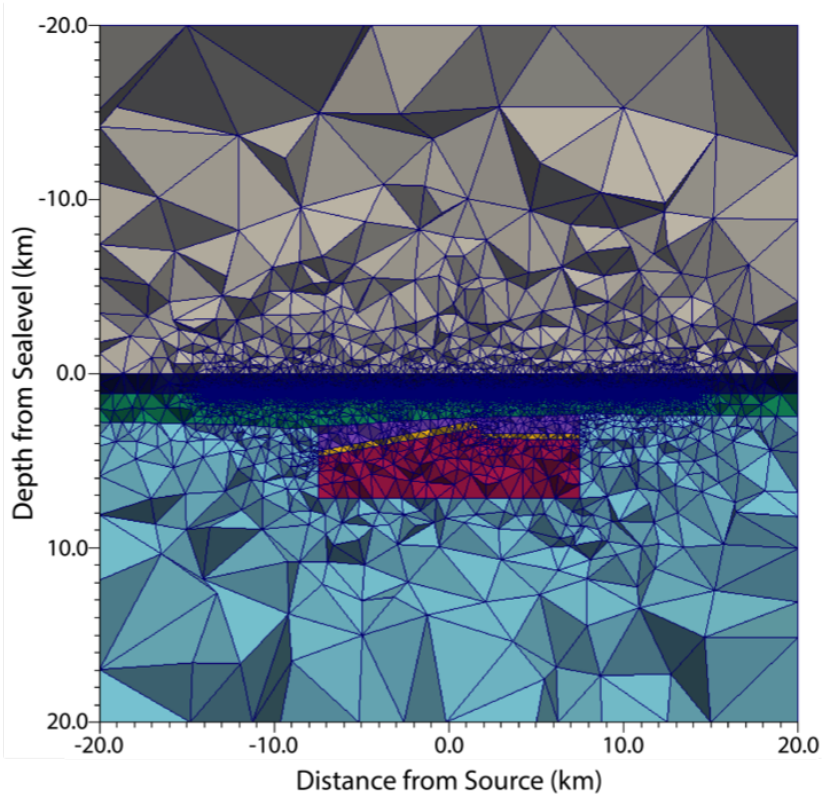

(a)

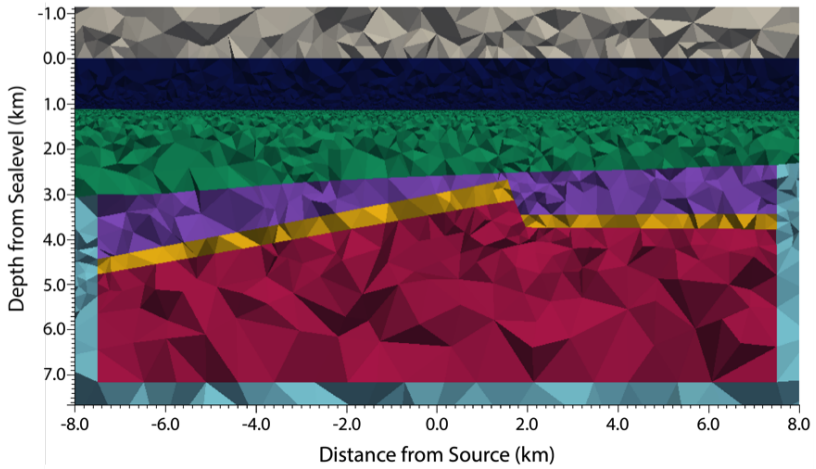

(b)

Figure 4.27: Cross-sections centered at $y = 0$ m of the single fault block system used in *Model 1* excluding the problematic wedge structure (compare with Figure 4.25). Panel (a) full view; panel (b) enhanced view of the reservoir geometry.

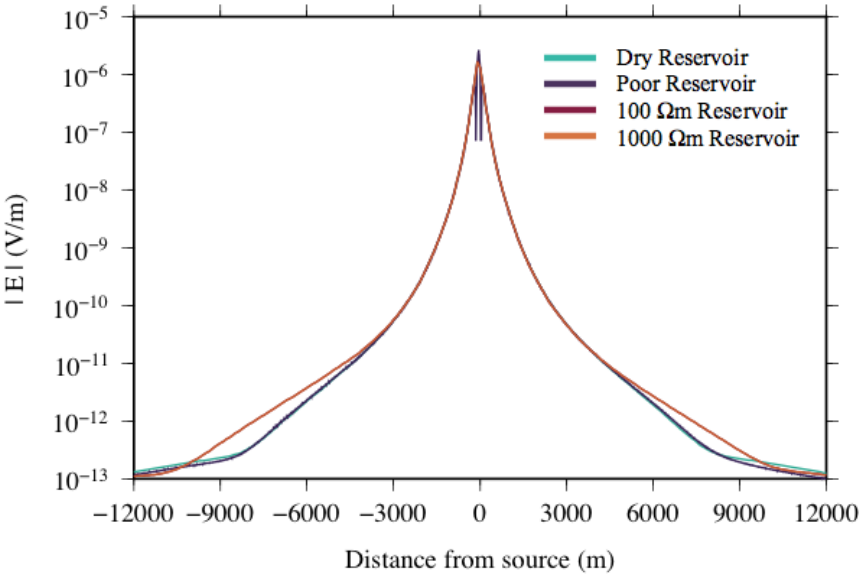

(a)

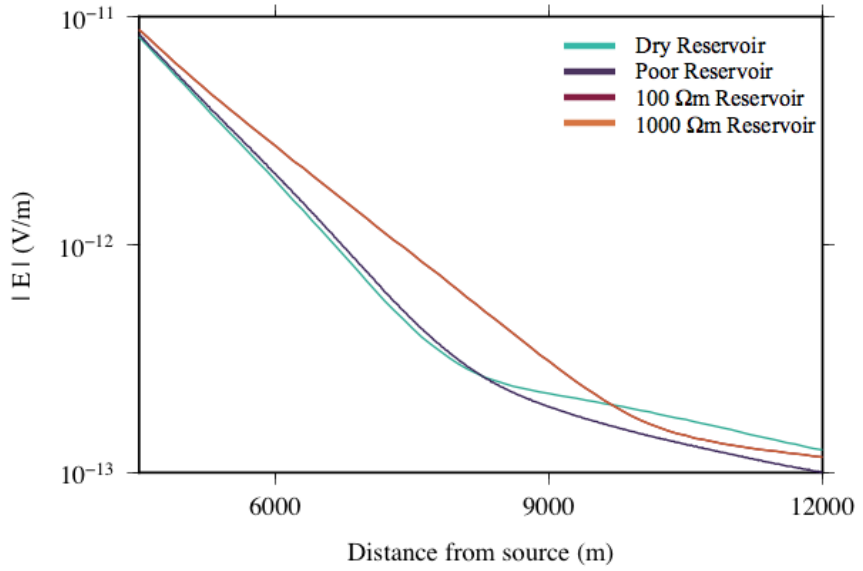

(b)

Figure 4.28: Panel (a) electric field amplitude results *Model 1* (Figure 4.27) for each respective reservoir quality; and panel (b) enhanced view of the electric field amplitude results for offsets of 5000 m to 12000 m. The results of the *100 Ωm Reservoir* are hidden by the results of the *1000 Ωm Reservoir*.

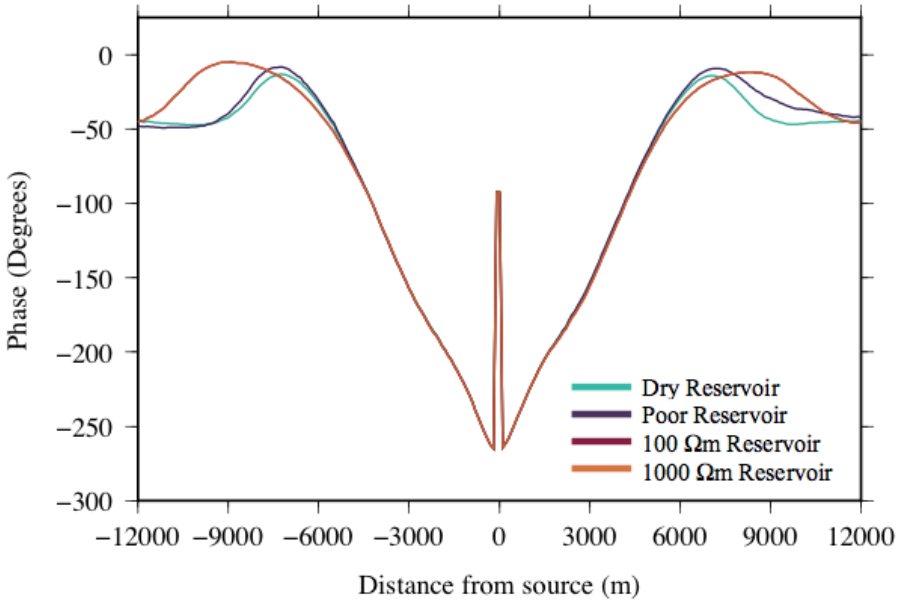

Figure 4.29: Phase results for *Model 1* (Figure 4.27) for the four reservoir qualities.

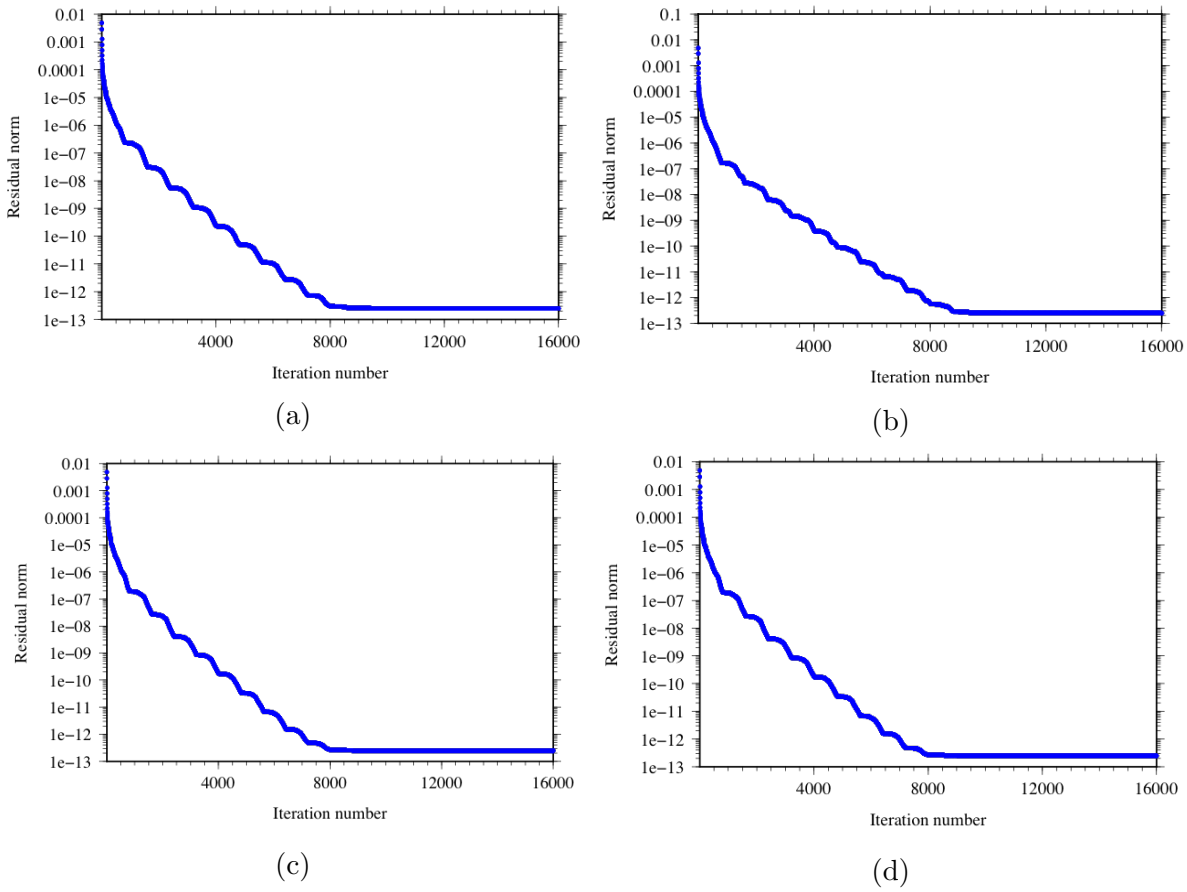

Figure 4.30: Convergence curves for *Model 1* (Figure 4.27). Panel (a) *Dry Reservoir*; panel (b) *Poor Reservoir*; panel (c) *100* Ωm *Reservoir*; panel (d) *1000* Ωm *Reservoir*.

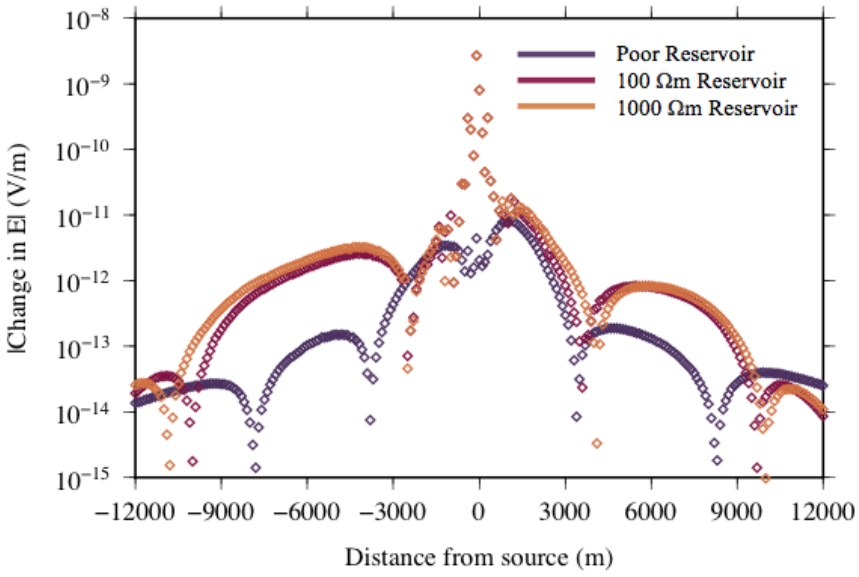

(a)

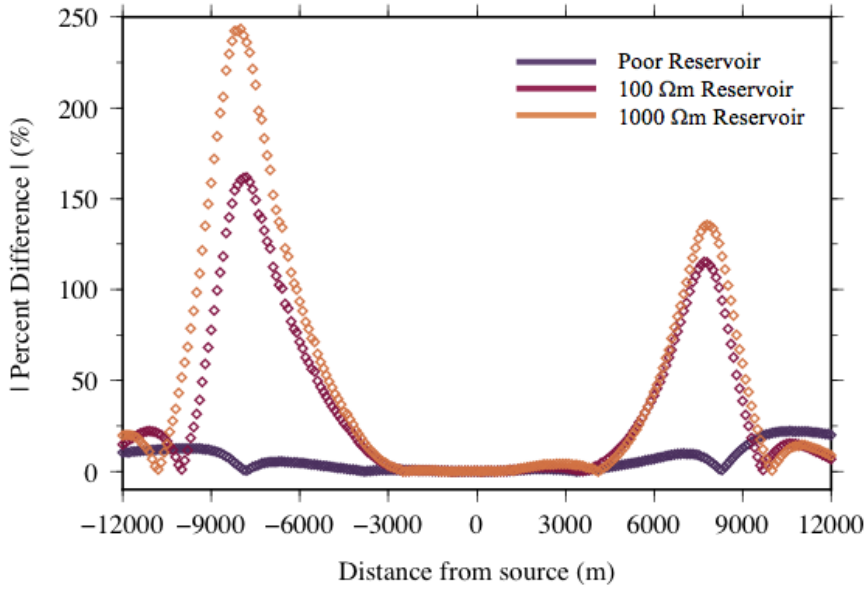

(b)

Figure 4.31: Panel (a) absolute differences in the electric field amplitude results of the *Dry Reservoir* and the *100 Ωm Reservoir* for *Model 1* (Figure 4.27); panel (b) corresponding percent differences in the electric field amplitude results. Each percent difference has been normalized by the results of the dry reservoir.

4.5.2 Model 2

Figure 4.32 shows the schematic provided by Suncor Energy second reservoir geometry (herein *Model 2*), and Figure 4.33 shows the mesh. The region is comprised of four distinct faults cutting the -5000 to 5000 m reservoir in the x-direction. The horizontal sand packages were deposited between the Early (green in the mesh) and Late (purple in the mesh) Cretaceous regions, and are strongly displaced by the fault system, placing them in the positions given in Table 4.3. Their thickness remains constant at $\sim$250 m. The change in lateral extent was suggested by Suncor Energy based on the most likely scenario in the Flemish Pass basin for this particular reservoir geometry. The reservoir and fault block system is invariant over its -5000 m to 5000 m extent in the y-direction.

Package Number	Left x-Position (m)	Right x-Position (m)	Depth to Package (m)
1	-5000	-4600	6250
2	-3800	-2200	3100
3	-2200	1200	4050
4	1750	3500	2800

Table 4.3: Positions of the sand packages used in *Model 2* (Figure 4.33).

To aid in model construction, regions of nodes were removed from the *Base Tertiary* horizon in areas where attachment to *Package 3* were to occur i.e. 500 m from either side of the lines $x = 1750$ m and $x = 3500$ m, and across the full extent of the reservoir (Figures 4.34 and 4.35). The creation of these straight contacts allowed for connection of the sand package where the Late Cretaceous is removed — in a similar vein as the reservoir boundary contact technique described at the beginning of Section 4.5 for *Model 1*. Two nodes were added at the contact of the reservoir with the lines $x = 1750$ m and $x = 3500$

m; these nodes were then joined by 2D facets using FacetModeller, the horizon exported into a *.poly* file, where the horizon can be discretized in 2D and incorporated into the 3D model. Production of this 3D model generated 1,427,609 cells, 232,695 nodes and 20,456 edges. Source and observation parameters and refinement are the same as those described in Section 4.5.

The electric field results for *Model 2* are displayed in Figures 4.36 to 4.38, and each achieved proper convergence (Figure 4.39). Detectability of reservoir characteristics is quantified by the results in Figure 4.40. The significant difference in the results of the *100* and *1000* Ωm *Reservoirs* reveal responses due to the hydrocarbon-filled reservoir. The difference values for the *Poor Reservoir* are quite large at large positive offsets, and thus there is potential for detection of this reservoir. However, the greater offset at which this significant difference is occuring could result in a lack of detention of this reservoir. The peak in percent difference of the *Poor Reservoir* is not indicitive of reservoir detection, but of a decrease in resistivity contrast between reservoir and bedrock at the edge of the reservoir muting the rate of decrease of the electric field amplitude (Figure 4.37) deviating from the effect of the *Dry Reservoir* to which it is compared.

The electric field amplitude of each reservoir classification in *Model 2* has a lower magnitude of response than the corresponding reservoirs in *Model 1*. This is likely due to the decrease in reservoir extension (from -7500 to 7500 m in *Model 1* to -5000 to 5000 m in *Model 2*) and the additional depth associated with the faulted blocks in *Model 2*'s formation. This is reflected in a decrease in the overall percent difference responses (Figure 4.40), with peaks of the *100* Ωm and *1000* Ωm *Reservoirs* reaching $\sim$15% percent difference for negative offsets (at $\sim$ -6500 m) and $\sim$40% for positive offsets (at $\sim$ 6500 m). Though

these values have decreased in magnitude, they still suggest detectability of the resistive reservoir.

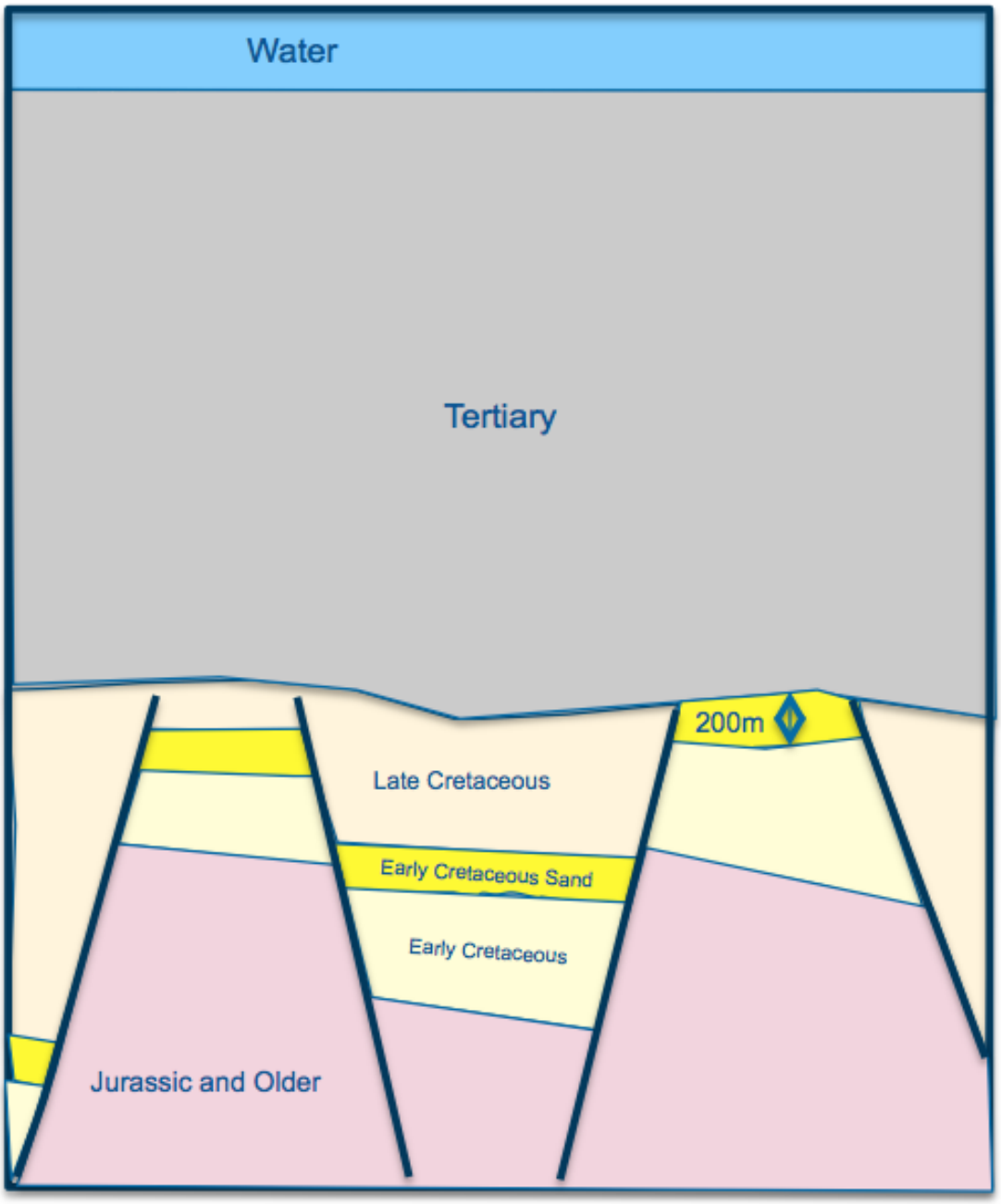

Figure 4.32: Schematic representation of the structural trap scenario used in *Model 2* (compliments of Brad Bonnell, Suncor Energy).

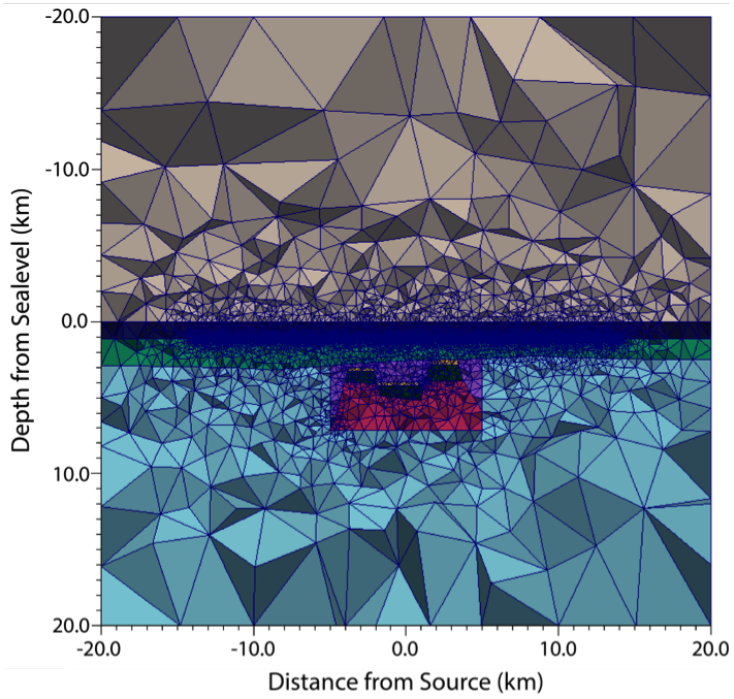

(a)

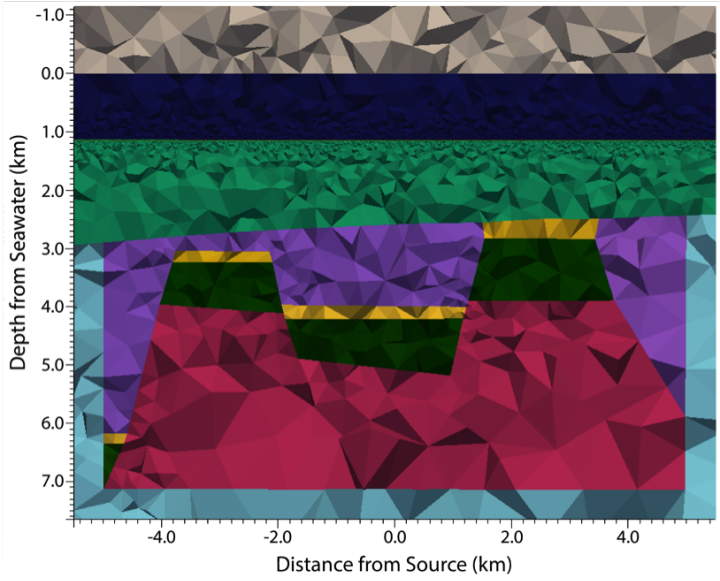

(b)

Figure 4.33: Cross-sections centered at $y = 0$ m of the multiple fault block system used in *Model 2*. Panel (a) full view; panel (b) enhanced view of the reservoir geometry.

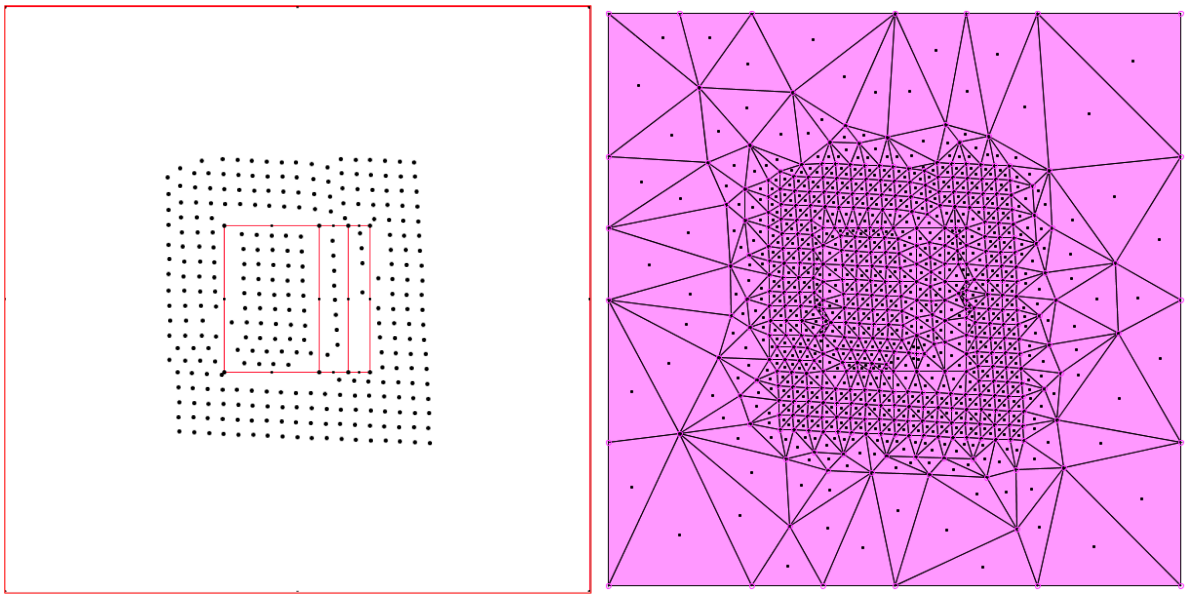

(a) (b)

Figure 4.34: Development of the contact between the sand package and the *Base Tertiary* unconformity for *Model 2*. Panel (a) projection of the nodes of the *Base Tertiary* horizon onto the plane $z = 0$ m. 2D facets used for the contact, reservoir boundary and model boundary are in red. Panel (b) map view of the discretized horizon. Each model boundary extends between -20 and 20 km in the x- and y-directions.

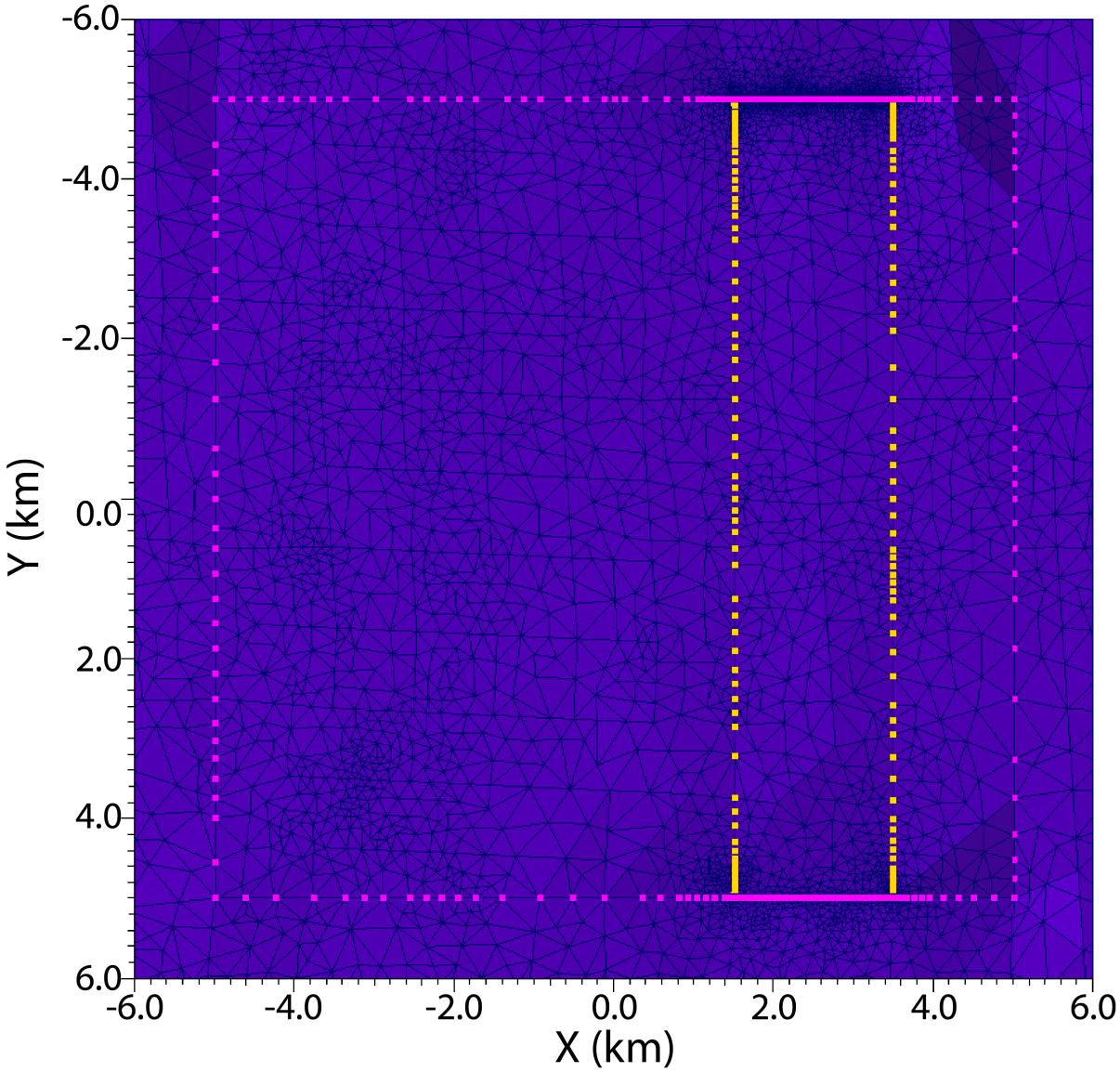

Figure 4.35: Map view of the *Base Tertiary* horizon with the nodes that form the straight boundary contacts for the perimeter of the reservoir highlighted in pink (at x = -5000 and 5000 m and y = -5000 and 5000 m) and the nodes that form the straight contacts for each edge of the sand package at the unconformity highlighted in yellow (at x = 1750 and 3700 m).

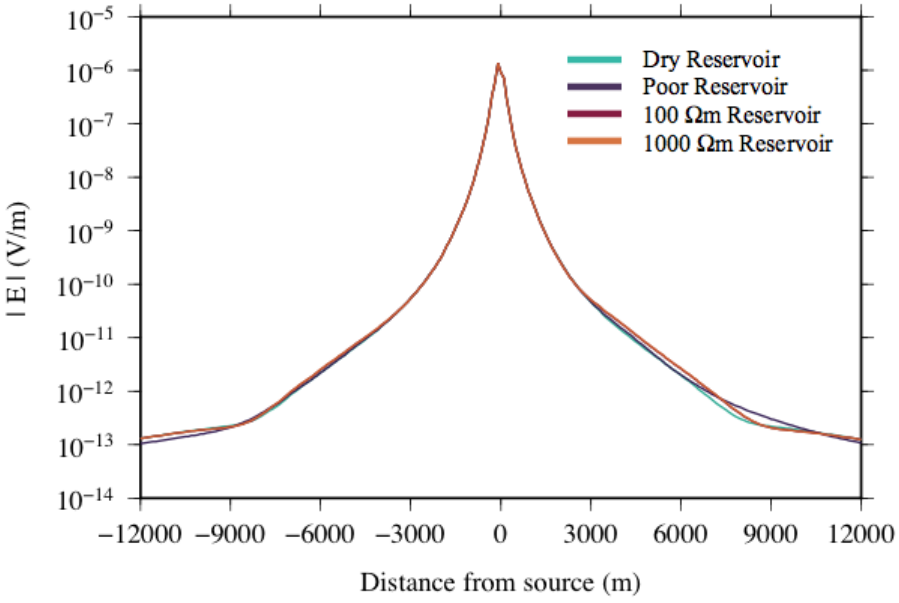

Figure 4.36: Electric field amplitude results for *Model 2* (Figure 4.33).

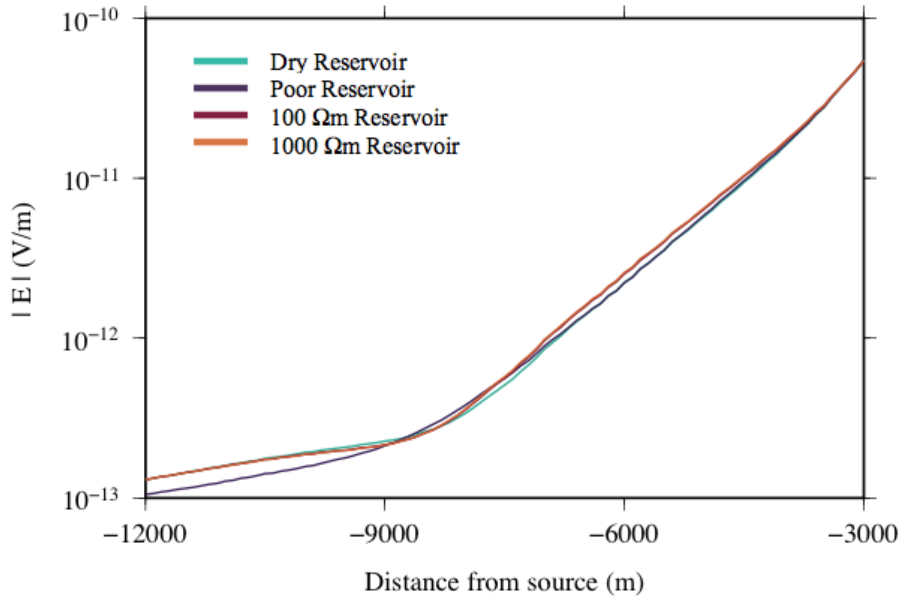

(a)

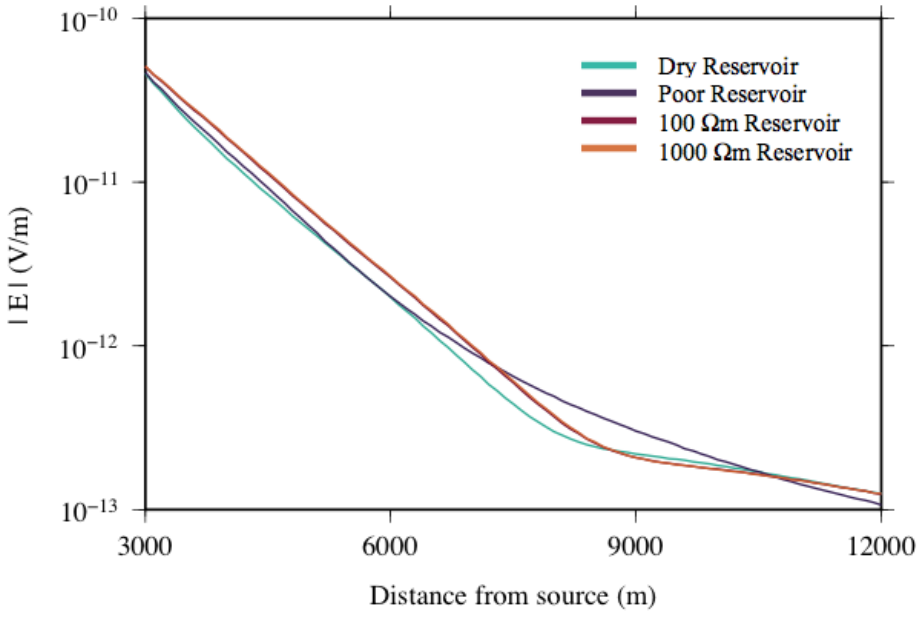

(b)

Figure 4.37: Enhanced views of the electric field amplitude results for *Model 2* (Figure 4.33).

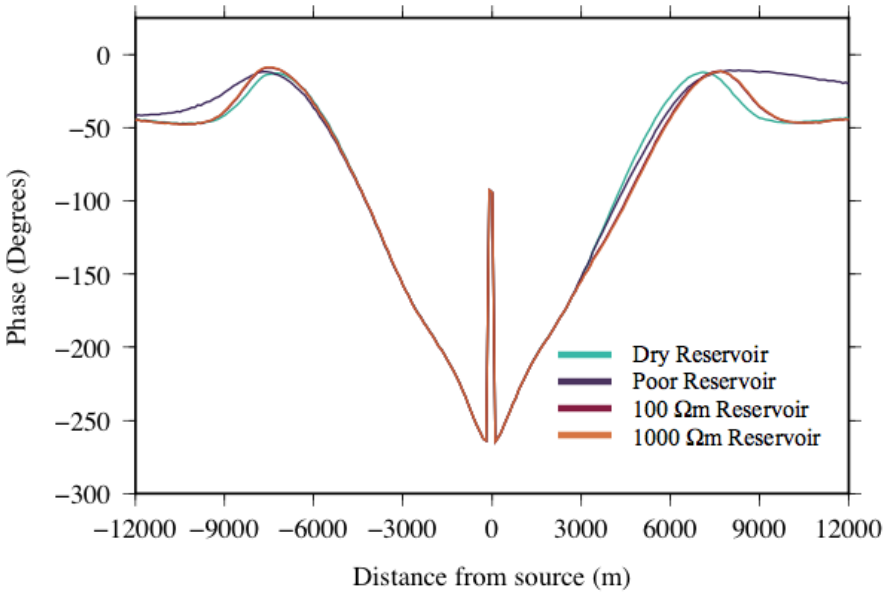

Figure 4.38: Phase results for *Model 2* (Figure 4.33).

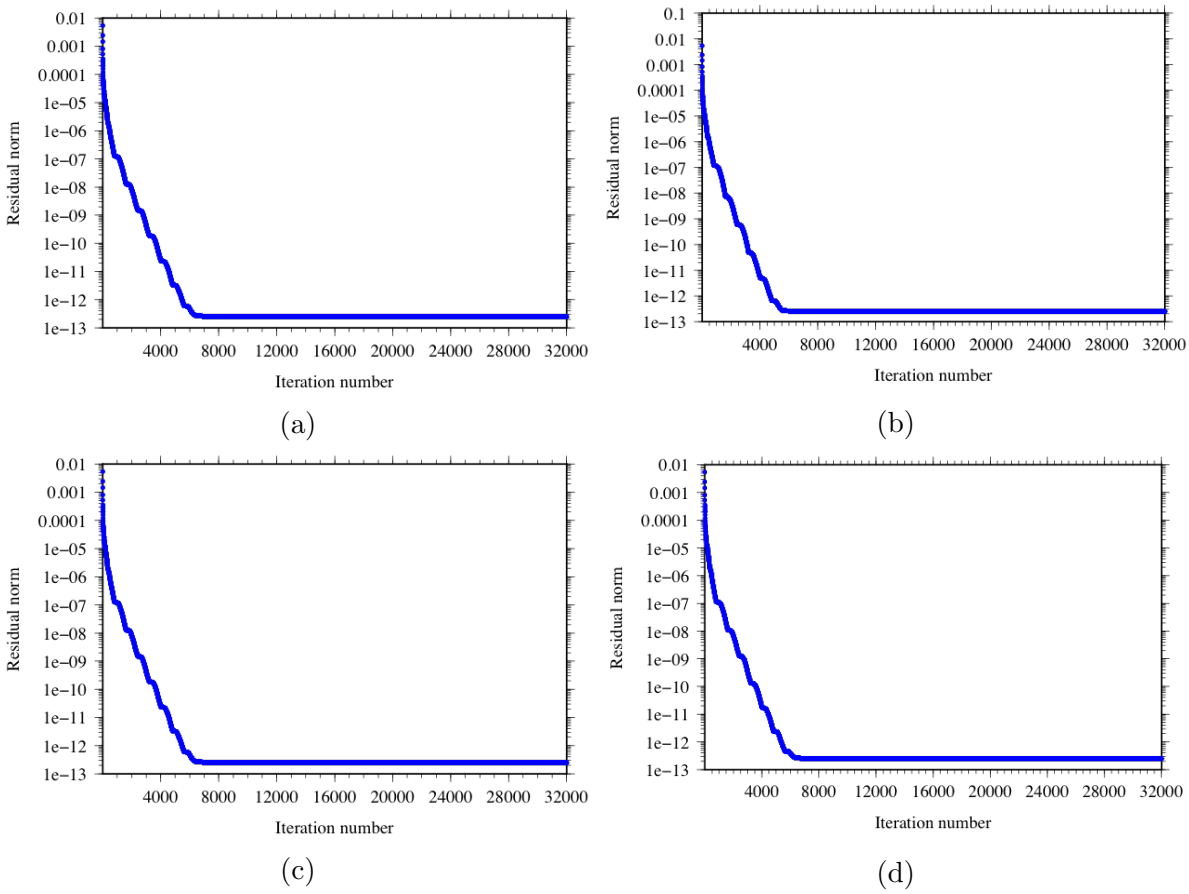

Figure 4.39: Convergence curves for *Model 2* (Figure 4.33). Panel (a) *Dry Reservoir*; panel (b) *Poor Reservoir*; panel (c) *100 Ωm Reservoir*; panel (d) *1000 Ωm Reservoir*.

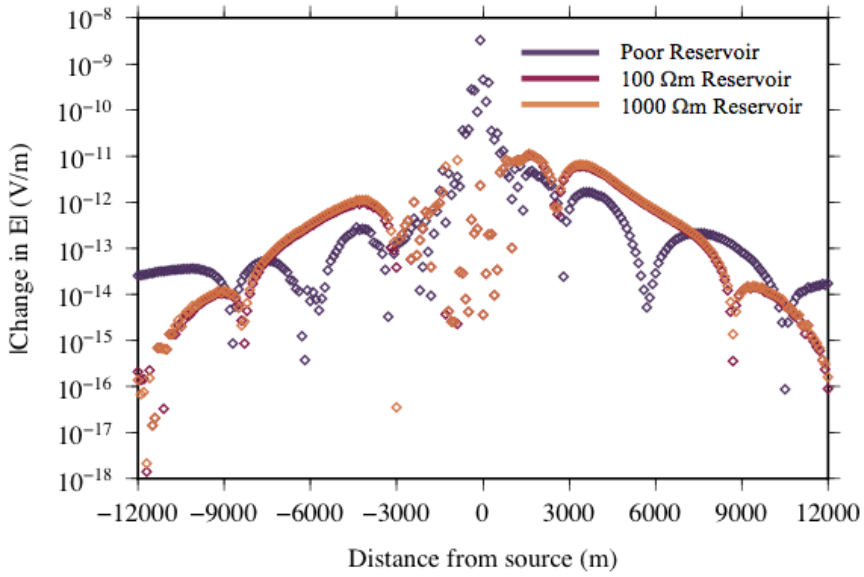

(a)

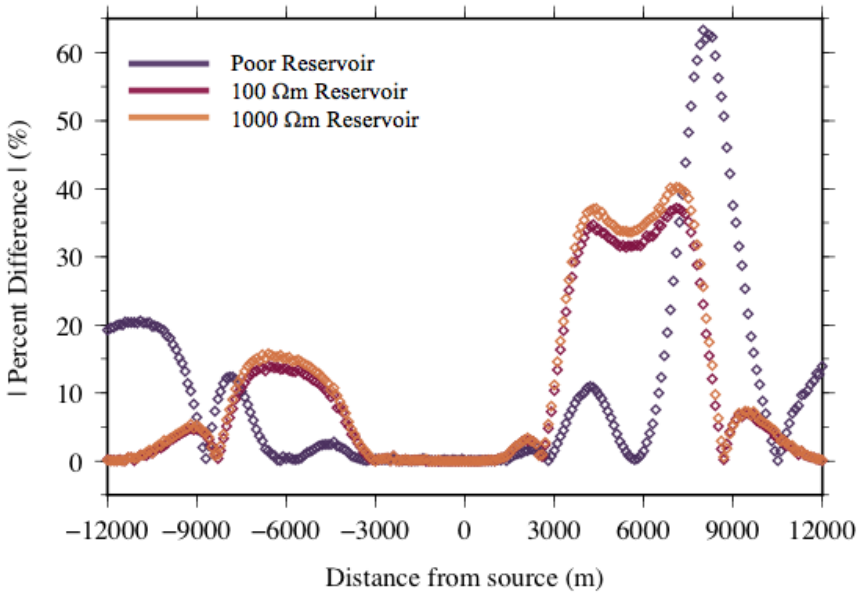

(b)

Figure 4.40: Panel (a) absolute differences in the electric field amplitude results of the *Dry Reservoir* and the *100 Ωm Reservoir* of *Model 2* (Figure 4.33); panel (b) corresponding percent differences in the electric field amplitude results. Each percent difference has been normalized by the results of the dry reservoir.

4.5.3 Model 3

The geometry used for the third reservoir configuration (herein *Model 3*) is very similar to that of *Model 2*, but with an earlier, and therefore deeper, deposition of the sand packages that constitute the hydrocarbon reservoir (derived from the schematic in Figure 4.41). These packages are now Early Cretaceous in age and are therefore deposited between the Jurassic and Late Cretaceous regions — the previous Early Cretaceous region in *Model 2* is removed. Despite this alteration, the thickness, lateral extent and offset of each of the packages mimic those of *Model 2*. With the later deposition, *Packages 1-4* (as described in Table 4.3) are positioned at the following depths, from east to west: 6250 m, 4000 m, 4800 m, and 3650 m. The source and observation configurations, parameters and refinements, along with reservoir boundary attachment technique, follow those used in *Models 1* and *2*.

Discretization of the computational domain produced 1,363,239 cells, 222,266 nodes and 18,699 edges (Figure 4.42), and forward modelling produced the results shown in Figures 4.43 to 4.45, with the corresponding convergence curves shown in Figure 4.46. As expected, the deeper position but similar structure of the reservoir packages in *Model 3* produce lower amplitudes, but similar trending results, to those for *Model 2*, with maximum percent difference (and therefore detection ability) of the highest quality reservoir (1000 Ωm) at $\sim$7% (Figure 4.47), whereas *Model 2* had a maximum percent difference of $\sim$40% for essentially the same reservoir. Though the synthetic data show clear percentage differences, it is very unlikely that such a configuration would be detectable in a real-world scenario when noise is taken into account. Again, the *Poor Reservoir* maximum difference results exceeds that of both higher quality reservoirs (100 Ωm and 1000 Ωm), but at significantly

greater offsets, where the amplitudes are substantially smaller.

The effect of the increase in depth of the reservoir is quantified by the absolute and percent differences between the electric field amplitudes of *Models 2* and *3* (Figure 4.48). Figure 4.48b shows a 30-35% increase in the response for the 100 Ωm and 1000 Ωm *Reservoirs* for intermediate offsets for *Model 2* relative to *Model 3* as a consequence of *Model 2*'s shallower burial depth. The apparent noisiness of the results in Figure 4.48 is because different meshes were used for the two models.

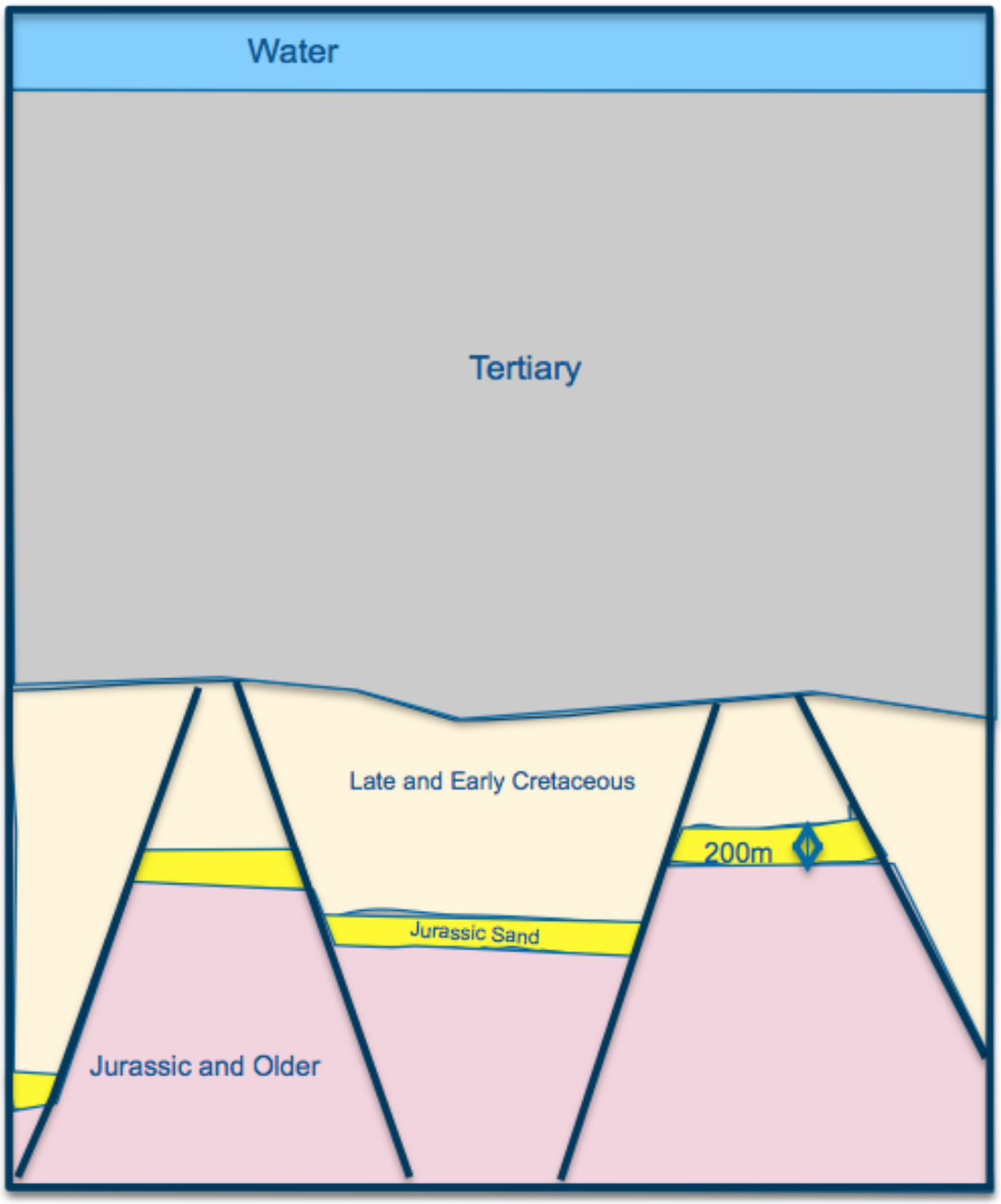

Figure 4.41: Schematic representation of the structural trap scenarios used in *Model 3* (compliments of Brad Bonnell, Suncor Energy).

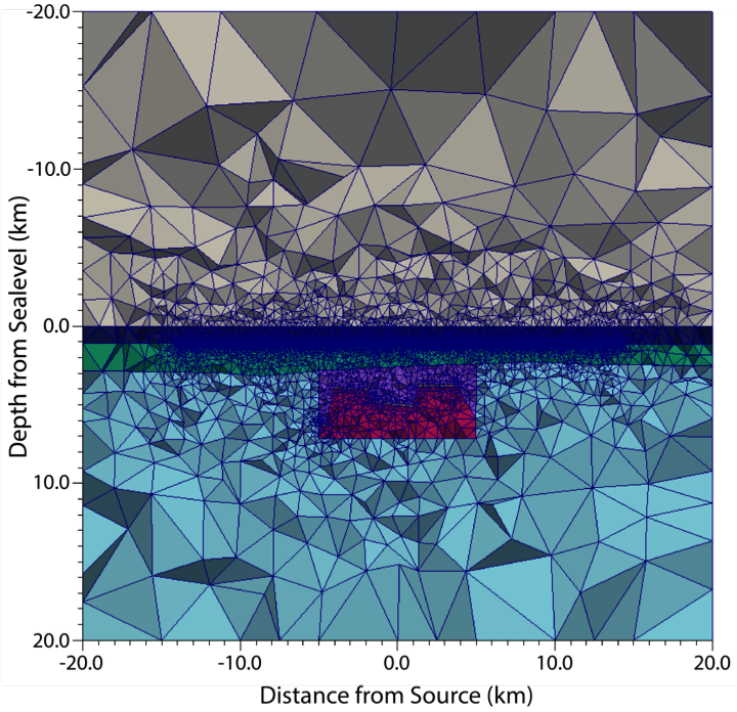

(a)

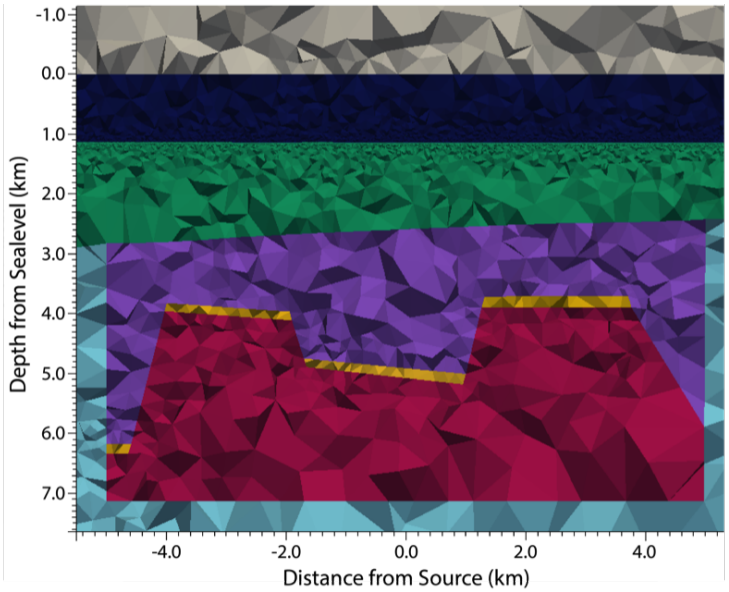

(b)

Figure 4.42: Cross-sections centered at $y = 0$ m of the multiple fault block system used in *Model 3*. Panel (a) full view; panel (b) enhanced view of the reservoir geometry.

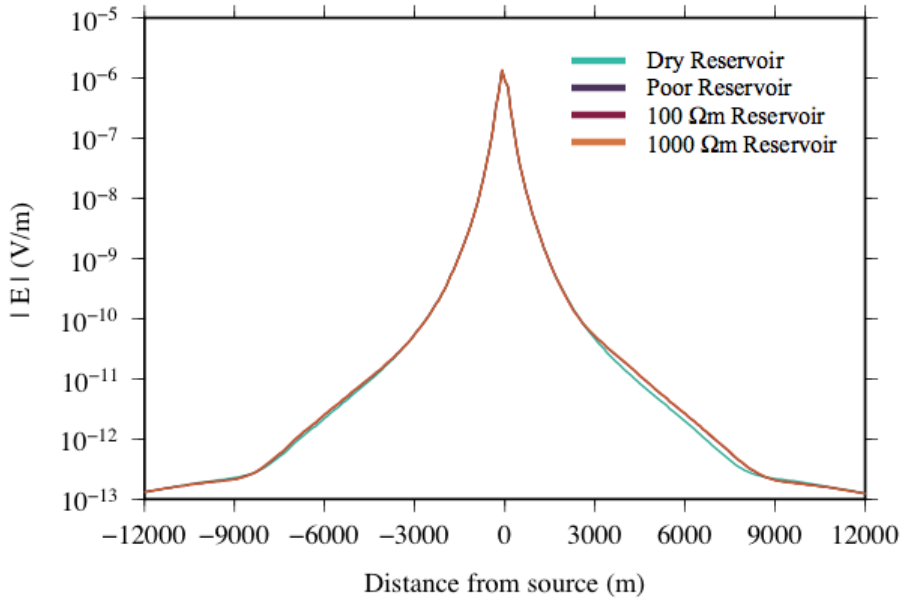

Figure 4.43: Electric field amplitude results for *Model 3* (Figure 4.42).

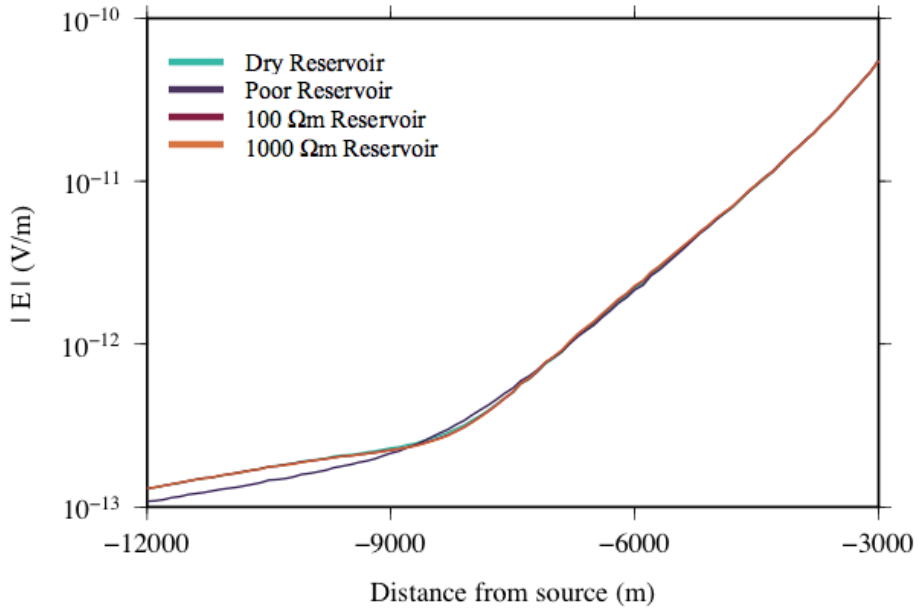

(a)

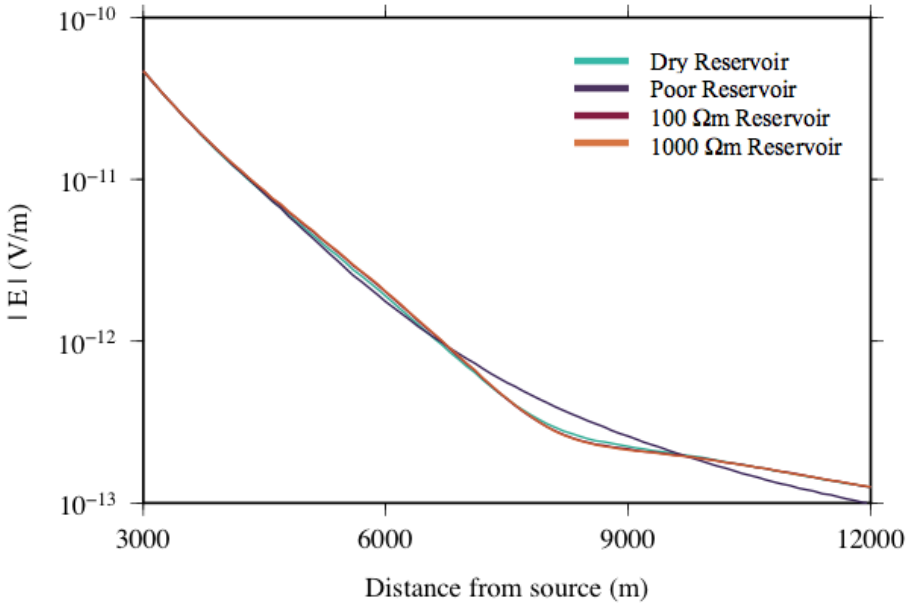

(b)

Figure 4.44: Enhanced views of the electric field amplitude results for *Model 3* (Figure 4.42).

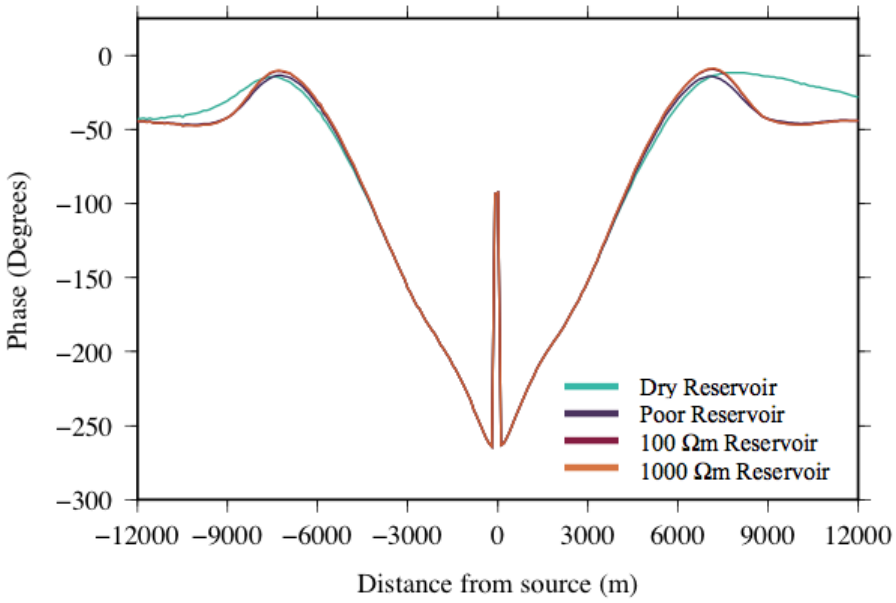

Figure 4.45: Phase results for *Model 3* (Figure 4.42).

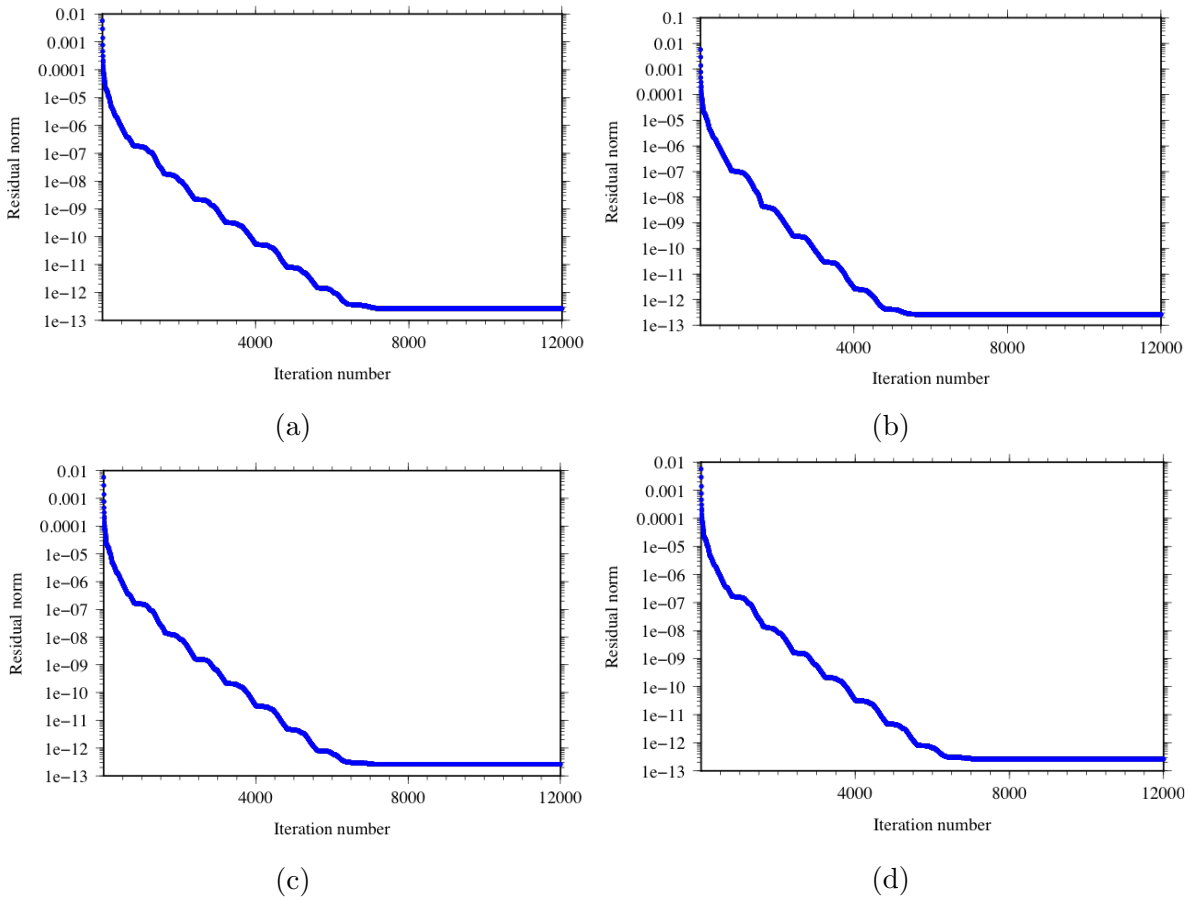

Figure 4.46: Convergence curves for *Model 3* (Figure 4.42). Panel (a) *Dry Reservoir*; panel (b) *Poor Reservoir*; panel (c) *100* Ωm *Reservoir*; panel (d) *1000* Ωm *Reservoir*.

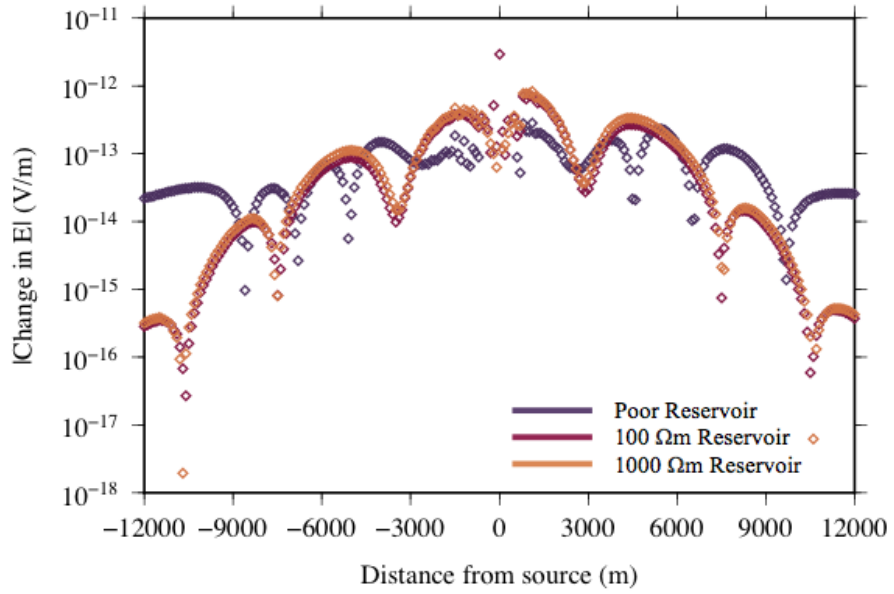

(a)

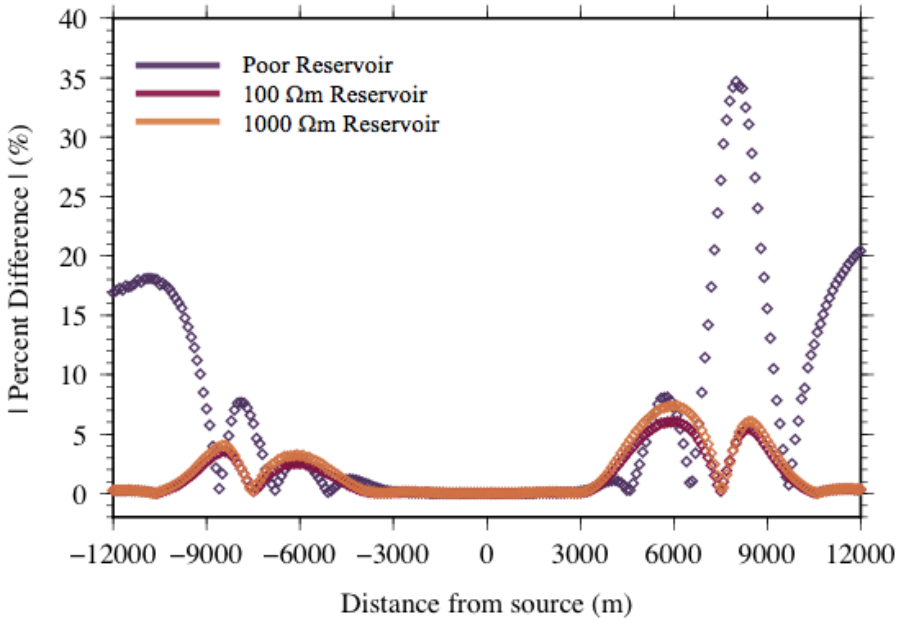

(b)

Figure 4.47: Panel (a) absolute differences in the electric field amplitude results of the *Dry Reservoir* and the *100 Ωm Reservoir* for *Model 3*; panel (b) percent differences in the electric field amplitude results. Each percent difference has been normalized by the results of the dry reservoir.

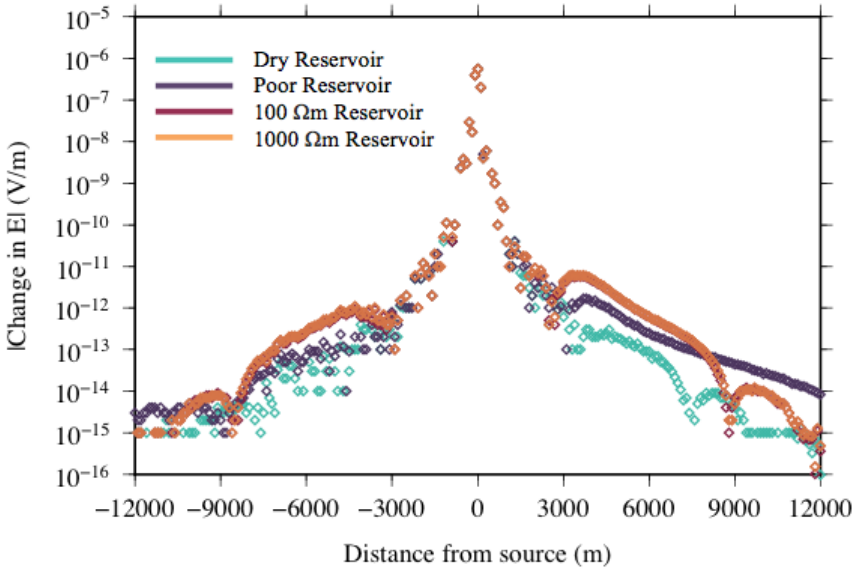

(a)

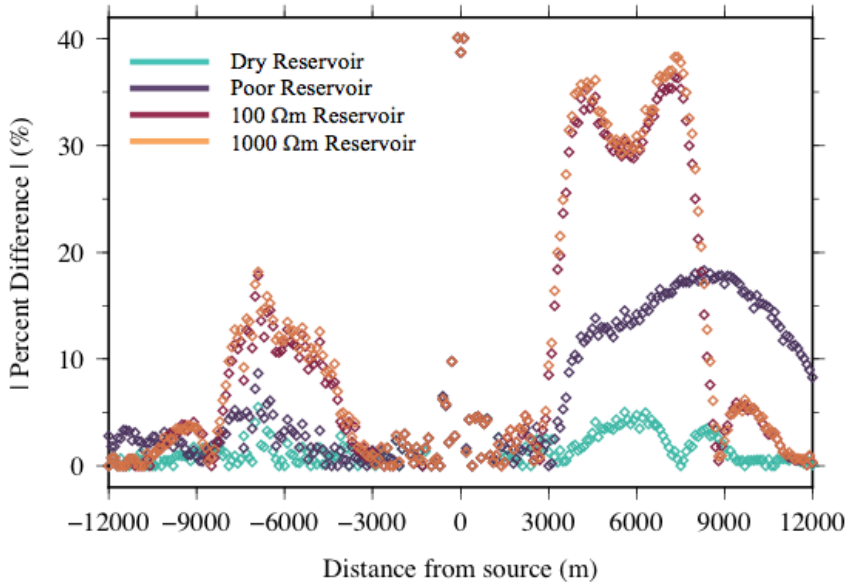

(b)

Figure 4.48: Panel (a) absolute differences in the electric field amplitude results of the *100 Ωm Reservoir* version of *Model 2* with the *100 Ωm Reservoir* version of Figure *Model 3*; panel (b) percent differences in the electric field amplitudes. Each percent difference has been normalized by the results for *Model 3*.

4.5.4 Models 4 and 5

The schematic shown in Figures 4.49 (herein, *Model 4*) and 4.50 (herein, *Model 5*), and the models shown in Figures 4.51 and 4.52 each exhibit a similar, single fault-block structure, extending from -7500 to 7500 m in both the x- and y-directions (there is no variation of the structure in the y-direction). *Model 4* positions the sand package at a relatively shallow depth ($\sim$3100 m; Figure 4.51), while *Model 5* represents a relatively deep reservoir ($\sim$4750 m; Figure 4.52). The fault exhibits an extreme reverse offset, particularly in comparison to the normal displacement of the package in *Model 1* (Figure 4.27). The thrust of this fault has placed the Jurassic (magenta) section at the *Base Tertiary* unconformity to the east, with the Cretaceous sand package or Late Cretaceous region at this unconformity for *Model 4* and *Model 5*, respectively, to the West. Using a similar technique as the sand package attachment for *Model 2*, nodes were removed on either side of the line $x = 1750$ m, allowing for a horizontal contact between the fault and the unconformity for both *Models 4* and *5*. The reservoir is solely located at negative offsets in both models.

Discretization of *Model 4* generated 1,462,283 cells, 238,361 nodes and 120,178 edges, while *Model 5* contained 1,446,120 cells, 235,745 nodes and 19,809 edges. The results for the two models using the same source and observation parameters as for previous sections are shown in Figures 4.53 to 4.61. The detectability of each reservoir is indicated by the absolute and percent differences of each of the reservoirs compared to the corresponding *Dry Reservoir* (Figure 4.56 for *Model 4* and Figure 4.60 for *Model 5*). The general increase in electric field amplitude over the reservoir sections can be seen in Figures 4.53 and 4.57. The effect of the increase in the depth of the reservoir between *Models 4* and *5* is quantified

by the absolute and percent differences in electric field amplitude of *Models 4* with respect to *Model 5* (Figure 4.61). The reservoir is far more detectable in *Model 4*, as shown by the massive (∼1650%) percent difference in electric field amplitude for offsets over the reservoir. The electric field amplitudes for both models exceed the thresholds of detection (Figures 4.56 and 4.60).

These simple reservoir configurations are fundamental to the understanding of detectability with offset. Since the reservoir is solely located at negative offsets in these two models and is comprised of a single, sub-horizontal sand package, increases in amplitude detection must solely be from the contribution and detection of that reservoir (compared to the multiple reservoir sections in *Models 1* to *3*). For example, in the case of *Model 4*, the 3000 m deep package that extends from -7500 m to 0 m in the x-direction is not detected until $\sim$ -8800 m offset for both highly resistive reservoirs. Conversely, in *Model 5* — a 4800 m deep reservoir extending from -6000 m to -2000 m in the x-direction — the reservoir package is detected at similar offsets but with lower magnitudes of percent differences.

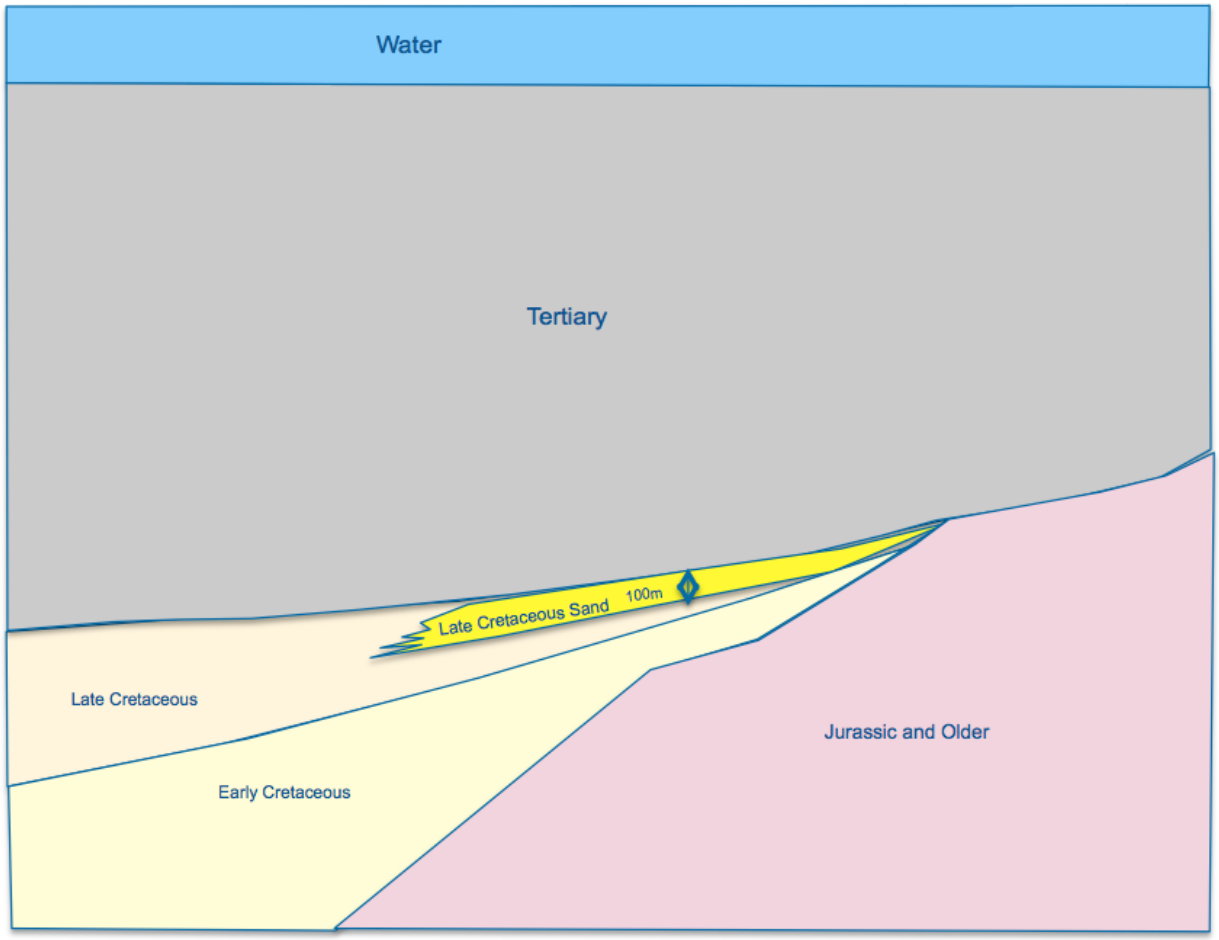

Figure 4.49: Schematic representation of the structural trap scenarios used in *Model 4* (compliments of Brad Bonnell, Suncor Energy).

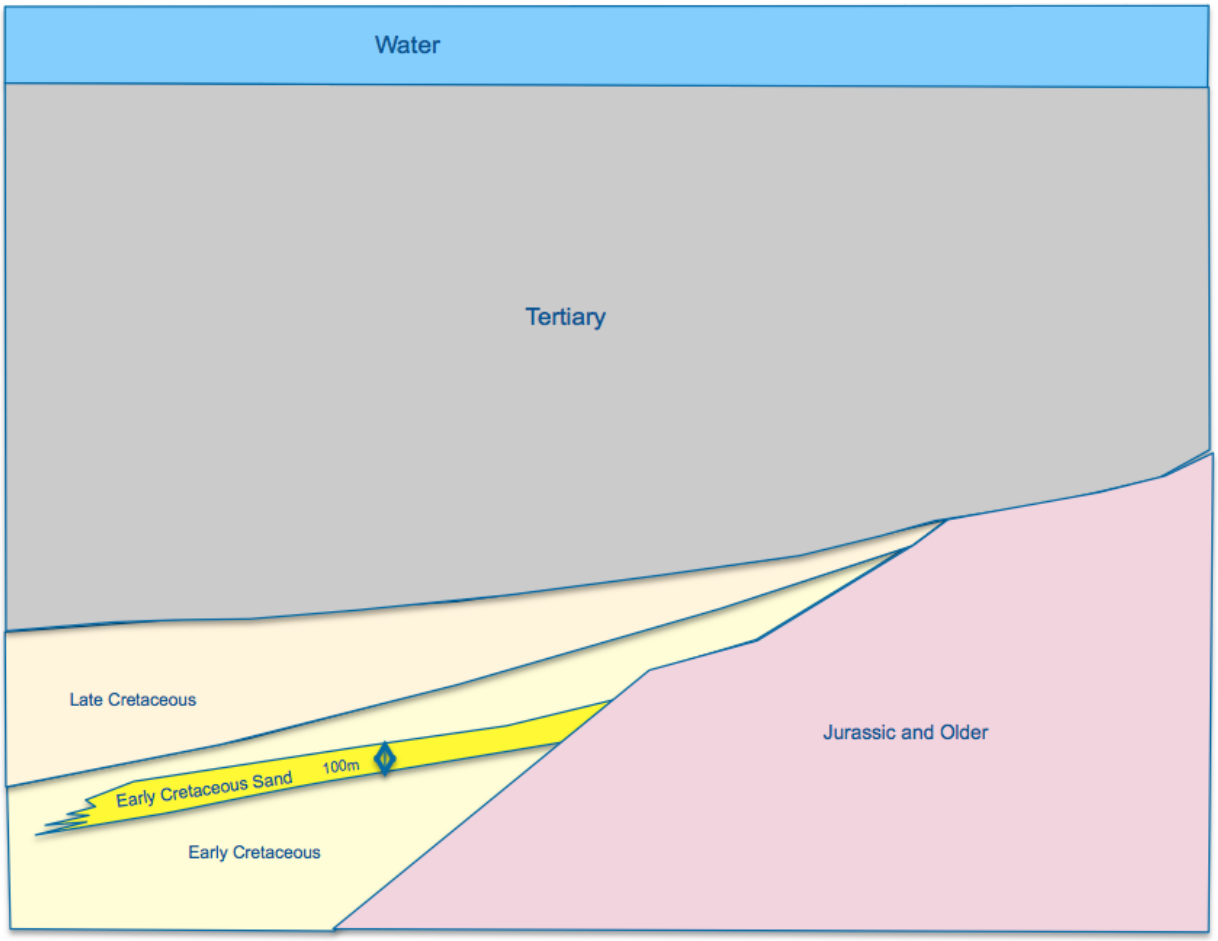

Figure 4.50: Schematic representation of the structural trap scenarios used in *Model 5* (compliments of Brad Bonnell, Suncor Energy).

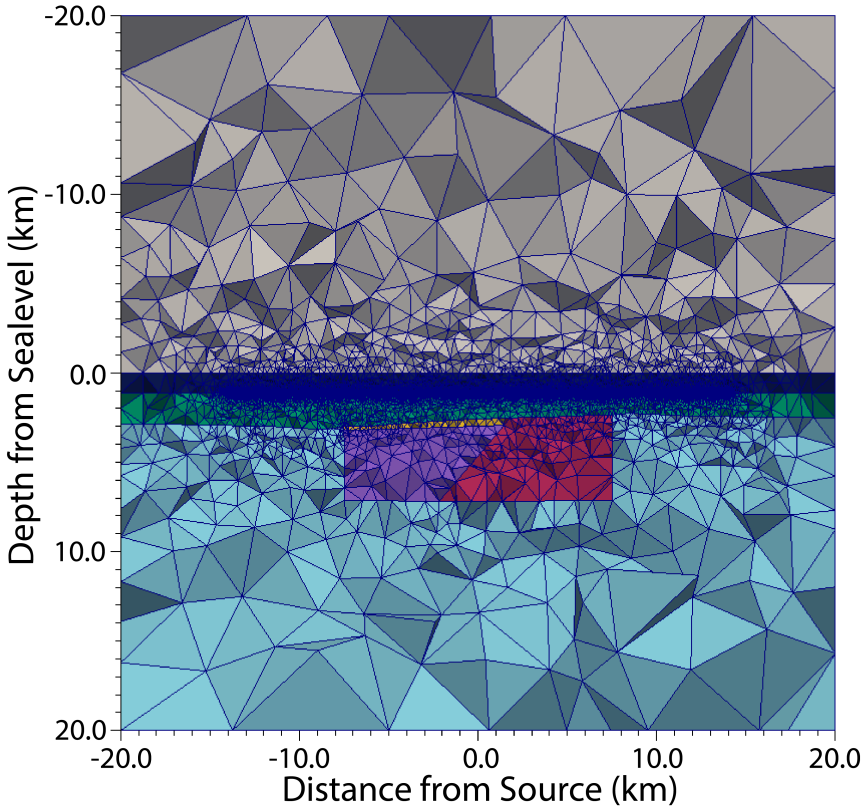

(a)

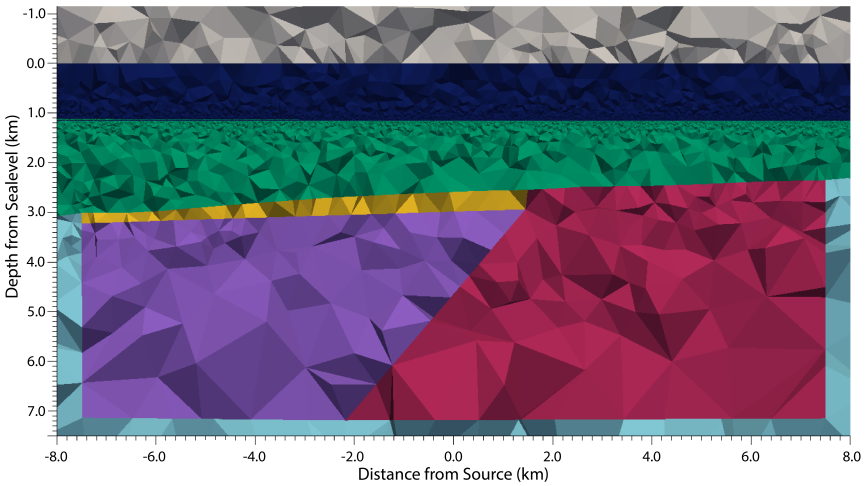

(b)

Figure 4.51: Cross-sections centered at $y = 0$ m of the multiple fault block system used in *Model 4*. Panel (a) full view; panel (b) enhanced view of the reservoir geometry.

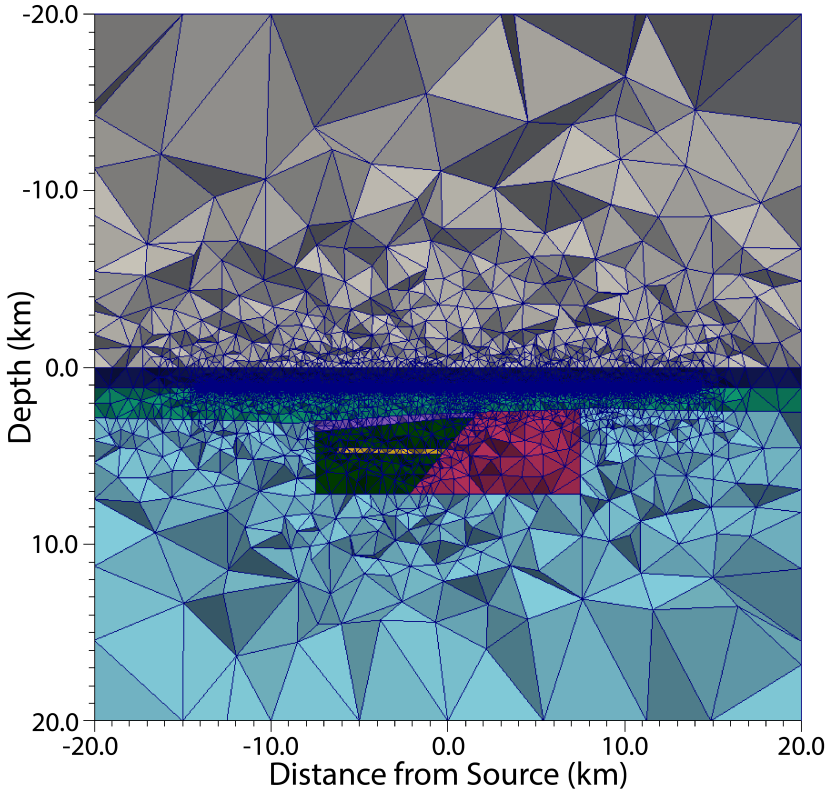

(a)

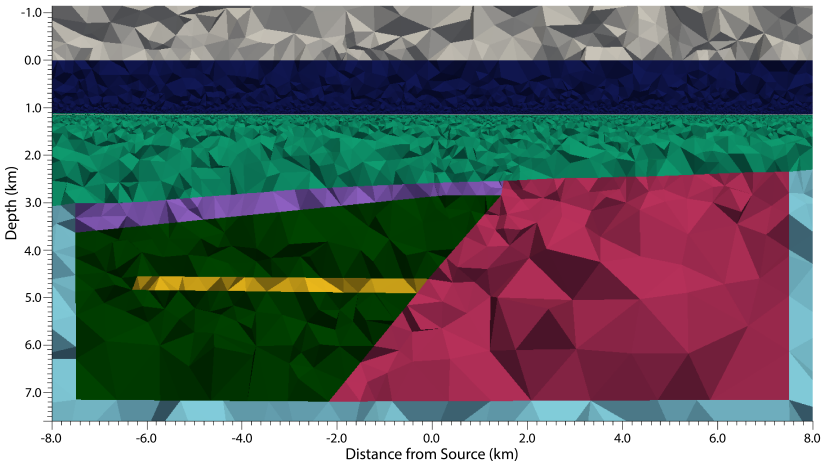

(b)

Figure 4.52: Cross-sections centered at $y = 0$ m of the multiple fault block system used in *Model 5*. Panel (a) full view; panel (b) enhanced view of the reservoir geometry.

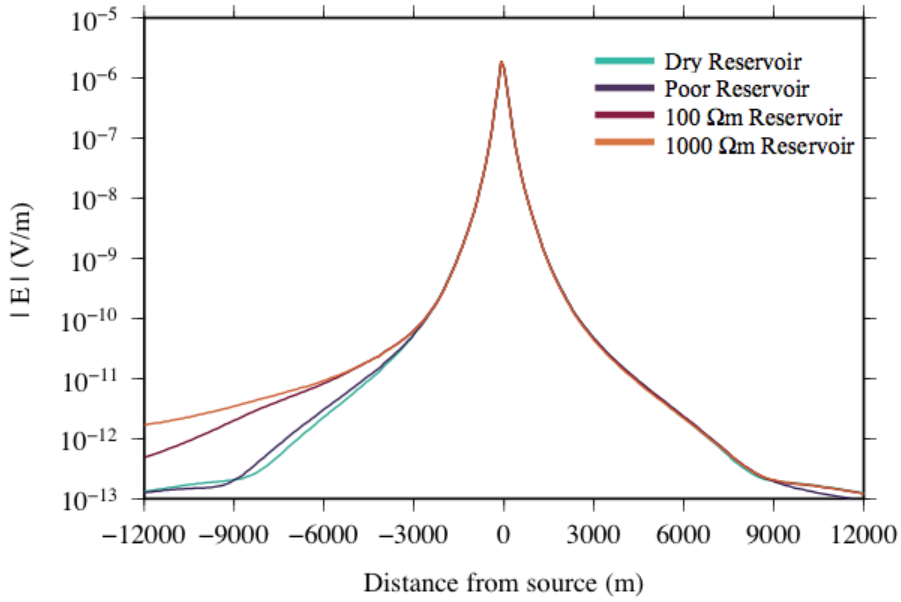

(a)

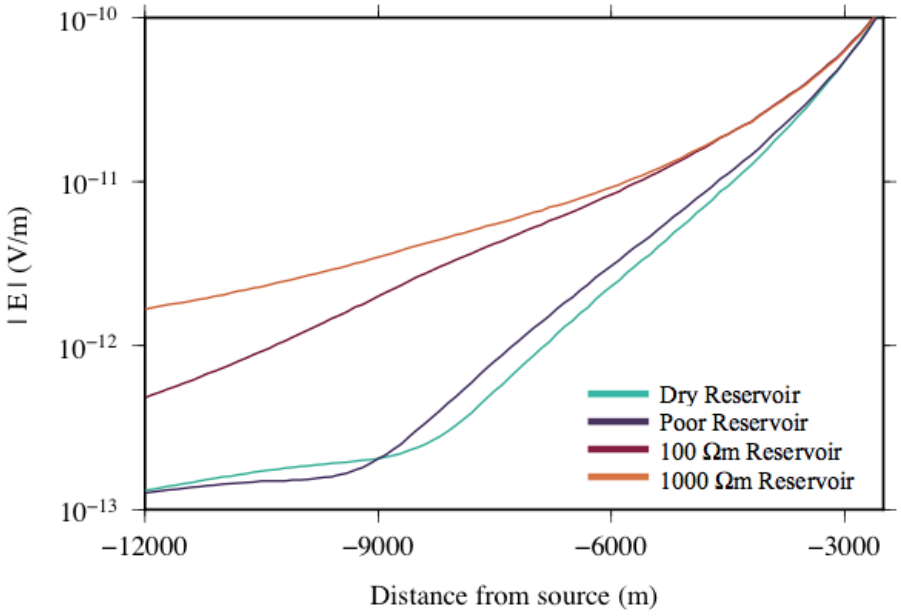

(b)

Figure 4.53: Panel (a) electric field amplitude results for *Model 4* (Figure 4.51) for each respective reservoir quality; and panel (b) enhanced view of the electric field amplitude results.

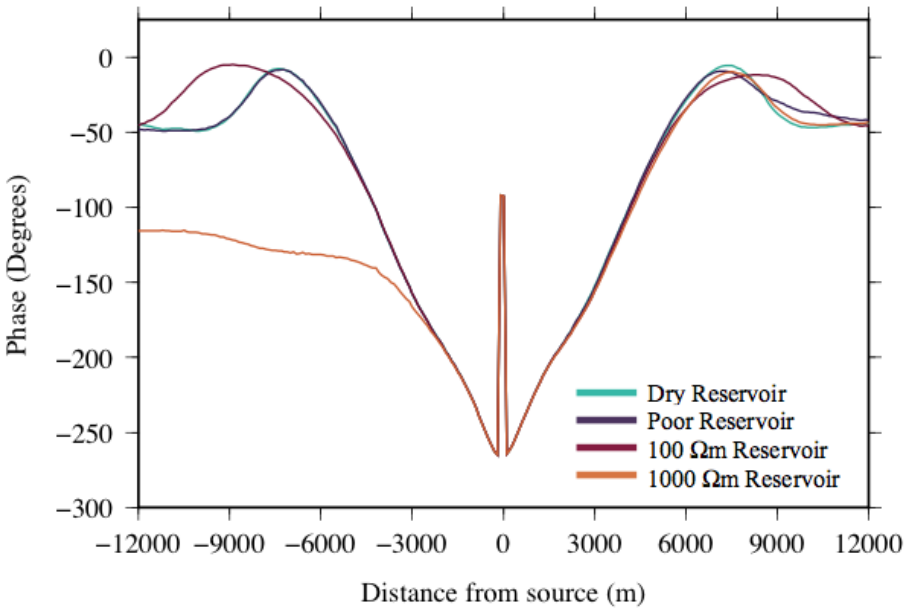

Figure 4.54: Phase results for *Model 4* (Figure 4.51).

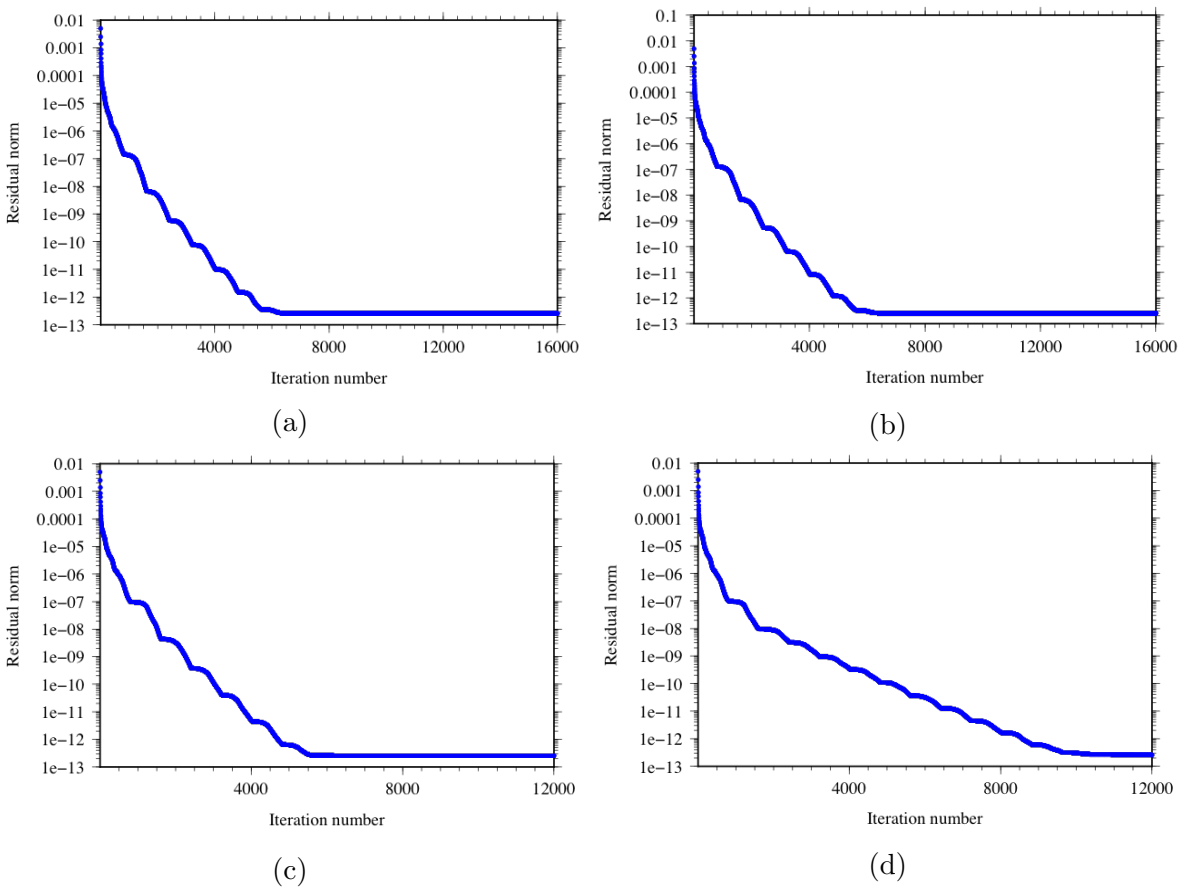

Figure 4.55: Convergence curves for *Model 4* (Figure 4.51). Panel (a) *Dry Reservoir*; panel (b) *Poor Reservoir*; panel (c) *100 Ωm Reservoir*; panel (d) *1000 Ωm Reservoir*.

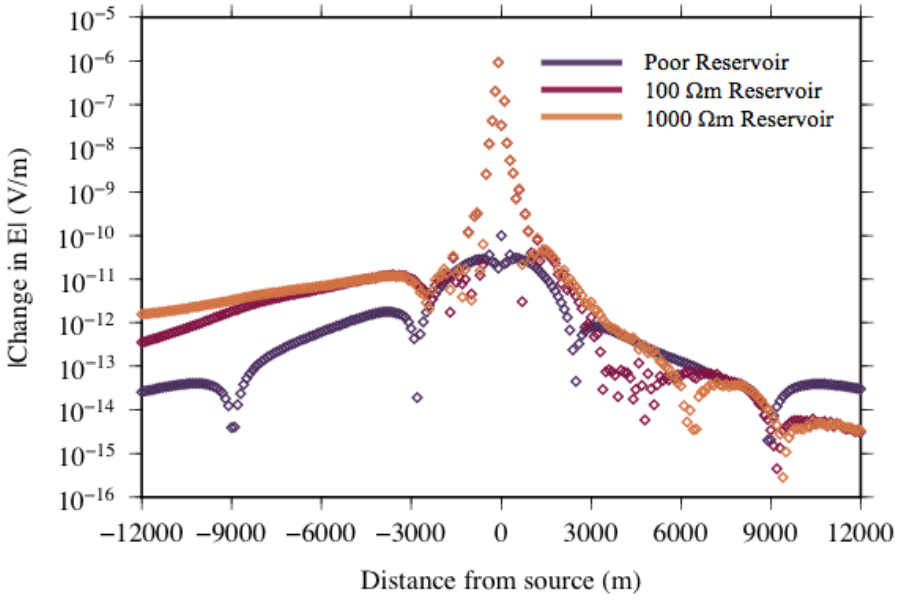

(a)

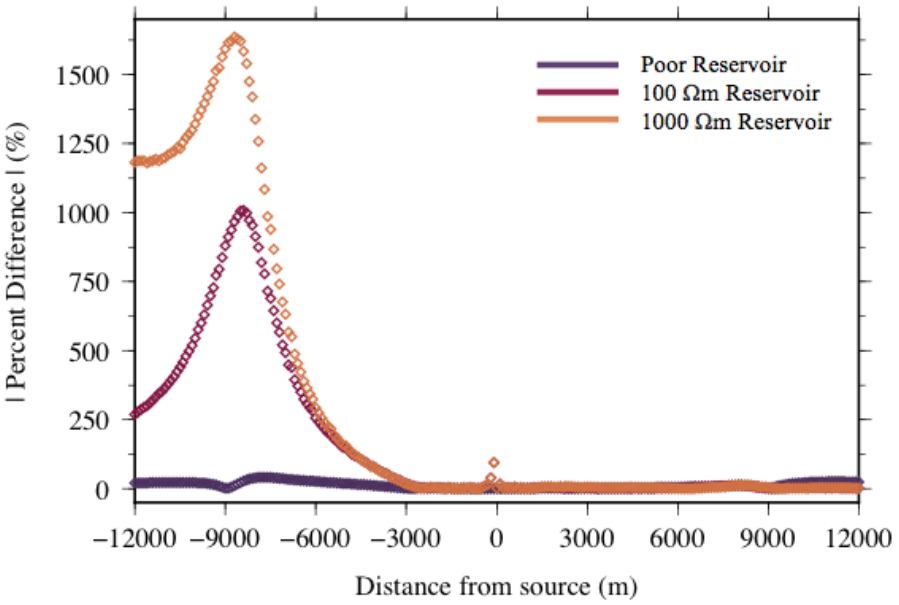

(b)

Figure 4.56: Panel (a) absolute differences in the electric field amplitude results of the *100 Ωm Reservoir* model with the *Dry Reservoir* for *Model 4* (Figure 4.51); panel (b) percent differences in the electric field amplitude results. Each percent difference has been normalized by the results of the dry reservoir.

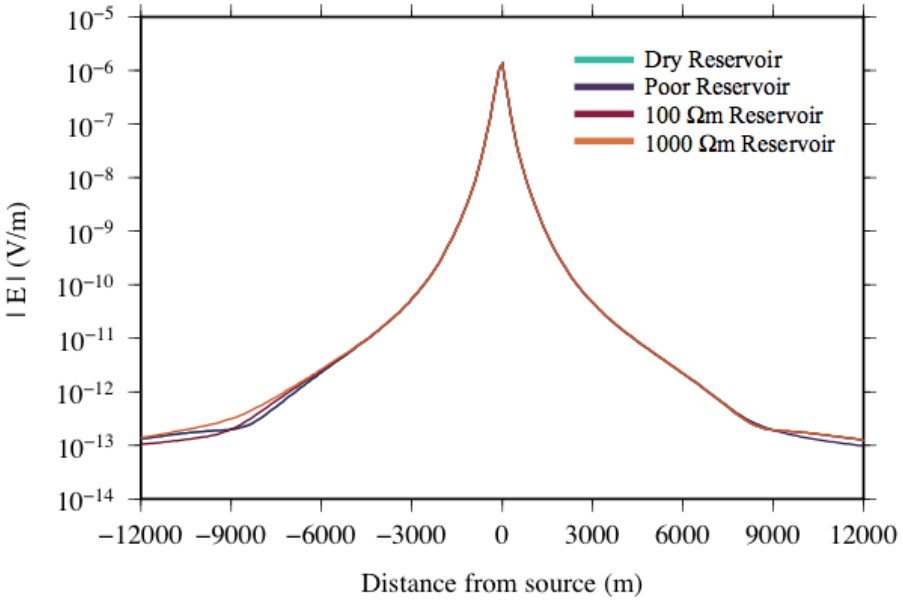

(a)

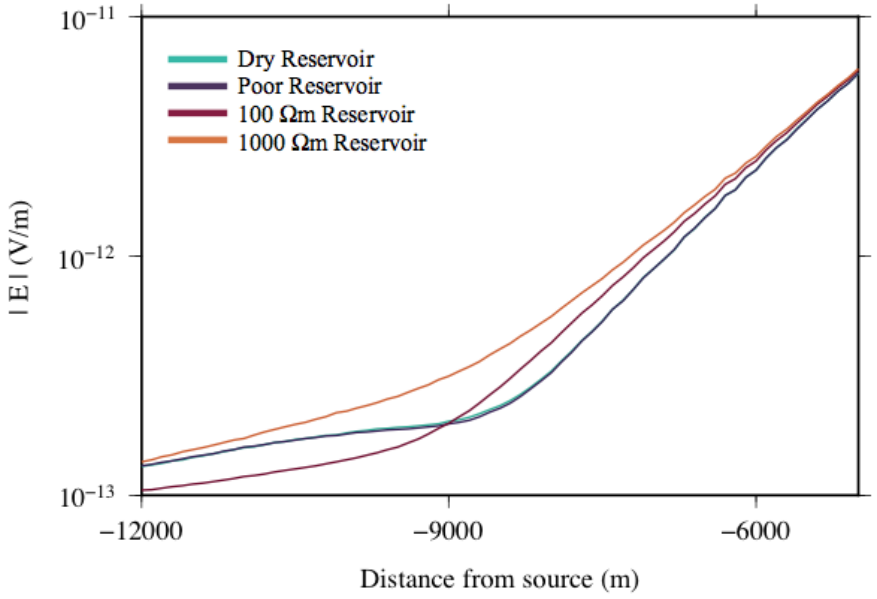

(b)

Figure 4.57: Panel (a) electric field amplitude results for *Model 5* (Figure 4.52) for each respective reservoir quality; and panel (b) enhanced view of the electric field amplitude results.

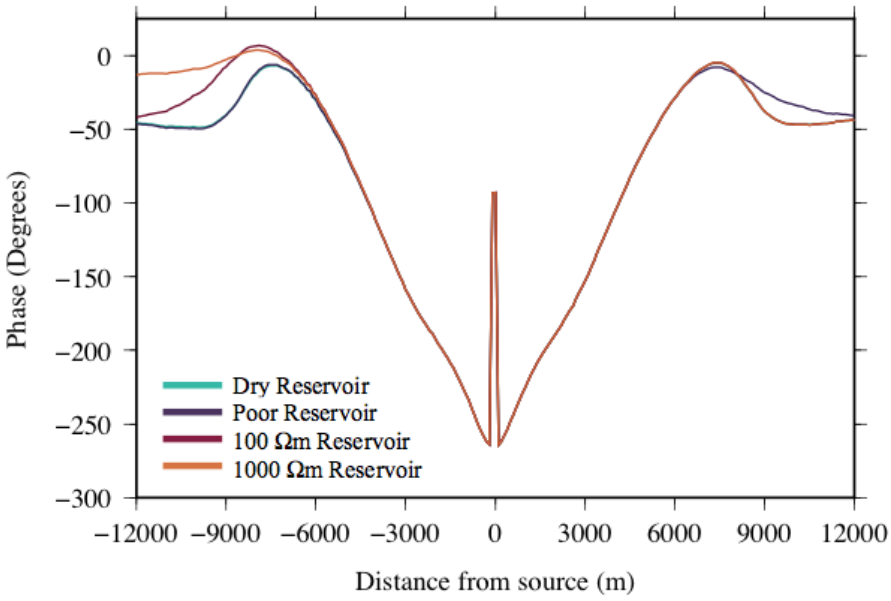

Figure 4.58: Phase results for *Model 5* (Figure 4.52).

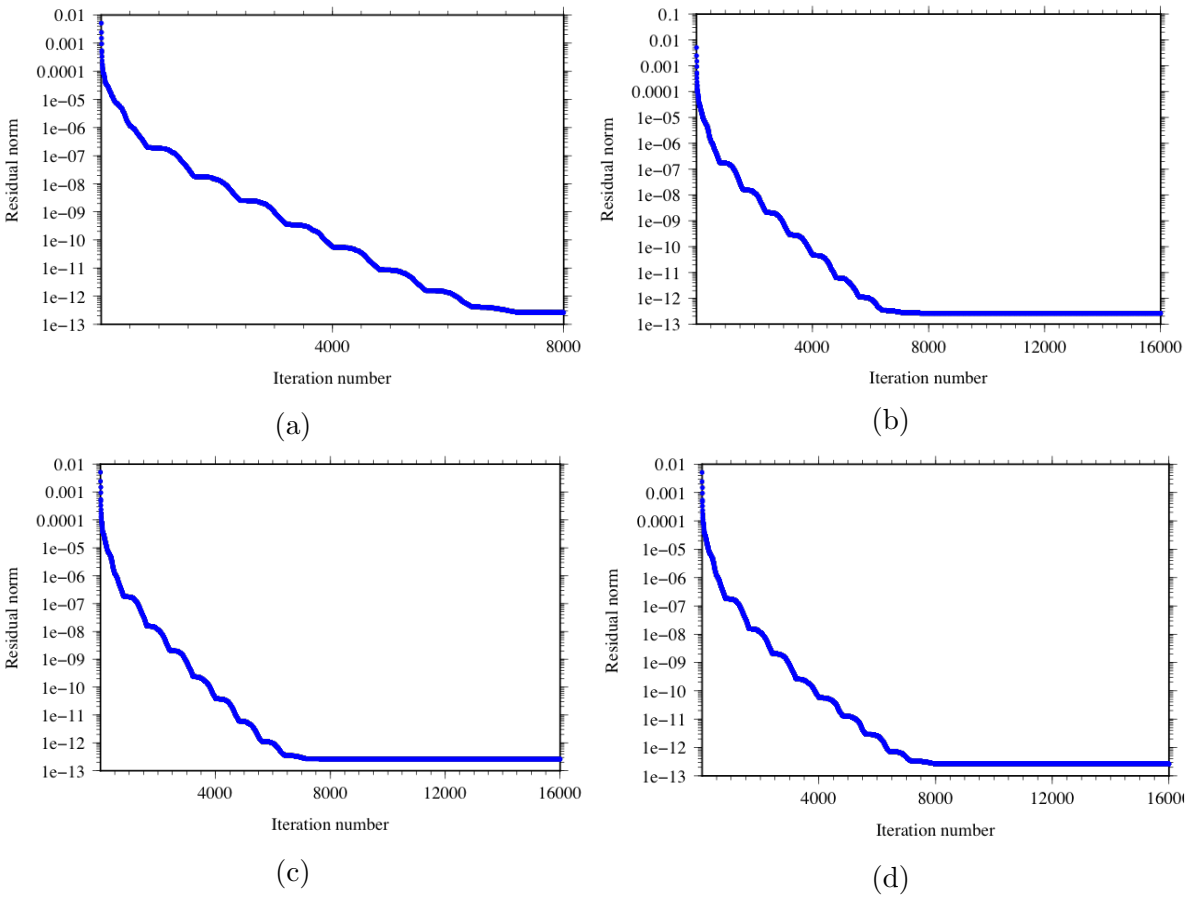

Figure 4.59: Convergence curves for *Model 5*. Panel (a) *Dry Reservoir*; panel (b) *Poor Reservoir*; panel (c) *100* Ωm *Reservoir*; panel (d) *1000* Ωm *Reservoir*.

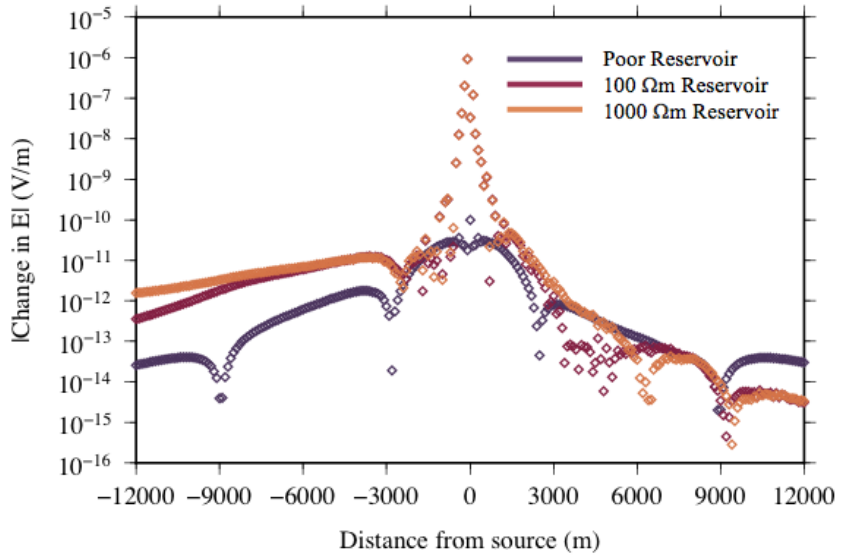

(a)

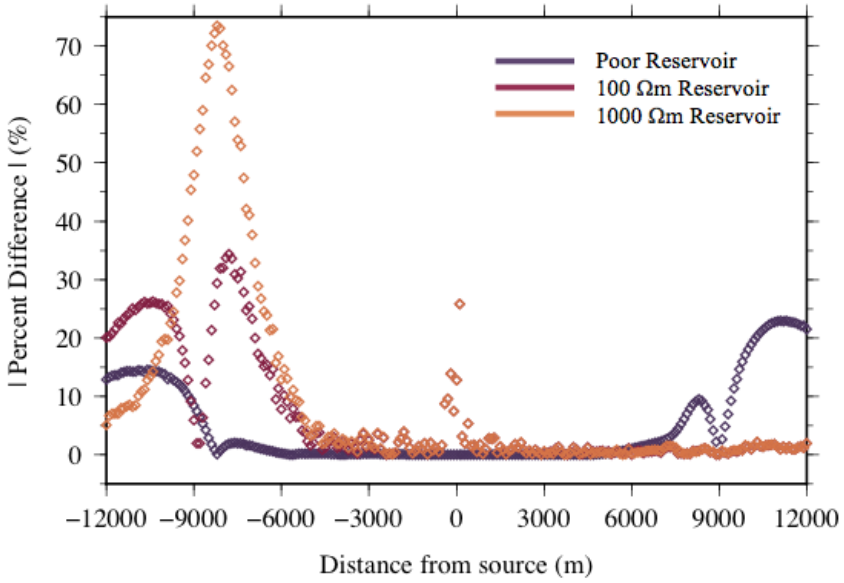

(b)

Figure 4.60: Panel (a) absolute differences in the electric field amplitude results of the *100 Ωm Reservoir* model with the *Dry Reservoir* for *Model 5* (Figure 4.52); panel (b) percent differences in the electric field amplitude results. Each percent difference has been normalized by the results of the dry reservoir.

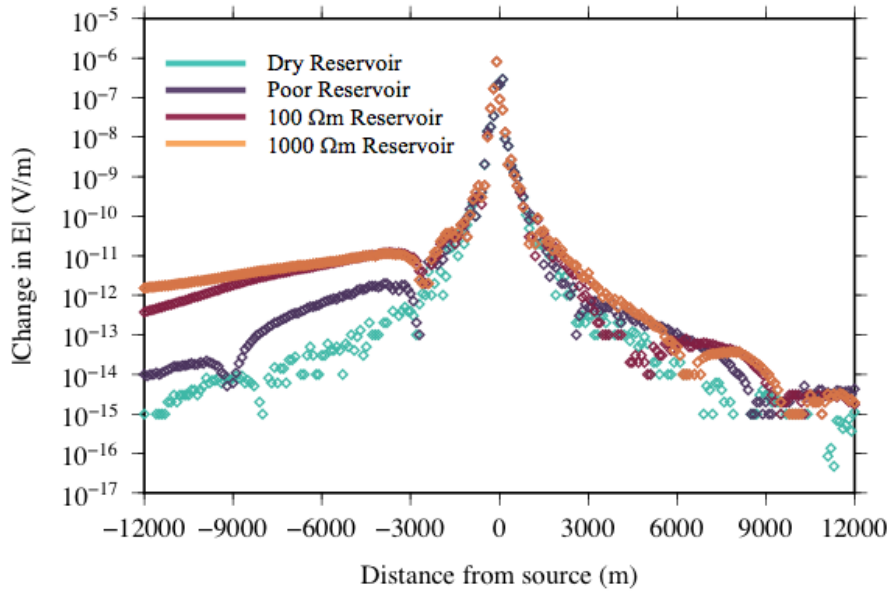

(a)

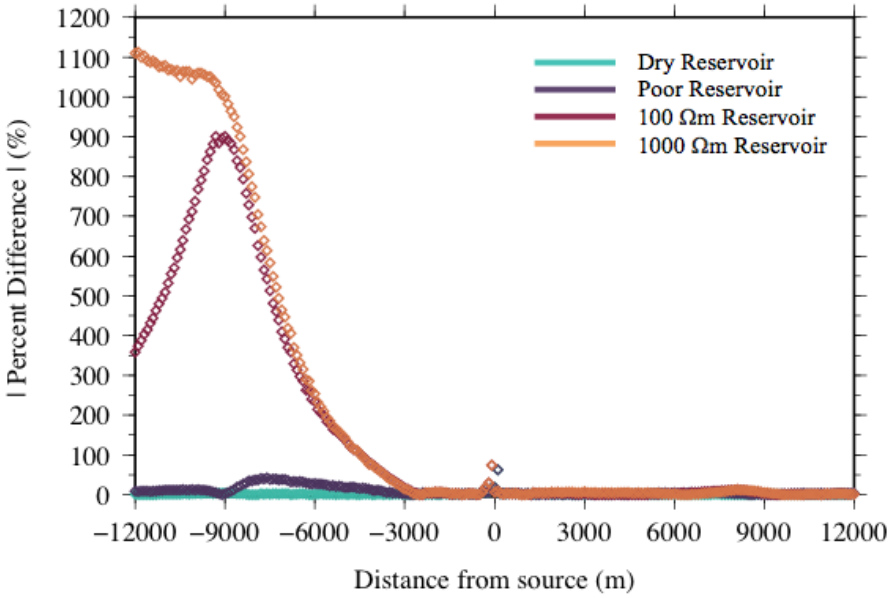

(b)

Figure 4.61: Panel (a) absolute differences in the electric field amplitude results for *Model 4* with respect to those for *Model 5*; panel (b) percent differences in the electric field amplitude results. Each percent difference has been normalized by the results of *Model 5*.

4.6 Source Position

As it is unlikely that the source will be positioned in the direct centre of the target area, a series of source configurations were also assessed. Since resistive bodies in the subsurface are only detectable from offsets of the source (e.g. Section 4.5), changing the source position changes the associated offset and hence target of detection. For example, by positioning the source on a reservoir edge, structures in the centre of the reservoir geometry that were previously overwhelmed by source energy, are now more detectable.

Three different source configurations were considered for the models from Section 4.5: the *Left Edge Source*, positioned from -7600 to -7500 m for reservoirs extending from x = -7500 to 7500 m (i.e. *Models 1, 4* and *5*), and from -5100 to -5000 m for reservoirs extending from x = -5000 to 5000 m (i.e. *Models 2* and *3*); the *Centre Source*, positioned from -100 to 0 m, as in Section 4.5; and the *Right Edge Source*, positioned from 7500 to 7600 m for reservoirs extending from -7500 to 7500 m, and 5000 to 5100 m for reservoirs extending from -5000 to 5000 m. As a result of these position changes, source refinement was altered: it followed a similar strategy as Section 4.5, but shifted in the x-direction to the appropriate source position. For example, the source refinement region for the *Left Edge Source* of the -7500 to 7500 m reservoir extended from -1 to 1 m in the y-direction and 1045 to 1055 m above the sealevel in the z-direction as before, but now extended from -7510 to -7490 m in the x-direction.

The results were computed for each of these source positions over a 100 Ωm reservoir, with 1.0 Hz, 1.0 Am source parameters. In order to compare the variations of electric field with offset for the source positions more easily, the results were shifted to show the

electric field amplitude and phase with offset from the respective source, as opposed to the offset from the centre of the domain, as in the previous section. Because the left and right sources considered offsets outside of the observation locations of the previous examples, the observation refinement region was extended to between -19000 to 19000 m in the x-direction, but maintained the same geometry as previously. This increased the mesh statistics substantially: for example the cell number in *Model 1* increased from 1,363,926 for the *Centre Source* model (Section 4.5.1) to 1,733,784 for the new source configuration (Table 4.4). This also increases the number of iterations required for appropriate convergence of the GMRES solver. Each model number of this section corresponds to the same model in Section 4.5, using the conductivities in Table 4.2. Cell, node and edge statistics for all models are displayed in Tables 4.4 and 4.5

Model Number	Cells	Nodes	Edges
Model 1	1,733,784	282,789	23,595
Model 2	1,722,604	280,885	23,933
Model 3	1,657,970	270,270	22,262
Model 4	1,675,125	278,789	22,966
Model 5	1,643,688	268,065	22,812

Table 4.4: Mesh characteristics for the left source configuration.

4.6.1 Model 1

Forward modelling results for each of the source configurations of *Model 1* are shown in Figures 4.62 and 4.63; the corresponding convergence curves are shown in Figure 4.64. Through analysis of the reservoir geometry (Figure 4.27) with the offset from source

Model Number	Cells	Nodes	Edges
Model 1	1,717,611	280,033	23,472
Model 2	1,761,600	287,109	24,569
Model 3	1,685,037	274,693	22,262
Model 4	1,709,888	276,969	23,164
Model 5	1,746,695	284,752	23,395

Table 4.5: Mesh characteristics for the right source configuration.

position, the region of detection for each source position can be interpreted. The *Left Edge Source* shows a positive amplitude deviation from the *Centre Source* with positive x-direction offsets, and negative amplitude deviation with negative x-direction offsets. This indicates that the *Left Edge Source* is more capable of detecting both the more resistive reservoir section to the right of the source, and the more conductive basement the left. The *Right Edge Source* detects the conductive basement to with a decrease in electric field amplutide to the right of the source (positive x-offset), and the resistive reservoir to the left with an increase in electric field amplitude (negative x-offset); however, because the reservoir to the immediate left is at a greater depth, the increase is not as large as with the *Left Edge Source*.

This is comparably reflected in the difference results (Figure 4.65). The percent difference results — which are produced by normalizing the hydrocarbon-saturated reservoir results by the dry reservoir for each respective source configuration — give distinctive offset positions of reservoir detection, indicated by peaks in the results. As the entire reservoir exists only at positive offset (right) of the *Left Edge Source*, the peak occurs at a positive offset: $\sim$375% difference at $\sim$ 9000 m offset from the source, or at $x \approx 2500$ m in the com-

putational domain. This suggests that source energy overwhelms the amplitude response until the detection of the reservoir at this position, but the large magnitude of response is reflective of the proximity of the source to the shallowest portion of the reservoir, as the source is positioned at the edge of the hanging wall (see Figure 4.27). The reservoir exists at both negative (left) and positive (right) offset positions for the *Centre Source* as indicated by two peaks: ∼250% at ∼ -8500 and 8500 m offsets. The narrower offsets are indicative of poorer detection of the reservoir in comparision of the *Left Edge Source* configuration, but magnitudes of percent difference between the shallow (hanging wall) and deep (footwall) parts of the reservoir are indicative of the reservoir depth. Mirroring the *Left Edge Source* configuration, the entire reservoir is at negative offsets (left) of the *Right Edge Source*, resulting in a single peak at negative offset: ∼130% at ∼ -8500 m offset. Though the fault displacement of the reservoir is slightly detected by a minor positive inflection at ∼ -6500 m offset, differentiating each portion of the reservoir from each other is difficult.

Detection is shown in the absolute difference by smooth curves: from 4000 to 12000 m offsets for the *Left Edge Source*, -12000 m to -3000 m and 3000 to 12000 m offsets for the *Centre Source*, and -12000 m to -3000 m offsets for the *Right Edge Source*. Detection is also apparent in the phase results (Figure 4.63) with a large dip in the phase curve before levelling off and returning to the phase value of the *Centre Source* (and the air layer effect). This is most evident in the dip in the *Left Edge Source* at ∼ 10000 m offset.

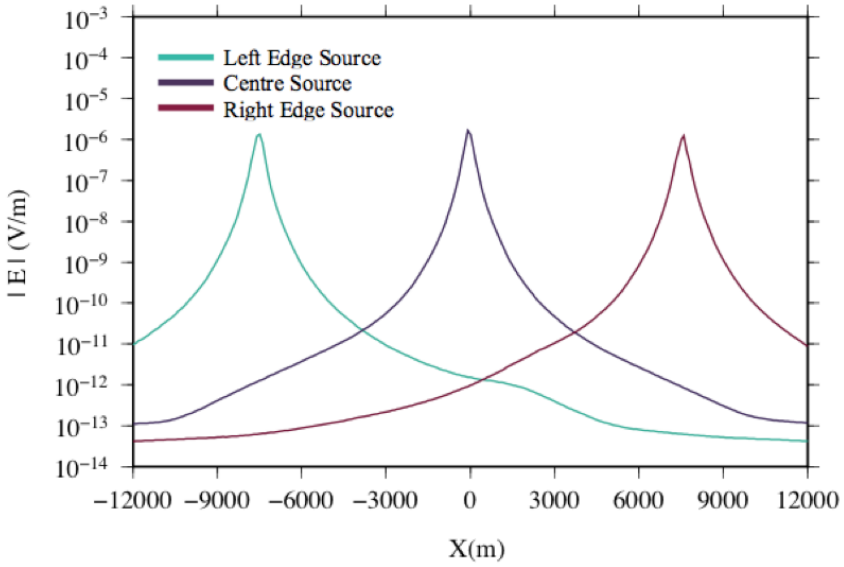

(a)

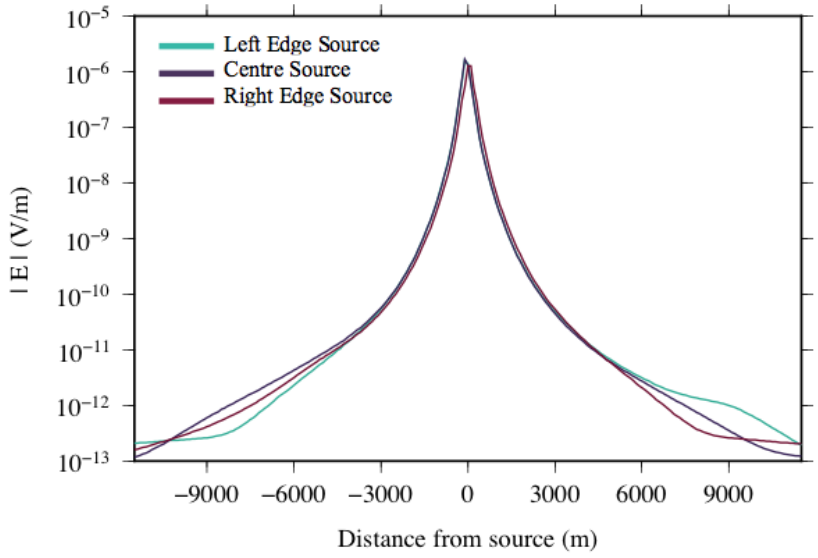

(b)

Figure 4.62: Panel (a) electric field amplitude results for *Model 1* with source positions from x = -7600 to -7500 m (*Left Edge Source*), -100 to 0 m (*Centre Source*), and 7500 to 7600 m (*Right Edge Source*); panel (b) electric field amplitude results for *Model 1* plotted as a function of offset from their respective source.

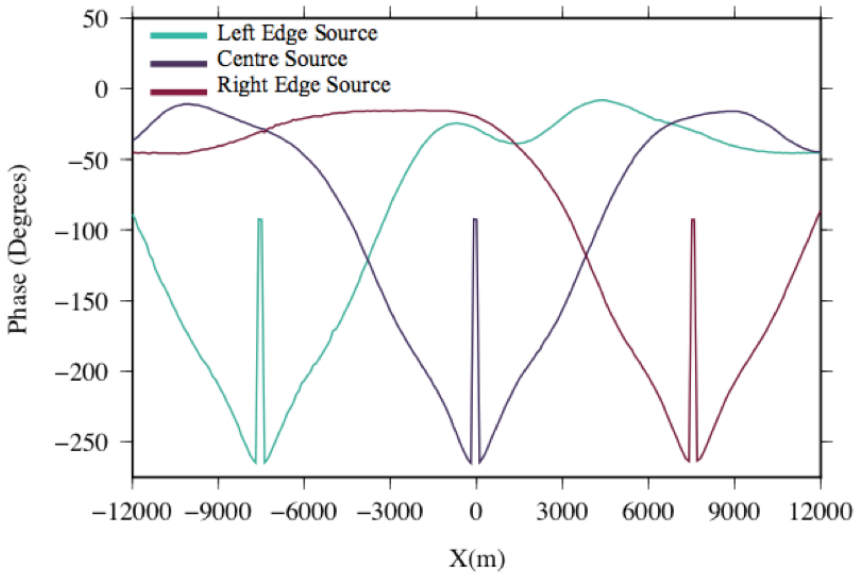

(a)

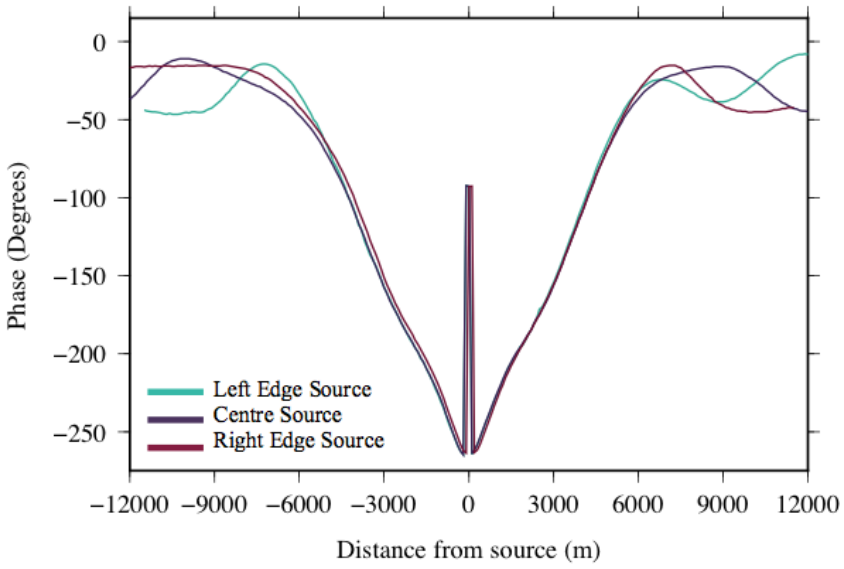

(b)

Figure 4.63: Panel (a) phase results for *Model 1* with source positions from x =-7600 to -7500 m (*Left Edge Source*), -100 to 0 m (*Centre Source*), and 7500 to 7600 m (*Right Edge Source*); panel (b) phase results plotted as a function of offset from their respective source.

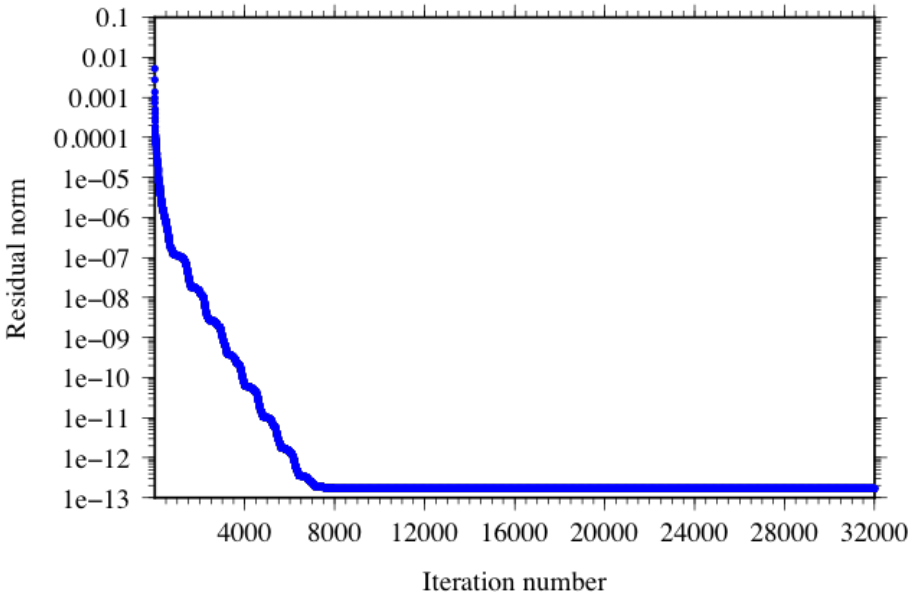

(a)

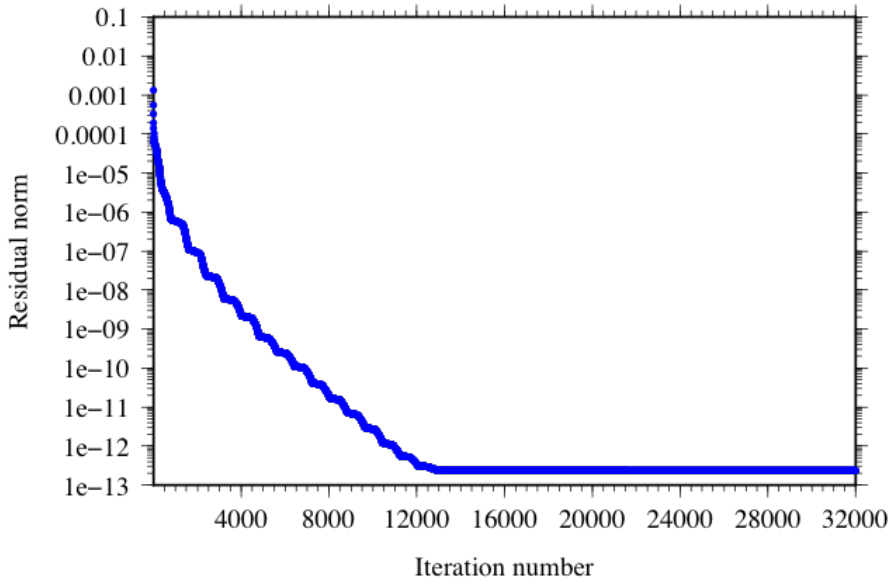

(b)

Figure 4.64: Convergence curves for *Model 1*. Panel (a) *Left Edge Source*; panel (b) *Right Edge Source*.

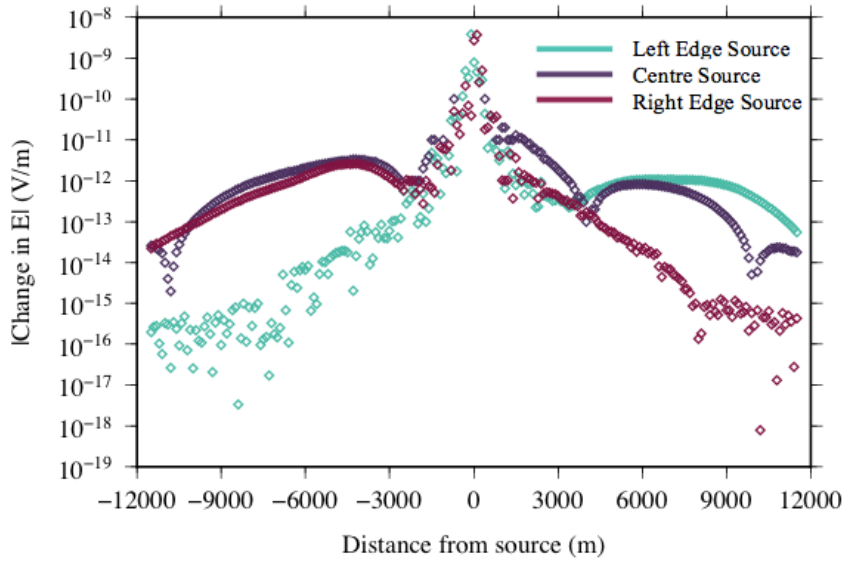

(a)

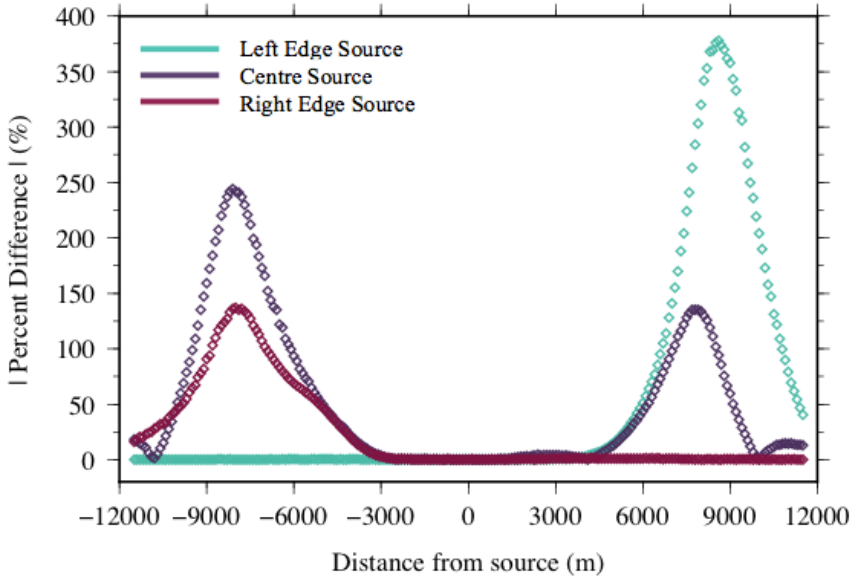

(b)

Figure 4.65: Panel (a) absolute differences in the electric field amplitude results for *Model 1* and the *Dry Reservoir*; panel (b) corresponding percent differences in the electric field amplitude. Each percent difference has been normalized by the results of the dry reservoir for the same source position.

4.6.2 Models 2 and 3

The reservoir geometry of *Model 2* (Figure 4.33) is relatively horizontal in its extent, and has sections at greater depths than *Model 1* because of the increased number of fault blocks. As a result, the electric field amplitude and phase results of *Model 2* (Figures 4.66 and 4.67) and convergence (Figure 4.68) do not show the dramatic deviations as for *Model 1*. Though comparison of the amplitude response for each source configuration is difficult, regions of detection can be delineated by analyzing model differences (Figure 4.69).

The *Right Edge Source* maximizes the detection of the two shallowest reservoir packages (*Packages 2* and *4*; Table 4.3) as indicated by two percent difference peaks at ∼-8000 and -4000 m offsets with magnitudes of 75% and 40%, respectively. The peak at ∼ -10000 m offset represents a negative amplitude difference generated by increased reservoir to basement contrast between the *100 Ωm Reservoir* and *Dry Reservoir* models at this position. The *Centre Source*'s source energy masks the detection of the central reservoir structures, but accurately detects reservoirs with negative (∼ -6000 m) and positive (∼ 6000 m) offsets from the source position. The magnitude difference between these reservoirs is indicative of the change in depth of each package: the reservoir detected at negative offsets, with a depth of ∼3200 m has a maximum percent difference of 13%, while the reservoir at positive offsets, at ∼2500 m depth, has a maximum percent difference of 40%. The *Left Edge Source* has a similar, mirrored trend in results as the *Right Edge Source*, but has lower magnitudes. The *Left Edge Source* is positioned at further offset from the shallowest, and therefore strongest response package (*Package 4* in Table 4.3), and therefore gives a lower magnitude response in the detection of this reservoir than the *Right Edge Source*. Deeper

structures are slightly detected via an inflection at $\sim$ 5500 m, but the percent differences straddle the threshold of reservoir detection.

Model 3 (see Figure 4.42) comprises a similar reservoir structure as *Model 2*, with an earlier, and therefore deeper, deposition of the reservoir packages (see details in Section 4.5.3). As a result, the electric field amplitude and phase responses to the resistive reservoirs — and therefore reservoir detectability — are significantly reduced, and exhibit much smaller magnitudes (see Figures 4.70 and 4.71 and convergence curve in Figure 4.72). The *Left Edge Source* percent difference apparent for *Model 2* (see Figure 4.69) is only slightly resolved at $\sim$ 9000 m offset with a peak difference of 8%, which falls below the threshold of reservoir detection in real world scenarios. In fact, the only result that exists above the threshold is the *Right Edge Source*'s detection of *Package 4* (Table 4.3) at $\sim$ -9000 m offset at 12% difference, though there are several peaks visible along the profile in these synthetic data. For example, the *Centre Source* configuration detects resistivity contrasts at offsets of $\sim$ -9000, -6000, 5500 and 8800 m. Though peak values, each of these responses has less than 7% difference, and therefore would be undetectable in experimental recreation of the scenario.

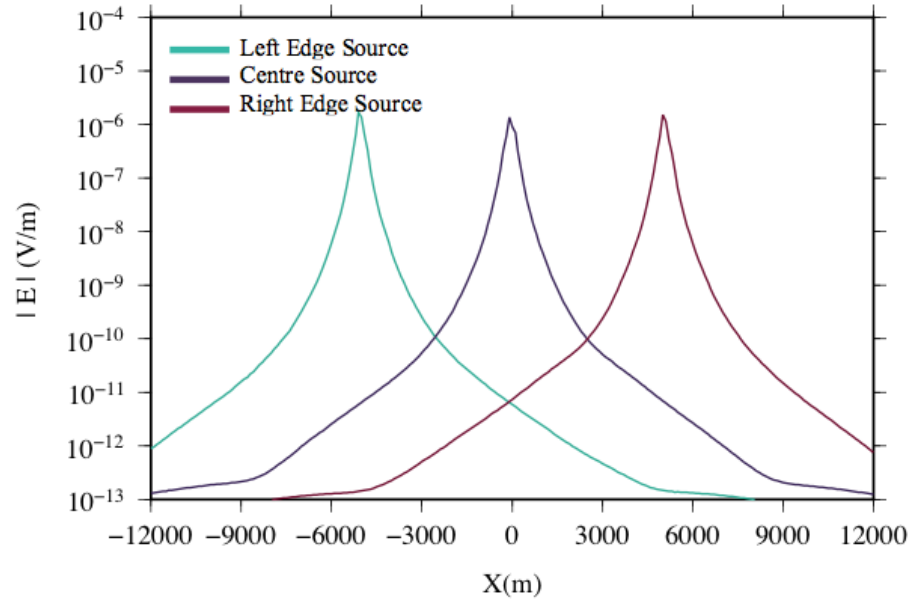

(a)

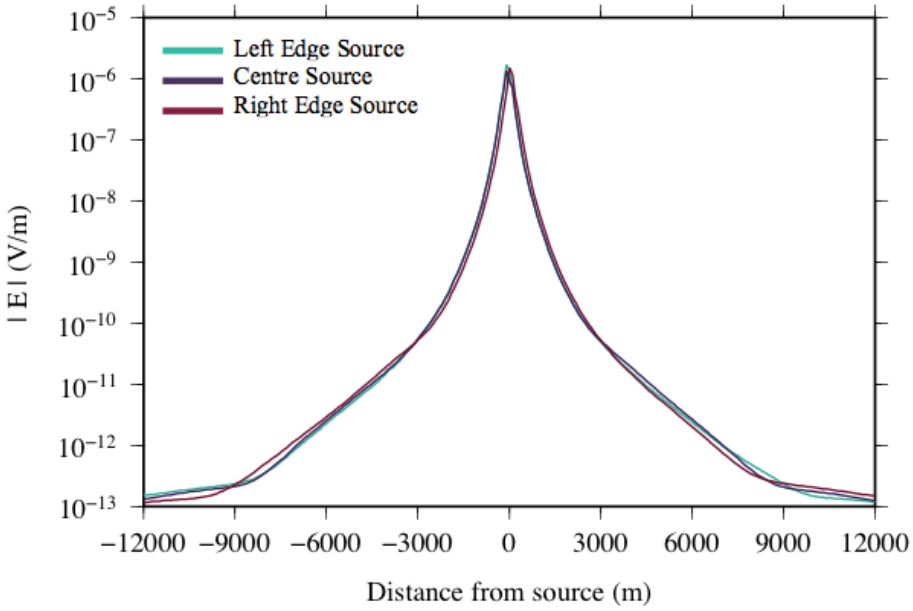

(b)

Figure 4.66: Panel (a) electric field amplitude results for *Model 2* with source positions from x = -5100 to -5000 m (*Left Edge Source*), -100 to 0 m (*Centre Source*), and 5000 to 5100 m (*Right Edge Source*); panel (b) electric field amplitude results plotted as a function of offset from source.

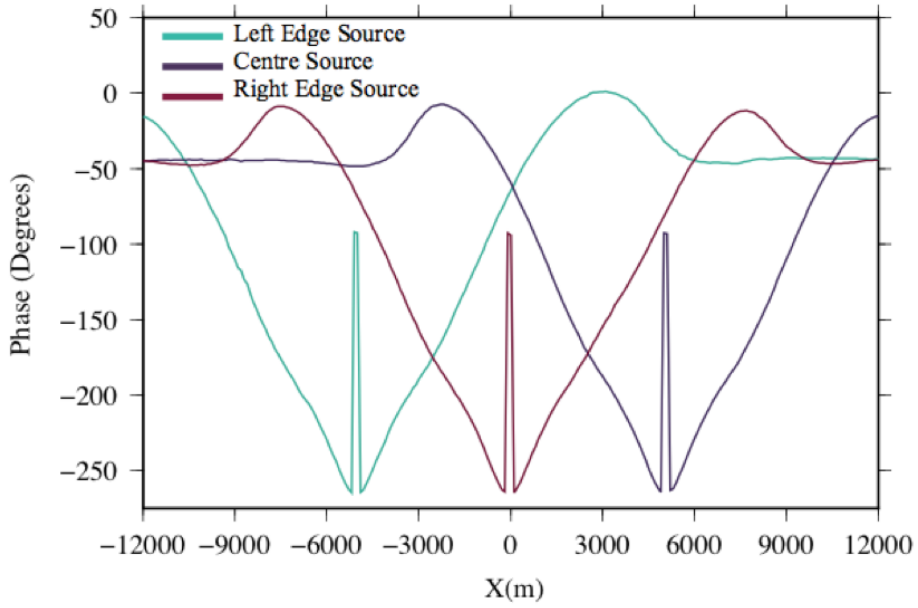

(a)

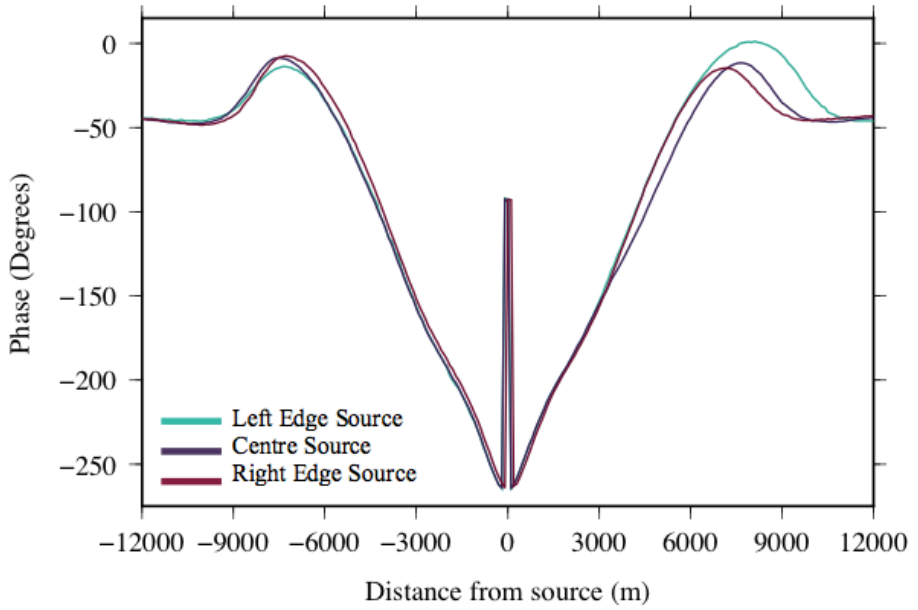

(b)

Figure 4.67: Panel (a) phase results for *Model 2* with source positions from x = -5100 to -5000 m (*Left Edge Source*), -100 to 0 m (*Centre Source*), and 5000 to 5100 m (*Right Edge Source*); panel (b) phase results plotted as a function of offset from source.

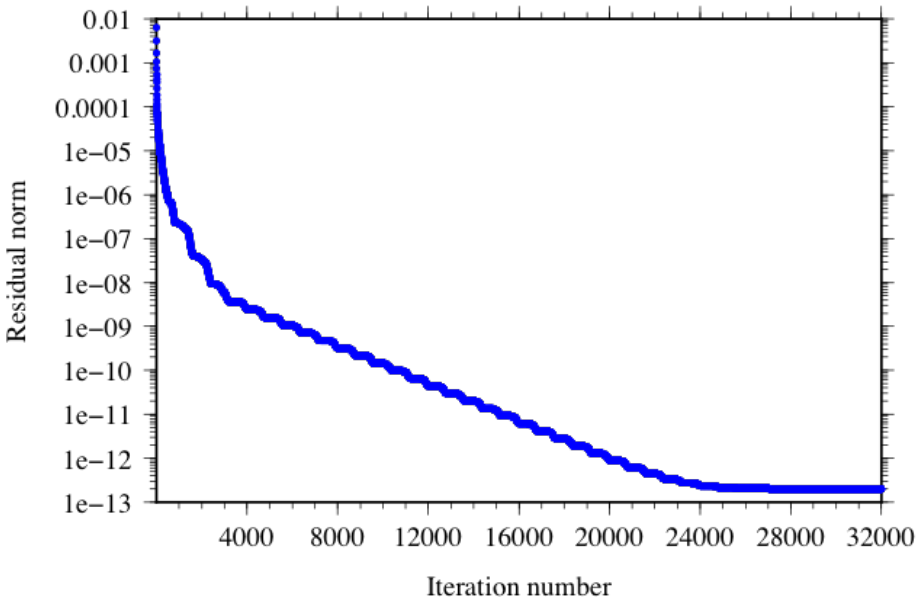

(a)

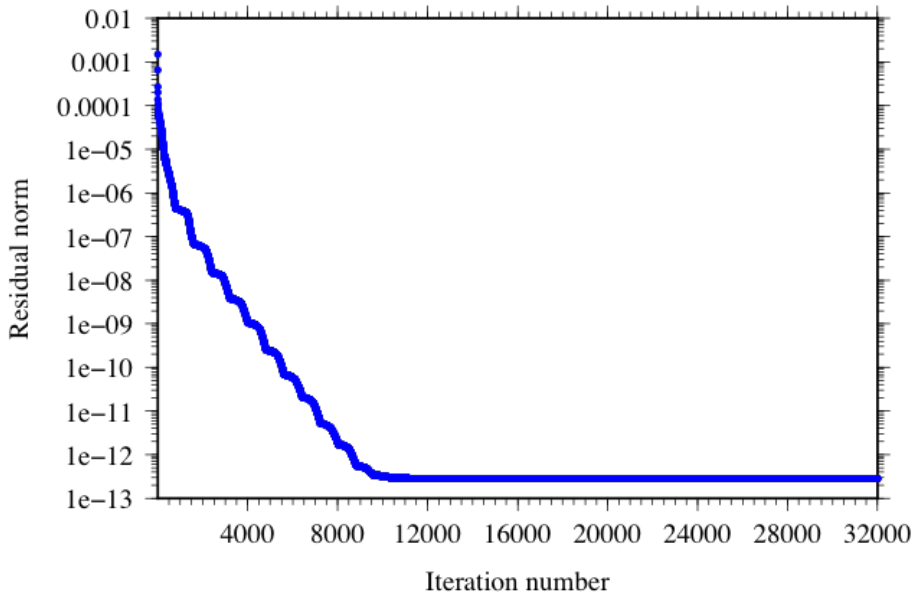

(b)

Figure 4.68: Convergence curves for *Model 2*. Panel (a) *Left Edge Source*; panel (b) *Right Edge Source*.

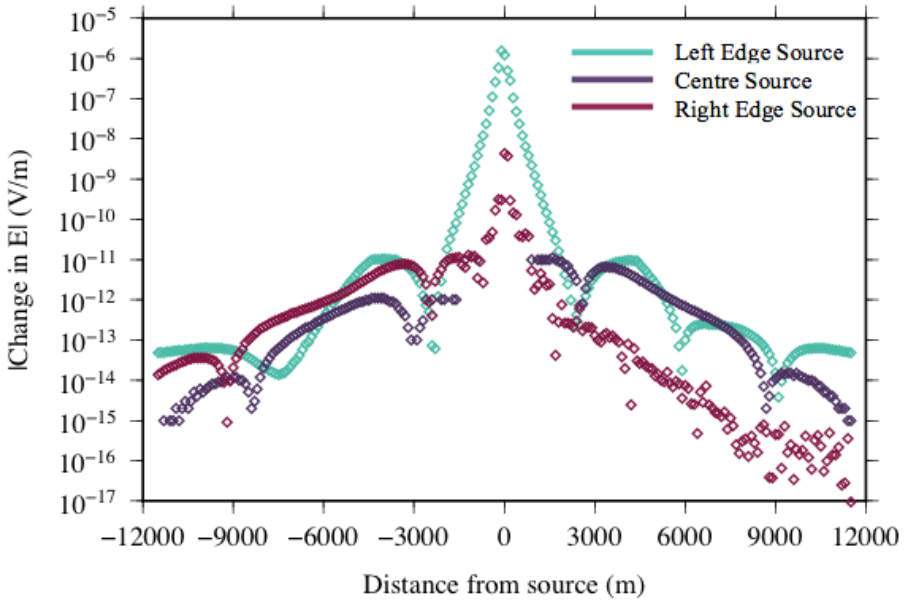

(a)

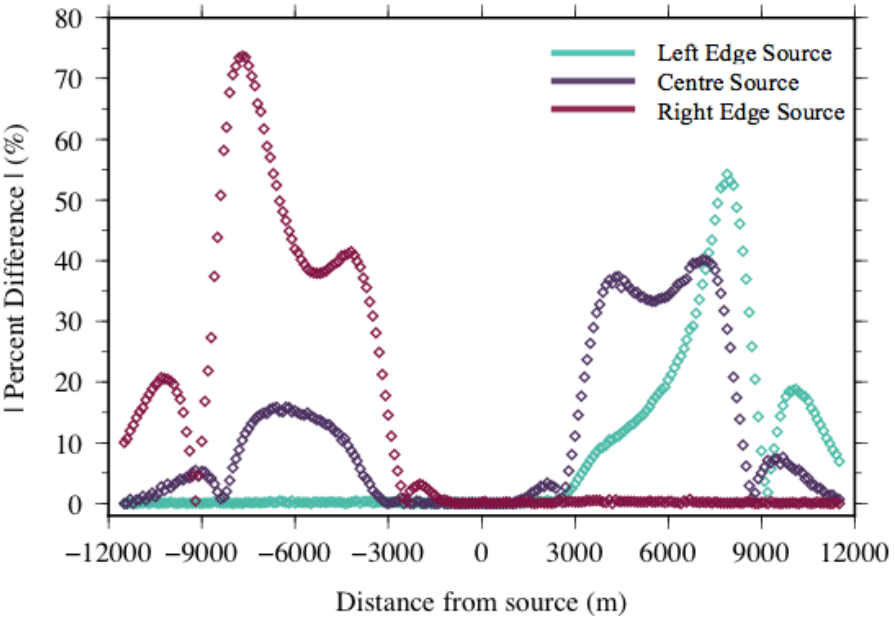

(b)

Figure 4.69: Panel (a) absolute differences in the electric field amplitude results for *Model 2* and the *Dry Reservoir*; panel (b) percent differences in the electric field amplitudes. Each percent difference has been normalized by the results for the dry reservoir for the same source.

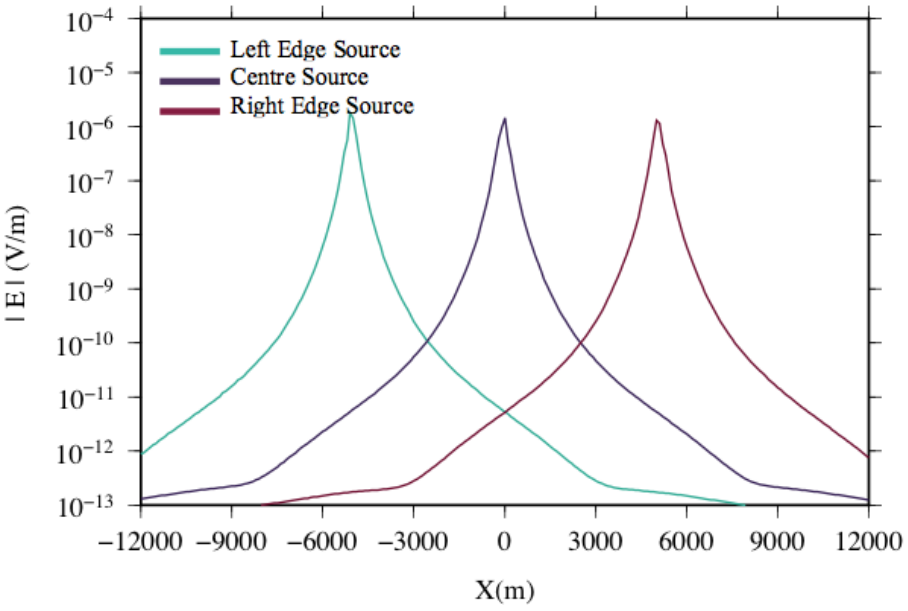

(a)

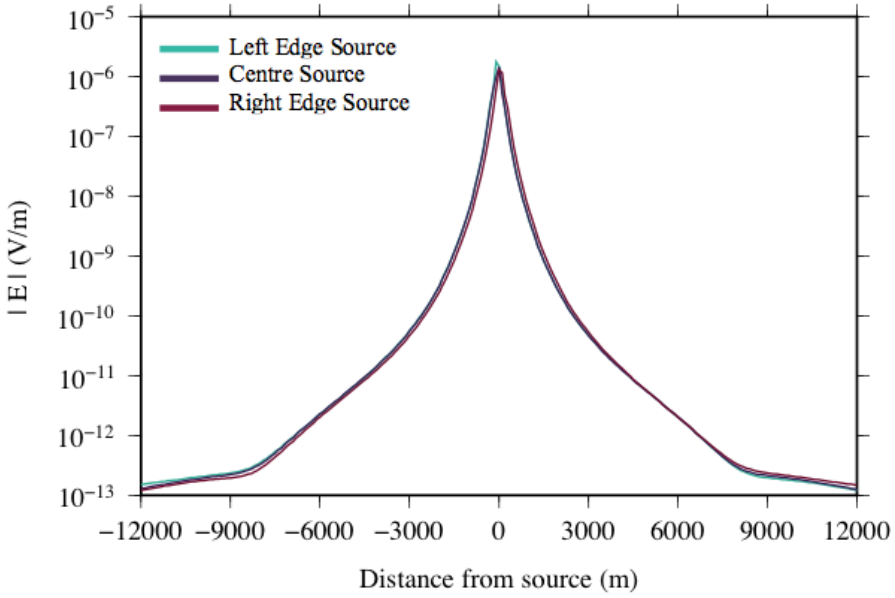

(b)

Figure 4.70: Panel (a) electric field amplitude results for *Model 3* with source positions from x = -5100 to -5000 m (*Left Edge Source*), -100 to 0 m (*Centre Source*), and 5000 to 5100 m (*Right Edge Source*); panel (b) electric field amplitude results plotted as a function of offset from source.

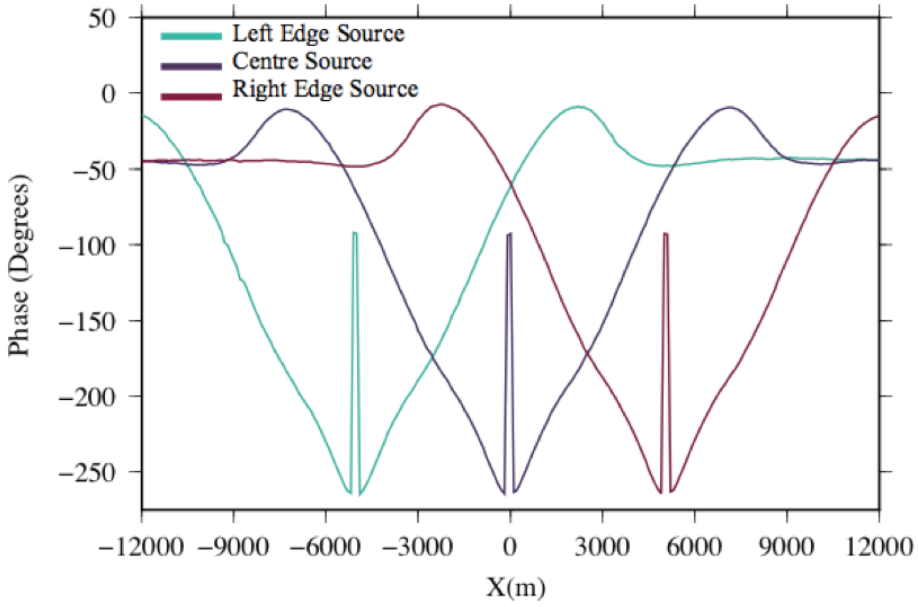

(a)

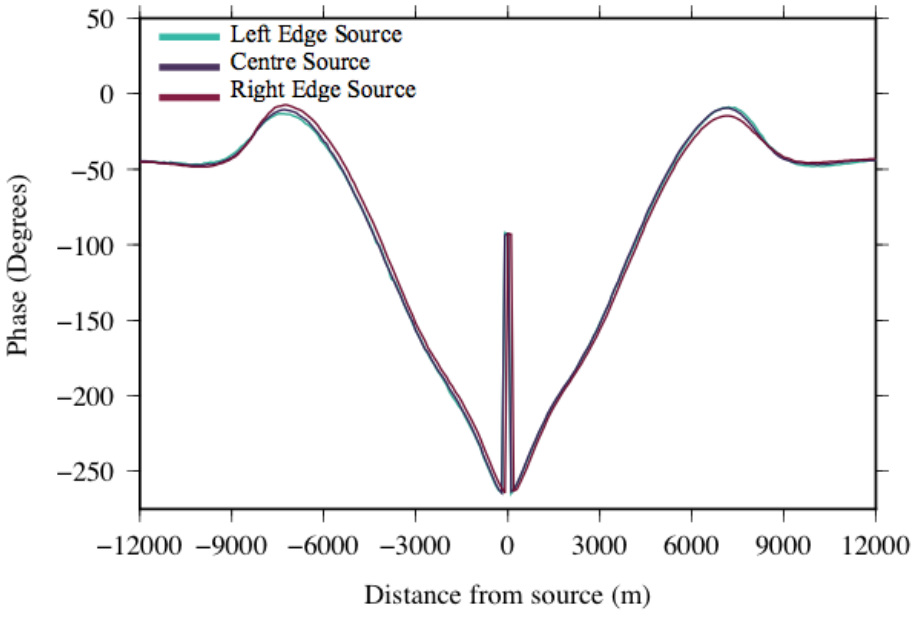

(b)

Figure 4.71: Panel (a) phase results for *Model 3* with source positions from x = -5100 to -5000 m (*Left Edge Source*), -100 to 0 m (*Centre Source*), and 5000 to 5100 m (*Right Edge Source*); panel (b) phase results for*Model 3* plotted as a function of offset from source.

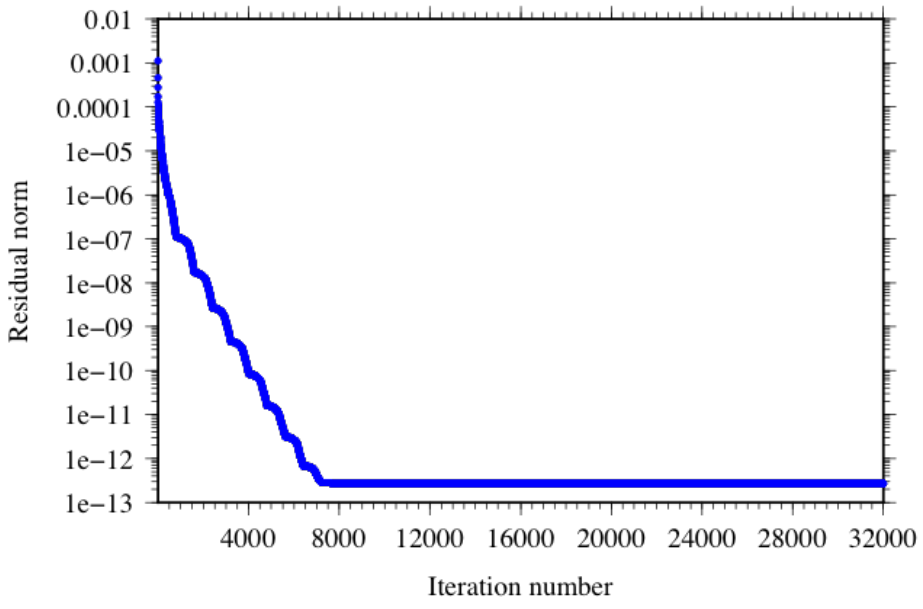

(a)

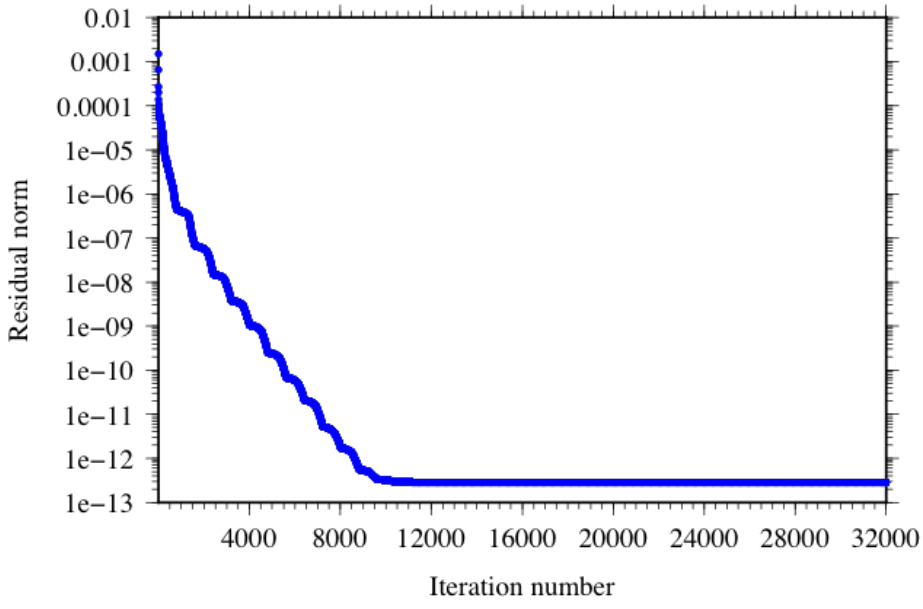

(b)

Figure 4.72: Convergence curves for *Model 3*. Panel (a) *Left Edge Source*; panel (b) *Right Edge Source*.

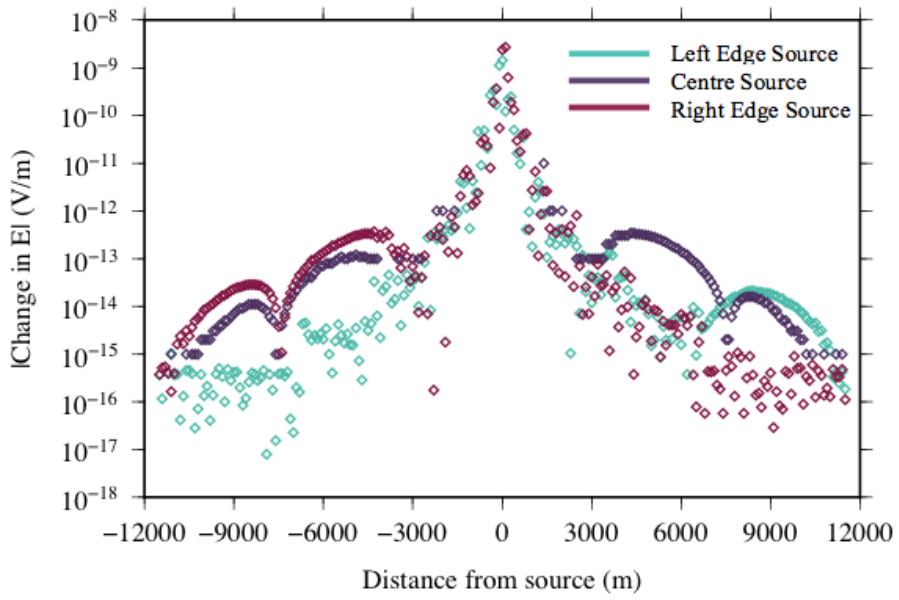

(a)

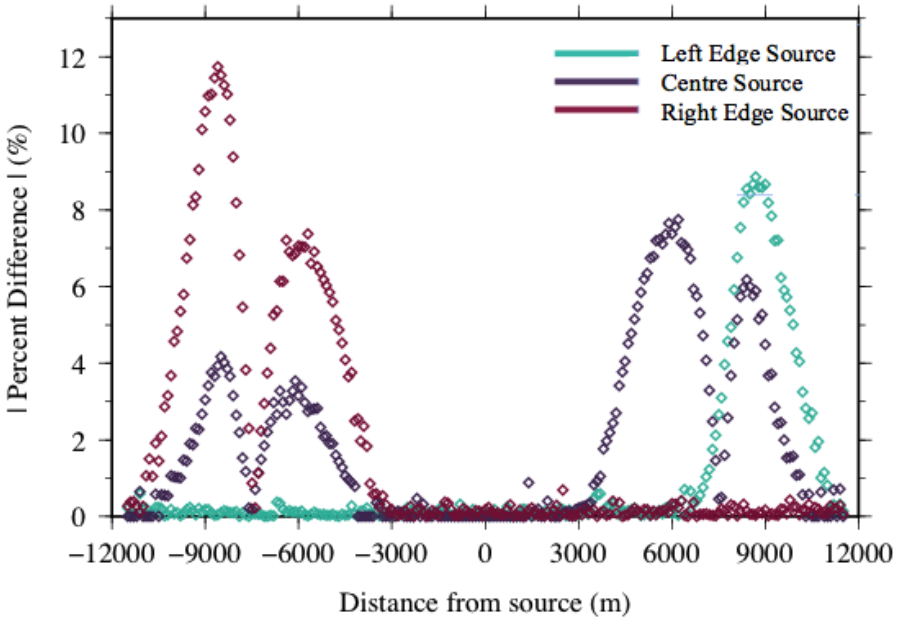

(b)

Figure 4.73: Panel (a) absolute differences in the electric field amplitudes for *Model 3* and the *Dry Reservoir*; panel (b) percent differences in the electric field amplitudes. Each percent difference has been normalized by the results for the dry reservoir of each source.

4.6.3 Models 4 and 5

Models 4 (Figure 4.51) and *5* (Figure 4.52) represent a single fault block structure as in *Model 1*, but the hydrocarbon-saturated sand package is removed by the *Base Tertiary* unconformity from the Jurassic footwall. As a consequence, results give excellent insight into the issue of reservoir detection with offset, as changes between hydrocarbon-saturated and dry reservoirs originate from a single region. This is of particular interest in the source configuration assessment, as it can optimally define the ideal source position — i.e. whether near or far offset — relative to a target reservoir. The results for *Model 4* are shown in Figures 4.74 to 4.77, and those for *Model 5* are shown in Figures 4.78 to 4.81.

Since the sand package in *Model 4* extends from x = -7500 to 1800 m, the *Left Edge Source* and *Centre Source* configurations represent source positions close to each end of the package. As a result, both show similarly high magnitude peaks at $\sim$ -9000 m offset at 1250% for the *Centre Source* response and $\sim$ 9000 m offset at 2115% for the *Left Edge Source* response (see Figure 4.77). The position of offset is due to the position of the reservoir with respect to the source, and the large magnitude of difference is due to the large lateral extent ($\sim$9300 m in the x-direction) and shallowness ($\sim$3000 m depth) of the highly resistive reservoir, generating a large electric field amplitude response. The *Right Edge Source* is positioned 5700 m to the right of the right-most edge of the reservoir, and therefore detectability is significantly decreased, shown with a 27% peak at $\sim$ -8500 m offset. Though this magnitude is significantly less than the results for the *Left Edge Source* and *Centre Source*, it is still above the standard threshold of detection for this study.

The magnitude of the peaks of percent difference for *Model 5* (see Figure 4.81) are

significantly decreased in magnitude due to the increased depth (∼4750 m) and narrower lateral extent of the reservoir (from x = -6400 to -50 m): the *Left Edge Source* has a peak magnitude of 55% at ∼7500 m offset, while the *Centre Source* has a peak magnitude of 75% at ∼ -9000 m offset. These values are well above the magnitude of detection. These differences are seen between ∼ -12000 to -5000 m offset for the *Centre Source* and *Left Edge Source* between ∼ 3000 to 12000 m offset. The right-most peak of ∼ 10000 m offset for the *Left Edge Source* is due to a negative percent difference once detection of the neighbouring Jurassic (0.6 S/m) region is detected. The *Right Edge Source* is incapable of producing any detectable changes in the reservoir, reflected in minute deviations from zero percent difference. This is expected given the great offset between the source and reservoir for this configuration.

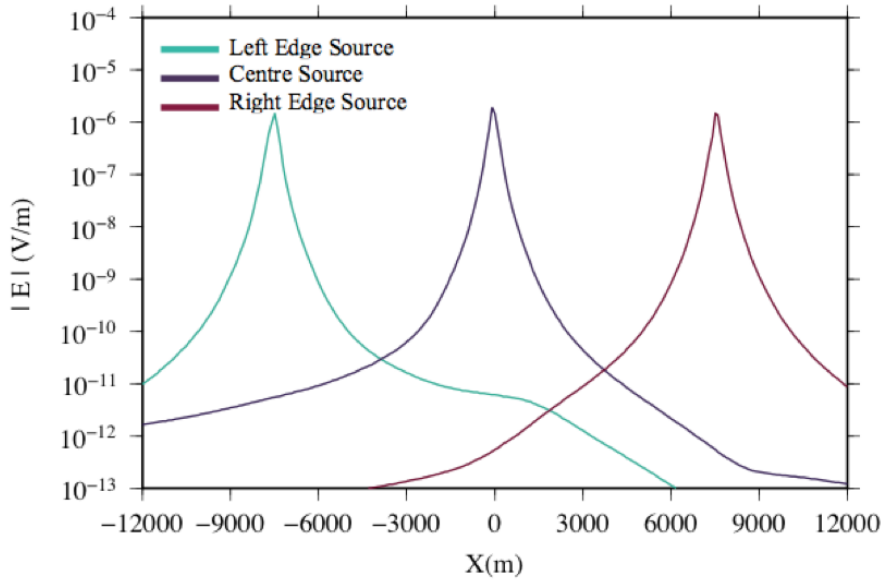

(a)

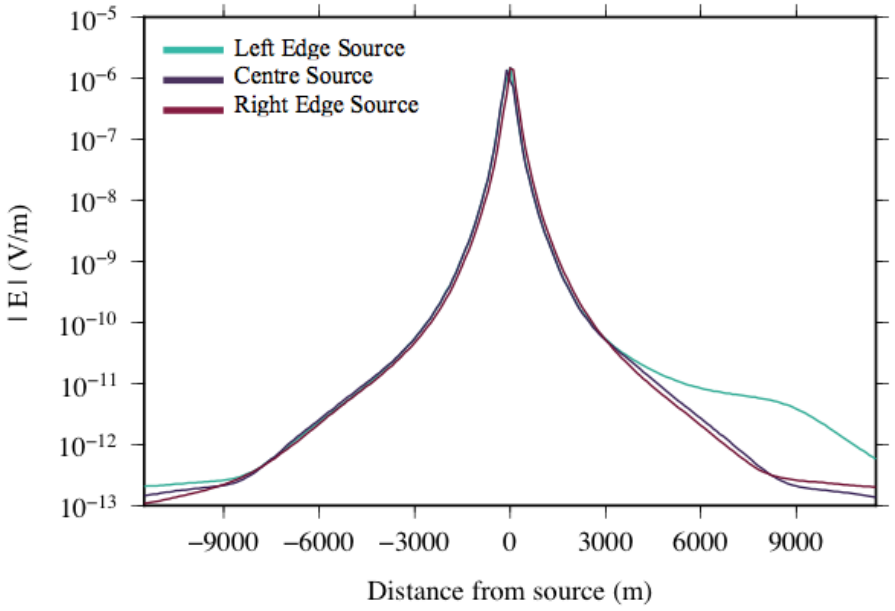

(b)

Figure 4.74: Panel (a) electric field amplitude results for *Model 4* with source positions from x = -7600 to -7500 m (*Left Edge Source*), -100 to 0 m (*Centre Source*), and 7500 to 7600 m (*Right Edge Source*); panel (b) electric field amplitudes plotted as a function of offset from source.

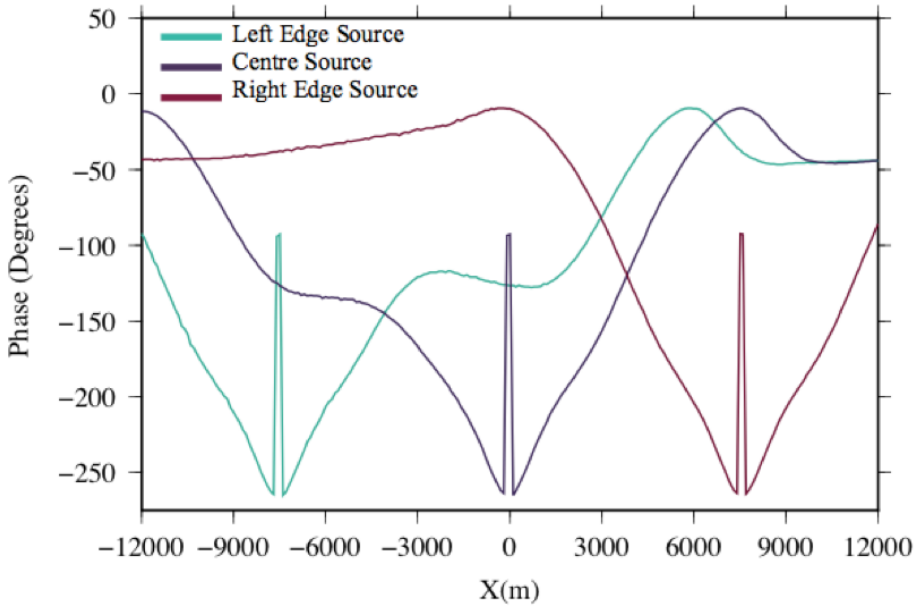

(a)

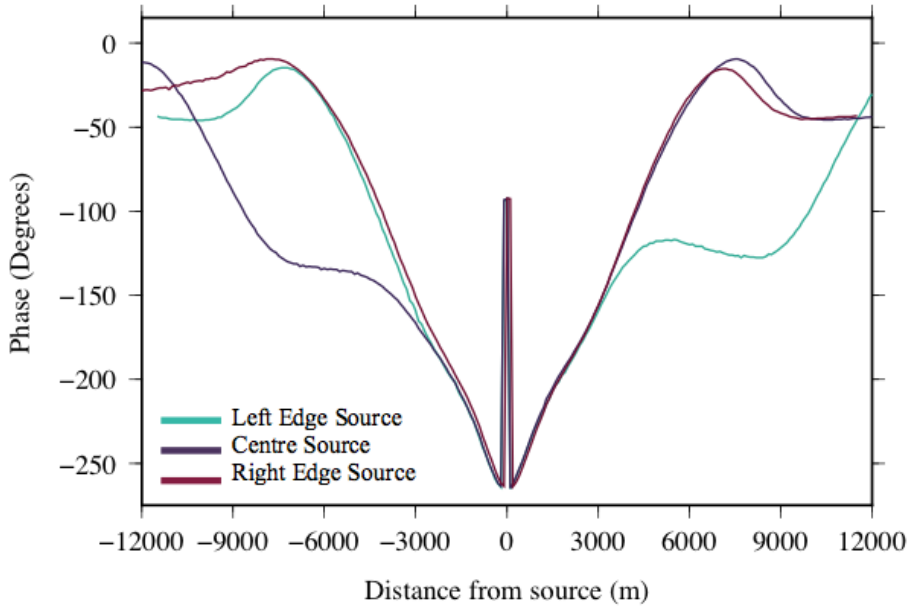

(b)

Figure 4.75: Panel (a) phase results for *Model 4* with source positions from x = -7600 to -7500 m (*Left Edge Source*), -100 to 0 m (*Centre Source*), and 7500 to 7600 m (*Right Edge Source*); panel (b) phase results plotted as a function of offset from source.

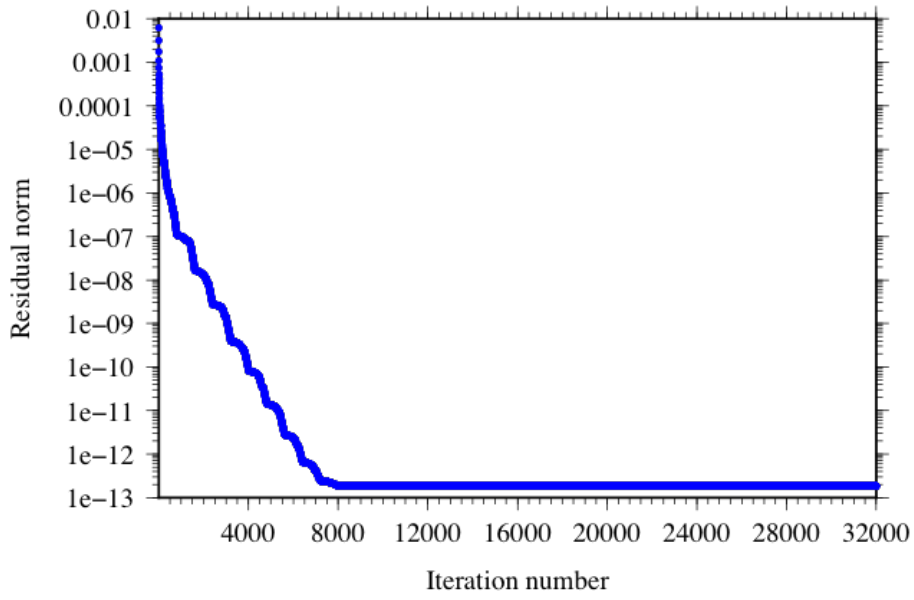

(a)

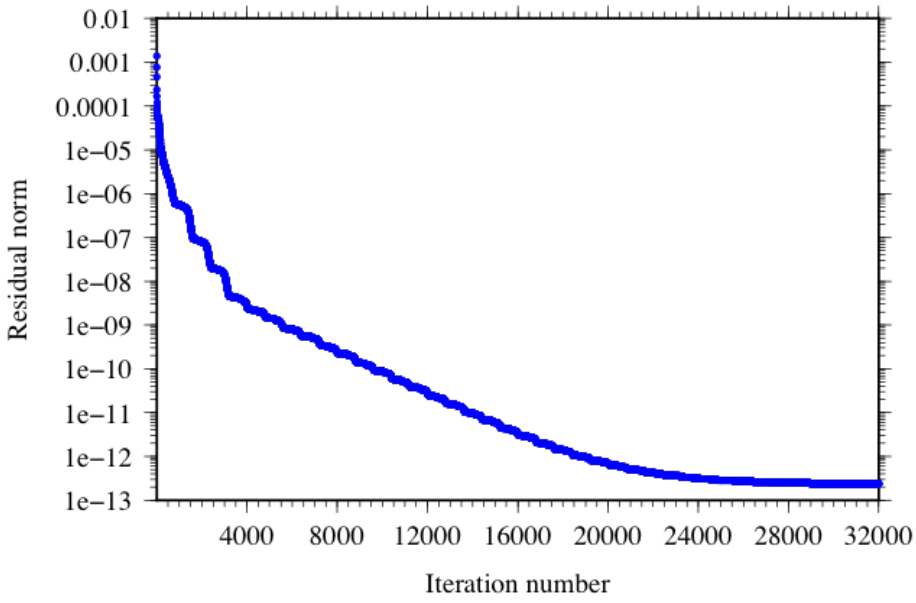

(b)

Figure 4.76: Convergence curves for *Model 4*. Panel (a) *Left Edge Source*; panel (b) *Right Edge Source*.

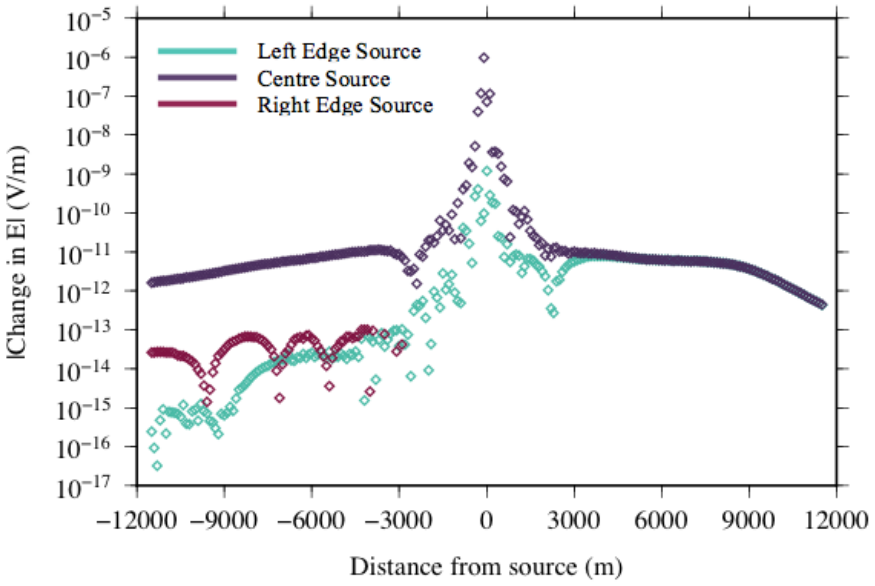

(a)

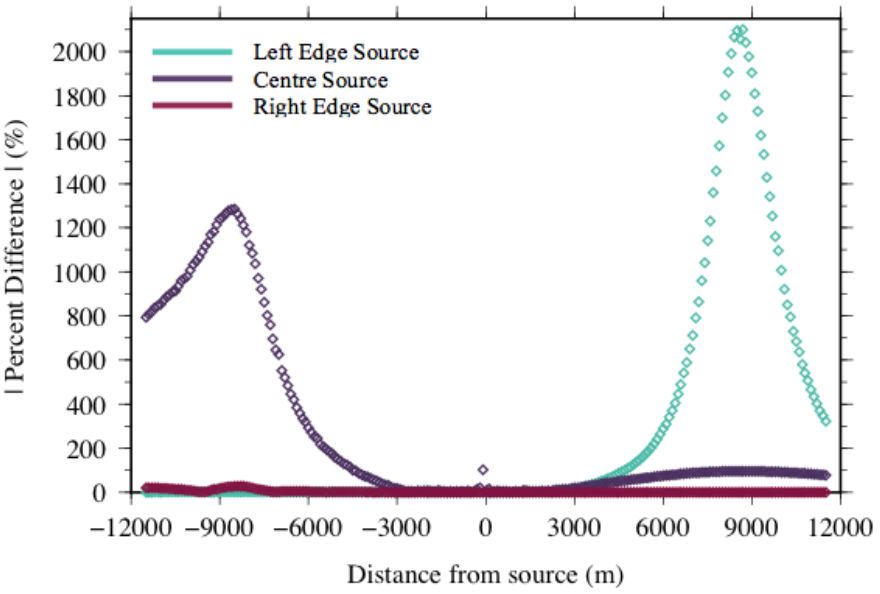

(b)

Figure 4.77: Panel (a) absolute differences in the electric field amplitude results for *Model 4* and the *Dry Reservoir*; panel (b) corresponding percent differences in the electric field amplitudes. Each percent difference has been normalized by the results of the dry reservoir for the same source location.

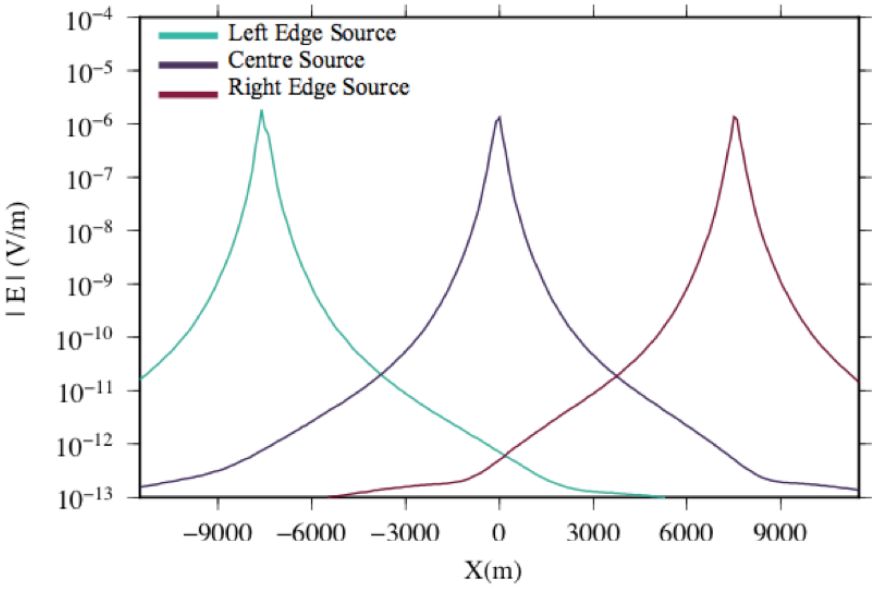

(a)

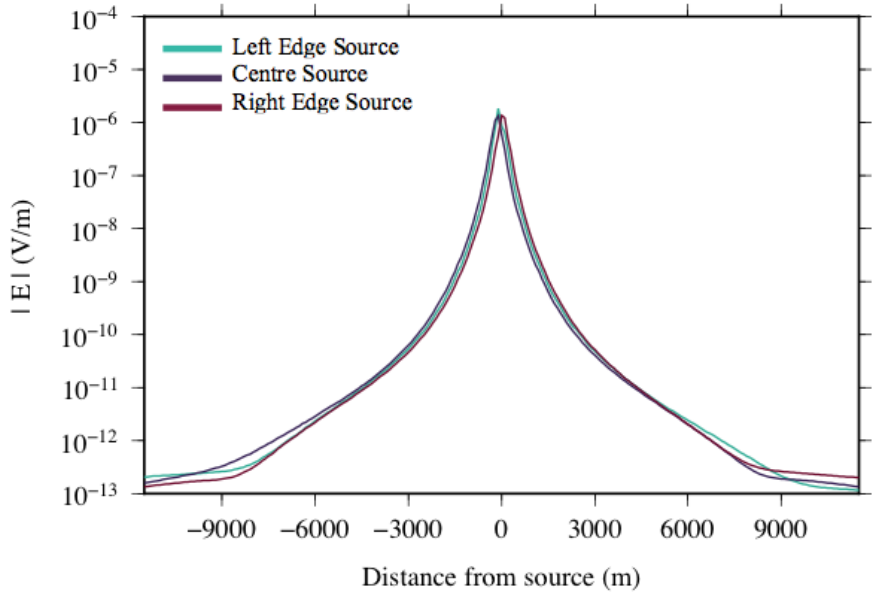

(b)

Figure 4.78: Panel (a) electric field amplitude results for *Model 5* with source positions from x = -7600 to -7500 m (*Left Edge Source*), -100 to 0 m (*Centre Source*), and 7500 to 7600 m (*Right Edge Source*); panel (b) electric field amplitude results plotted as a function of offset from source.

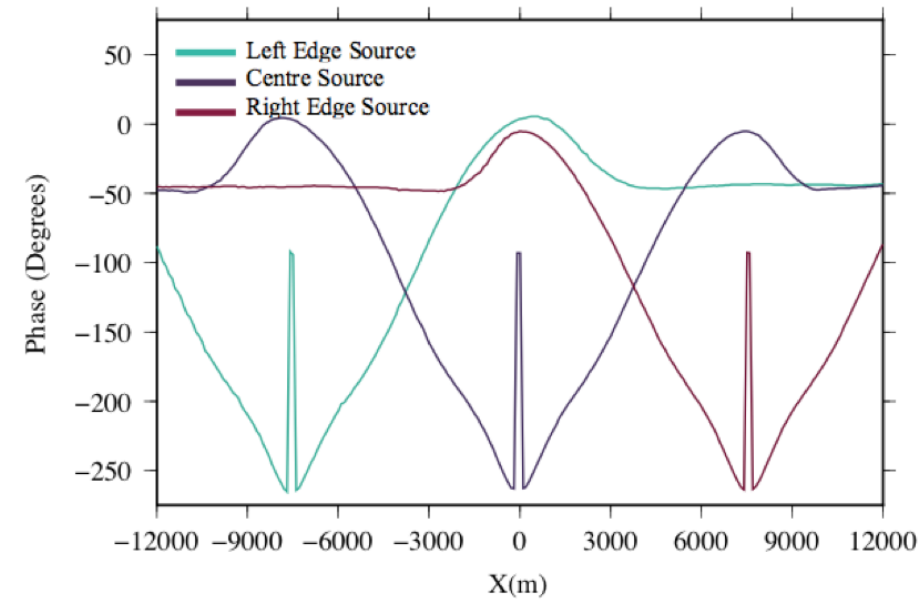

(a)

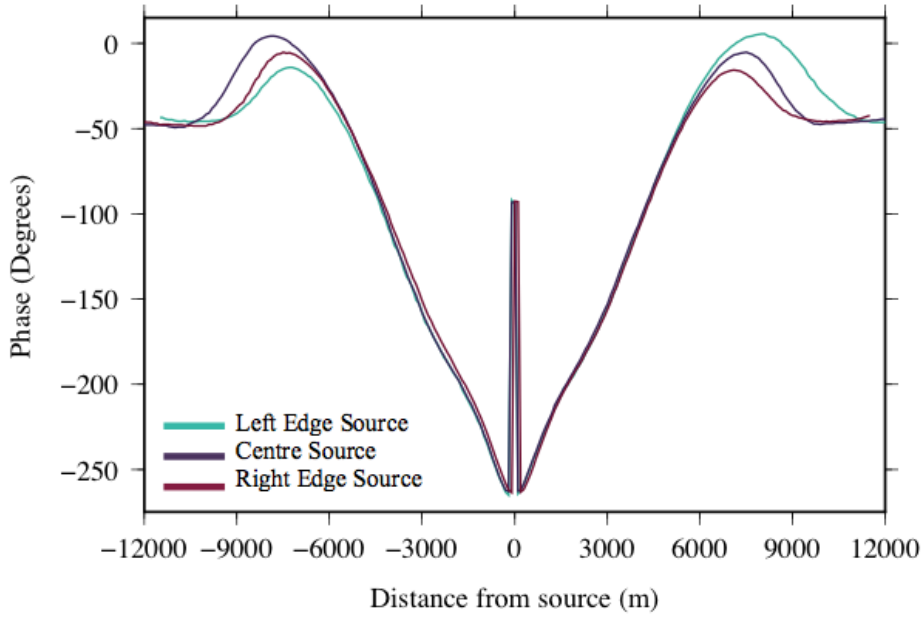

(b)

Figure 4.79: Panel (a) phase results for *Model 5* with source positions from x = -7600 to -7500 m (*Left Edge Source*), -100 to 0 m (*Centre Source*), and 7500 to 7600 m (*Right Edge Source*); panel (b) corresponding phase results plotted as a function of offset from source.

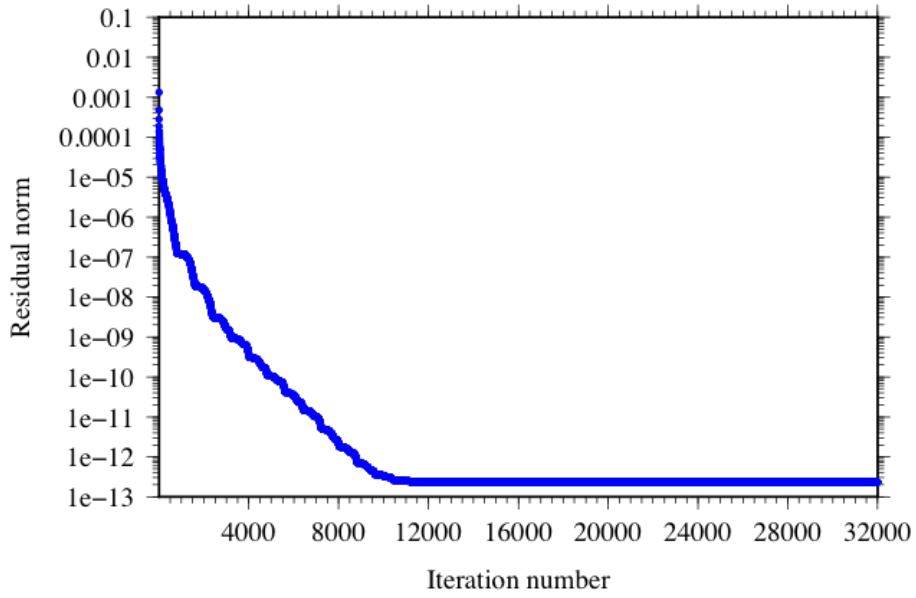

(a)

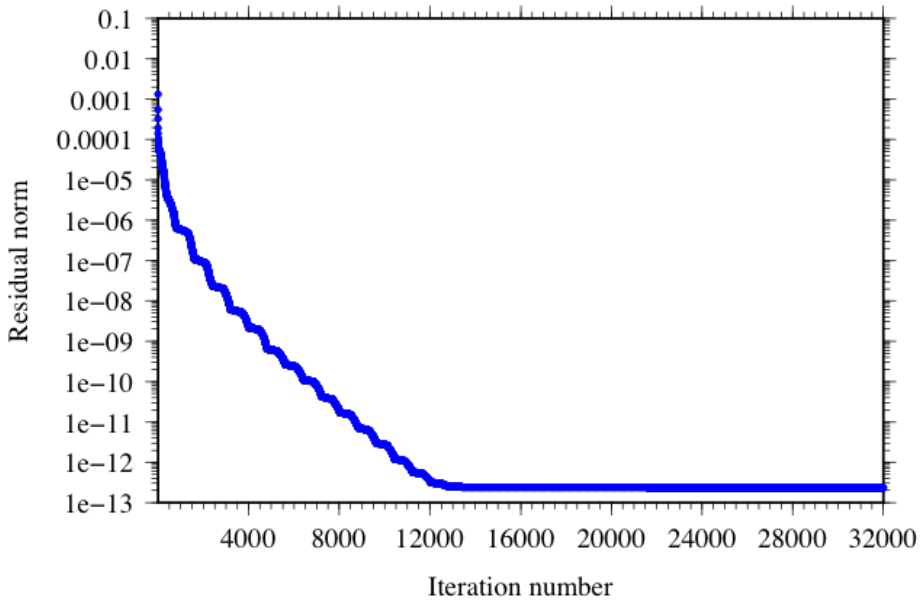

(b)

Figure 4.80: Convergence curves for the *Model 5*. Panel (a) *Left Edge Source*; panel (b) *Right Edge Source*.

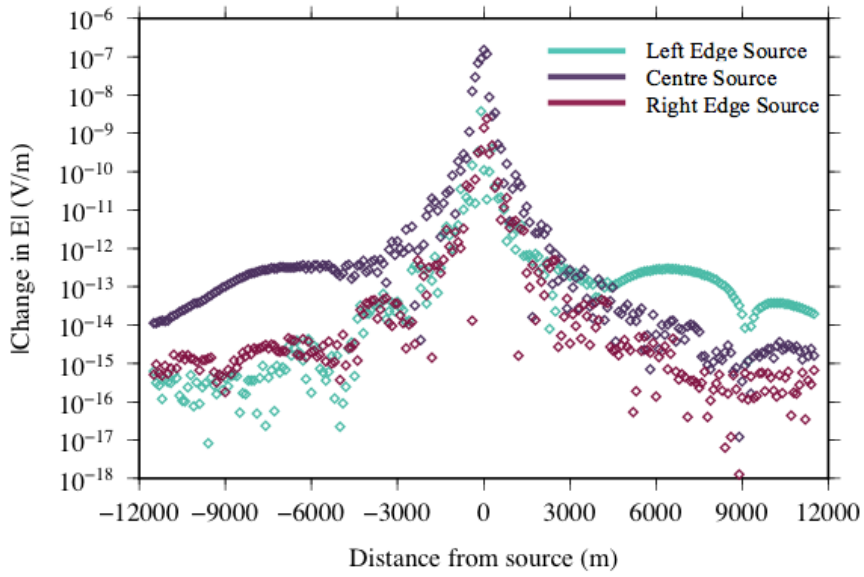

(a)

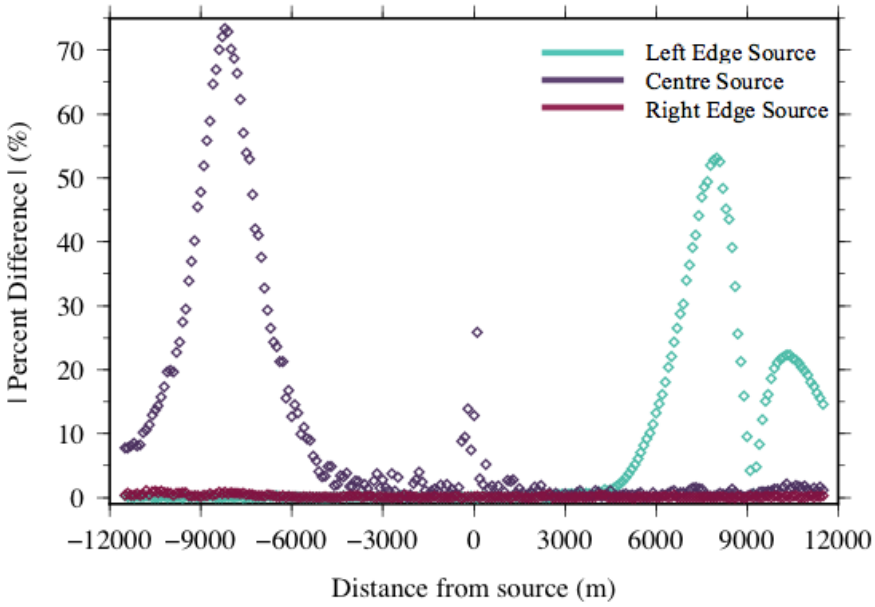

(b)

Figure 4.81: Panel (a) absolute differences in the electric field amplitude results for *Model 5* and the *Dry Reservoir*; panel (b) corresponding percent differences in the electric field amplitudes. Each percent difference has been normalized by the results of the dry reservoir for the same source location.

4.7 Oil Water Contact Models

Previous models based their reservoir resistivities on 100% hydrocarbon saturation. Although the change of quality parameters (e.g. 0.25 S/m for the *Poor Reservoir* versus 0.001 S/m for the highest saturation case) can account for heterogeneous or uncertain reservoir saturation estimates, the nature of the densities of water and hydrocarbons create sharp oil-water contacts (OWC) in marine environments. As the hydrocarbon ($\rho_{HC} \approx 800$ kg/m^3) has a much lower density than water ($\rho_w \approx 1000$ kg/m^3), it is typically stratified to the upper portion of the reservoir volume (Dennis et al., 2005).

Two configurations were considered for each of the models: *Case 1* had water saturation, with a conductivity of 1.5 S/m, for approximately one-third of the reservoir and hydrocarbon saturation, with a conductivity of 0.01 S/m, in the remaining two thirds; *Case 2* assesses the reverse case, with one-third hydrocarbon saturation and two-thirds hydrocarbon saturation. These segments were generated by adding subvertical facets using FacetModeller in appropriate locations for each of the OWCs. Several subhorizontal configurations were explored (e.g. Figure 4.82), but generated poor cells at the small-angle contact region. This produced poor results that were subsequently omitted. Subvertical OWCs in the models assisted in giving a better representation of a percent volume saturation estimate, which is a detectable measure in offshore exploration (Salathiel, 1973). The resolution of the CSEM method would create a negligible difference in a real-world scenario between the results of the more modellable subvertical OWCs and the more geologically accurate subhorizontal OWCs. Mesh statistics for each of the oil-water contact models are listed in Table 4.6.

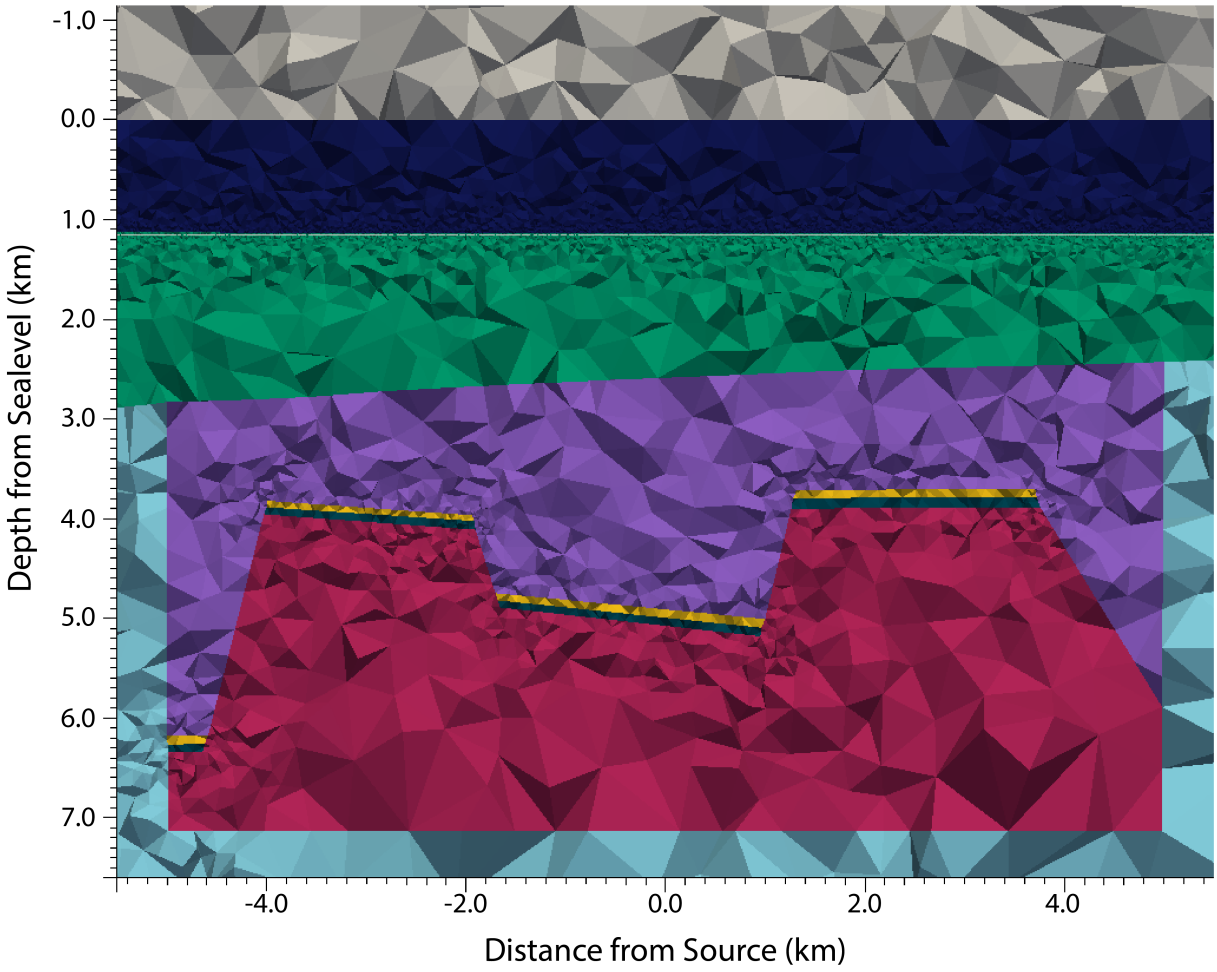

Figure 4.82: Sample enhanced view cross-section centered at $y = 0$ of a subhorizontal oil-water contact model for *Model 3*. This model configuration was omitted in further results. Water-filled pore space is indicated by steel blue, while hydrocarbon-filled pore space is indicated in yellow.

Model Number	Cells	Nodes	Edges
Model 1	1,313,366	214,253	19,431
Model 2	1,426,508	232,550	21,555
Model 3	1,395,236	227,488	20,179
Model 4	1,401,915	228,549	20,492
Model 5	1,374,965	224,139	20,145

Table 4.6: Mesh characteristics for each oil-water contact model.

4.7.1 Model 1

In the oil-water contact geometry used in *Model 1*, two facets were added to each sand package creating y-trending near-vertical planes at $x \approx$ -5000 and -2000 m for the hanging wall package, and $x \approx$ 4400 and 6400 m for the footwall package, dividing each package into three equal regions using the method shown in Figure 4.83. In the high case scenario, *Case 1* (Figure 4.84), the two right-most regions are saturated with hydrocarbons (0.01 S/m) while the left-most region is water saturated (1.5 S/m); in the low case scenario, *Case 2* (Figure 4.85), the two left-most regions are water saturated, with the remaining region saturated with hydrocarbons. Every model in this and subsequent sections will follow this workflow of package separation and allotment of pore space saturation.

The results for the two cases for *Model 1* are shown in Figures 4.86 to 4.88. Results are compared to *Model 1*'s electric field and phase responses for the *Dry Reservoir* to determine overall detection and with the *100 Ωm Reservoir* for assessment of the detection decrease associated with added water to the pore space (Figure 4.88). The conductive contribution of the water in the sand package significantly decreases the electric field amplitude (Figure 4.86a): the amplitudes for *Case 1* are typically higher than the *Dry Reservoir* results

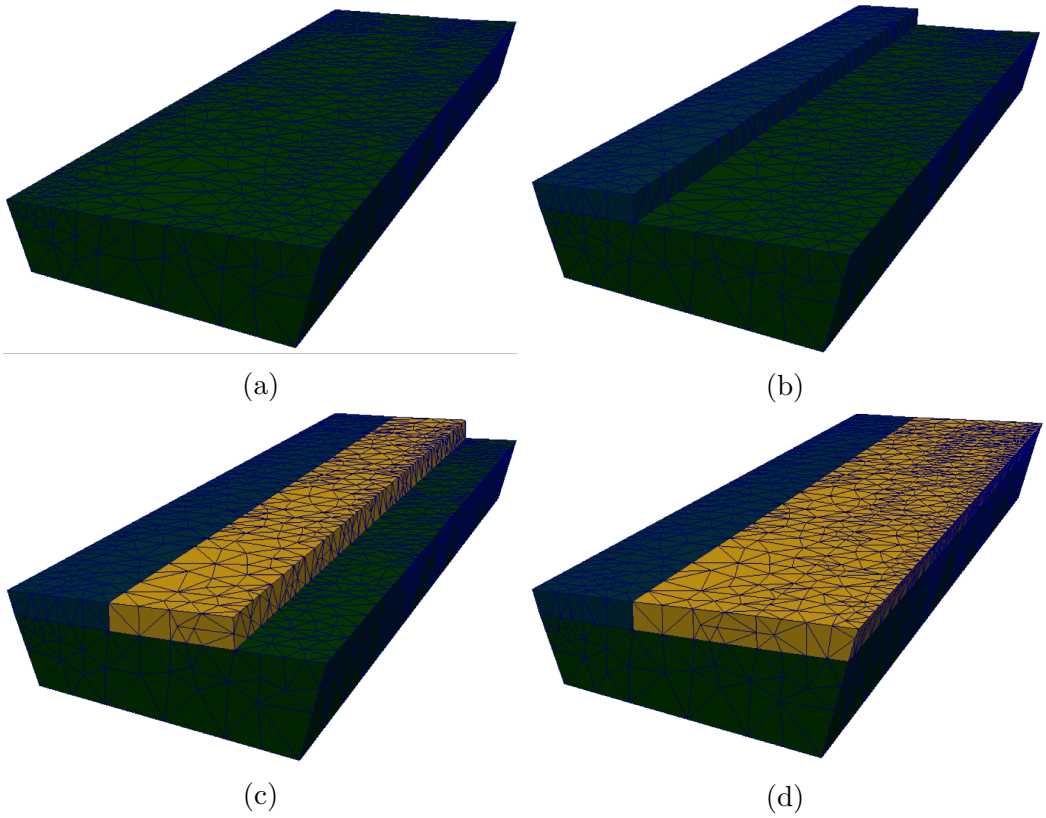

Figure 4.83: Sequence of oil-water contact sectioning of a reservoir comprised of a water-saturated region (blue), a hydrocarbon-saturated region (yellow) and fault block (green).

and lower than the *100 Ωm Reservoir* results; the results for *Case 2* almost completely parallel those for the *Dry Reservoir*, suggesting poor detectability. The phase information (Figure 4.86b) distinguishes these reservoir parameters from one another, specifically, with the slightly higher phase associated with *Case 2* results compared to the *Dry Reservoir* between ∼-8000 to -6000 m offset — a distinction that could not be made in the electric field amplitude results. The contribution of the respective reservoirs to their phase results is defined by the broadness of the side lobes before the air layer levelling off: the more resistive the detected body is, the wider the lobe. This is consistent with results in Chapter

3.

Figure 4.88 displays the difference of each case in comparison to the *Dry Reservoir* (labelled *Case 1* and *Case 2*) and to one another (labelled Δ *(Case 1, Case 2)*). The smooth curves in the absolute difference results between $\sim$ -9000 to -3000 m offsets and peak results at $\sim$ 7000 m ($\sim$60% difference) show detectability of the hanging wall reservoir of *Case 1*. The peaks at $\sim$ -9500 and 9000 m represent the negative difference between *Case 1* and the *Dry Reservoir*, as *Case 1* has a larger resistivity contrast with the basement at the edge of the reservoir. The reservoir in the footwall is detected by a peak at $\sim$ 7000 m, but likely falls below the threshold of detection at 8% difference. The reservoirs in *Case 2* are very poorly detected, as all results fall below the threshold for detection. This is supported by the high magnitude difference between *Case 1* and *Case 2* at the reservoir detection offsets.

In Figure 4.89, the results of each oil-water contact case are compared to the *100* Ωm *Reservoir*, where percentage values are representative of the percent amplitude decrease between the fully hydrocarbon saturated sand package and each case. As anticipated, *Case 1* has a lower magnitude of percent difference than *Case 2* at negative offsets — for example, 55% versus 63% for detection of the hanging wall reservoir — as it contains a higher hydrocarbon saturation value.

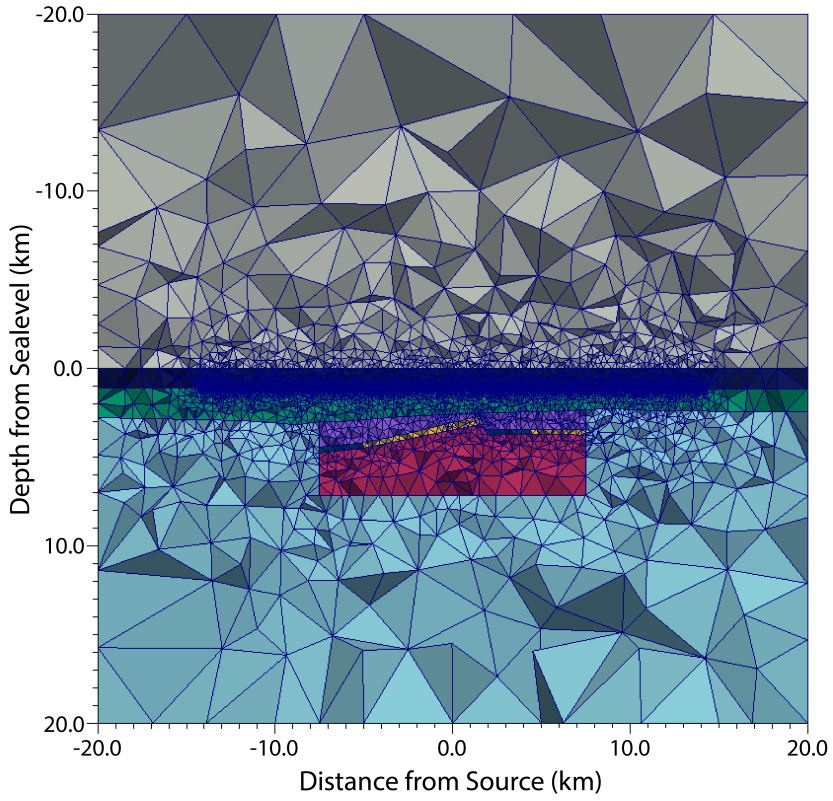

(a)

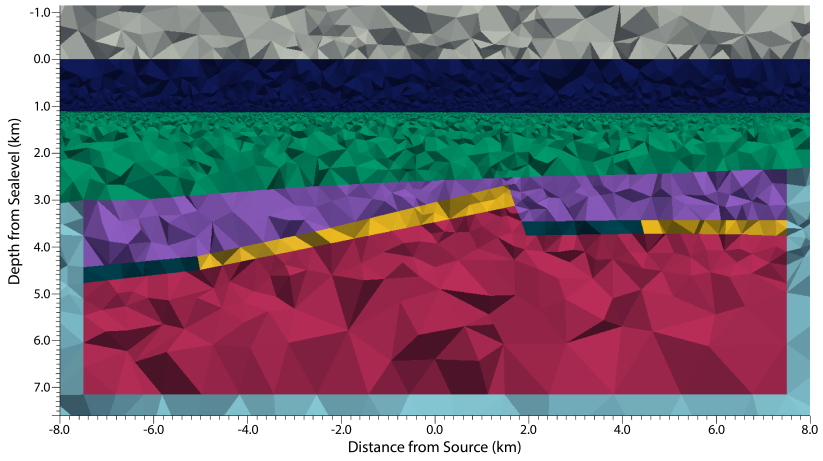

(b)

Figure 4.84: Cross-sections centered at $y = 0$ m of *Case 1* of an oil-water contact model for *Model 1*. Panel (a) full view; panel (b) enhanced view of the reservoir geometry. Water-filled pore space is indicated by steel blue, while hydrocarbon-filled pore space is indicated in yellow.

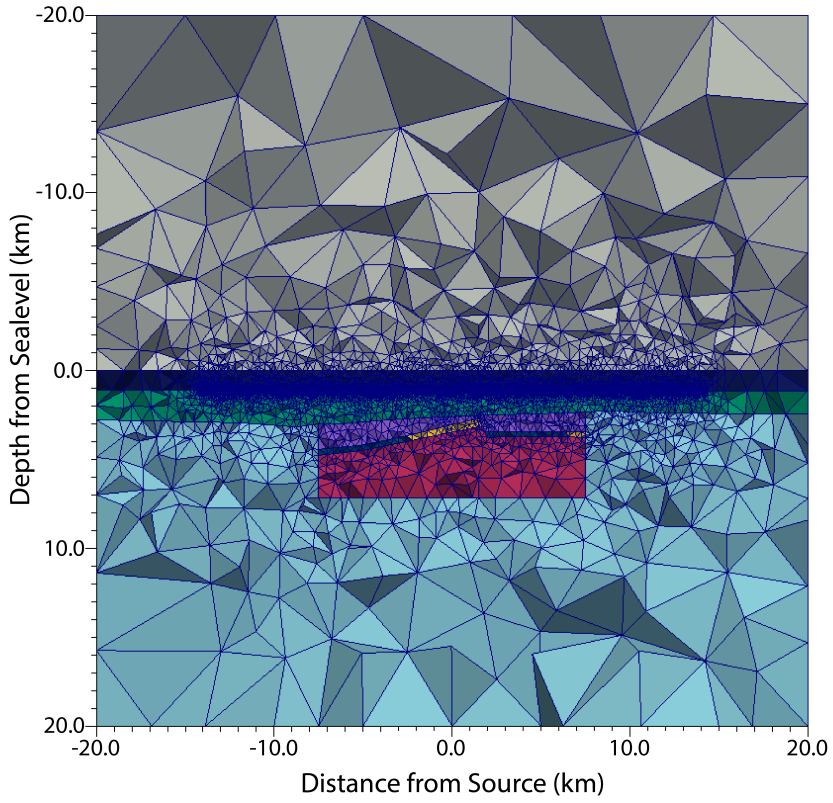

(a)

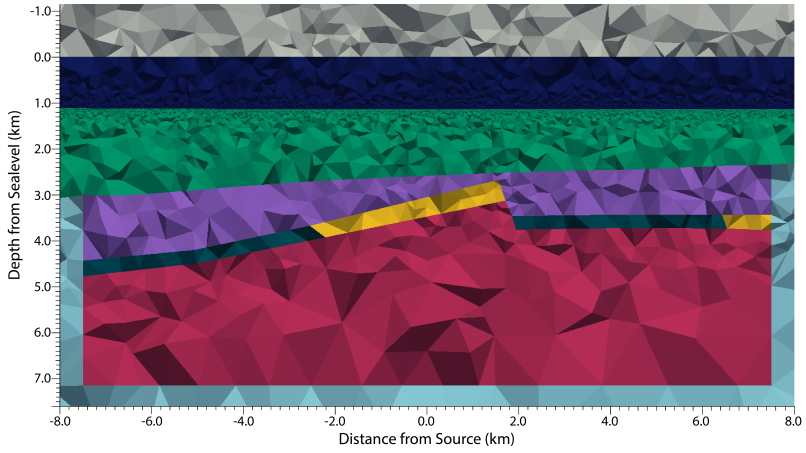

(b)

Figure 4.85: Cross-sections centered at $y = 0$ m of *Case 2* of an oil-water contact model for *Model 1*. Panel (a) full view; panel (b) enhanced view of the reservoir geometry. Water-filled pore space is indicated by steel blue, while hydrocarbon-filled pore space is indicated in yellow.

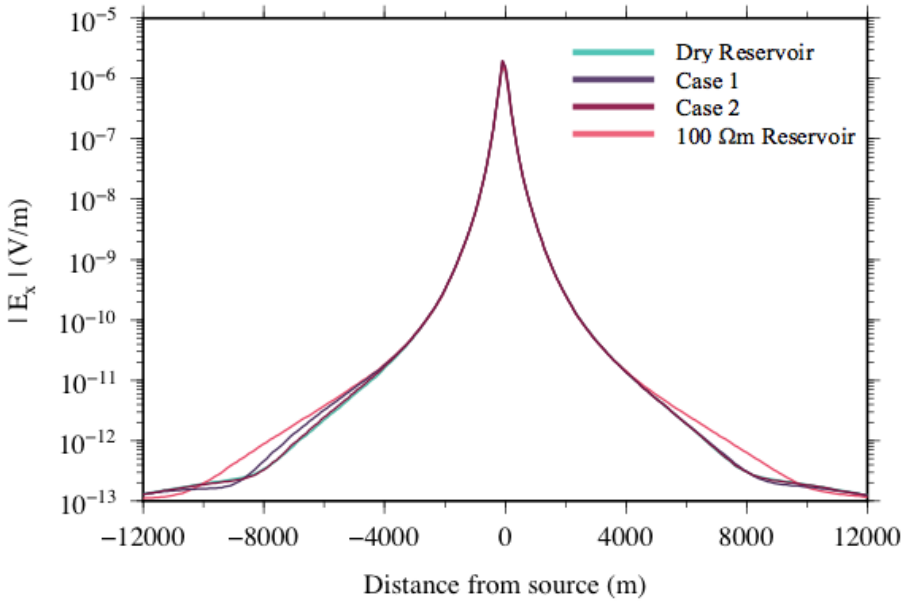

(a)

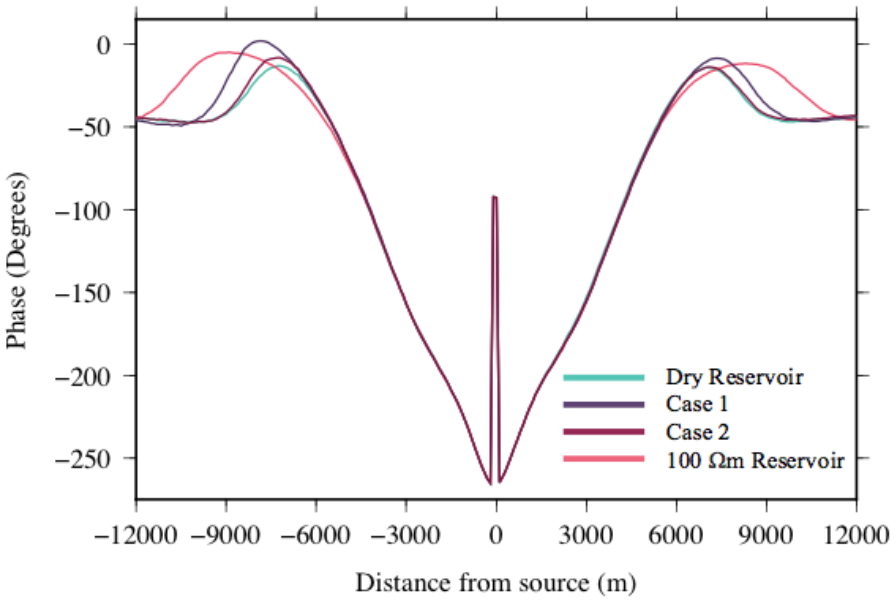

(b)

Figure 4.86: Forward modelling results for *Model 1, Case 1* and for *Model 1, Case 2*. Panel (a) electric field amplitude; panel (b) phase.

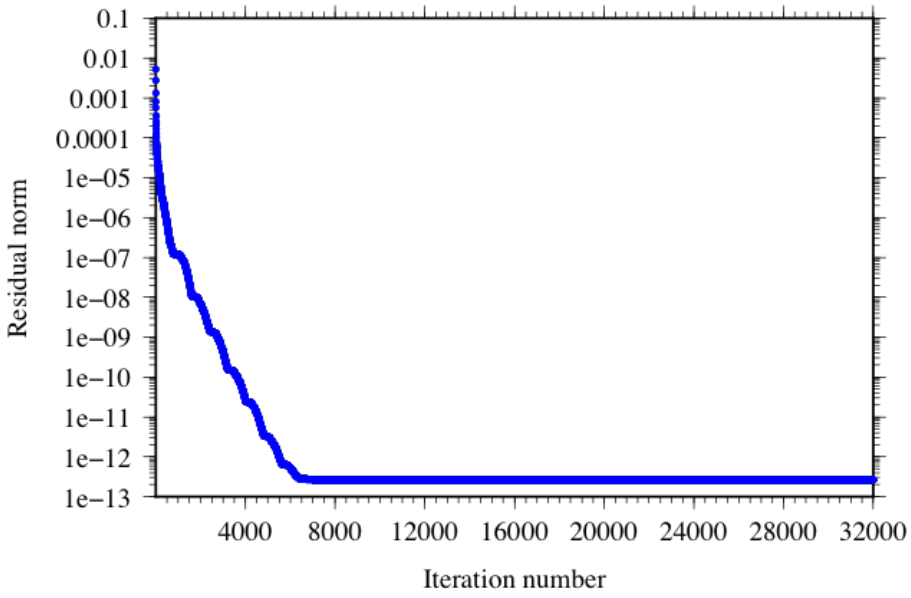

(a)

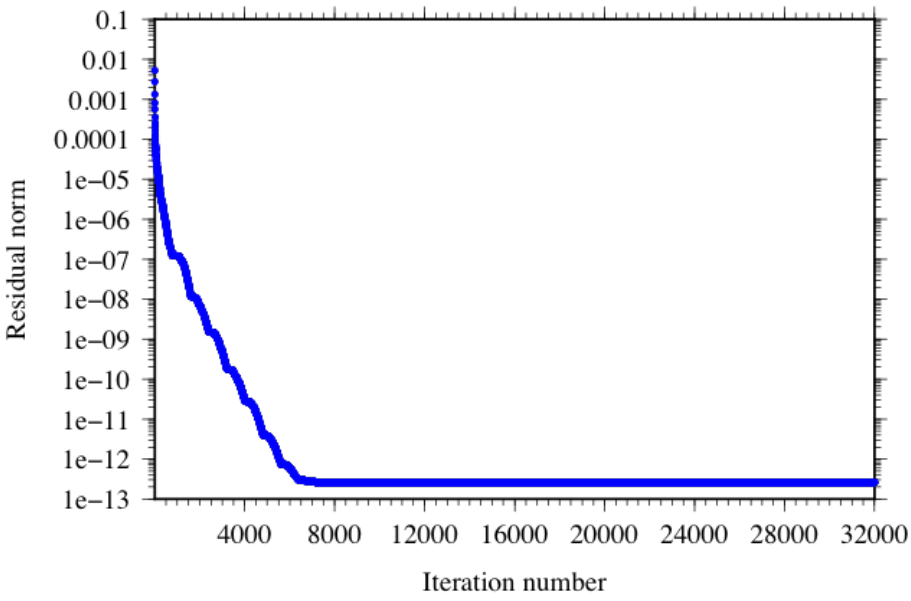

(b)

Figure 4.87: Convergence curves of each of the *Model 1* oil-water contact models. Panel (a) *Case 1*; panel (b) *Case 2*.

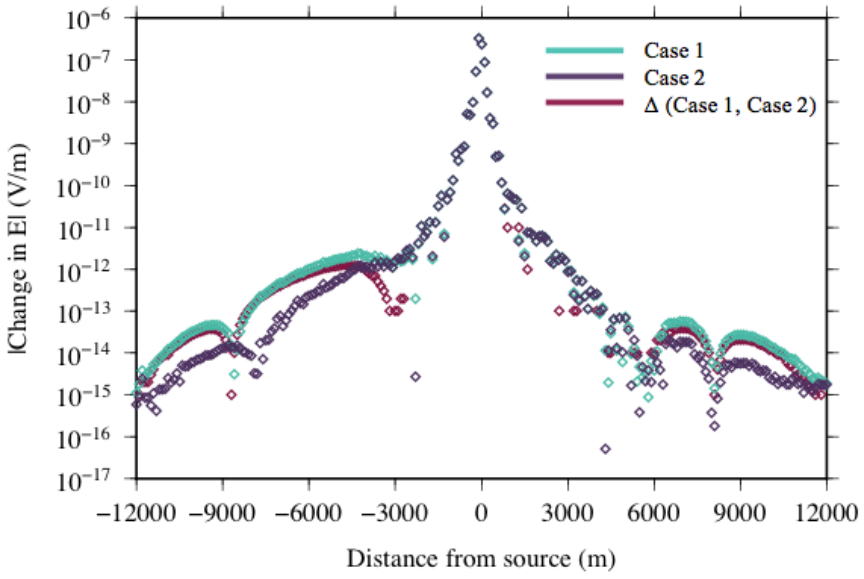

(a)

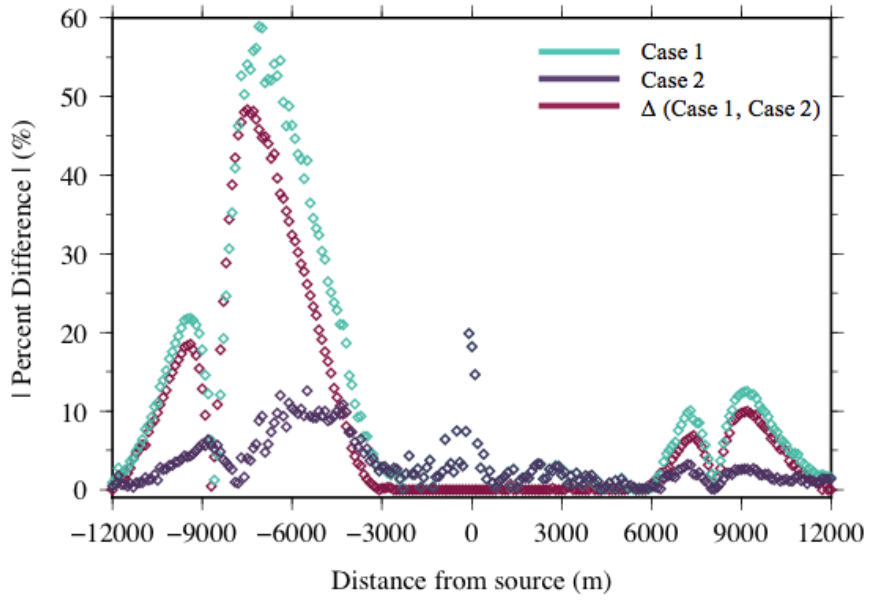

(b)

Figure 4.88: Differences in the electric field amplitude results for *Model 1, Case 1* and *Model 1, Case 2* and those for the *Dry Reservoir* (Figure 4.27). Panel (a) absolute differences; panel (b) percent differences normalized by the results of the dry reservoir for *Cases 1* and *2*, and by the results of *Case 2* for Δ*(Case 1, Case 2)*.

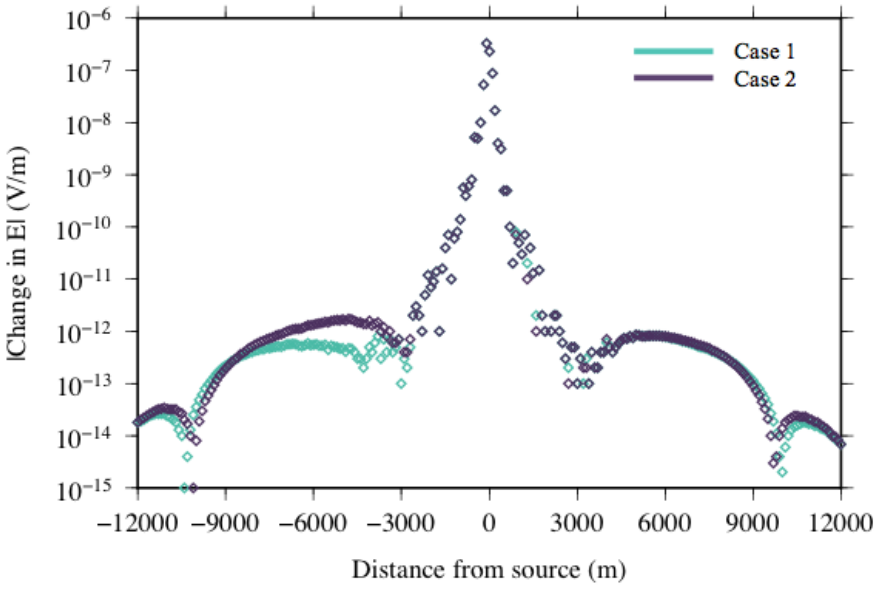

(a)

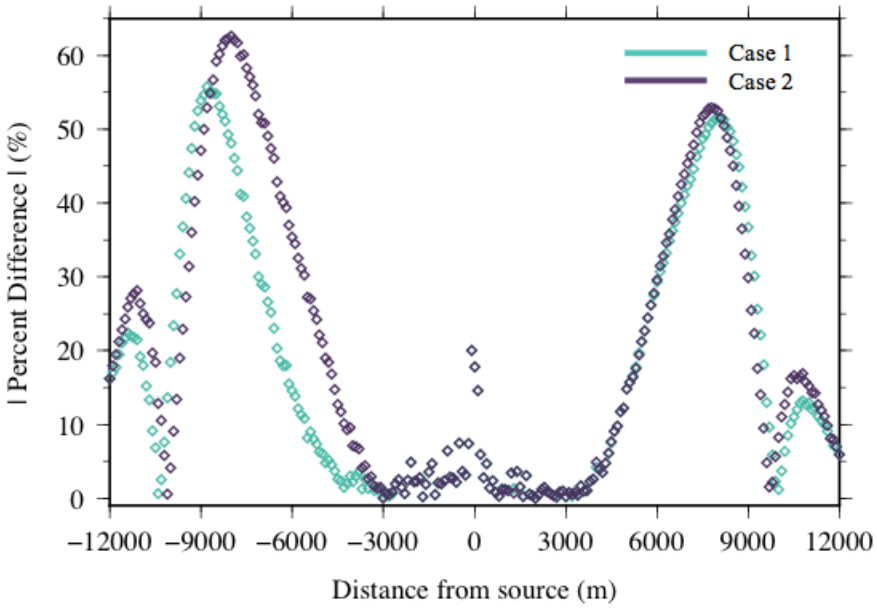

(b)

Figure 4.89: Differences in the electric field amplitude results for *Model 1, Case 1* and *Model 1, Case 2* with those for the *100 Ωm Reservoir* (Figure 4.27) . Panel (a) absolute differences; panel (b) percent differences normalized by the results of the fully saturated reservoir.

4.7.2 Models 2 and 3

The segregation of regions for the oil-water contact models for *Models 2* and *3* is shown in Figures 4.90 to 4.93, and followed the method described in Section 4.7.1. The results are shown in Figures 4.94 to 4.102. Detection of all reservoirs in these models is significantly less than in *Model 1*, shown by the minimum deviation of amplitudes and phases for those from the lowest resistivity (*Dry Reservoir*): the only visual difference in the results is for positive offsets in *Model 2* and the response of the shallowest package (*Package 4*; Table 4.3; Figure 4.94). As expected, the high case (*Case 1*) generates a higher amplitude result than the low case (*Case 2*) between $\sim$ 3000 and 8500 m offset. The difference is more obvious in the phase results (Figure 4.95), with slightly greater digression from the highest and lowest cases in the same region of offset. There is no visual distinction of the electric field amplitude results of *Model 3*, but there is a slight detection at the peak phase value at $\sim$7000 m offset (Figure 4.99b).

For *Model 2*, only *Case 1* exceeds the threshold of detection for the shallowest sand package (*Package 4*), having a peak difference value of 17% (Figure 4.97) — considerably less than the 37% peak of the fully-saturated model (Figure 4.40). The difference between *Case 1* and *Case 2* peaks at the same offsets for reservoir detection for the fully-saturated model. The lower case (*Case 2*) is nearly completely undetectable, with all values falling below the threshold of detection, and only peaking at 5% for the offsets detecting *Package 4*. This great difference is also apparent in the comparison with the *100 Ωm Reservoir* (Figure 4.98), with maximum percent difference of *Case 2* at 25% and *Case 1* at 15% in the offset detection of *Package 4*.

As in previous examples, the contribution of the reservoirs in *Model 3* are nearly completely masked by the effects of the overburden. While *Package 4* generates a peak at $\sim$ 8000 m offset, it is still below the limits of detection. These results are to be expected, as even the most resistive reservoir tested for this geometry fell below percent detection (*1000 Ωm Reservoir* at 7%; Figure 4.47).

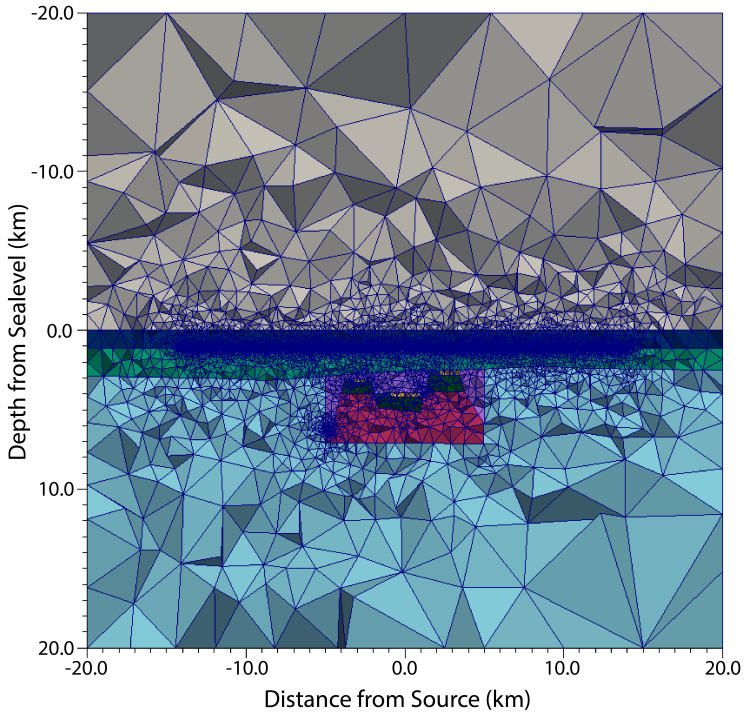

(a)

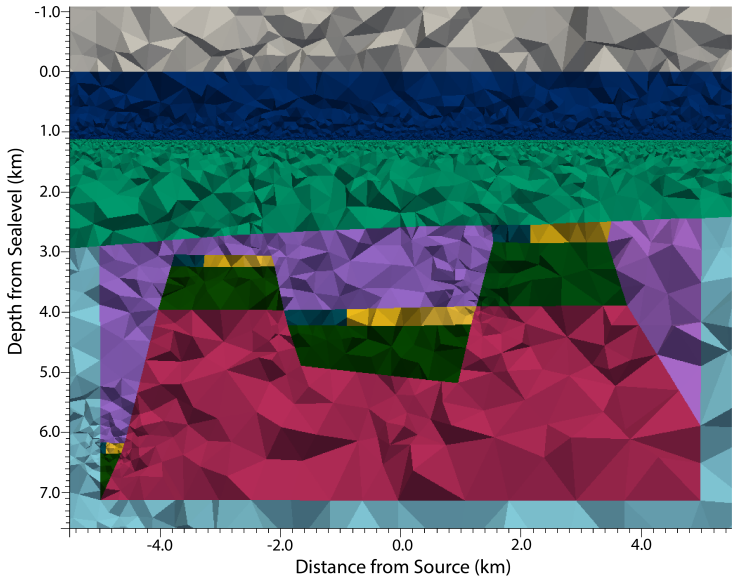

(b)

Figure 4.90: Cross-sections centered at $y = 0$ m of *Case 1* of an oil-water contact model for *Model 2*. Panel (a) full view; panel (b) enhanced view of the reservoir geometry.

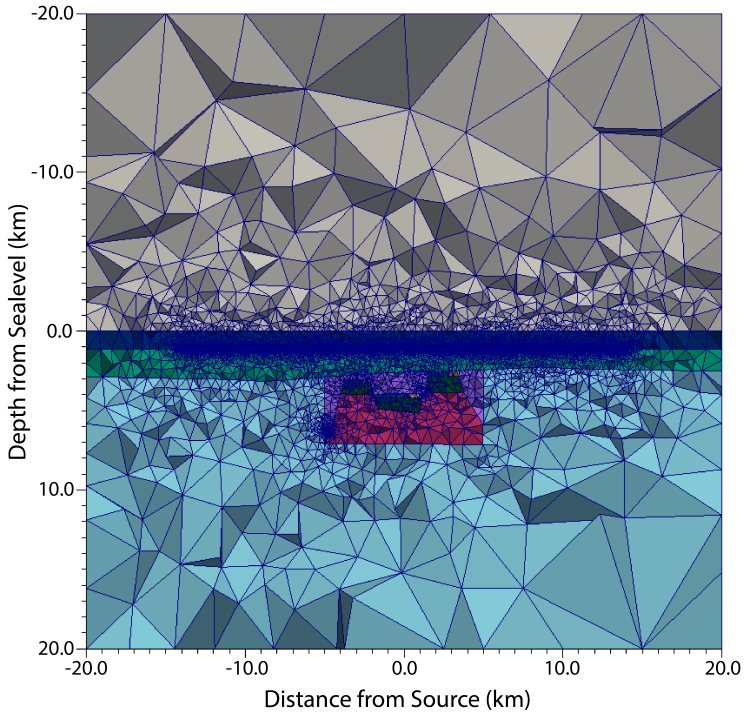

(a)

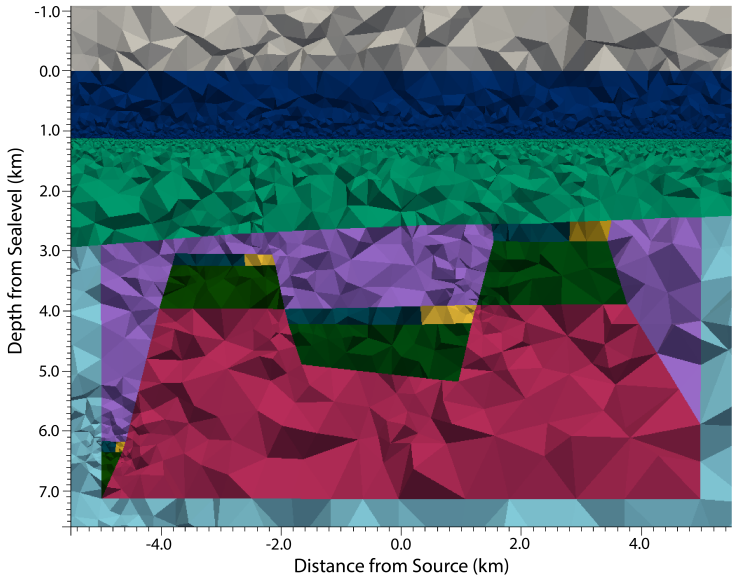

(b)

Figure 4.91: Cross-sections centered at $y = 0$ m of *Case 2* of an oil-water contact model for *Model 2*. Panel (a) full view; panel (b) enhanced view of the reservoir geometry.

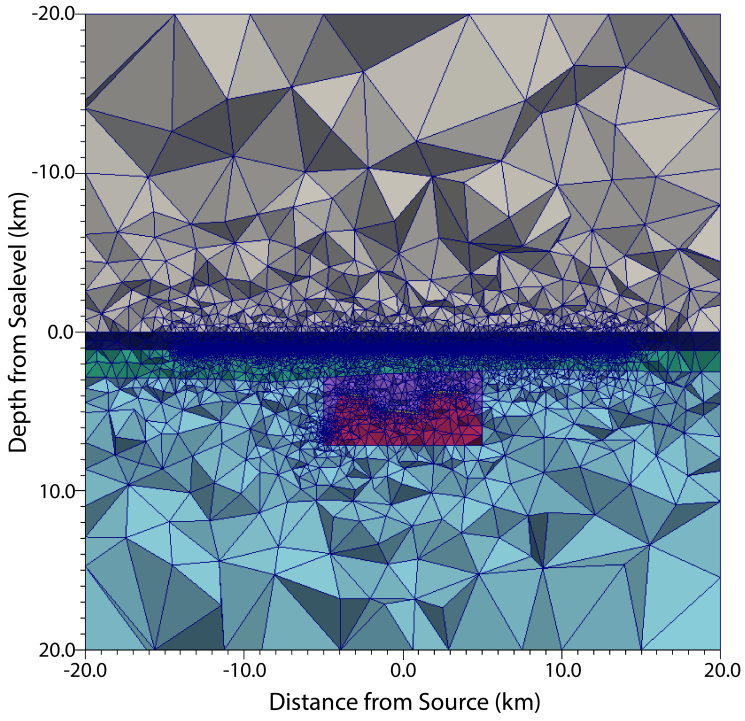

(a)

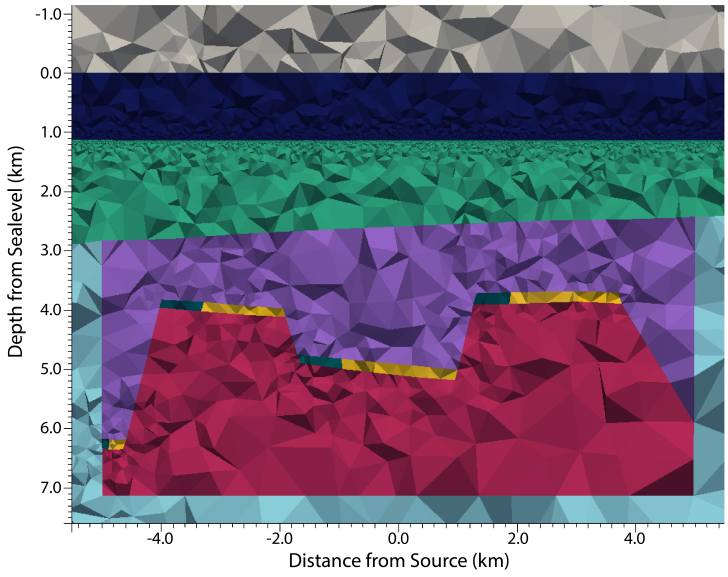

(b)

Figure 4.92: Cross-sections centered at $y = 0$ m of *Case 1* of an oil-water contact model for *Model 3*. Panel (a): full view; panel (b) enhanced view of the reservoir geometry.

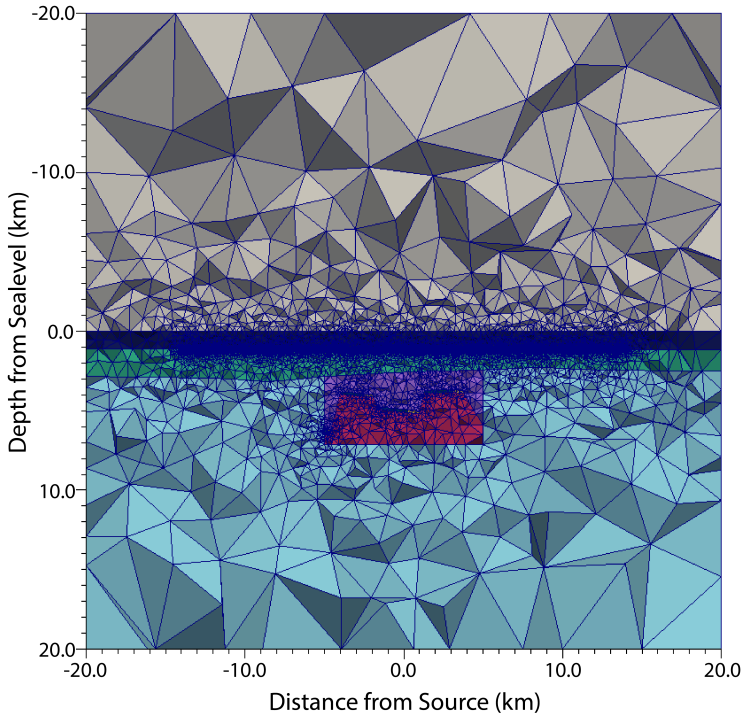

(a)

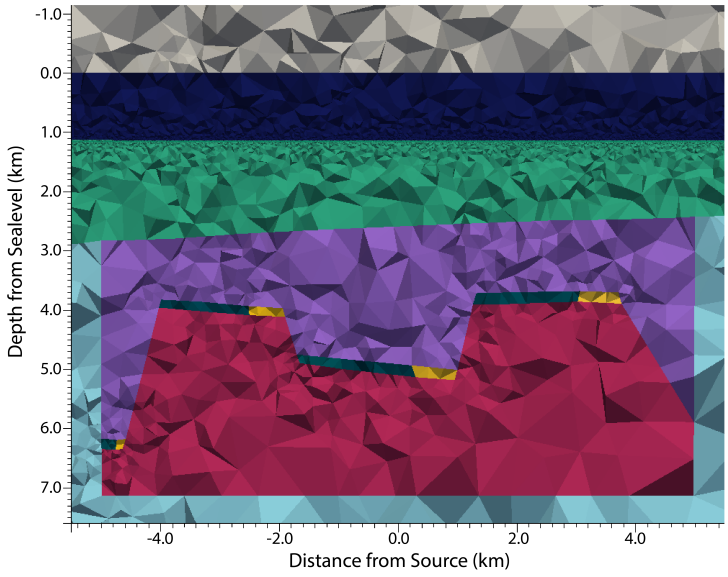

(b)

Figure 4.93: Cross-sections centered at $y = 0$ m of *Case 2* of an oil-water contact model for *Model 3*. Panel (a) full view; panel (b) enhanced view of the reservoir geometry.

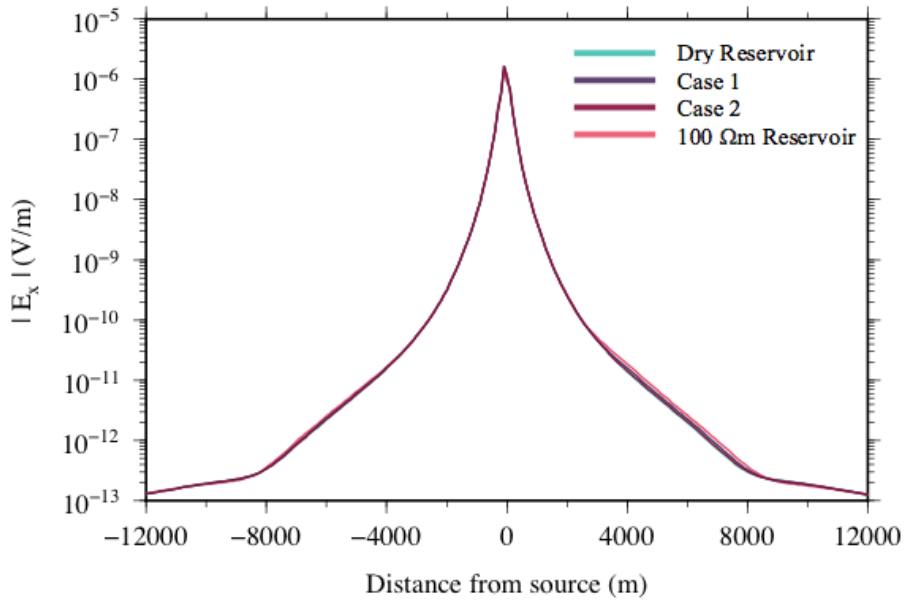

(a)

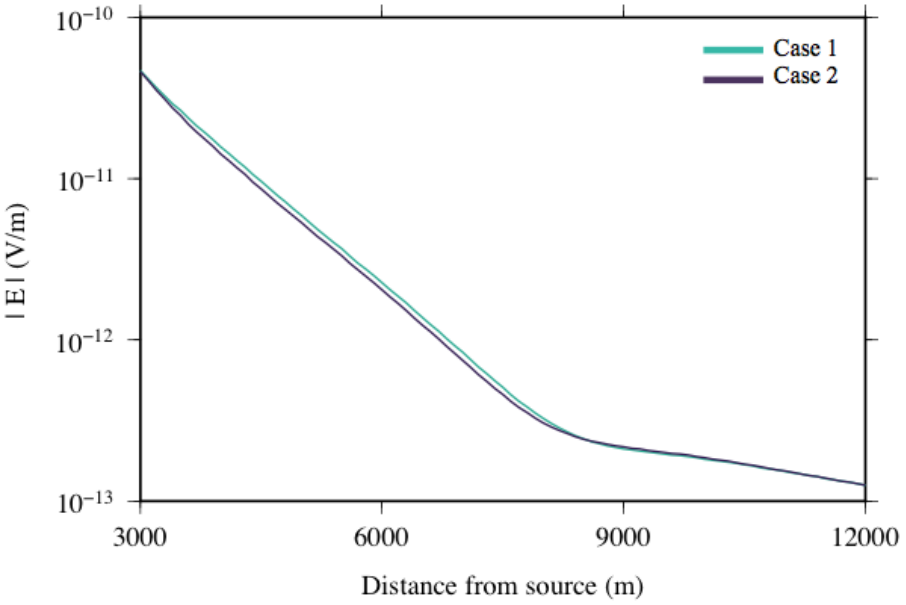

(b)

Figure 4.94: Electric field amplitude results for *Model 2, Case 1* and *Model 2, Case 2*. Panel (a) full offset results; panel (b) enlarged view to enhance amplitude difference.

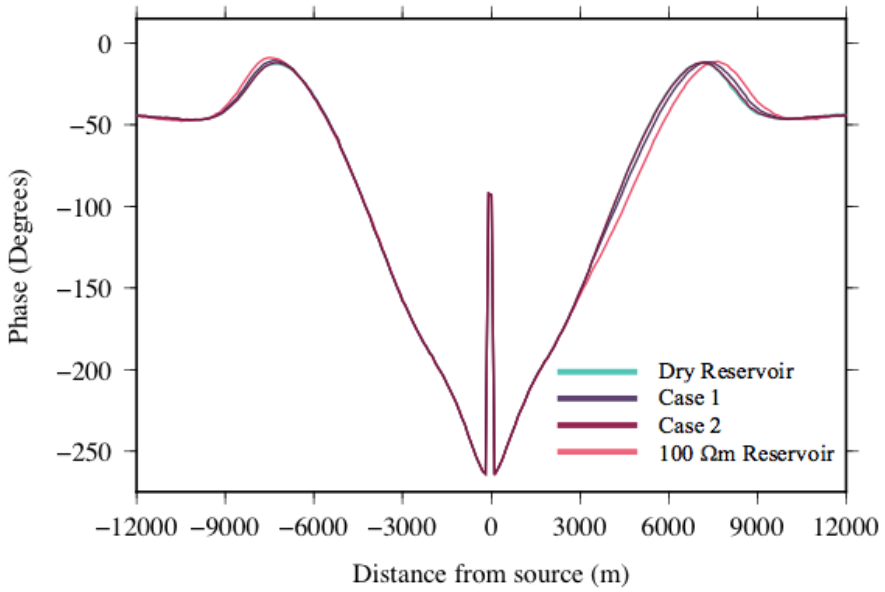

Figure 4.95: Phase results for *Model 2, Case 1* and *Model 2, Case 2*.

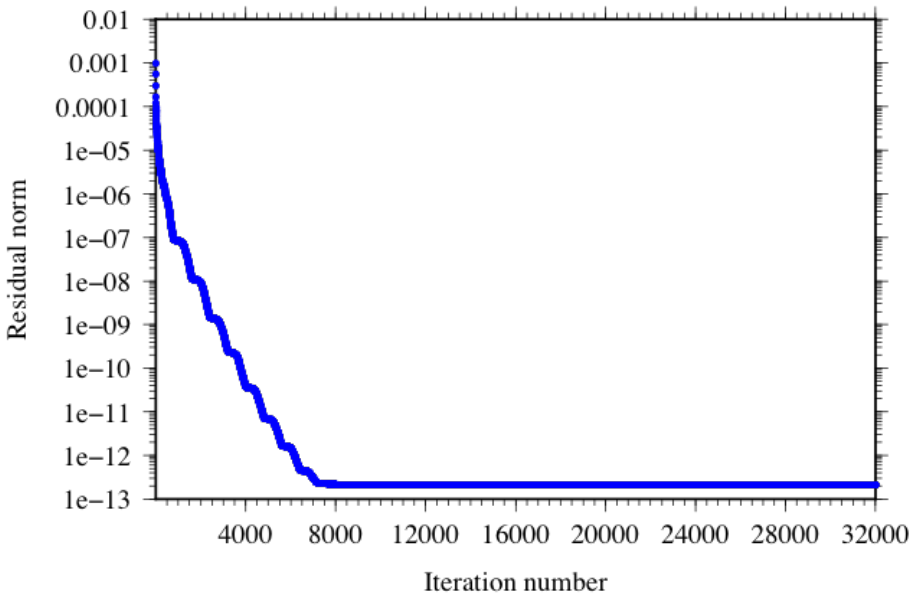

(a)

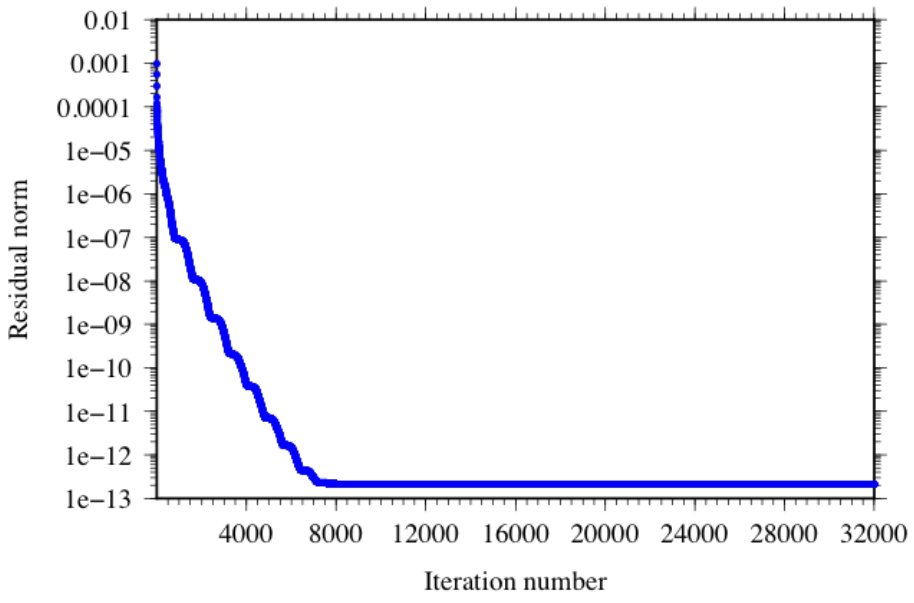

(b)

Figure 4.96: Convergence curves for each of the *Model 2* oil-water contact models. Panel (a) *Case 1*; panel (b) *Case 2*.

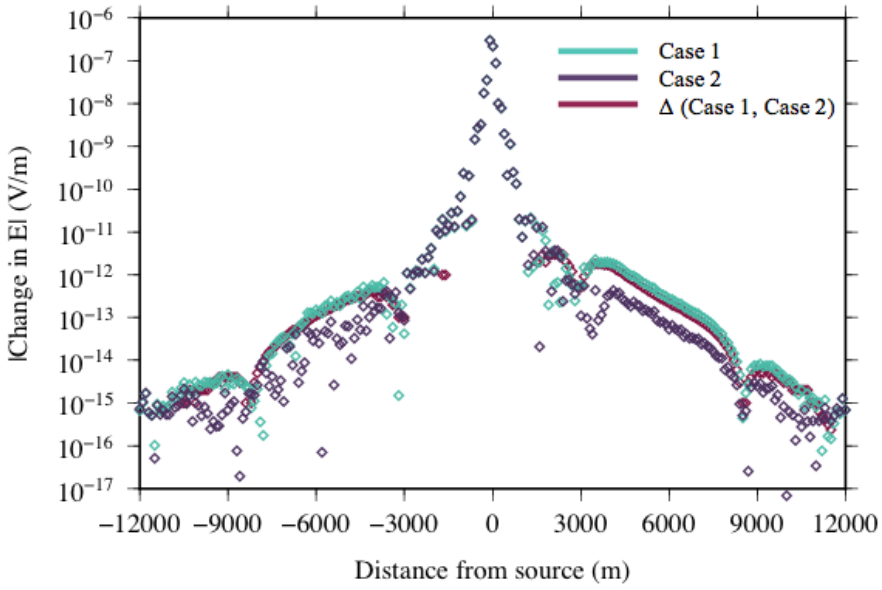

(a)

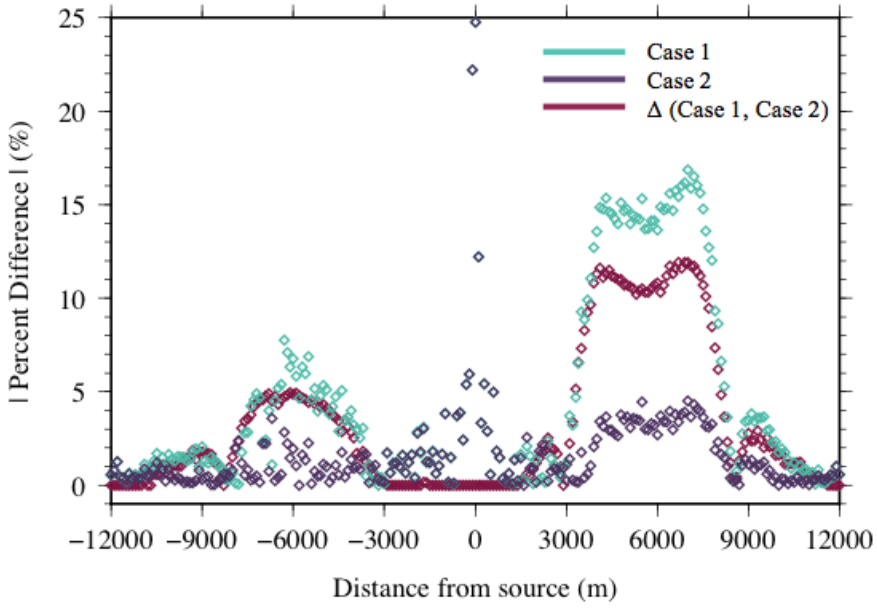

(b)

Figure 4.97: Differences in the electric field amplitude results for *Model 2, Case 1* and *Model 2, Case 2*. Panel (a) absolute differences; panel (b) percent differences normalized by the results of the dry reservoir for *Cases 1* and *2*, and by the results of *Case 2* for Δ*(Case 1, Case 2)*.

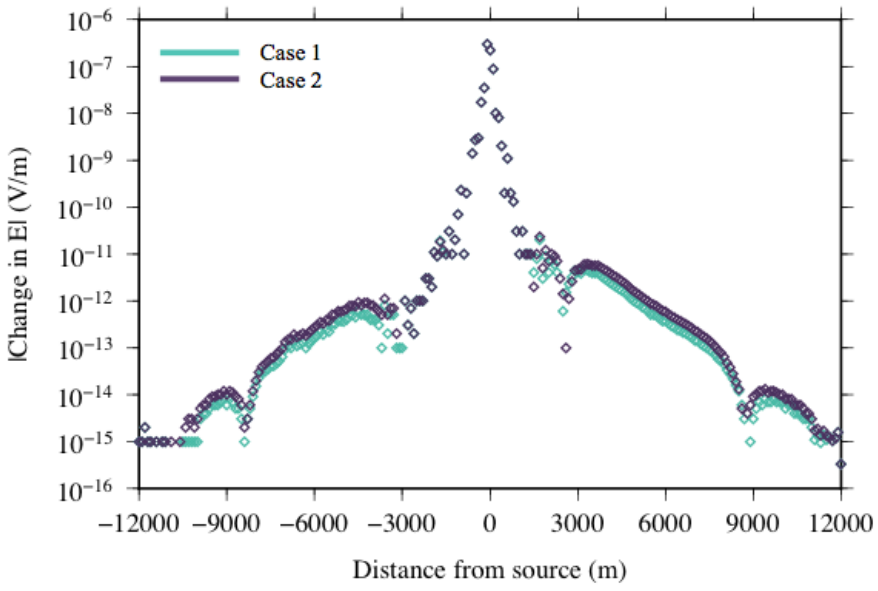

(a)

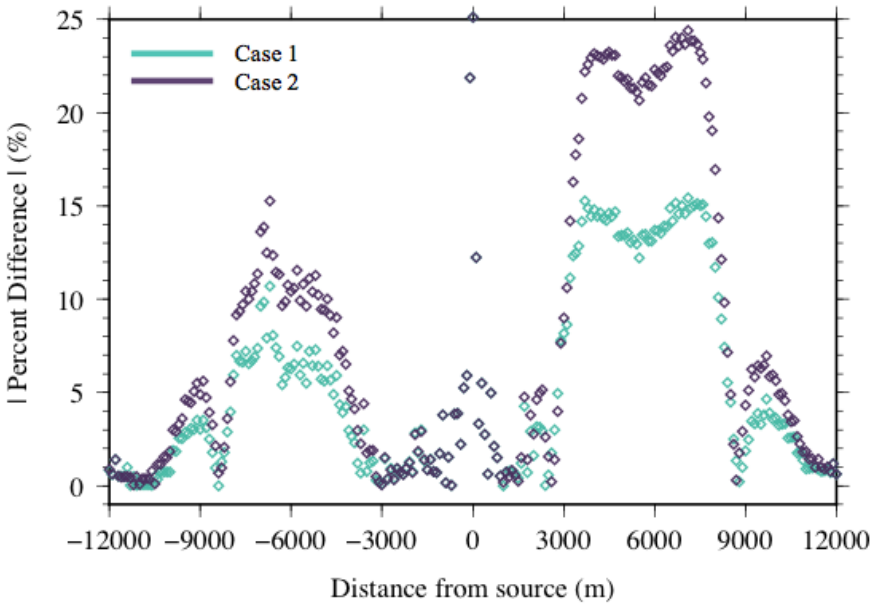

(b)

Figure 4.98: Differences in the electric field amplitude results for *Model 2, Case 1* and *Model 2, Case 2* with the *100* Ω*m Reservoir*. Panel (a) absolute differences; panel (b) percent differences normalized by the results of the fully saturated reservoir, i.e. the *100* Ω*m Reservoir*.

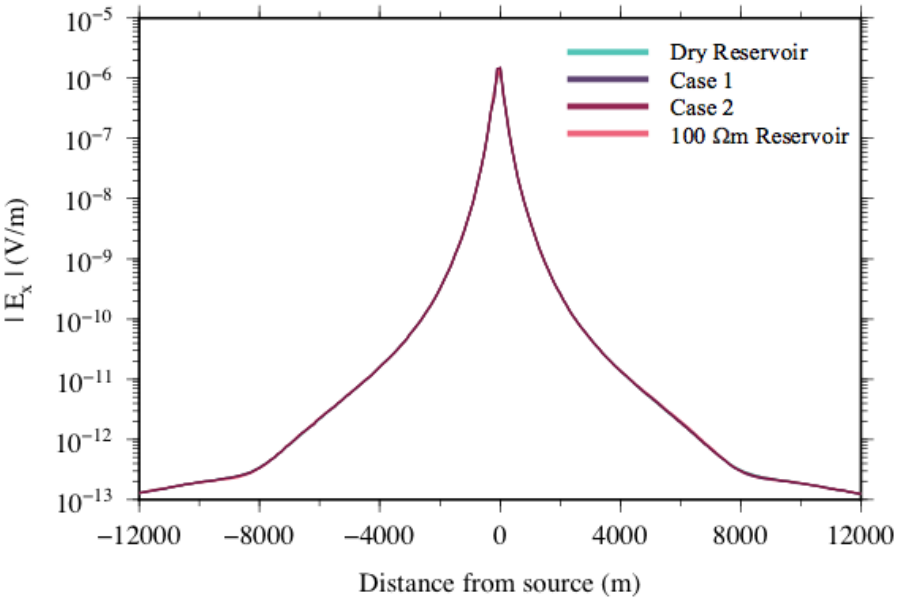

(a)

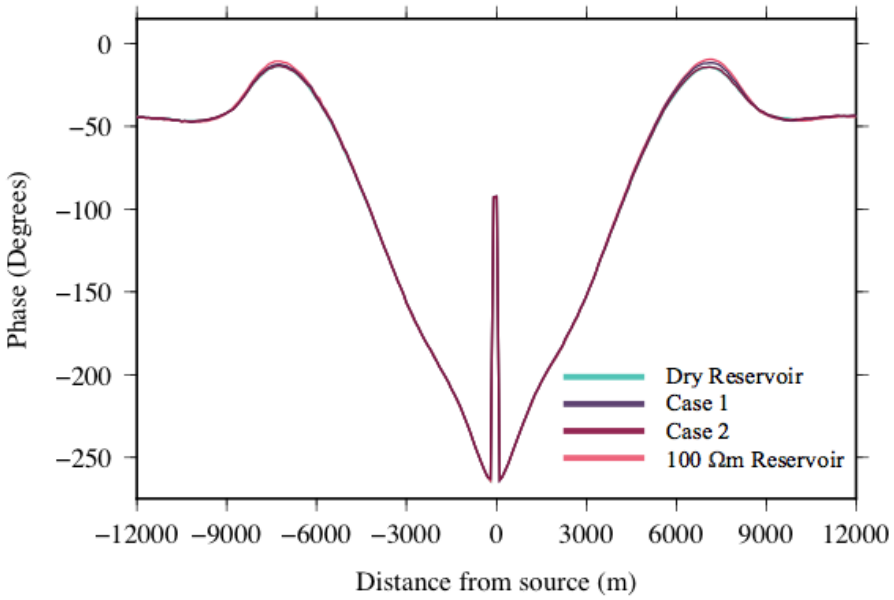

(b)

Figure 4.99: Forward modelling results for *Model 3, Case 1* and *Model 3, Case 2*. Panel (a) electric field amplitude; panel (b) phase.

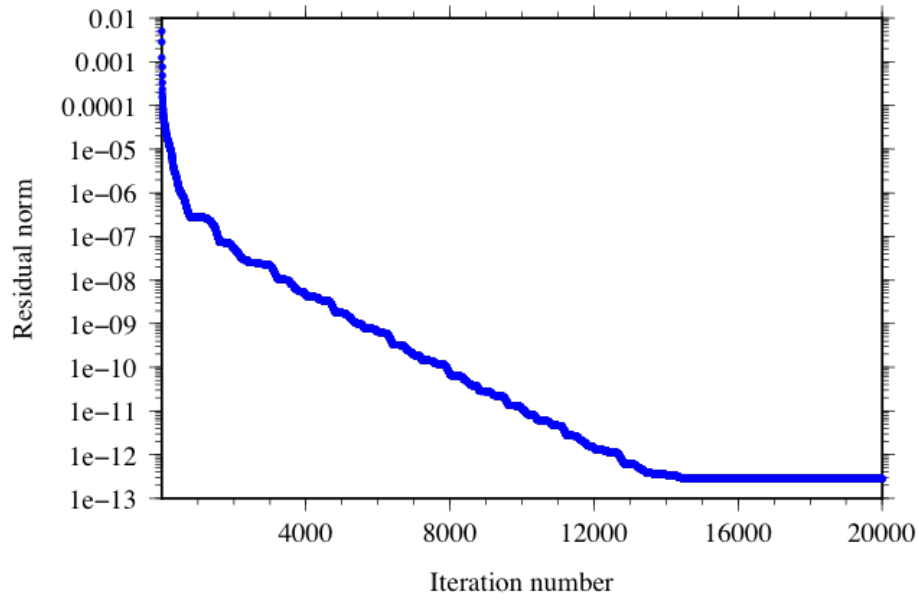

(a)

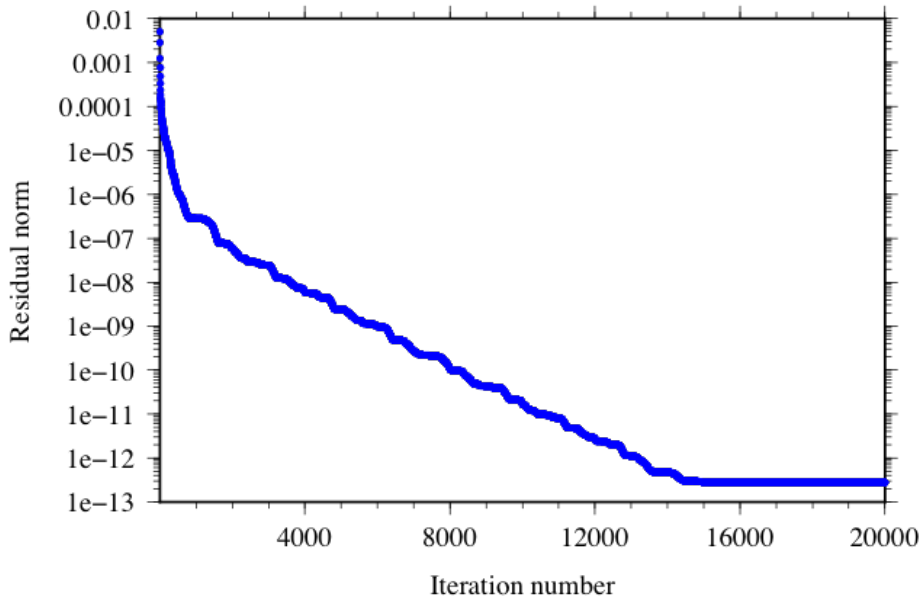

(b)

Figure 4.100: Convergence curves for each of the *Model 3* oil-water contact models. Panel (a) *Case 1*; panel (b) *Case 2*.

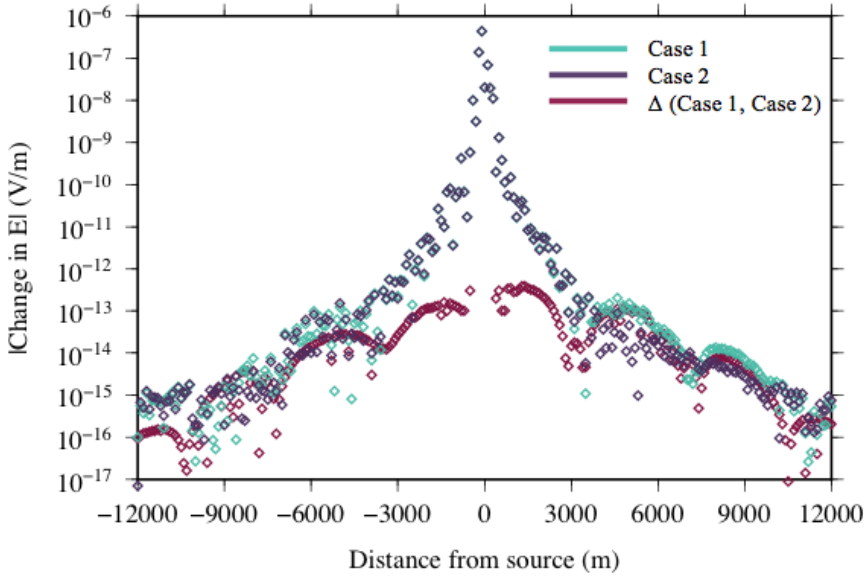

(a)

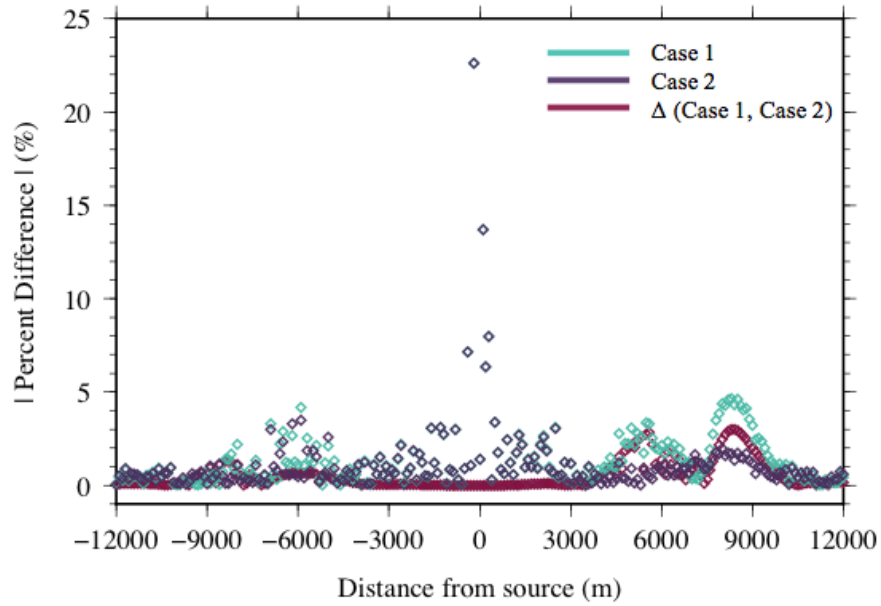

(b)

Figure 4.101: Differences in the electric field amplitude results for *Model 3, Case 1* and *Model 3, Case 2*. Panel (a) absolute differences; panel (b) percent differences normalized by the results of the dry reservoir for *Cases 1* and *2*, and by the results of *Case 2* for Δ*(Case 1, Case 2)*.

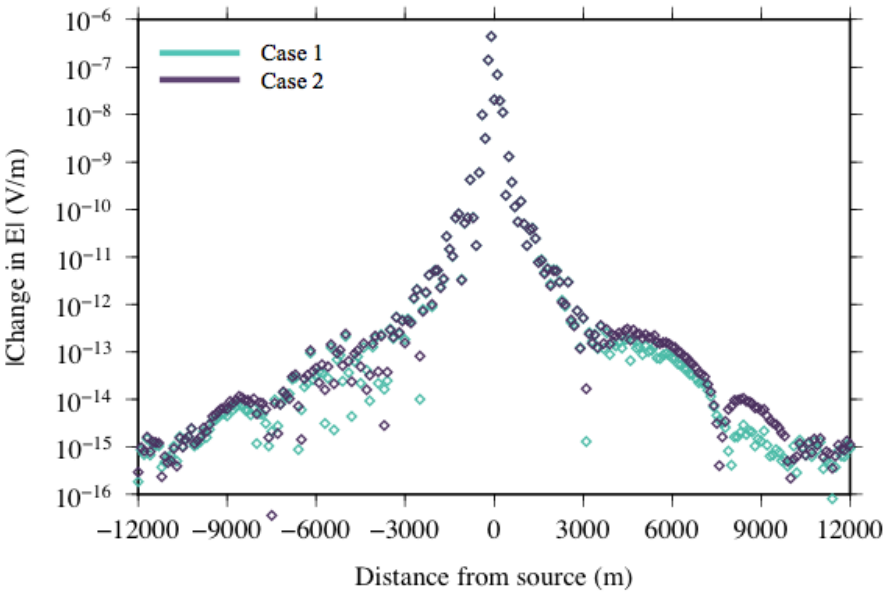

(a)

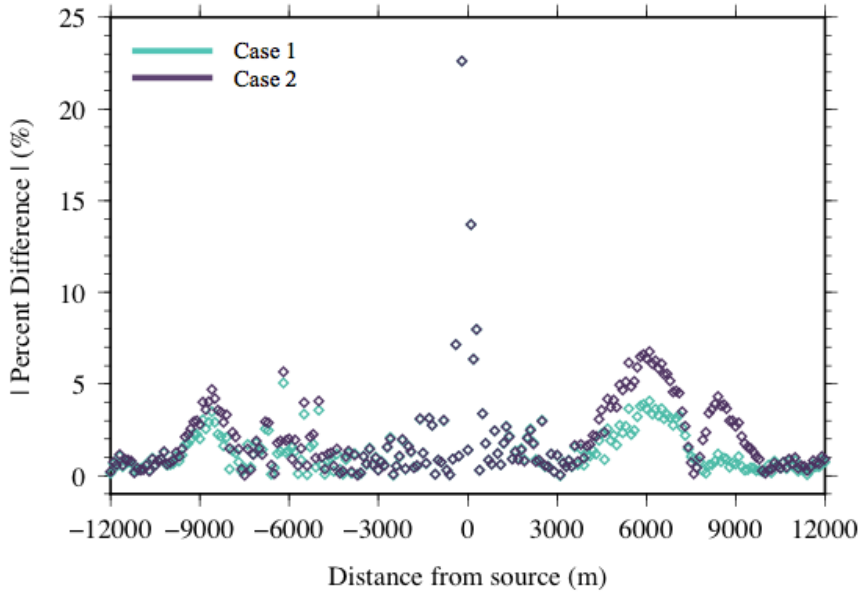

(b)

Figure 4.102: Differences in the electric field amplitude results for *Model 3, Case 1*) and *Model 3, Case 2* with the *100* Ωm *Reservoir*. Panel (a) absolute differences; panel (b) percent differences normalized by the results of the fully saturated reservoir.

4.7.3 Models 4 and 5

The method described in Section 4.7.1 was employed over the reservoir sections of *Models 4* and *5* and further discretized to form the oil-water contact models shown in Figures 4.103 to 4.106. The electric field results are shown in Figures 4.107 to 4.115. As in previous results (namely, Figure 4.53), the shallow depth and lateral extension of the single sand package in *Model 4* generates strong results, with substantial divergence of electric amplitude results from those for the *Dry Reservoir*. However, it is because of this large volume that great drops in magnitude are seen as water-saturation of the reservoir increases and thus overall resistivity values decrease (Figure 4.107). While results in *Model 5* are less dramatic with the added overburden above the reservoir, there is still a distinct separation of *Case 1* and *Case 2* both from each other and the *Dry* and *100 Ωm Reservoirs* (Figure 4.111). Similar results are apparent in the phase values for each model (Figures 4.107b and 4.112).

As in the results for the meshes in Figures 4.51 and 4.52, all oil-water contact reservoir contributions — and thus percent and absolute differences — are at negative offsets, which is reflective of the position of the reservoir relative to the source (described in Section 4.5.4). The peaks generated by reservoir detection of the oil-water contact models (Figure 4.109) have a distinctly different shape from the fully-saturated model, namely from an added inflection at $\sim$ -6000 m offset. This is likely detection of the resistivity change from the water-saturated sediment, but the high magnitude of the greatest peak — 200% at $\sim$-8000 m offset — falls well within the range of detectability. The low magnitude ($< 5\%$) percent differences for the results in *Case 2* are inconclusive to any reservoir contribution. Both cases exhibit very large deviations from the *100 Ωm Reservoir*, with up to 90% difference

with *Case 2* and 85% with *Case 2* (Figure 4.110).

The poor detectability of the deeper reservoir in fully-saturated models (Figure 4.60) is further augmented by the addition of water into the reservoir pore space (Figure 4.114 and 4.115). The highest peak in percent difference (which, at 12% is bordering detection levels) is due to a negative percent change at the reservoir edge hightened by the more conductive water-saturation. This is supported by high magnitude (35% at maximum) digression from the *100 Ωm Reservoir*.

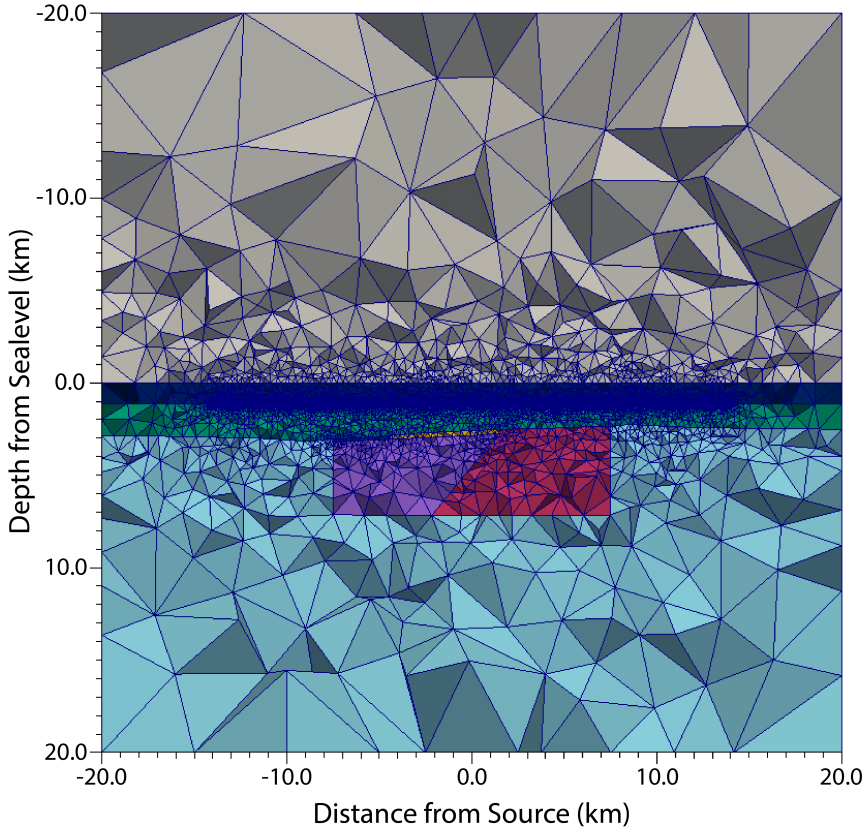

(a)

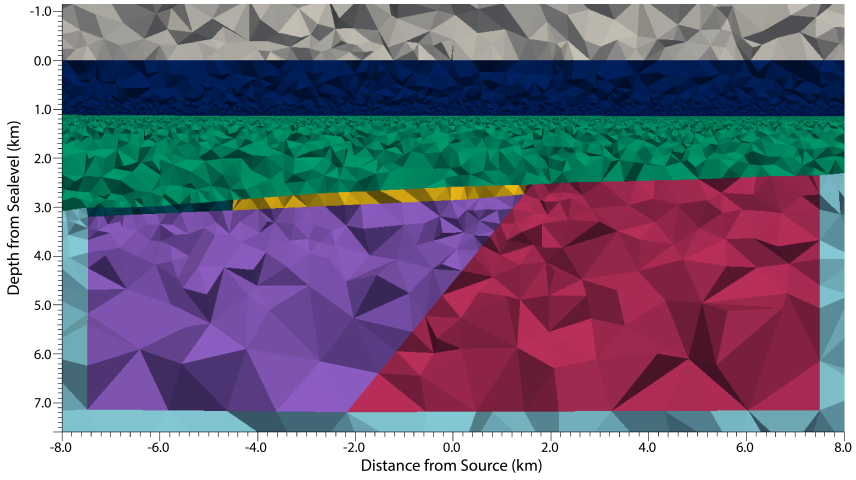

(b)

Figure 4.103: Cross-sections centered at $y = 0$ m of *Case 1* of an oil-water contact model for *Model 4*. Panel (a) full view; panel (b) enhanced view of the reservoir geometry.

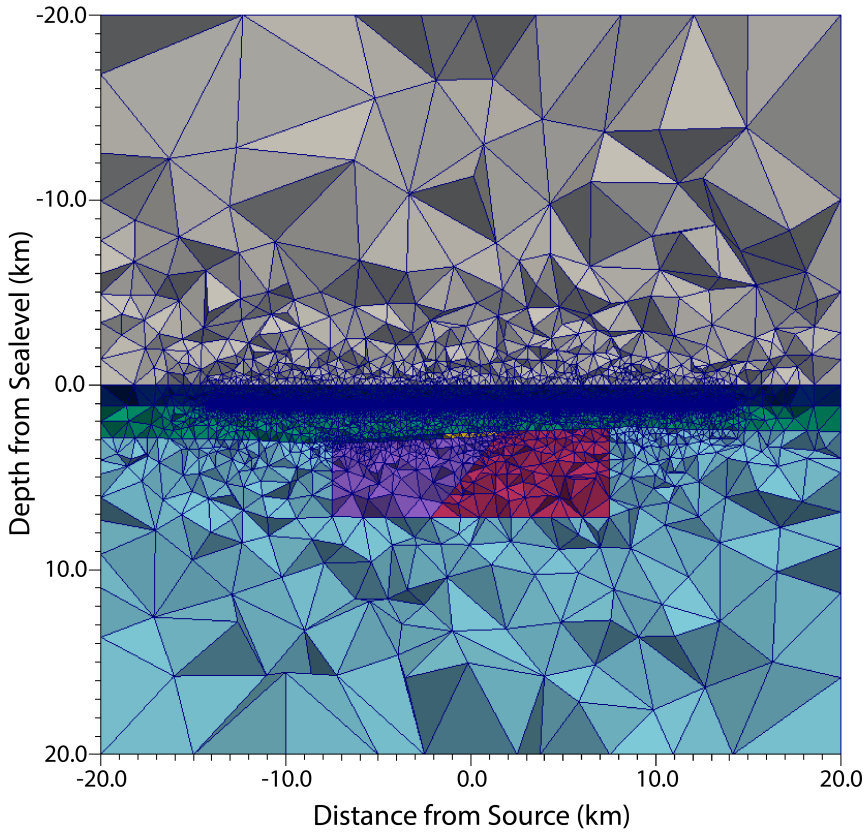

(a)

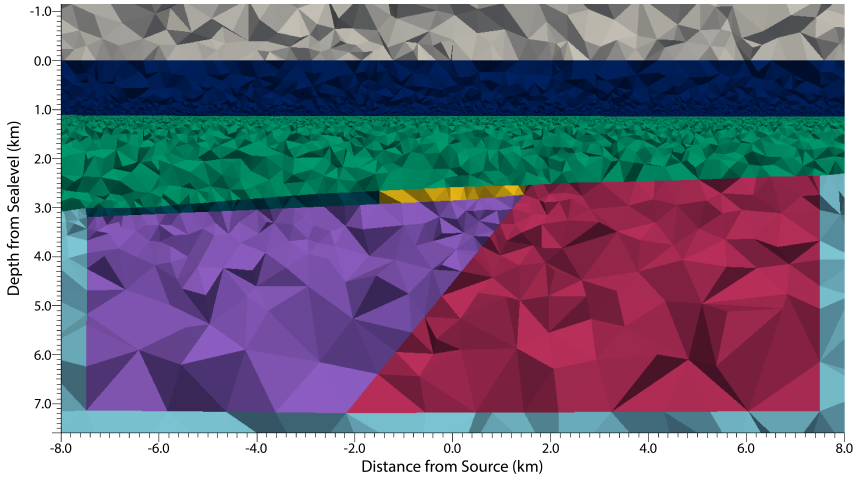

(b)

Figure 4.104: Cross-sections centered at $y = 0$ m of *Case 2* of an oil-water contact model for *Model 4*. Panel (a) full view; panel (b) enhanced view of the reservoir geometry.

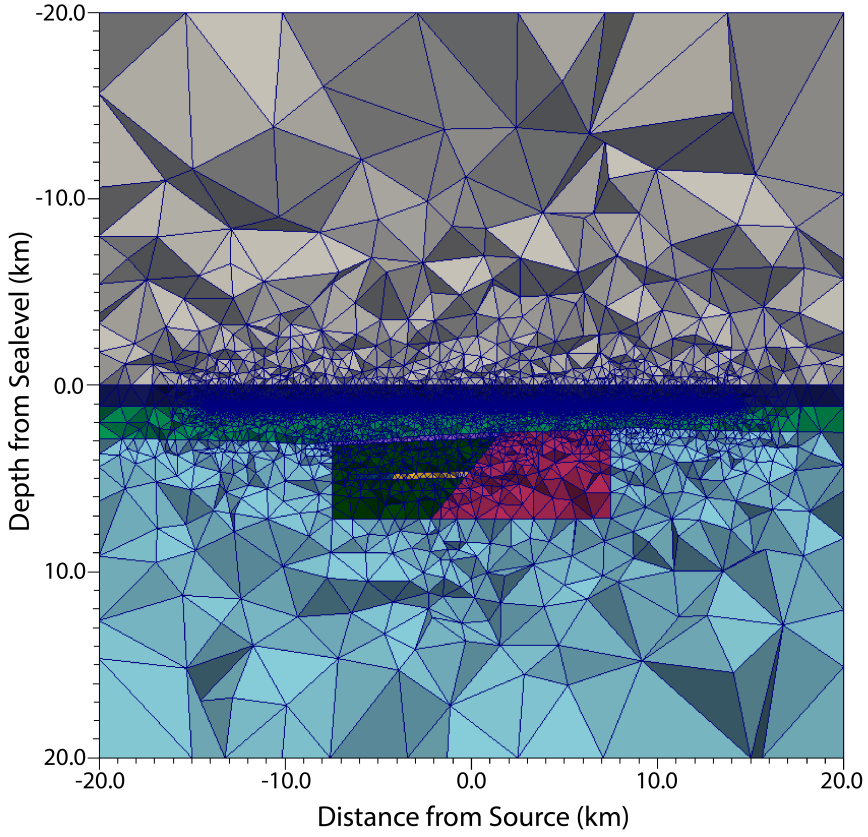

(a)

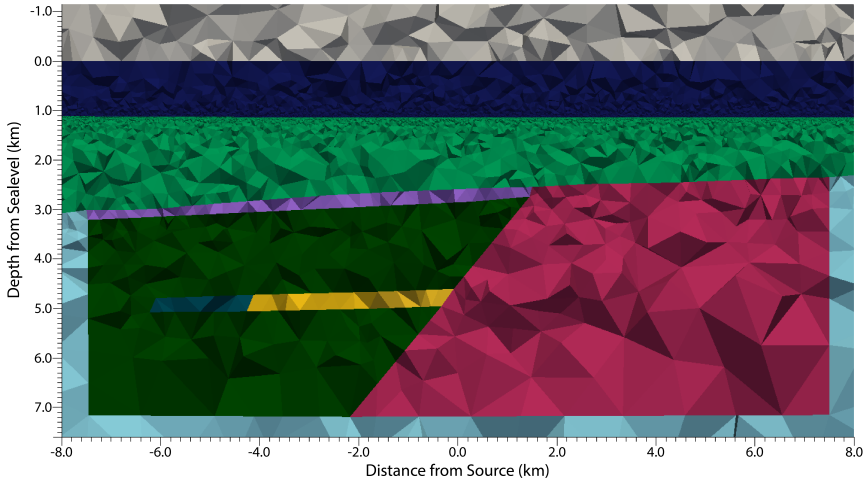

(b)

Figure 4.105: Cross-sections centered at $y = 0$ m of *Case 1* of an oil-water contact model for *Model 5*. Panel (a): full view; panel (b) enhanced view of the reservoir geometry.

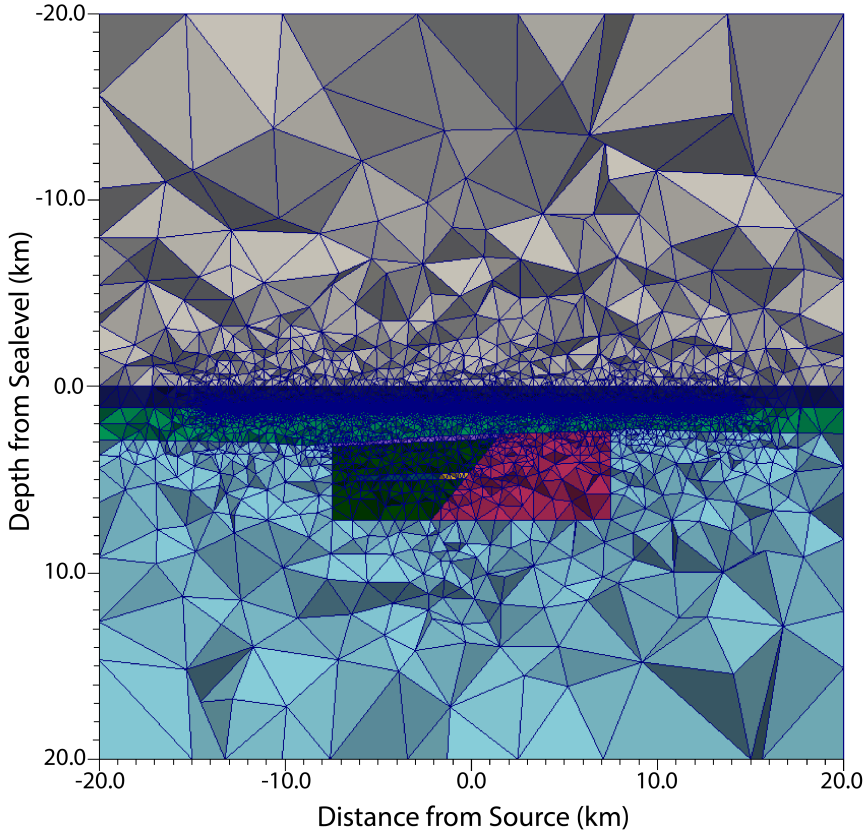

(a)

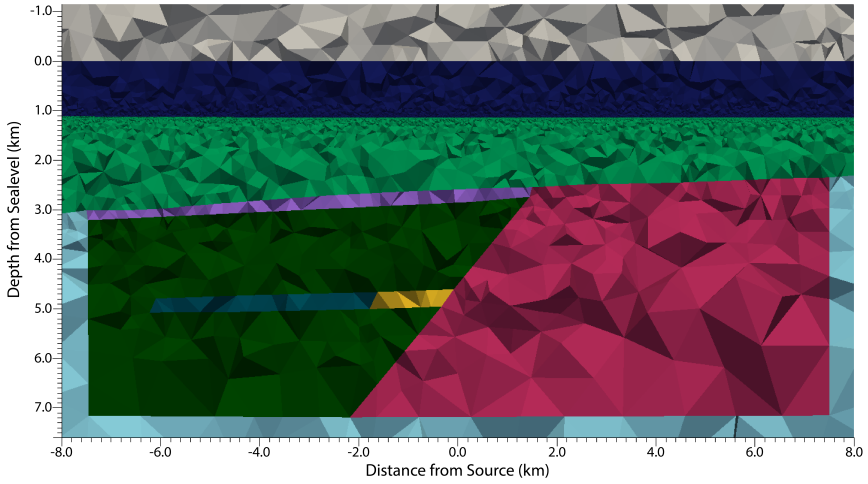

(b)

Figure 4.106: Cross-sections centered at $y = 0$ m of *Case 2* of an oil-water contact model for *Model 5*. Panel (a) full view; panel (b) enhanced view of the reservoir geometry.

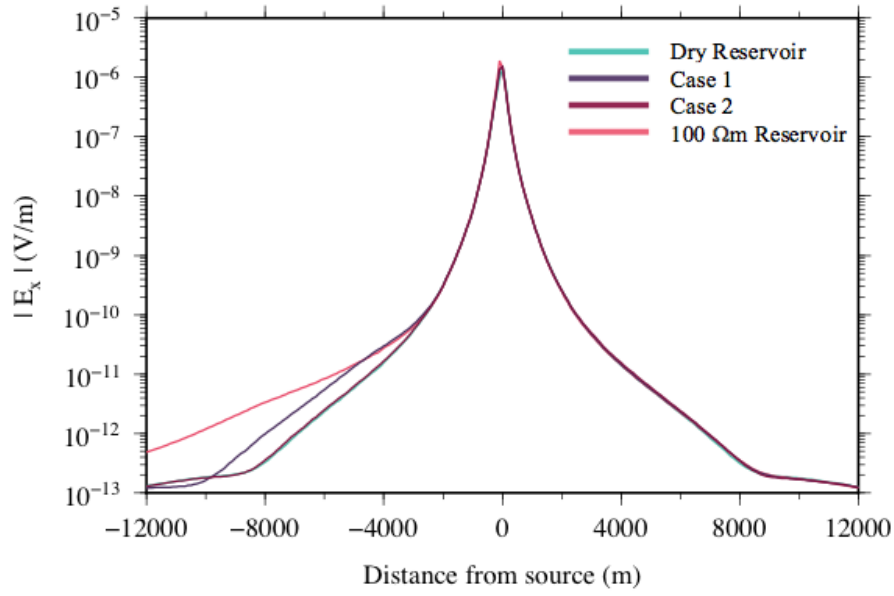

(a)

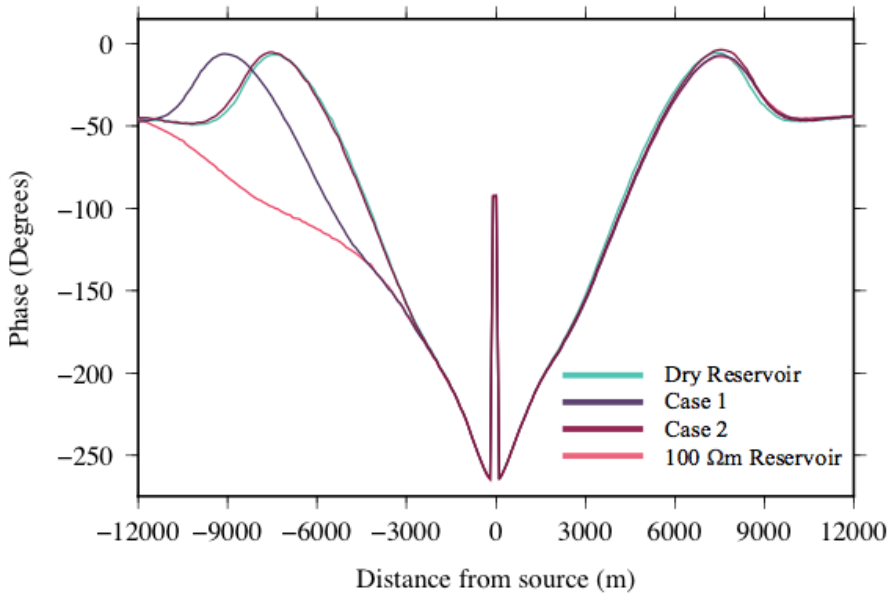

(b)

Figure 4.107: Forward modelling results for *Model 4, Case 1* and 4.104 *Model 4, Case 2*. Panel (a) electric field amplitude; panel (b) phase.

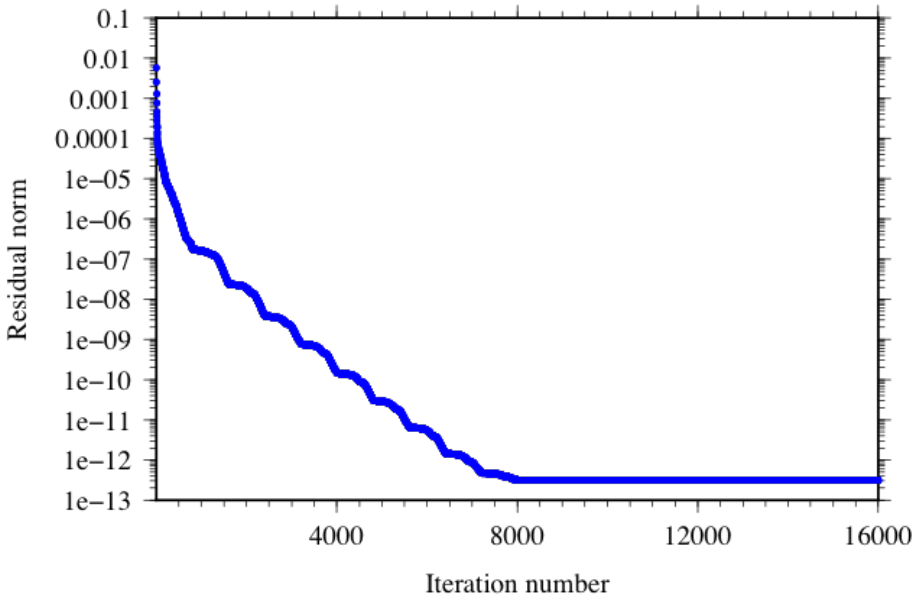

(a)

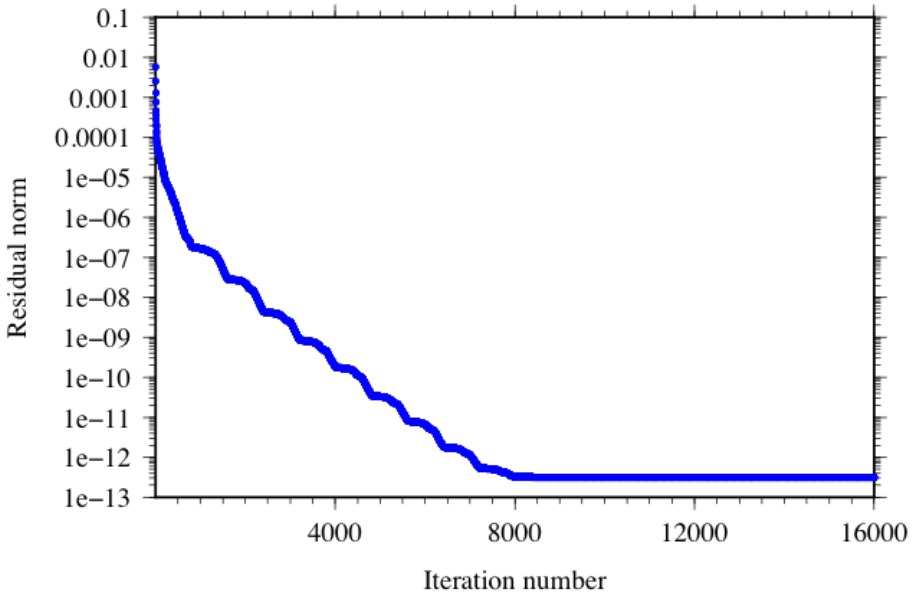

(b)

Figure 4.108: Convergence curves for each of the *Model 4* oil-water contact models. Panel (a) *Case 1*; panel (b) *Case 2*.

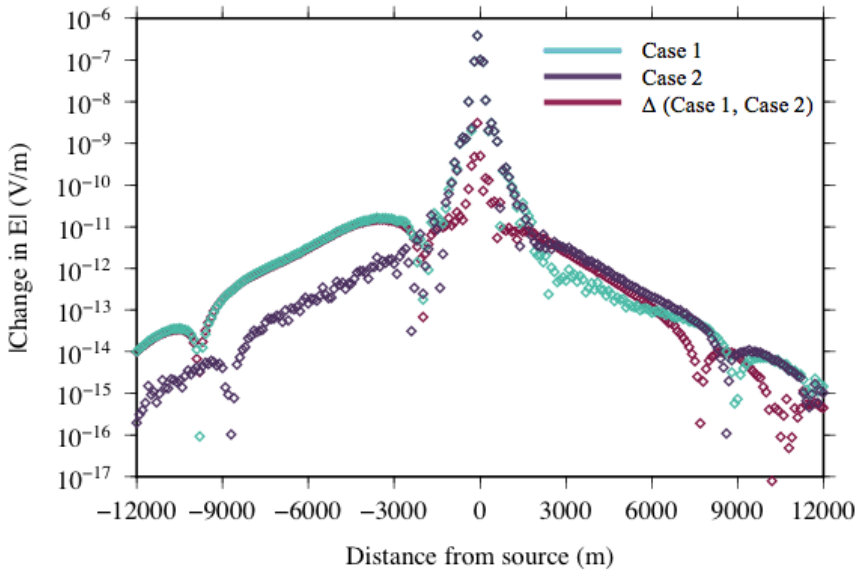

(a)

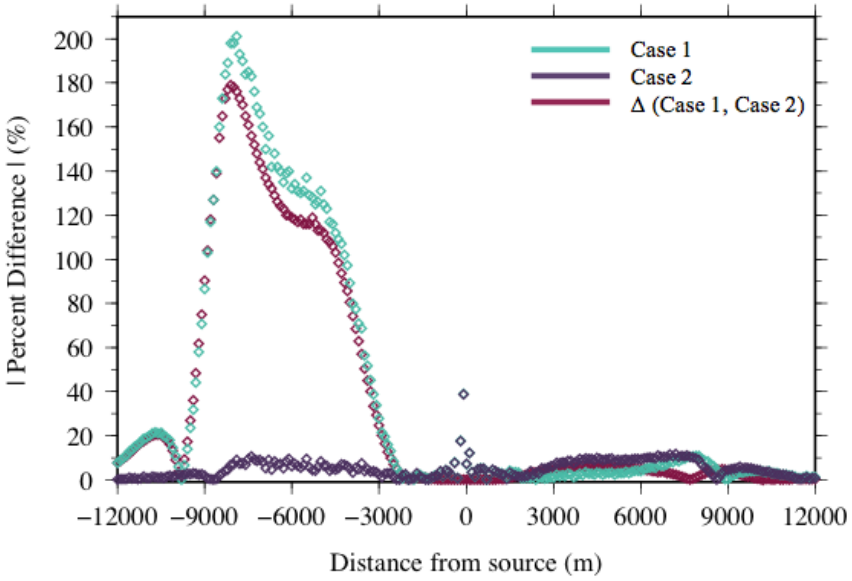

(b)

Figure 4.109: Differences in the electric field amplitude results for *Model 4, Case 1* and *Model 4, Case 2*. Panel (a) absolute differences; panel (b) percent differences normalized by the results of the dry reservoir for *Cases 1* and *2*, and by the results of *Case 2* for Δ*(Case 1, Case 2)*.

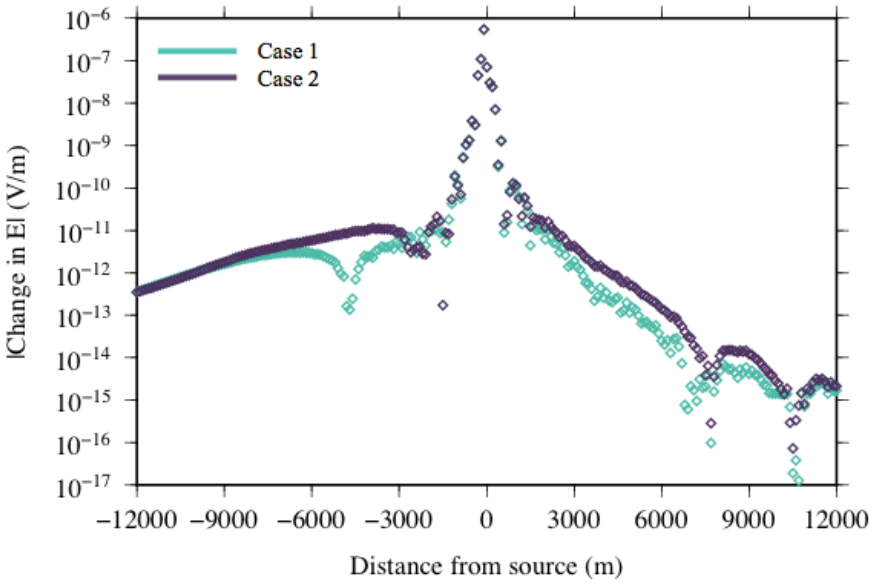

(a)

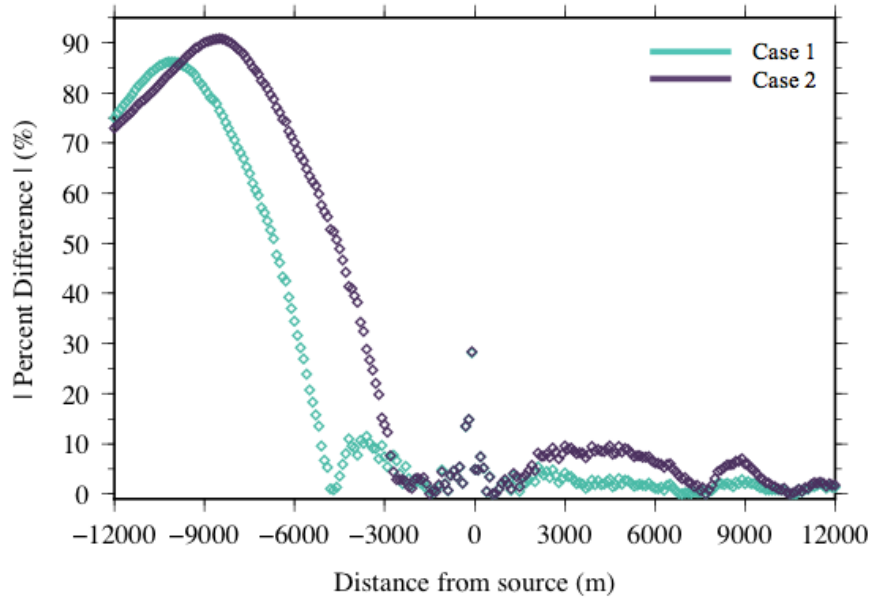

(b)

Figure 4.110: Differences in the electric field amplitude results for *Model 4, Case 1* and *Model 4, Case 2* with the *100 Ωm Reservoir*. Panel (a) absolute differences; panel (b) percent differences normalized by the results of the *100 Ωm Reservoir*.

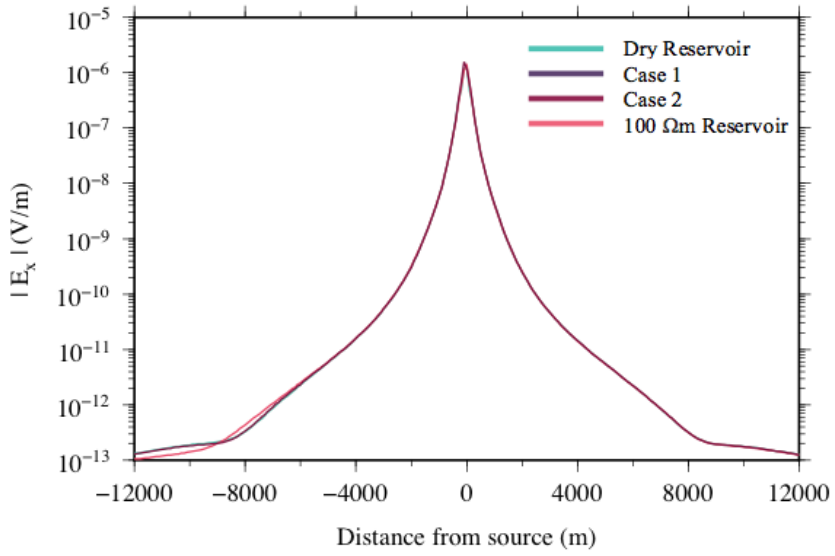

(a)

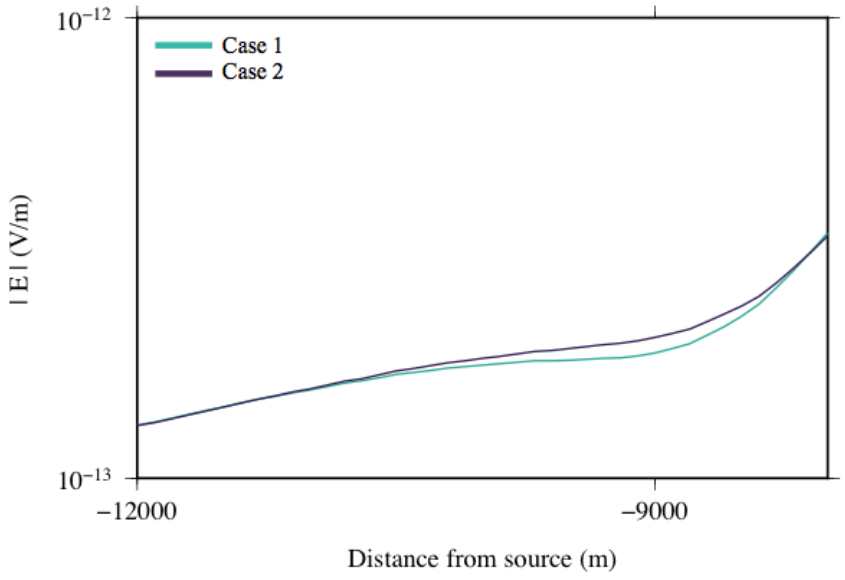

(b)

Figure 4.111: Electric field amplitude results for *Model 5, Case 1* and *Model 5, Case 2*. Panel (a) full offset results; panel (b) enlarged view to enhance amplitude difference.

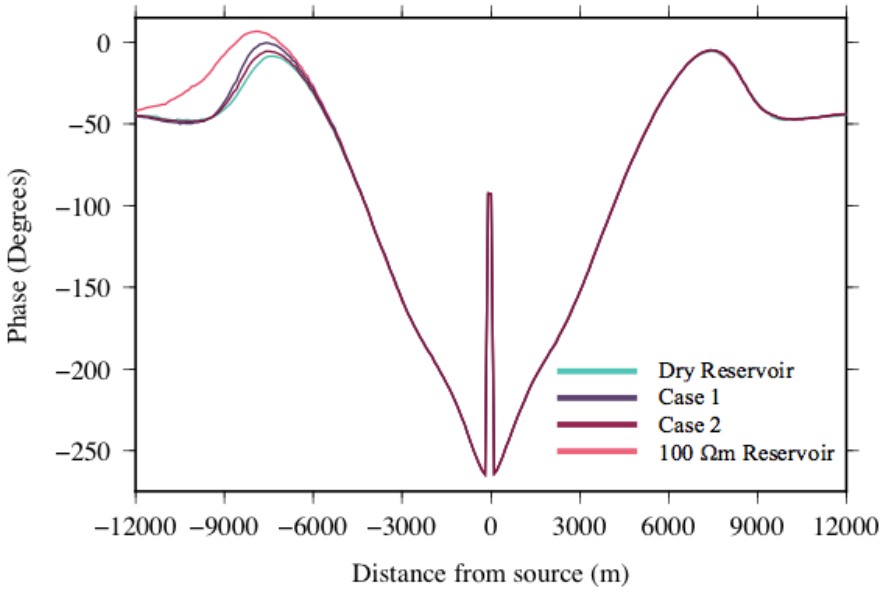

Figure 4.112: Phase results for *Model 5, Case 1* and *Model 5, Case 2*.

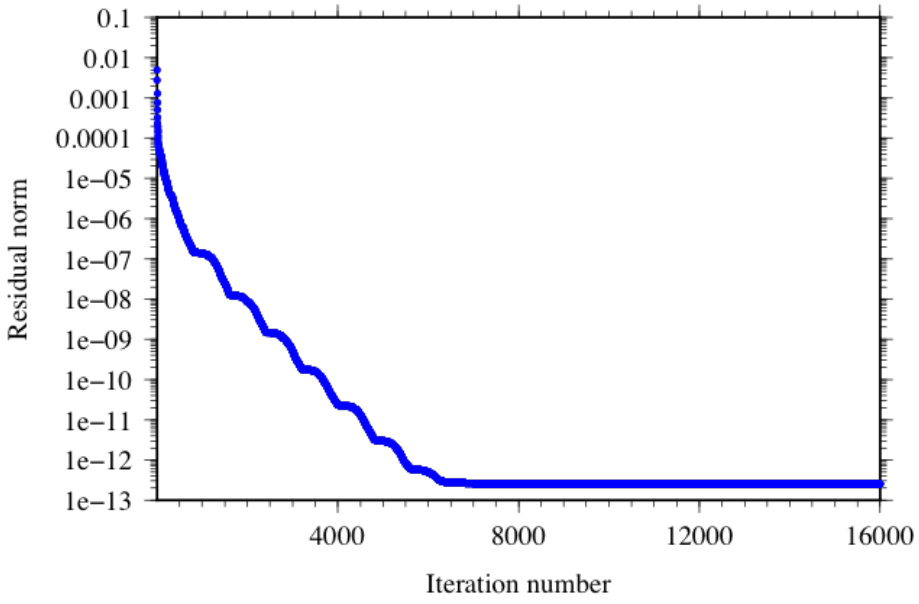

(a)

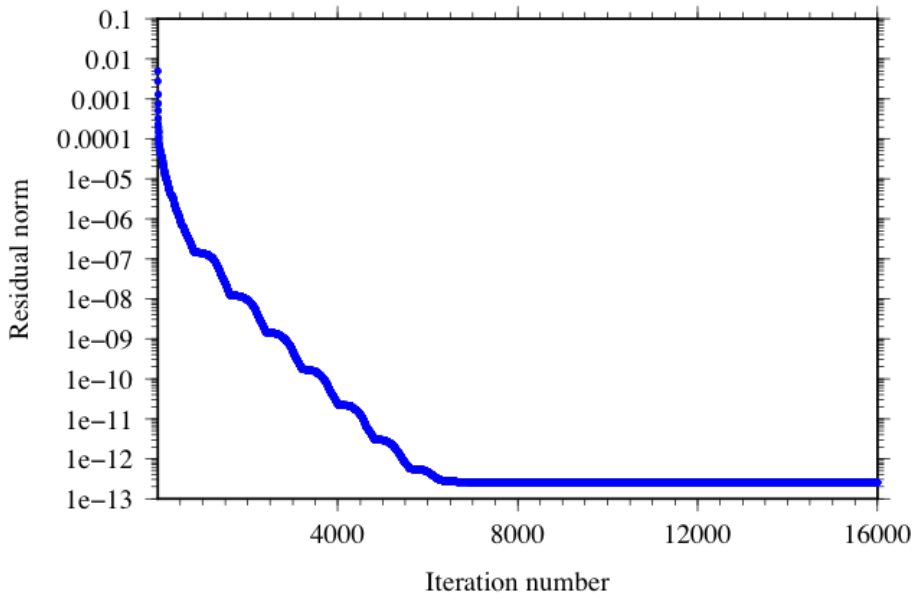

(b)

Figure 4.113: Convergence curves for each of the *Model 5* oil-water contact models. Panel (a) *Case 1*; panel (b) *Case 2*.

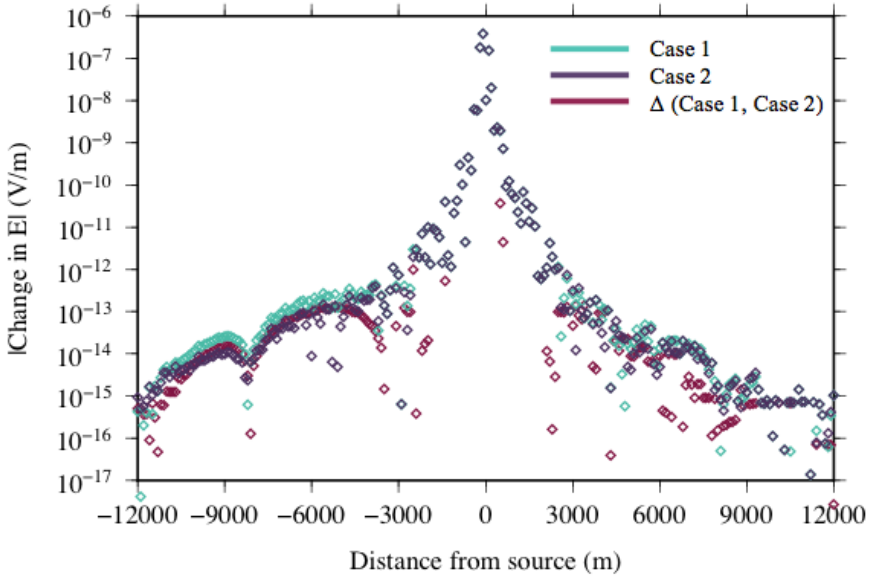

(a)

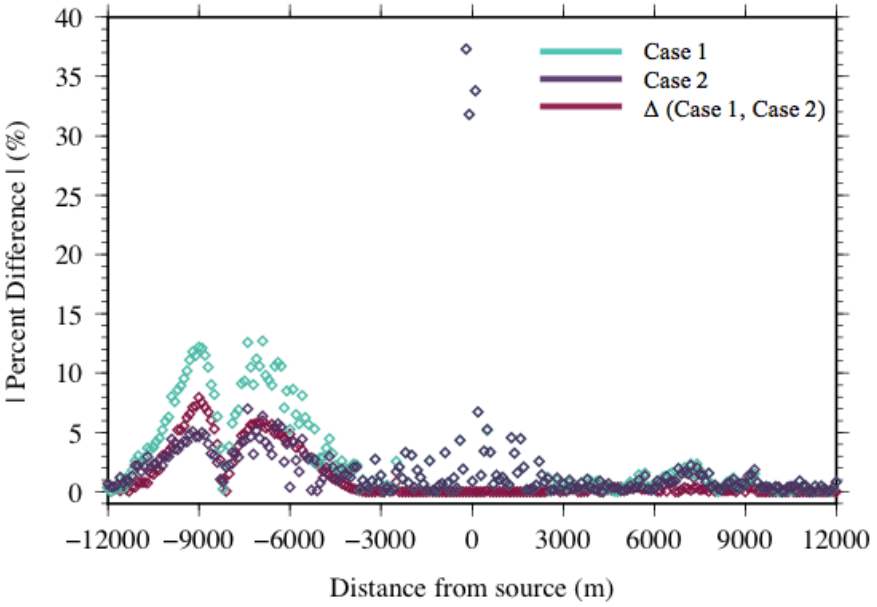

(b)

Figure 4.114: Differences in the electric field amplitude results for *Model 5, Case 1* and *Model 5, Case 2*. Panel (a) absolute differences; panel (b) percent differences normalized by the results of the dry reservoir for *Cases 1* and *2*, and by the results of *Case 2* for Δ*(Case 1, Case 2)*.

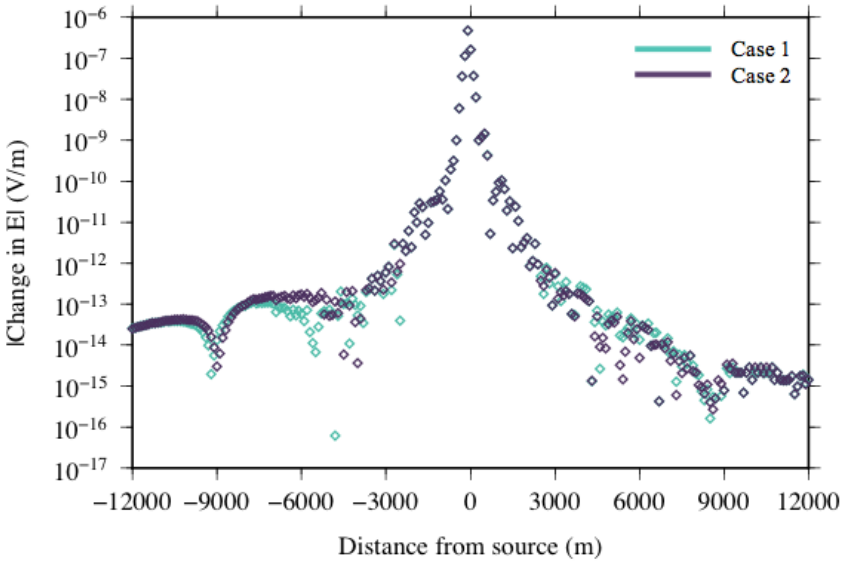

(a)

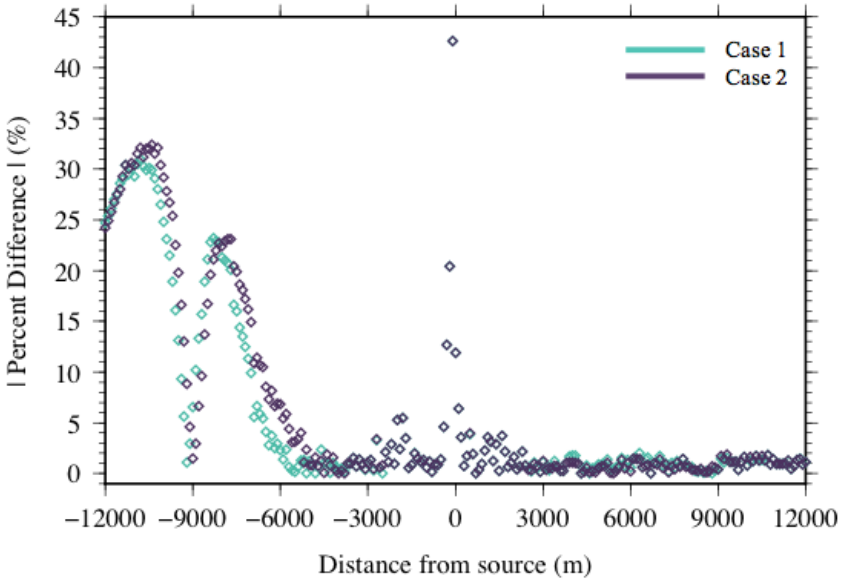

(b)

Figure 4.115: Differences in the electric field amplitude results for *Model 5, Case 1* and *Model 5, Case 2* with the *100 Ωm Reservoir* (Figure 4.52). Panel (a) absolute differences; panel (b) percent differences normalized by the results of the fully saturated reservoir i.e. the *100 Ωm Reservoir*.

Chapter 5

Conclusion

Controlled Source Electromagnetics (CSEM) is a frontier method of resistivity mapping that has a significant ability to detect and delineate highly resistive hydrocarbon reservoirs in the subsurface. Raw CSEM data can be used as an independent exploratory tool or as a supplemental integration to existing borehole, seismic and seabed logging data, garnering the potential to be a fundamental component in risk assessment for drilling potential targets.

In the current period, knowledge of the CSEM method and its results are fairly limited. CSEM surveys — particularly in three-dimensions — were previously discounted for their expense. However, through the use of forward modelling to synthesize these data, conclusions can be drawn to more efficiently and cost-effectively assess the quality and necessity of CSEM surveying as a geophysical tool. This study makes use of the finite-element method to model the behaviour of electromagnetic fields throughout a discretized mesh

of the resistivity variations in the Earth's subsurface. Though this method is less studied than its counterparts, the nature of finite-elements allow for the computational domain to be discretized using unstructured tetrahedral meshes, which more accurately represent geological contacts than previous methods employing rectilinear meshes. This accuracy is particularly important when modelling hydrocarbon reservoirs, as precise estimates of reservoir volumes are required to assess the economic potential of the target.

The effectiveness of the forward-modelling approach was assessed through a series of test scenarios in both one- and three-dimensions: the 1D models allowed for verification of the CSEM3DFWD approach with those of known analytical and semi-analytical solutions, while the 3D models gave an understanding of potential 3D CSEM results of proposed structures analogous to those found offshore Newfoundland.

The process for the 1D models was stepwise in its approach: each model designed in the sequence increased in complexity (i.e. added layers or structures) to specifically assess the effect of each addition. Immediately — through the process of modelling homogeneous halfspaces — the difficulty of choosing the appropriate refinement to generate accurate results was encountered. The halfspaces — at approximately 15,000 cells — are excellent for this experimental approach, as their low memory usage allow for models to be ran quickly (on the order of 30 - 90 minutes), and a refinement configuration to be chosen quickly for the finite-element model in question. In the context of this study, the preferred and most accurate refinement method involved adding small, rectangular regions about the source and directly below the seabed for the observation location. This constraint generates numerous, small cells at these locations which effectively increased the areas where the electric field has been computed. This effect is represented visually by smooth results,

whose accuracy are validaded with the comparison to known semi-analytical methods.

The main aim of the 3D suite of models is to explore limits of detectability for proposed subsurface structures, as there are no semi-analytical results available for comparison. The high level of detection for several of the reservoir and array configurations assessed in this study give great promise to future use and development of CSEM technologies. Though shallow reservoirs were naturally more easily detected, the detectability with depth and reservoir complication (with above-threshold reservoirs resolved at over 3500 m depth) suggests that the method is now capable of handling even more complex scenarios. There is also an obvious decrease in the detectability with deeper structures, and structures that have decreases in the conductivity of the reservoir section due to foreign saturations (i.e. water in the pore space). Though high detectability is preferred, as it indicates a potential economic play, low detectability will assist in de-risking potential drilling scenarios that are less promising.

It is important to note that the results of this study are restricted due to the non-unique nature of the forward problem. This study may be built on to include a synthetic inversion study, which would increase confidence in the detectability of hydrocarbon reservoirs (or other resistive bodies of interest) using the CSEM method.

The results of this study have several potential applications. The flexibility of the model-generating software establishes opportunities for several other environments to be considered: any scenario dominated by resistivity contrasts is a great candidate for CSEM modelling. The data generated for the specific environments expressed in this study may be integrated into known data sets to redefine risk and potential for emerging assets. The

collection of real-world data over these assets will confirm the direct potential of the CSEM method.

References

Ainsworth, N. R., L. A. Riley, S. Haynes, M. McDonough, and E. A. Stacey, A Late Jurassic, Tithonian to Early Eocene, Ypresian, stratigraphic framework for the Mizzen F-09, L-11 and O-16 exploration wells, Flemish Pass Basin, Offshore Newfoundland, *GeoConvention 2015*, Canadian Society of Exploration Geophysicists, 2015.

Ansari, S. M., and C. G. Faquharson, 3D finite-element forward modeling of electromagnetic data using vector and scalar potentials and unstructured grids, *Geophysics, 79,* 4, E149-E165, 2014.

Archie, G. E., The electrical resistivity log as an aid in determining some reservoir characteristics, *Transactions of the AIME, 146,* 01, 54-62, 1942.

Cameron, D. E., X. Wu, J. K. Welford, A. Selnes, Renewed exploration and new insights into the slope and deep water regions of the Flemish Cap and Labrador Sea, Offshore Newfoundland and Labrador, Canada, *GeoConvention 2015*, Canadian Society of Exploration Geophysicists, 2015.

Chave, A.D., S. C. Constable and R. N. Edwards, Electrical exploration methods for the seafloor, *Electromagnetic Methods in Applied Geophysics, 2*, 931-966, 1991.

Chandola, S. K., R. B. A. Karin, A. Mawarni, R. Ismail, N. Shahud, R. Rahman, P. Bernabe, and K. Brauti, Challenges in shallow water CSEM surveying: a case history from Southeast Asia, In *International Petroleum Technology Conference*, 2007.

Coggon, J. H., Electromagnetic and electrical modeling by the finite element method, *Geophysics, 36,* 1, 132-155, 1971.

Constable, S. C., Marine electromagnetic methods — A new tool for offshore exploration, *The Leading Edge, 25*, 4, 438-444, 2006.

Constable, S. C., Ten years of marine CSEM for hydrocarbon exploration, *Geophysics, 75,* 5, 75A67-75A81, 2010.

Constable, S. C., and C. J. Weiss, Mapping thin resistors and hydrocarbons with marine EM methods: Insights from 1D modeling, *Geophysics, 71,* 2, G43-G51, 2006.

Constable, S. C., and C. J. Weiss, Mapping thin resistors and hydrocarbons with marine EM methods: Part II — Modeling and analysis in 3D, *Geophysics, 71,* 6, G321-G332, 2006.

Constable, S. C., K. Key, and L. Lewis, Mapping offshore seidmentary structure using electromagnetic methods and terrain effects in marine magnetotelluric data, *Geophysical Journal International, 176,* 2, 431-442, 2009.

Constable, S. C., and L. J. Srnka, An introduction to marine controlled-source electromagnetic methods for hydrocarbon exploration, *Geophysics, 72,* 2, WA3-WA12, 2007.

Cox, C. S., On the electrical conductivity of the oceanic lithosphere, *Physics of the Earth and Planetary Interiors, 25*, 3, 196-201, 1981.

Cox, C. S., Controlled-source electromagnetic sounding of the oceanic lithosphere, *Nature, 320,* 52-54, 1986.

Dennis, H., P. Bergmo, T. Holt, Tilted oil-water contacts: modelling the effects of aquifer heterogeneity, *Geological Society, London, Petroleum Geology Conference Series, 6,* Geological Society of London, 2005.

Edwards, N., Marine controlled source electromagnetics: Principles, methodologies, future commercial applications, *Surveys in Geophysics, 26,* 675-700, 2005.

Eidesmo, T., S. Ellingsrud, L. M. MacGregor, S. C. Constable, M. C. Sinha, S. Johansen, F. N. Kong, and H. Westerdahl, *First Break, 20*, 3, 2002.

Ellingsrud, S., T. Eidesmo, S. Johansen, M. C. Sinha, L. M. MacGregor, and S. Constable, Remote sensing of hydrocarbon layers by seabed logging (SBL): Results from a cruise offshore Angola, *The Leading Edge, 21*, 10, 972-982, 2002.

Enachescu, M. E., Petroleum Exploration Opportunities in the Flemish Pass Basin, Newfoundland and Labrador Offshore Area; Call for Bids NL 13-01, Area "C" — Flemish Pass Basin, Parcel 1, *Government of Newfoundland Department of Natural Resources,* 2014.

Enachescu, M. E., S. Kearsey, V. Hardy, J. Sibuet, J. Hogg, S. Srivastava, A. Fagan, T. Thompson, and R. Ferguson, Evolution and petroleum potential of the Orphan Basin, offshore Newfoundland, and its relation to the movement and rotation of the Flemsih Cap based on plate kinmenatics of the North Atlantic, In *25th annual Gulf Coast section SEPM Foundation, Bob F. Perkins research conference, symposium on petroleum systems of divergent continental margin basins, Dallas, Texas: Society for Sedimentary Geology, Gulf Coast Section, 25,* 7-8, 2005.

Evans, R. L., S. C. Constable, M. C. Sinha, C. S. Cox, and M. J. Unsworth, Upper crustal resistivity structure of the East Pacific Rise near 13 °N, *Geophys. Res.Lett., 18,* 1917-1920, 1991.

Farquharson, C. G., P. G. Lelièvre, S. M. Ansari, and H. Jahandari, Towards Real Earth Models-Computational Geophysics on Unstructured Tetrahedral Meshes?, In *76th EAGE Conference and Exhibition-Workshops,* June 2014.

Farquharson, C. G., and M. P. Miensopust, Three-dimensional finite-element modelling of magnetotelluric data with a divergence correction, *J. of Applied Geophysics, 75,* 4, 699-710, 2011.

Gist, G., A. Ciucivara, R. Houck, M. Rainwater, D. Willen, and J. J. Zhou, Case Study of a CSEM Falst Positive-Orphan Basin, Canada, *2013 SEG Annual Meeting,* Society of Exploration Geophysicists, 2013.

Haber, E., U. M. Ascher, D. A. Aruliah, and D. W. Oldenburg, Fast simulation of 3D electromagnetic problems using potentials, *J. of Computational Physics, 163,* 1, 150-171, 2000.

Hansen, K. R., and R. Mittet, Incorporating seismic horizons in inversion of CSEM data, *2009 SEG Annual Meeting*, Society of Exploration Geophysicists, 2009.

Harris, P., and L. MacGregor, Determination of reservoir properties from the integration of CSEM and seismic data, First Break, 24, 15-21, 2006.

Harris, P., Z. Du, H. H. Soleng, L. M. MacGregor, and W. Olsen, Rock physics integration of CSEM and seismic data: a case study based on the Luva gas field, In *2009 SEG Annual Meeting*, Society of Exploration Geophysicists, 2009.

Heasley, E. C., R. H. Worden, J. P. Hendry, Cement distribution in a carbonate reservoir: recognition of a palaeo oil-water contact and its relationship with reservoir quality in the Humbly Grove field, onshore, UK, *Marine and Petroleum Geology, 17,* 5, 639-654, 2000.

Hesthammer, J., and M. Boulaenko, The offshore EM Challenge, *First Break, 23,* 11, 2005.

Hesthammer, J., A. Stefatos, M. Boulaenko, S. Fanavoll, and J. Danielsen, CSEM performance in light of well results, *The Leading Edge, 29,* 1, 34-41, 2010.

Hohmann, G. W., Three-dimensional induced polarization and electromagnetic modeling, *Geophysics, 40,* 2, 309-324, 1975.

Hoversten, G. M., J. Chen, E. Gasperikova, and G. A. Newman, Integration of marine CSEM and seismic AVA data for reservoir parameter estimation, In *2005 SEG Annual Meeting*, Society of Exploration Geophysicists, 2005.

Jin, J. M., The finite element method in electromagnetics, *John Wiley & Sons*, 2002.

Johansen, S. E., T. A. Wicklund and H. E. Amundssen, Interpretation example of marine CSEM data, *The Leading Edge, 26,* 3, 348-354, 2007.

Johansen, S. E., H. E. F. Amundssen, T. Røsten, S. Ellingsrud, T. Eidesmo, and, A. H. Bhuiyan, Subsurface hydrocarbons detected by electromagnetic sounding, *First Break, 23,* 2, 31-36, 2005.

Key, K., Application of broadband marine magnetotelluric exploration to a 3D salt structure and a fast spreading ridge, *Ph.D. thesis, University of California, San Diego, United States of America*, 2003.

Key, K., 1D inverstion of multicomponent, multifrequency marine CSEM data: Methodology and synethetic studies for resolving thin resistive layers, *Geophysics, 74,* 2, F9-F20, 2009.

Lajoie, J. J., G. F. West, Two selected field examples of EM anomalies in a conductive environment, *Geophysics, 42*, 3, 655-660, 1977.

Lelièvre, A. Carter-McAuslan, C. G. Farquharson, and C. Hurich, *The Leading Edge, 31,* 3, 322-328, 2012.

MacGregor, L. M., S. Constable, and M. C. Sinha, The RAMESSES experiment III: Controlled-source electromagnetic sounding of the Reykjanes Ridge at 57°45'N, *Geophys. J. Int., 135*, 773-789, 1998.

MacGregor, L. M., M. Sinha, and S. Constable, Electrical resistivity structure of the Valu Fa Ridge, Lau Basin, from marine controlled-source electromagnetic sounding, *Geophys. J. Int., 146,* 2001.

MacGregor, L., N. Barker, A. Overton, S. Moody, and, D. Bodecott, Derisking exploration prospects using integrated seismic and electromagnetic data — a Falkland Islands case study. *The Leading Edge, 26*, 3, 356-359, 2007.

Mackie, R. L., J. T. Smith, T. R. Madden, Three-dimensional electromagnetic modeling using finite difference equations: The magnetotelluric example, *Radio Science, 29,* 4, 923-935, 1994.

Mitsuhata, Y., and T. Uchida, 3D magnetotelluric modeling using the T-Ω finite-element method, *Geophysics, 69,* 1, 108-119, 2004.

Monk, P., Finite element methods for Maxwell's equations, *Oxford University Press,* 2003.

Myer, D., S. C. Constable, K. Key, M. E. Glinsky, G. Liu, Marine CSEM of the Scarborough gas field, Part 1: Experimental design and data uncertainty, *Geophysics, 77,* 4, E281-E299, 2012.

Nèdèlec, J. C., Mixed finite elements in $\mathbb{R}^3$, *Numerische Mathematik, 35,* 3, 315-341, 1980.

Saad, Y., SPARSKIT: a basic tool kid for sparse matrix computations, *Technical Report, 90,* 20, RIACS, NASA AMES Research Centre, 1990.

Saad, Y., Iterative methods for sparse linear systems, *Siam,* 2003.

Schwarzbach, C., Stability of finite element discretization of Maxwell's equations for geophysical application, *Ph.D. thesis, University of Frieberg, Frieberg, Germany,* 2009.

Shewchuk, J. R., Triangle: Engineering a 2D quality mesh generator and Delaunay triangulator, *Applied computational geometry towards geometric engineering, Spring Berlin Heidelberg,* 203-222, 1996.

Shewchuk, J. R., Delaunay refinement algorithms for triangular mesh generation, *Computational geometry, 22*, 1, 21-74, 2002.

Si, H. TetGen, A Quality Tetrahedral Mesh Generator and 3-Dimensional Delaunay Triangulator: Version 1.4.3. (Available at http://wias-berlin.de/software/tetgen/tegten143.html).

Si, H., and K. Gärtner, An algorithm for three-dimensional constrained Delaunay Tetrahedralizations, *Proceeding of the Fourth International Conference on Engineering Computational Technology, Lisbon, Portugal,* 2004.

Si, H., and K. Gärtner, Meshing piecewise linear complexes by constrained Delaunay tetrahedralizations, *Proceedings of the 14th international meshing roundtable, Spring Berlin Heidelberg,* 147-163, 2005.

Sinha, M. C., P.D. Patel, M. J. Unsworth, T. R. E. Owen, and M. D. MacCormack, An Electromagnetic Sounding System for Marine Use, *Marine Geophysical Research*, 12, 59-68, 1990.

Srnka, L. J., Method and apparatus for offshore electromagnetic soundign utilizing wavelength effects to determine optimum source and detector positions, *US Patent 4 617 518,* Oct. 14, 1986.

Stefatos, A., M. Boulaenko, J. Hesthammer, Marine CSEM technology performance in hydrocarbon exploration — limitations or opportunities? *First Break, 27,* 5, 2009.

Wait, J. R., Geo-electromagnetism, *Academic Press*, 1982.

Wang, T., G. W. Hohmann, A finite-difference, time-domain solution for three-dimensional electromagnetic modeling, *Geophysics, 58,* 6, 797-809, 1993.

Westerdahl, H., S.E. Johnstad, and B.A. Farrelly, Electromagnetic method on shallow water using a controlled source, *US Patent 0 278 541 A1,* Nov. 12, 2009.

Weiss, C., The fallacy of the shallow-water problem in marine CSEM exploration, *Geophysics, 72,* 6, A93-A97, 2007.

Wu, X., A. M. Ø. Ghazi, J. Rasmussen, B. Spindler, I. Atkinson, and, D. E. Cameron, EM survey in the Flemish Pass Basin, East Canada, *GeoConvention 2015*, Canadian Society of Exploration Geophysicists, 2015.

Appendices

Appendix A

Water Depth Models

Phase results from Key's DIPOLE1D semi-analytical method were shifted -270 degrees in order to match the results of this study.

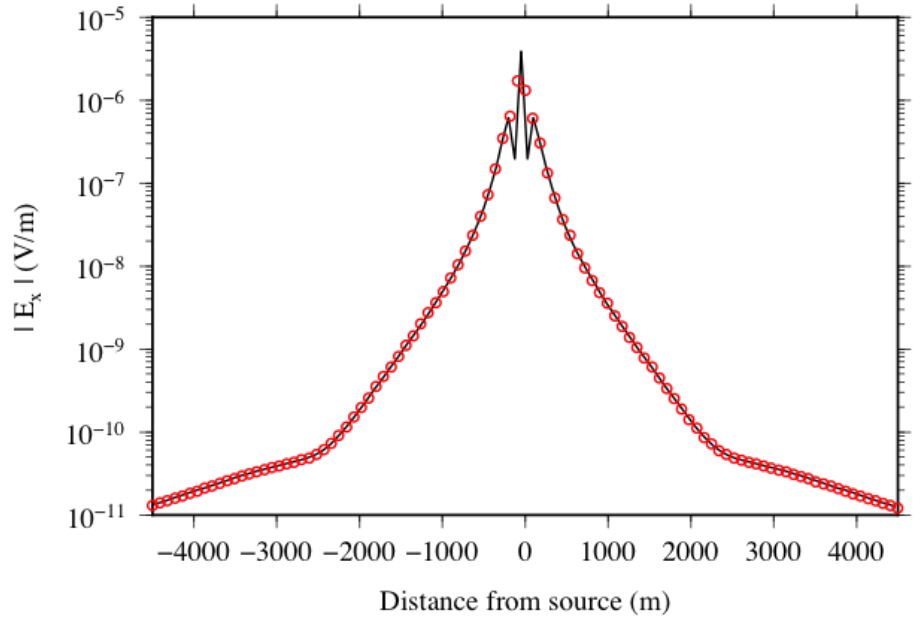

(a)

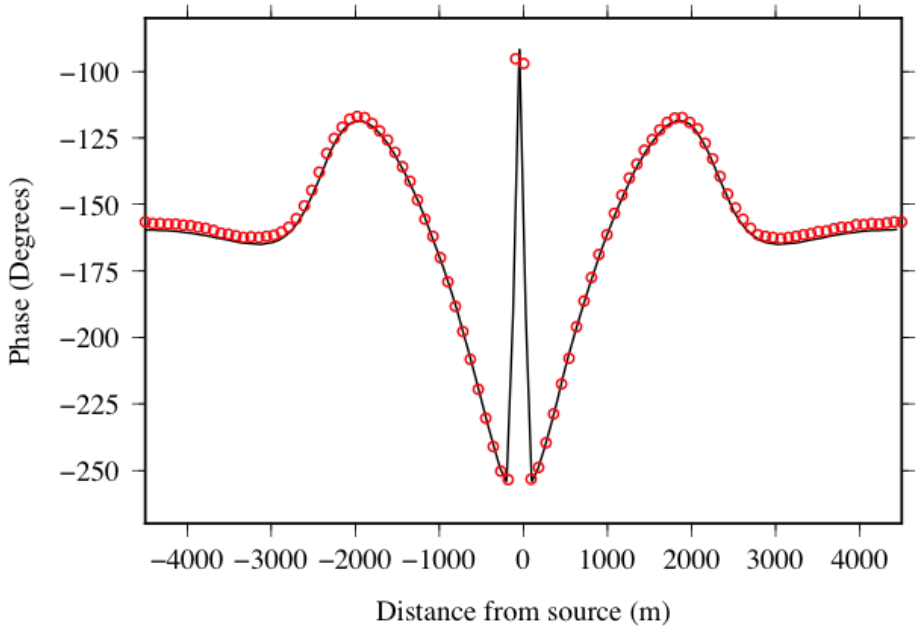

(b)

Figure A.1: Panel (a) electric field amplitude and panel (b) phase results for the *300 m Water Depth* model (Figure 3.11). Red circles indicate values computed using the mesh in Figure 3.11; the black lines indicate the results from DIPOLE1D.

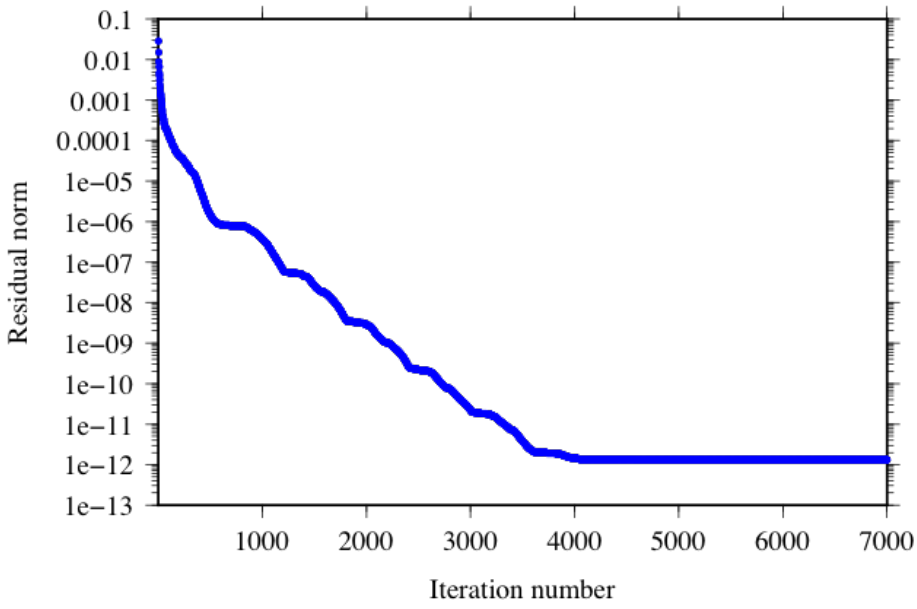

Figure A.2: Convergence cuve for the *300 m Water Depth* model (Figure 3.11).

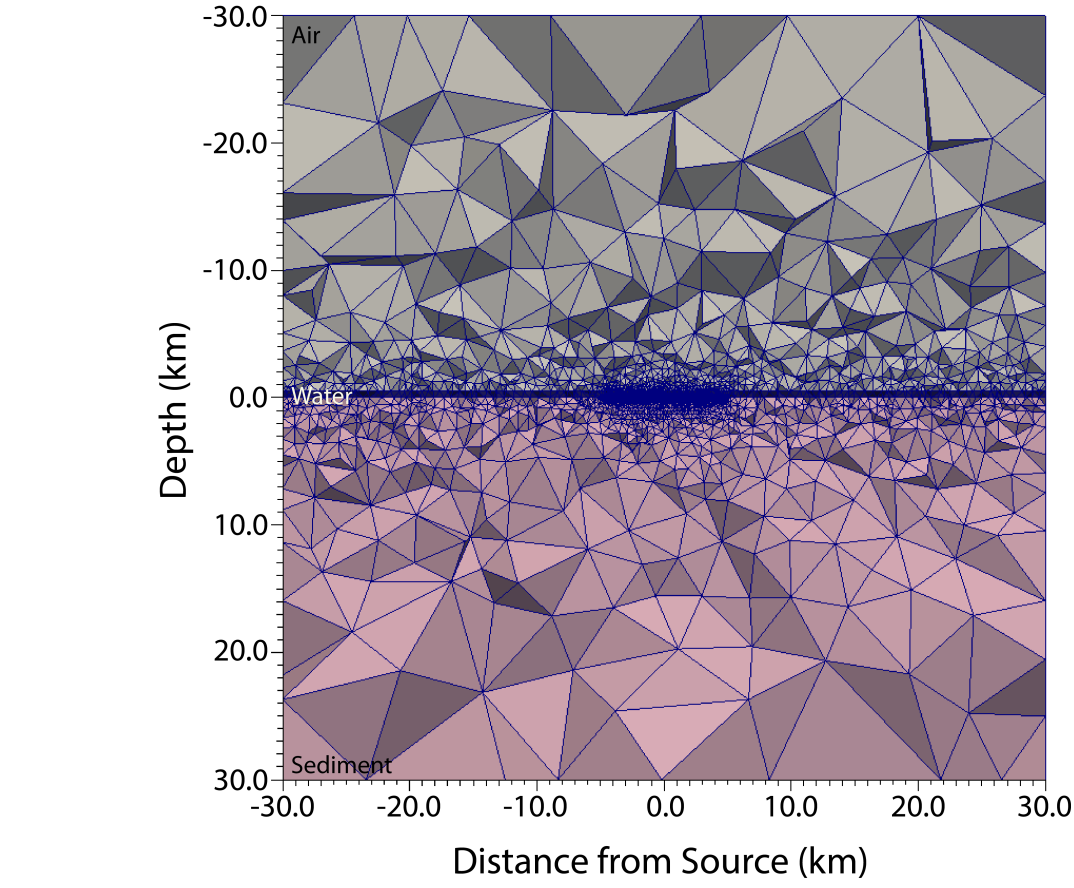

(a)

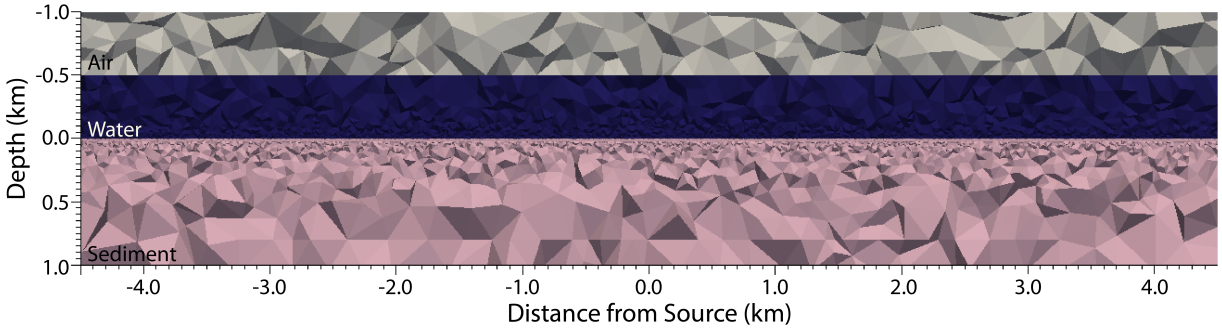

(b)

Figure A.3: Cross-sections centered at $y = 0$ m of the *500 m Water Depth* model. Panel (a) full view; panel (b) enhanced view of the central section of the mesh and water layer. The air layer has a conductivity of 10^{-8} S/m, the water layer (navy) has a conductivity of 3.2 S/m and the sediment layer (pink) has a conductivity of 1.0 S/m.

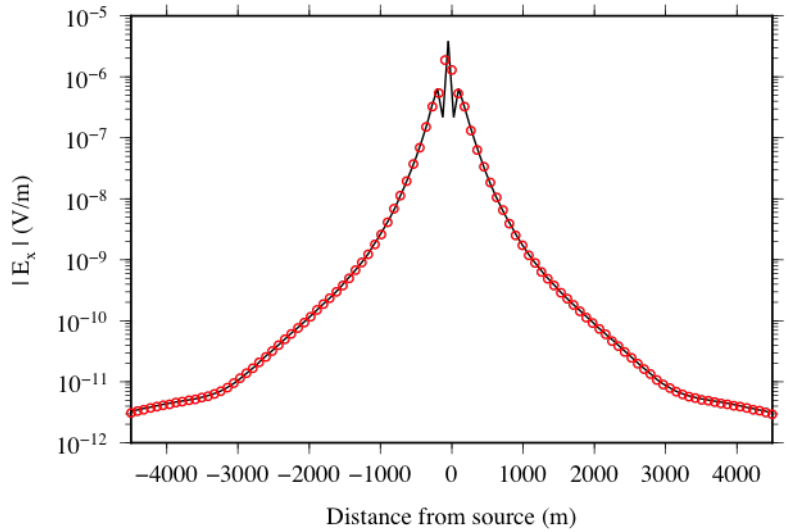

Figure A.4: Electric field amplitude results for the *500 m Water Depth* model (Figure A.3) shown as red circles, with the results from DIPOLE1D as black lines.

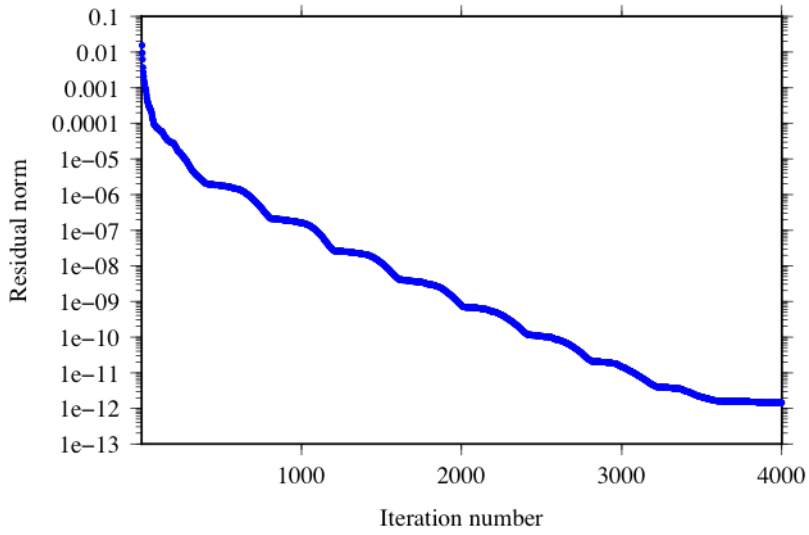

Figure A.5: Convergence curve of the *500 m Water Depth* model (Figure A.3).

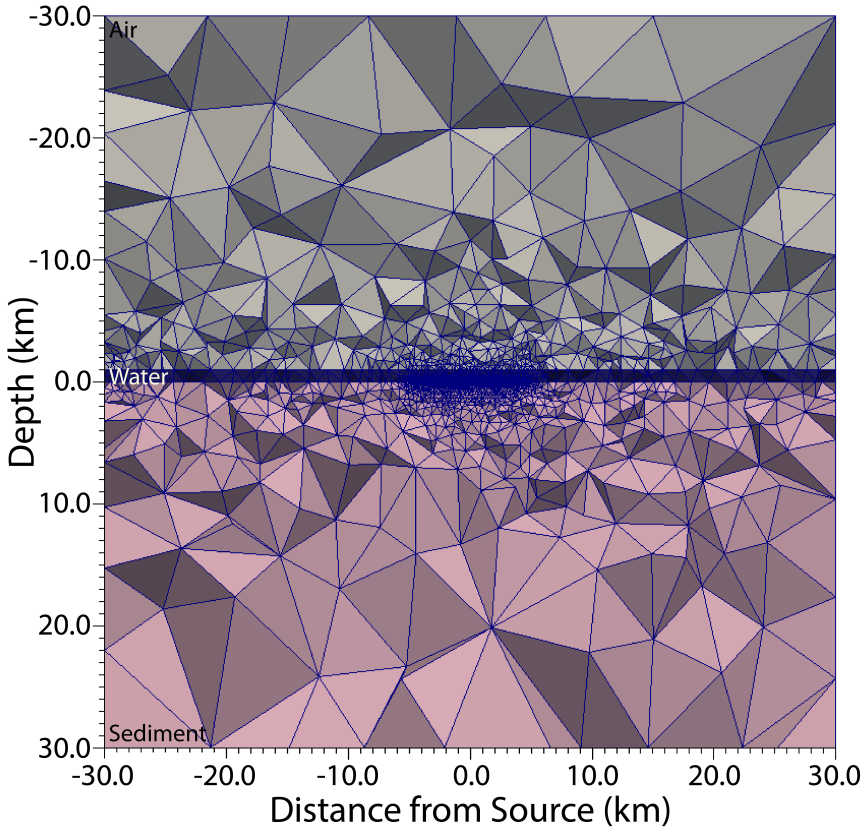

(a)

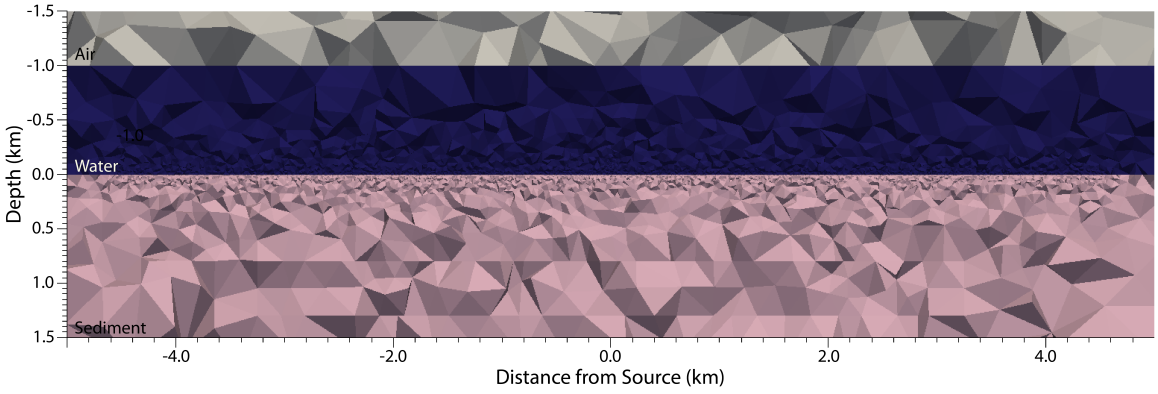

(b)

Figure A.6: Cross-sections centered at $y = 0$ m of the 1000 m water depth model. Panel (a) full view; panel (b) enhanced view of the central section of the mesh and water layer. The air layer has a conductivity of 10^{-8} S/m, the water layer (navy) has a conductivity of 3.2 S/m and the sediment layer (pink) has a conductivity of 1.0 S/m.

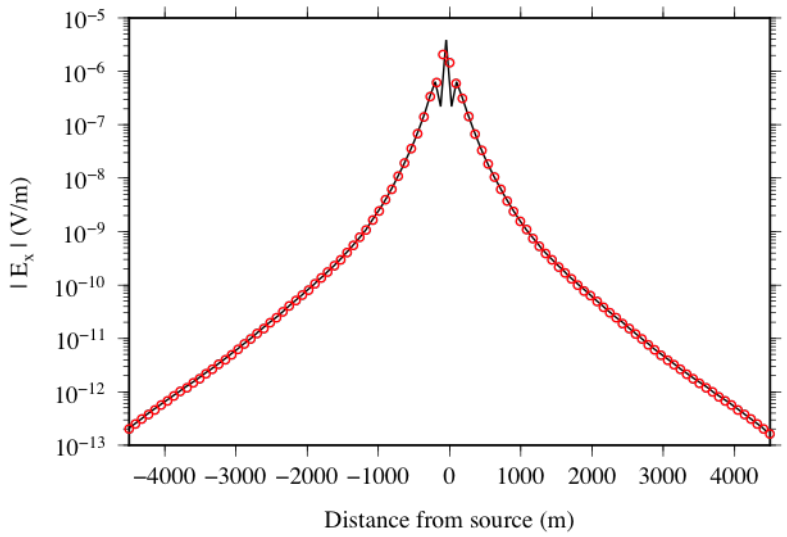

Figure A.7: Electric field amplitude results for the *1000 m Water Depth* model (Figure A.6) shown as red circles, with the results from DIPOLE1D as black lines.

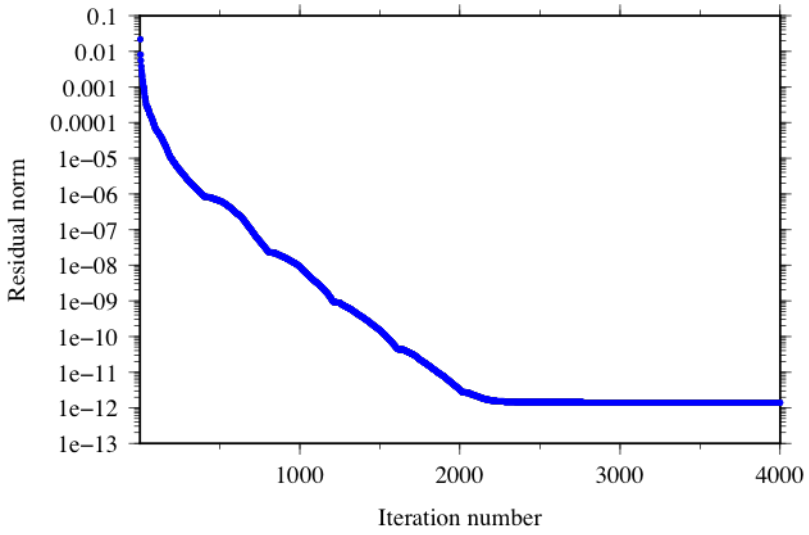

Figure A.8: Convergence curve of the *1000 m Water Depth* model (Figure A.6).

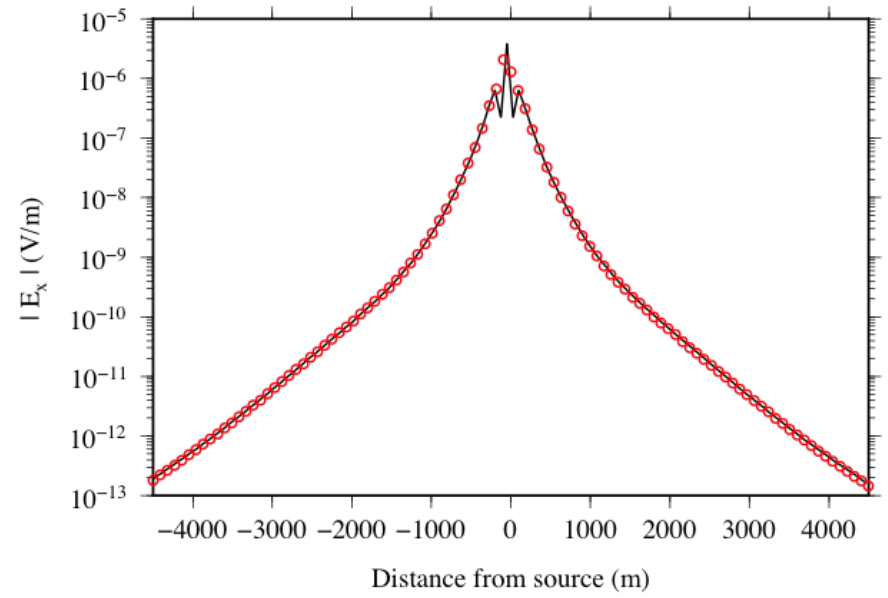

(a)

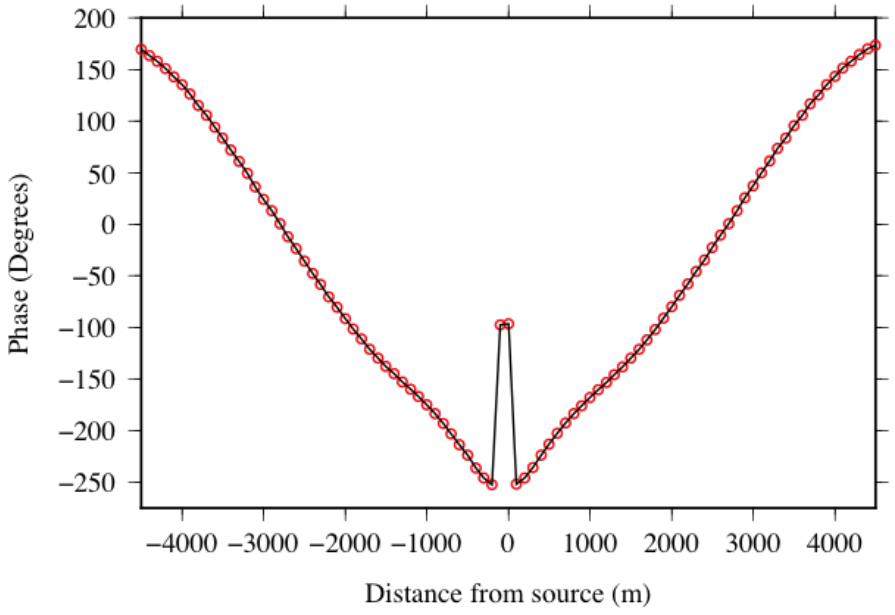

(b)

Figure A.9: Panel (a) electric field amplitude and panel (b) phase results for the *1150 m Water Depth* model (Figure 3.12). Red circles indicate values computed using the mesh in Figure 3.12; the black lines indicate the semi-analytical results from DIPOLE1D.

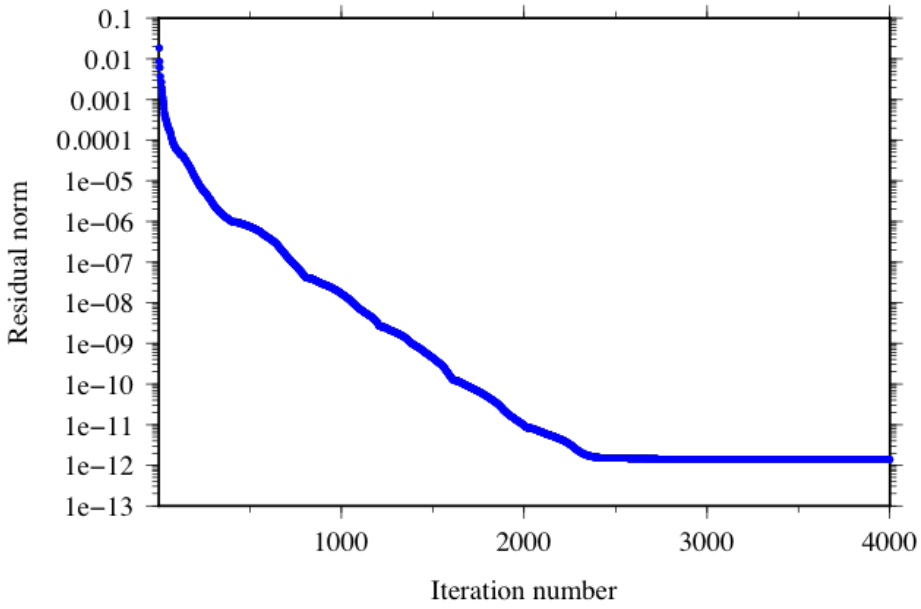

Figure A.10: Convergence cuve for the *1150 m Water Depth* model (Figure 3.12).

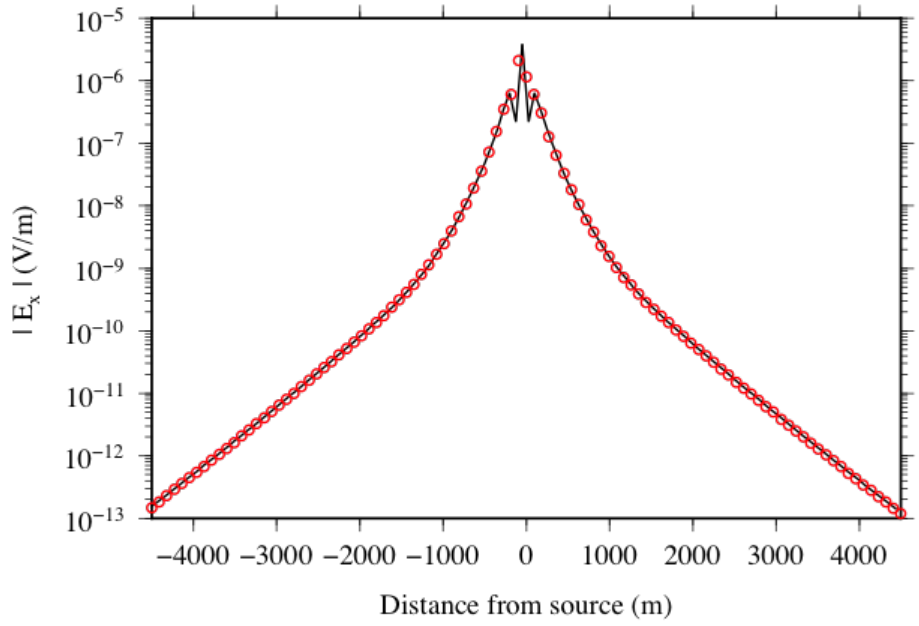

(a)

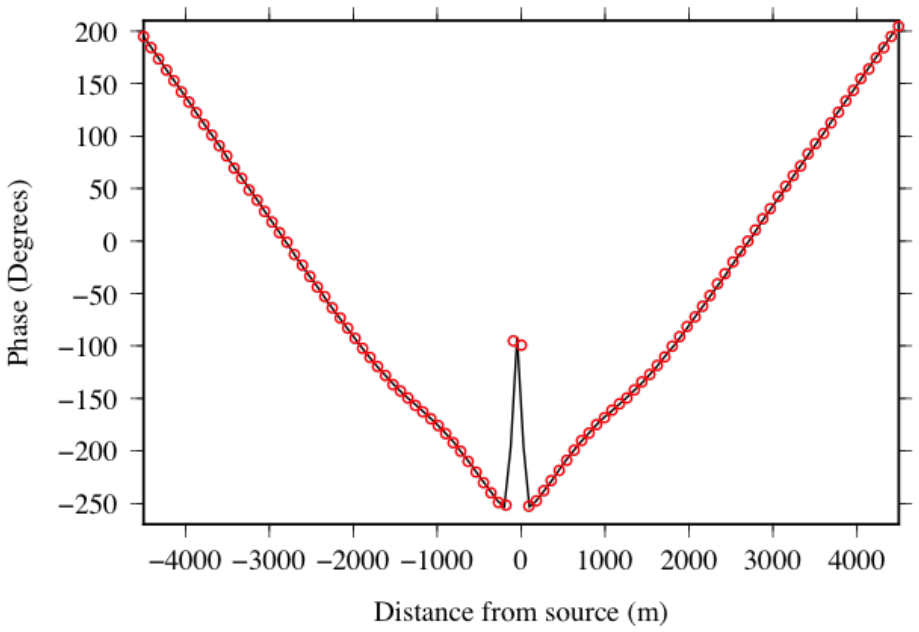

(b)

Figure A.11: Panel (a) electric field amplitude and panel (b) phase results for the model and mesh in Figure 3.13 (*3000 m Water Depth*). Red circles indicate values computed using the mesh in Figure 3.13; the black lines indicate the results from DIPOLE1D.

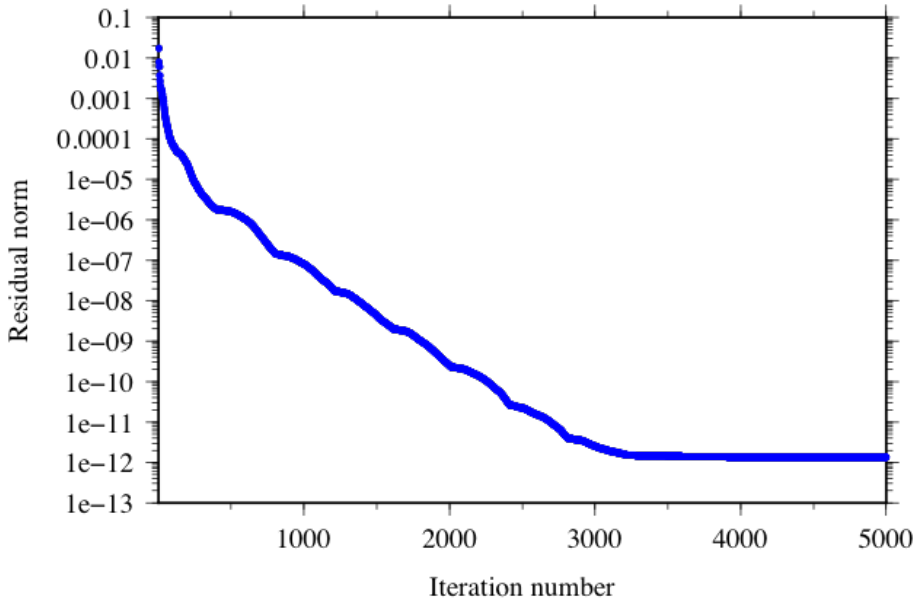

Figure A.12: Convergence curve for the *3000 m Water Depth* model (Figure 3.13).

Appendix B

Additional Canonical Disk Models

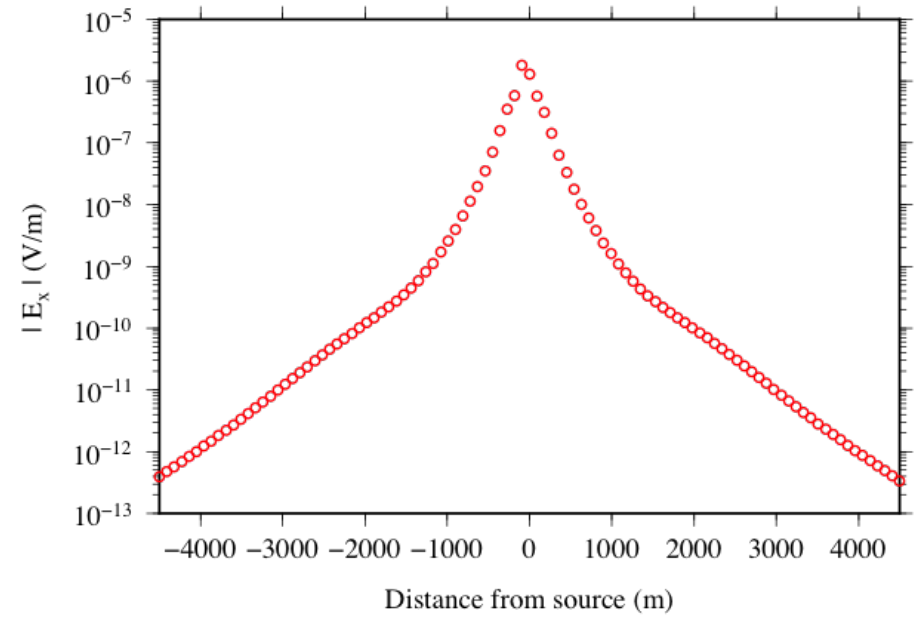

(a)

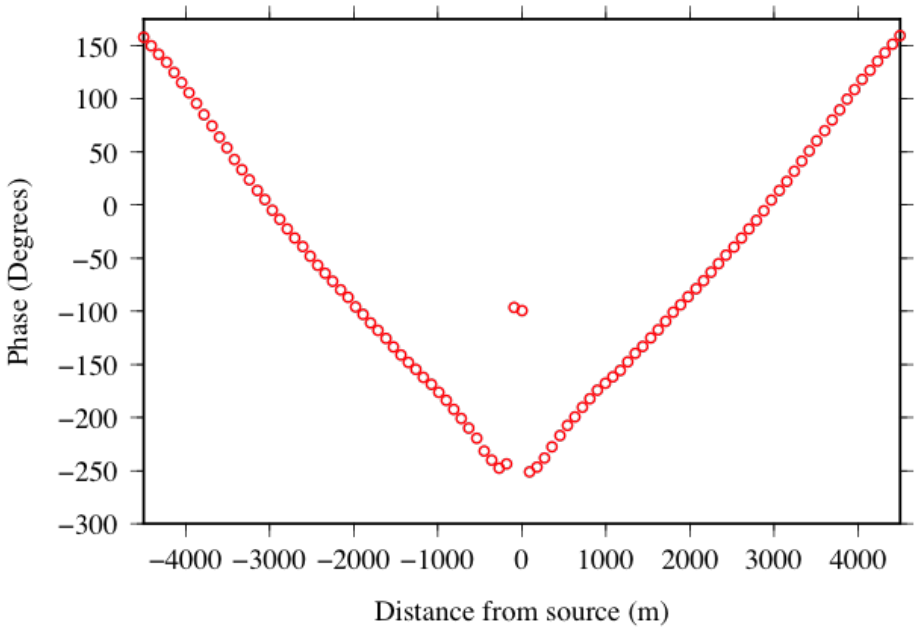

(b)

Figure B.1: Panel (a) electric field amplitude and panel (b) phase results for the model and mesh of the *50 m Disk Thickness* scenario in Figure 3.19.

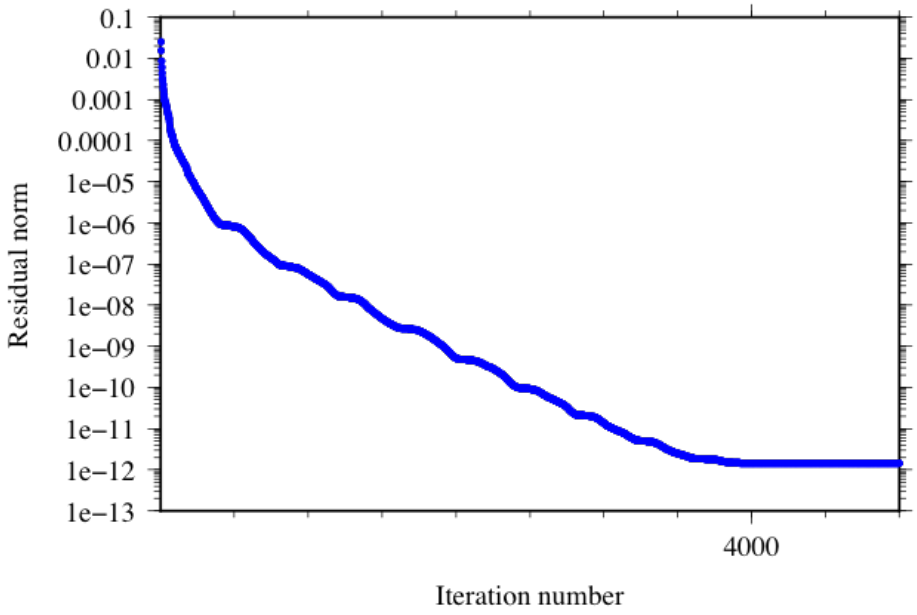

Figure B.2: Convergence curve for the model and mesh of the *50 m Disk Thickness* scenario in Figure 3.19.

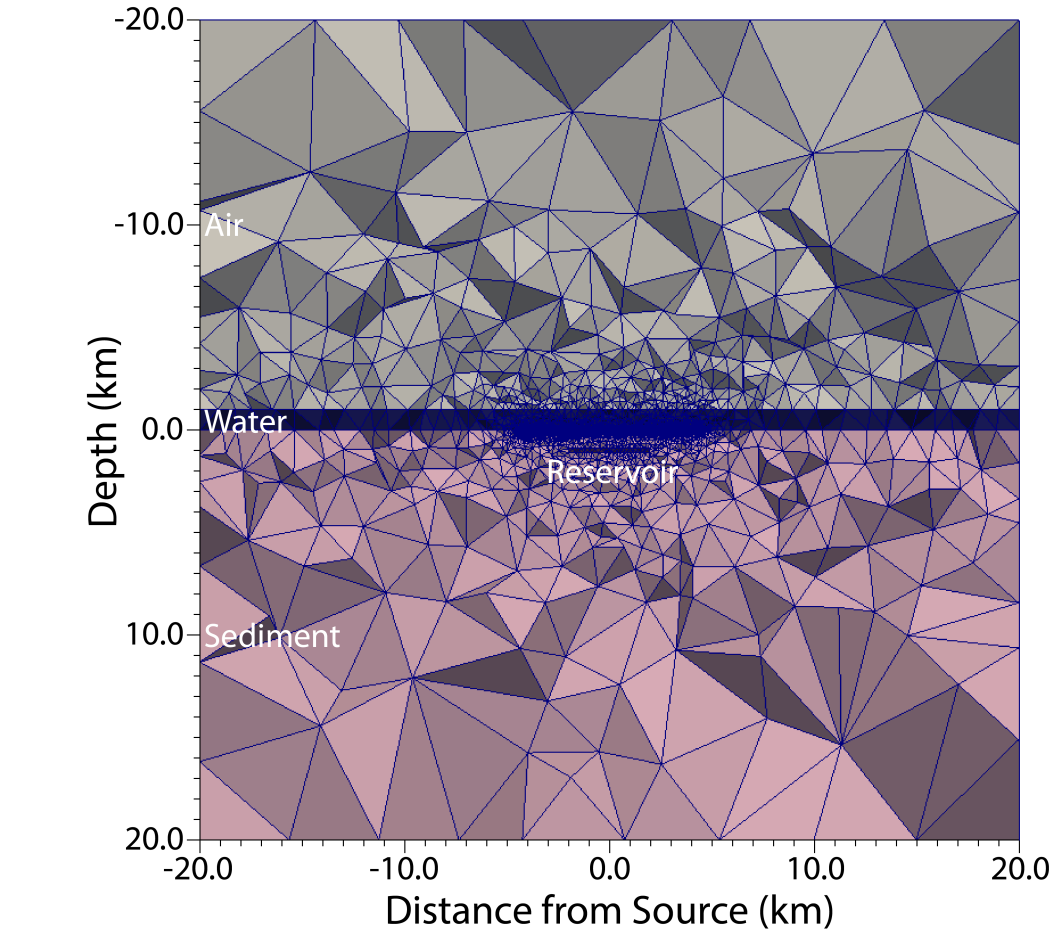

(a)

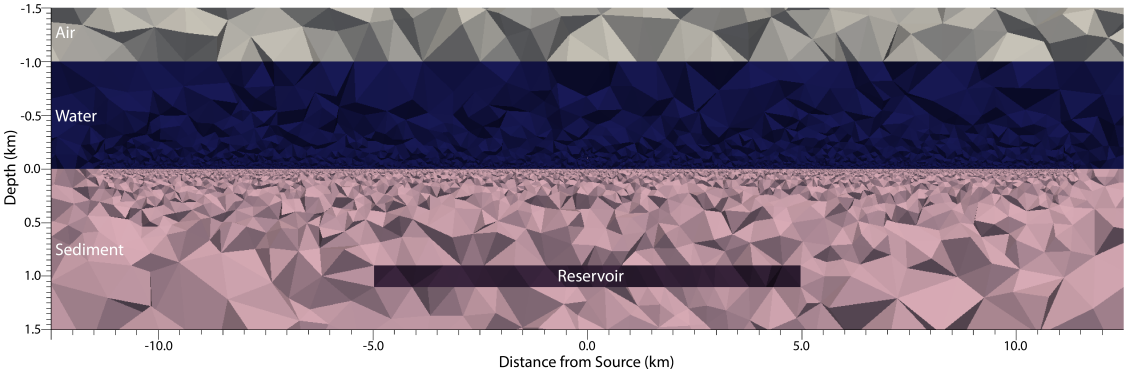

(b)

Figure B.3: Cross-sections centered at $y = 0$ m of the disk model with *200 m Thickness* and 1000 m depth. Panel (a) full view; panel (b) enhanced view of the reservoir.

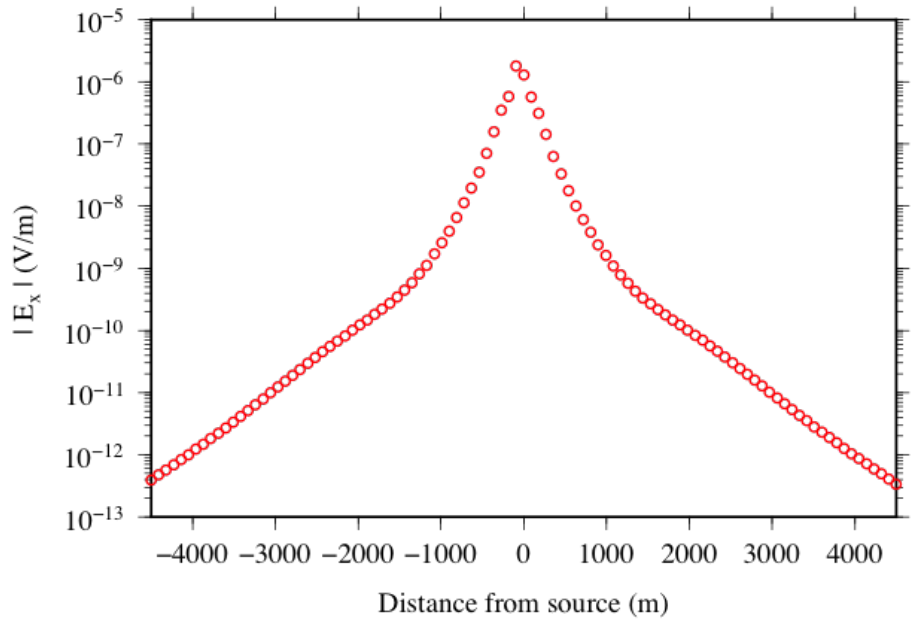

(a)

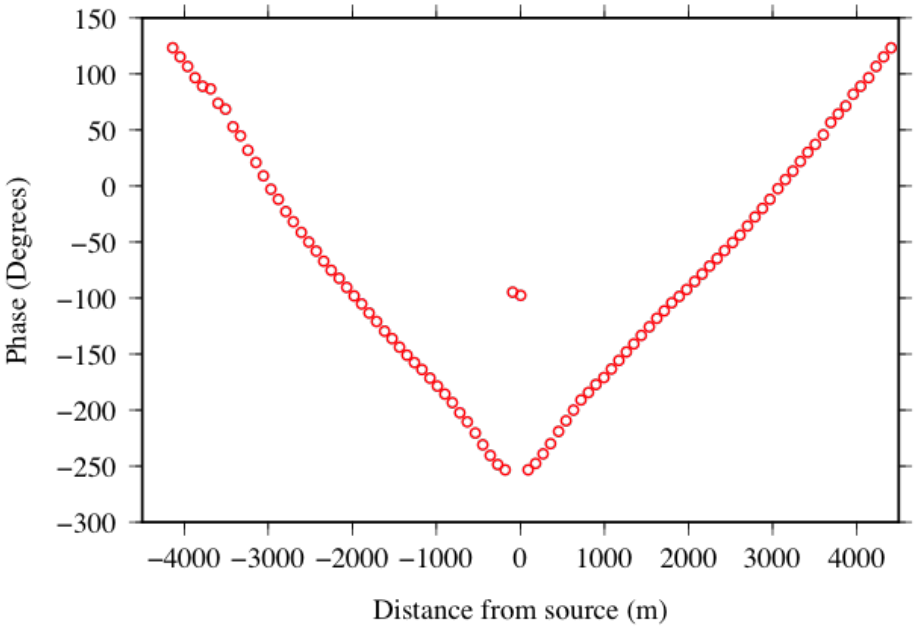

(b)

Figure B.4: Panel (a) electric field amplitude and panel (b) phase results for the model and mesh of the *200 m Disk Thickness* scenario (Figure B.3) .

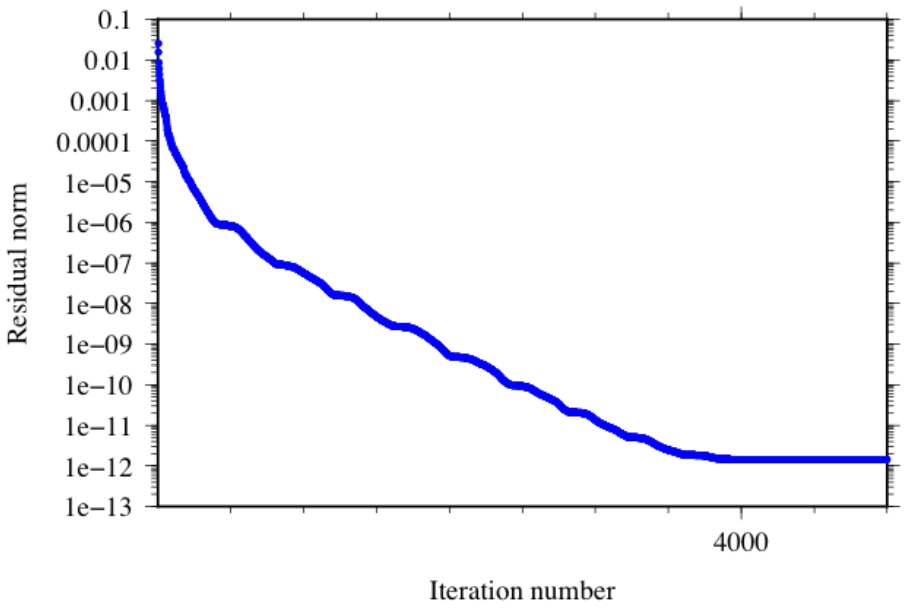

Figure B.5: Convergence curve for the model and mesh of the *200 m Disk Thickness* scenario (Figure B.3) .

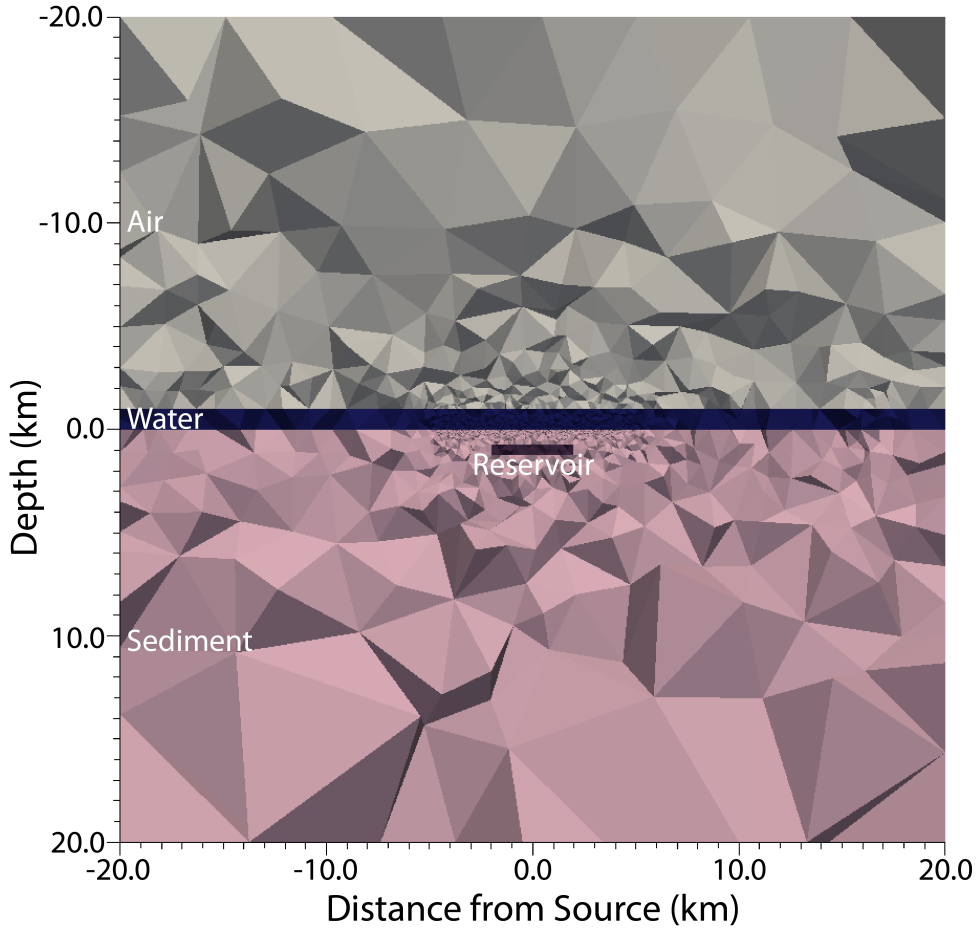

(a)

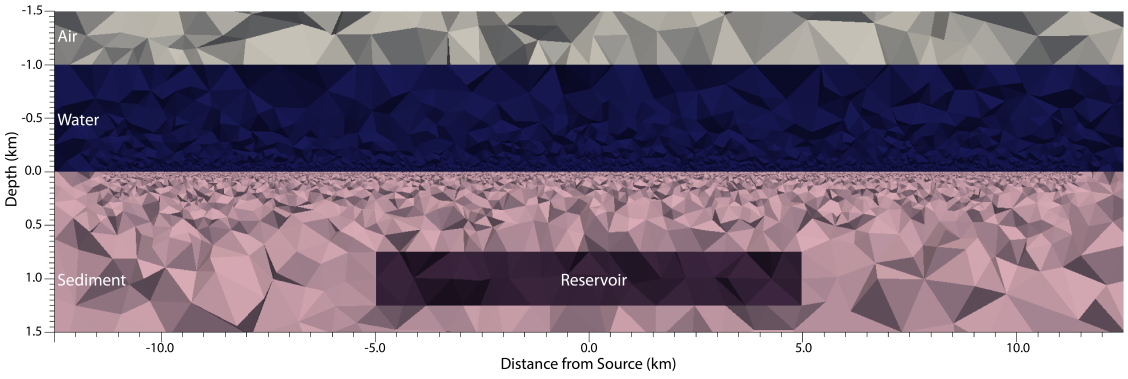

(b)

Figure B.6: Cross-sections centered at $y = 0$ m of the disk model with *500 m Thickness* and 1000 m depth. Panel (a) full view; panel (b) enhanced view of the reservoir.

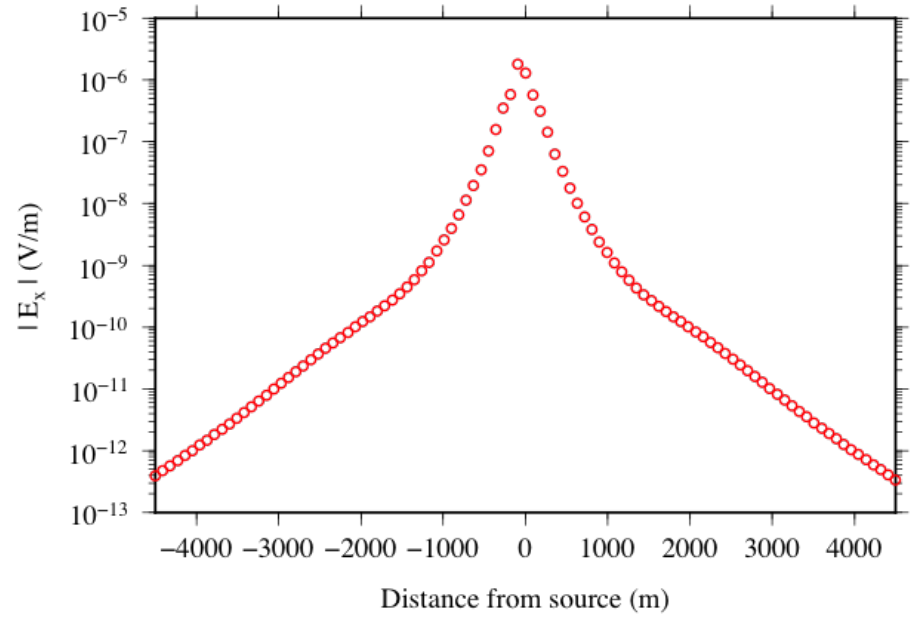

(a)

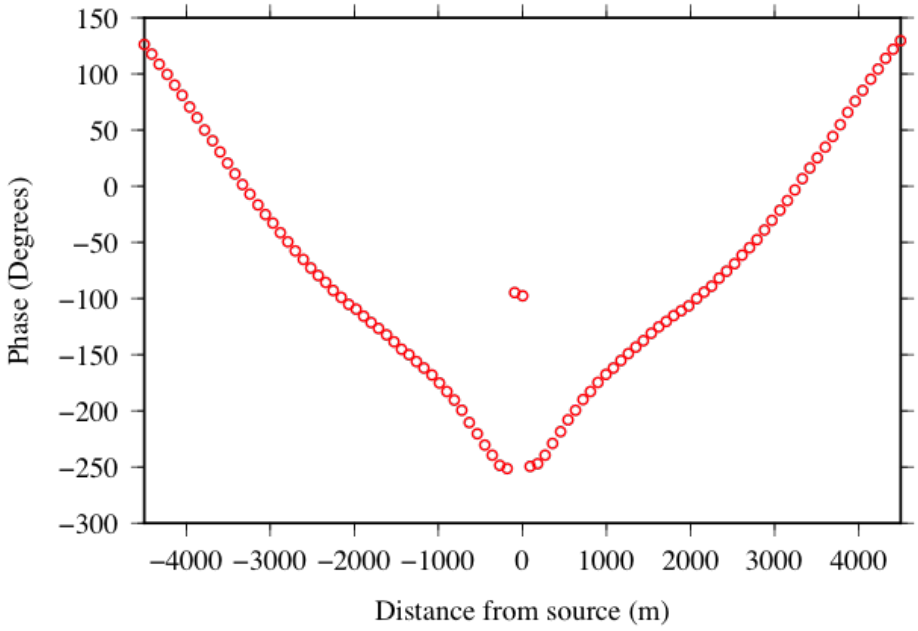

(b)

Figure B.7: Panel (a) electric field amplitude and panel (b) phase results for the model and mesh for the *500 m Disk Thickness* scenario (Figure B.6).

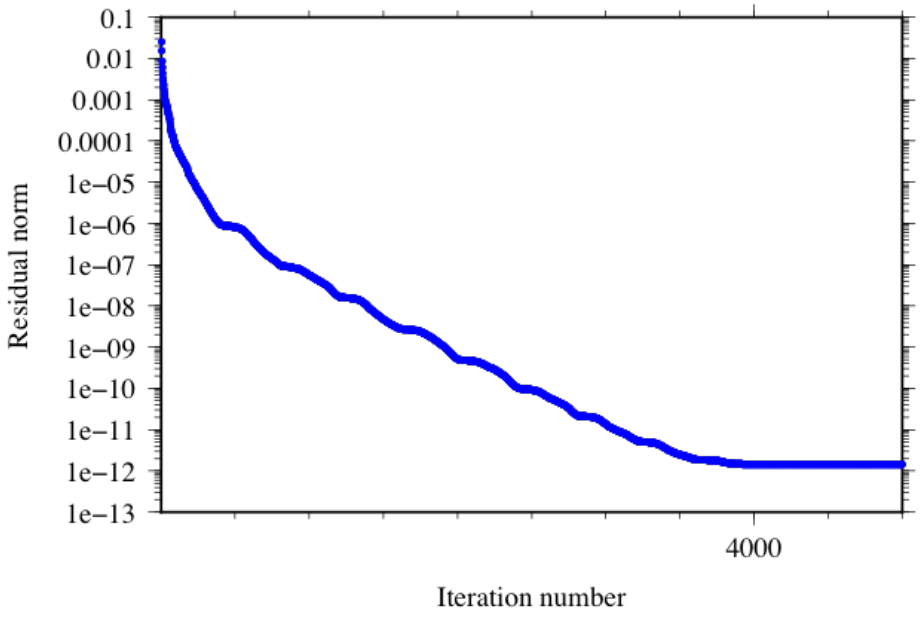

Figure B.8: Convergence curve for the model and mesh for the *500 m Disk Thickness* scenario (Figure B.6) .

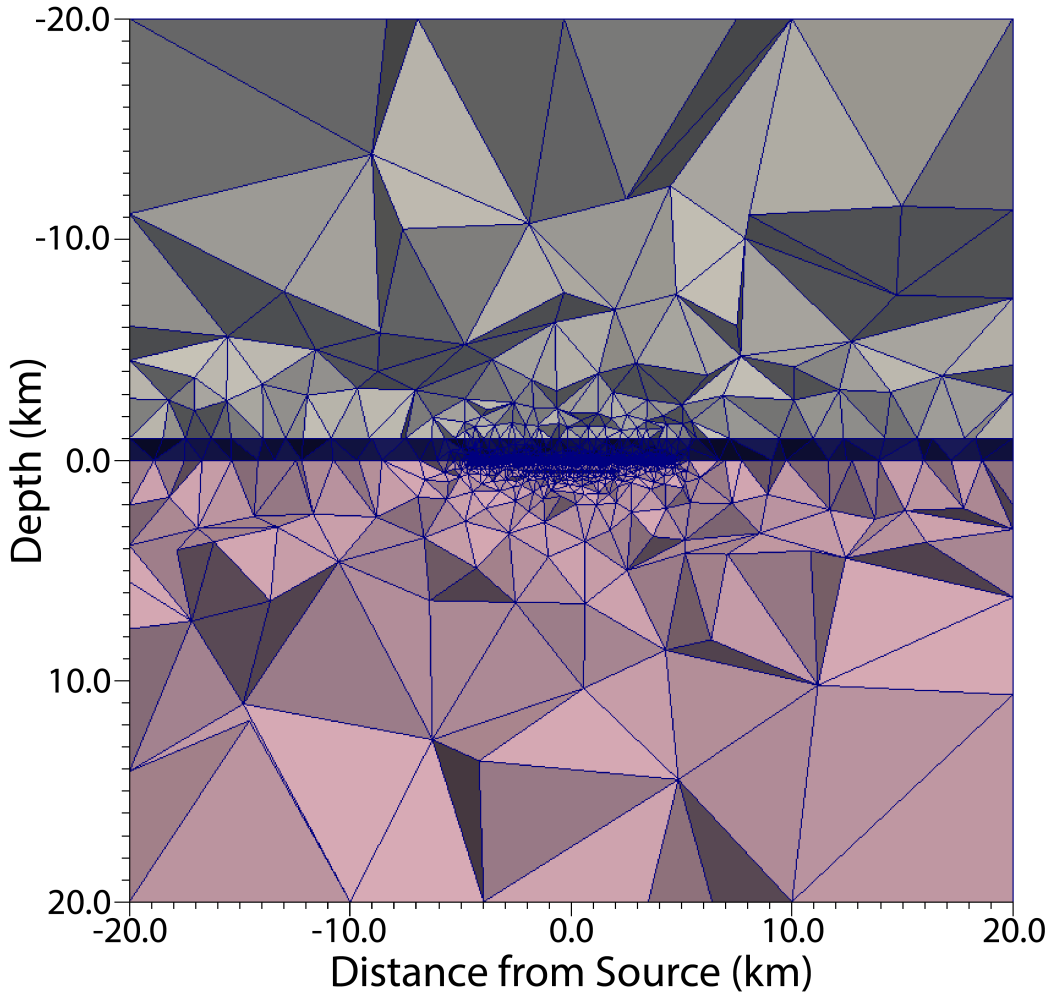

(a)

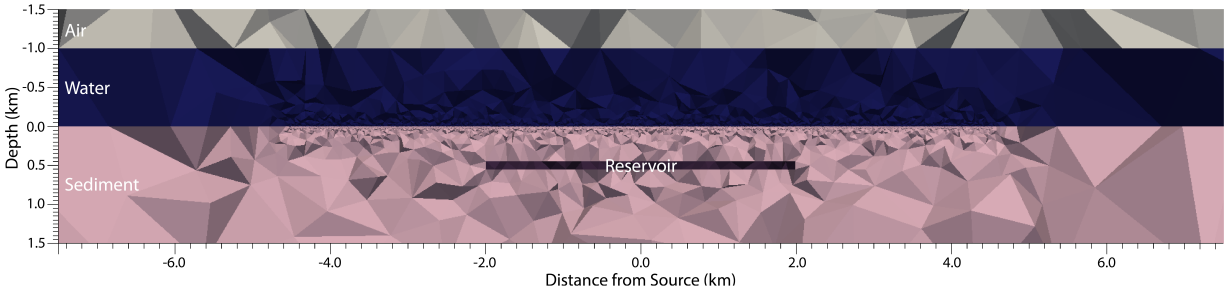

(b)

Figure B.9: Cross-sections centered at $y = 0$ m of the disk model at *500 m Depth* and 100 m thickness. Panel (a) full view; panel (b) enhanced view of the reservoir.

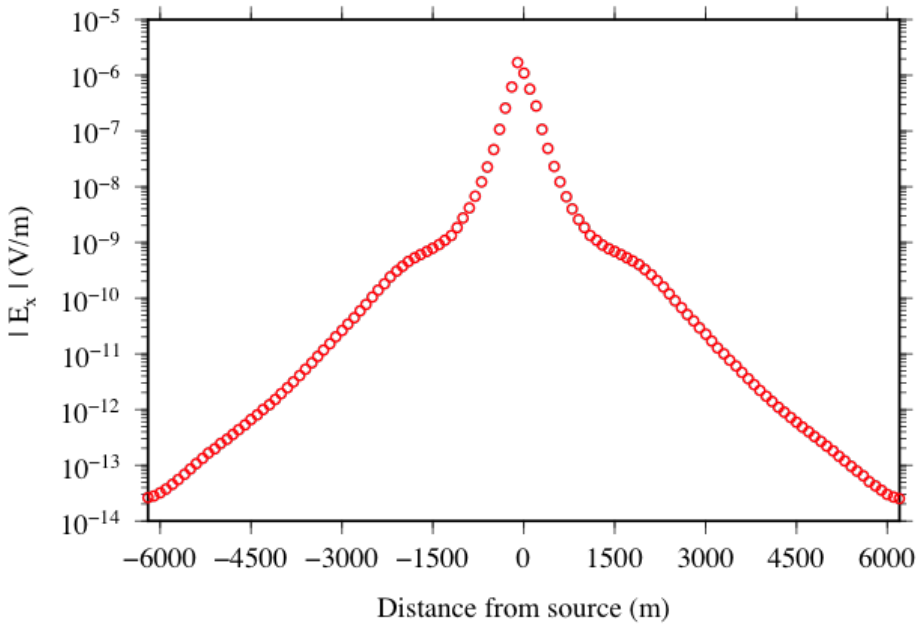

(a)

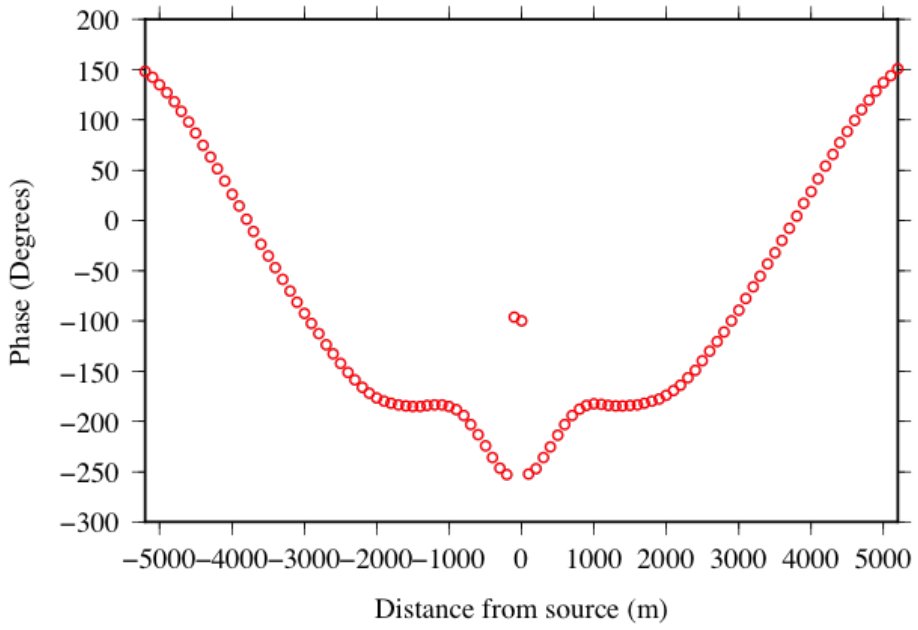

(b)

Figure B.10: Panel (a) electric field amplitude and panel (b) phase results for the model and mesh of the *500 m Disk Depth* scenario (Figure B.9).

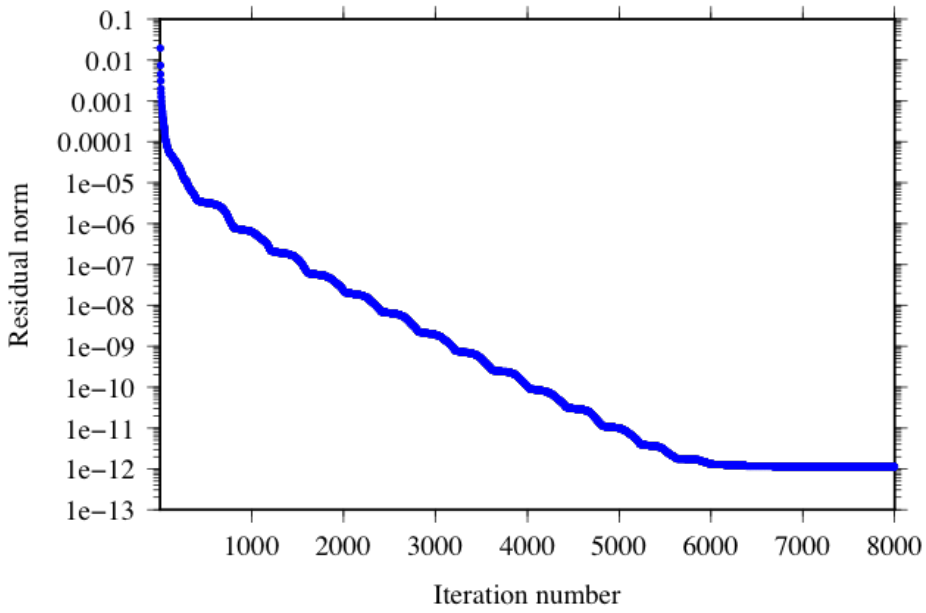

Figure B.11: Convergence curve for the model and mesh of the *500 m Disk Depth* scenario (Figure B.9).

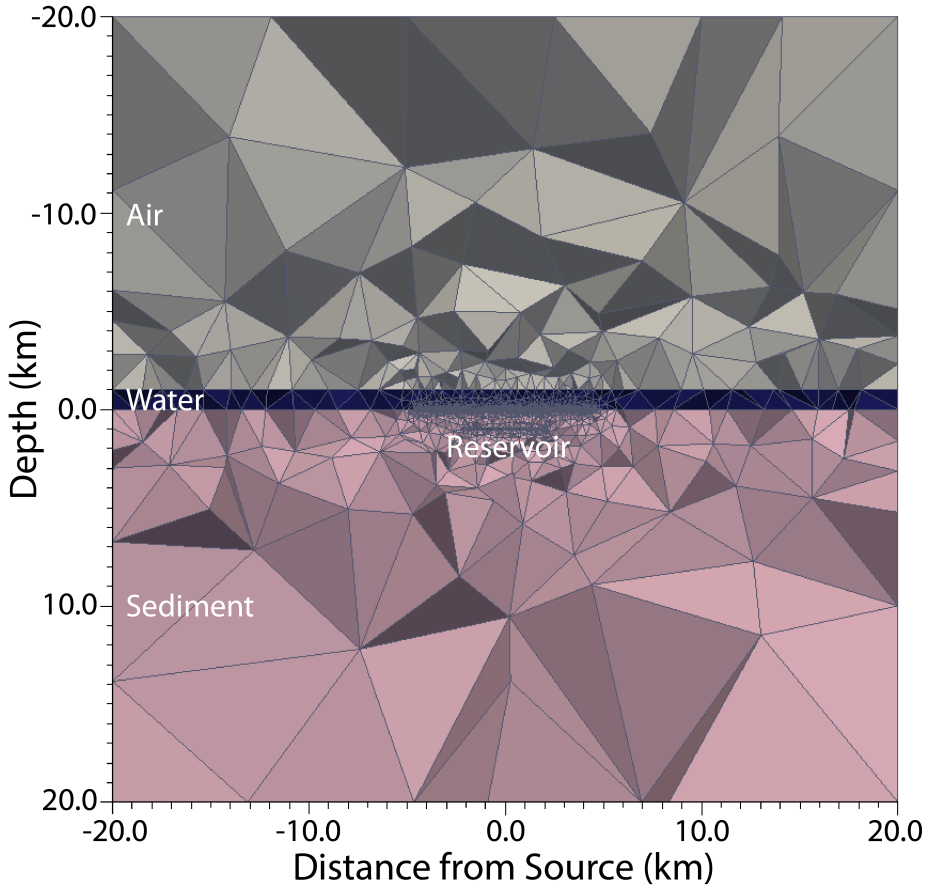

(a)

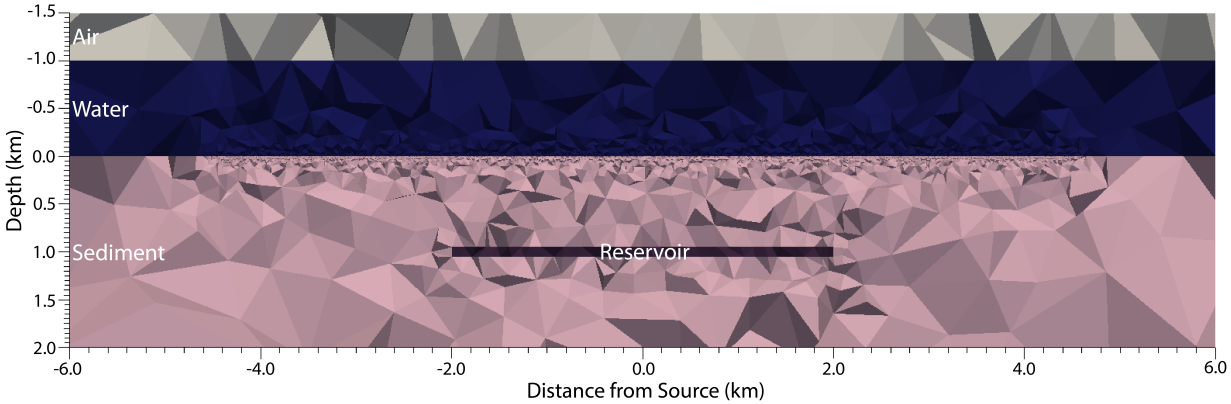

(b)

Figure B.12: Cross-sections centered at $y = 0$ m of the disk model at *1000 m Depth* and 100 m thickness. Panel (a) full view; panel (b) enhanced view of the reservoir.

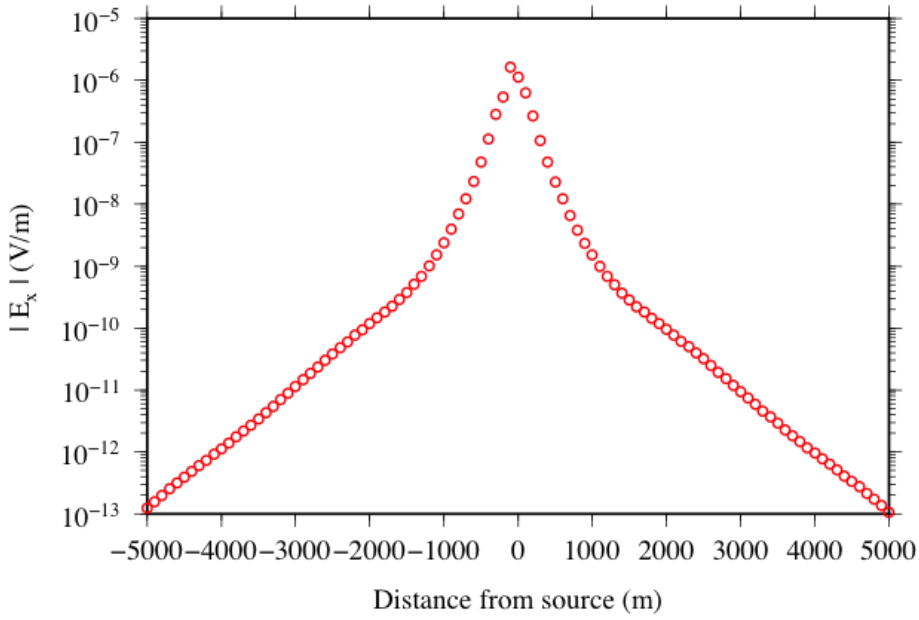

(a)

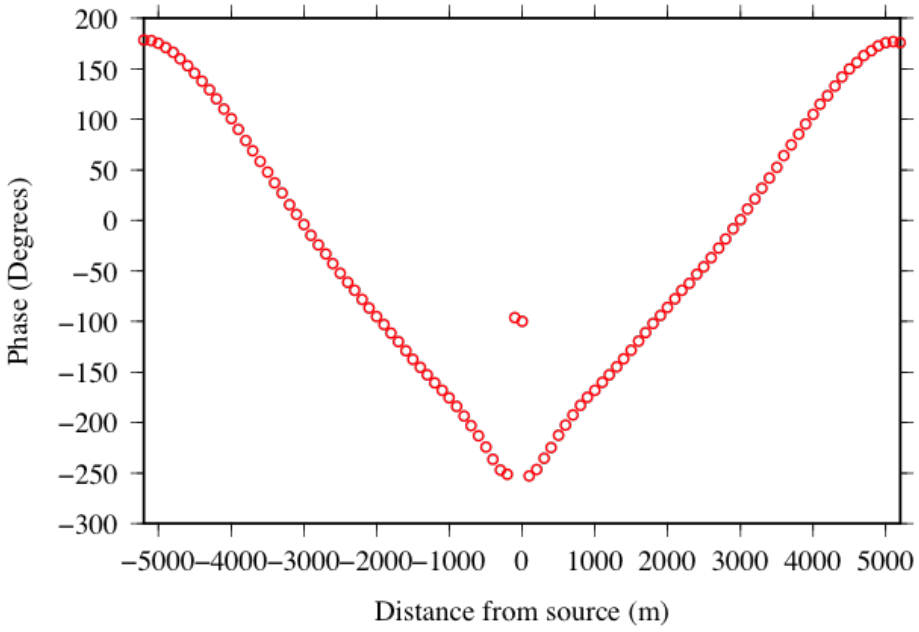

(b)

Figure B.13: Panel (a) electric field amplitude and panel (b) phase results for the model and mesh of the *1000 m Disk Depth* scenario (Figure B.12).

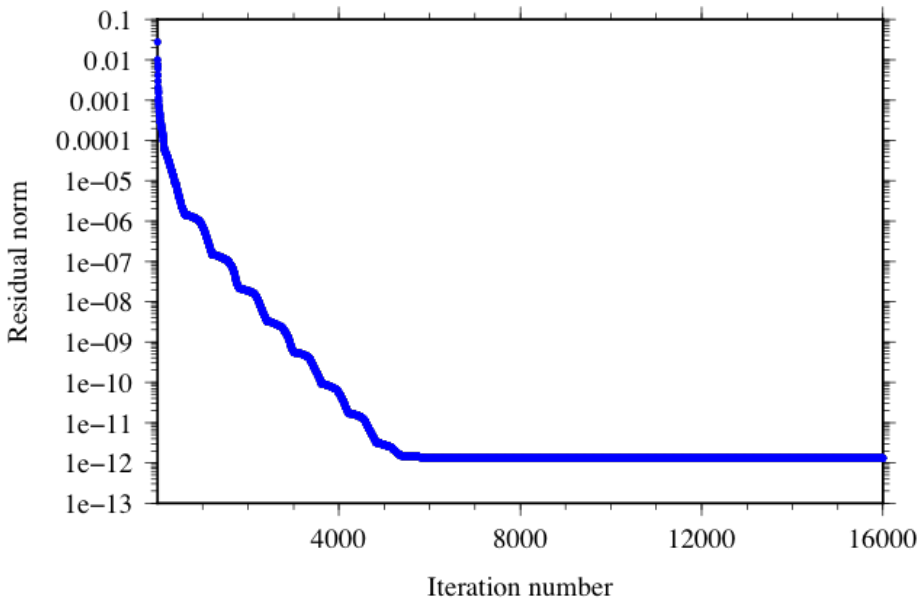

Figure B.14: Convergence curve of the *1000 m Disk Depth* scenario (Figure B.12) .

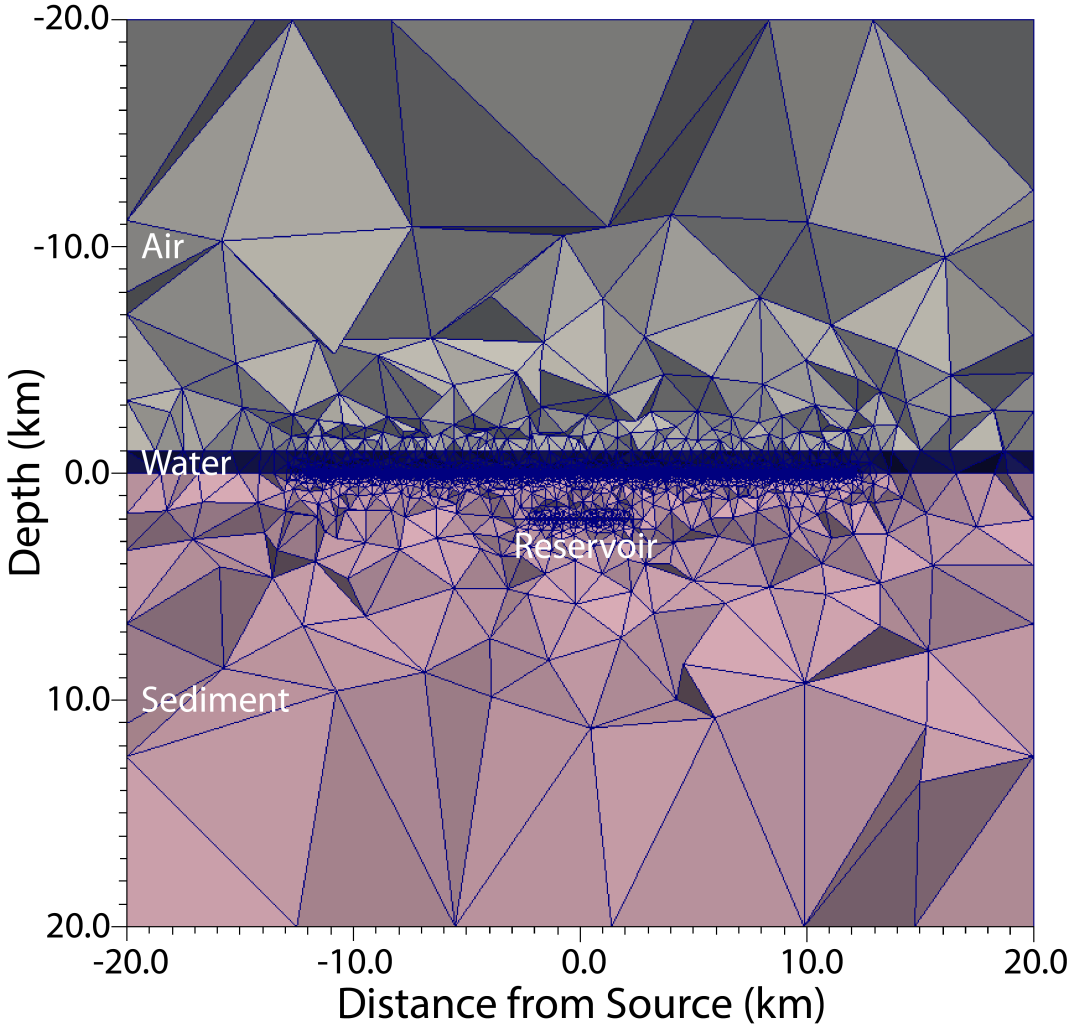

(a)

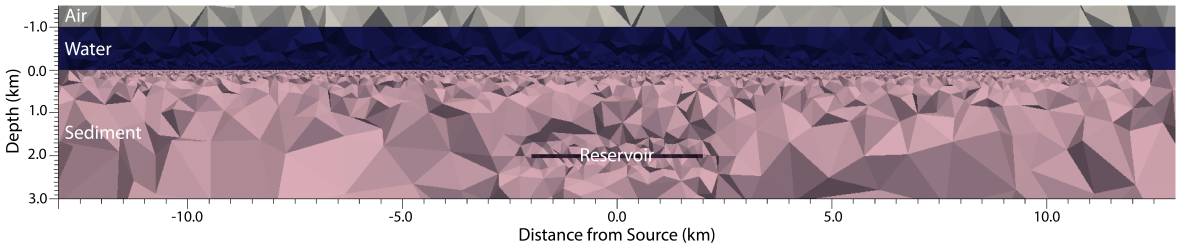

(b)

Figure B.15: Cross-sections centered at $y = 0$ m of the disk model at *2000 m Depth* and 100 m thickness. Panel (a) full view; panel (b) enhanced view of the reservoir.

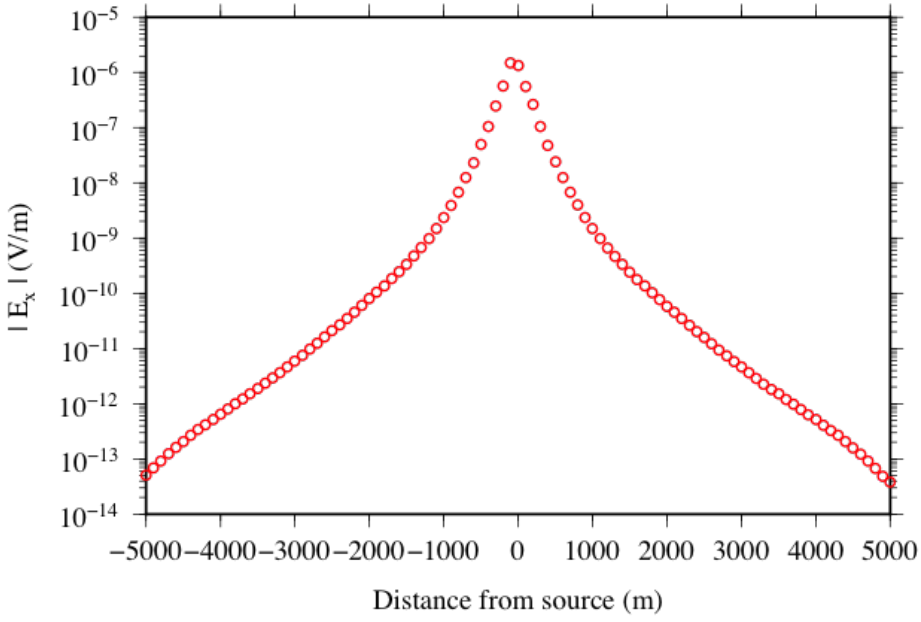

(a)

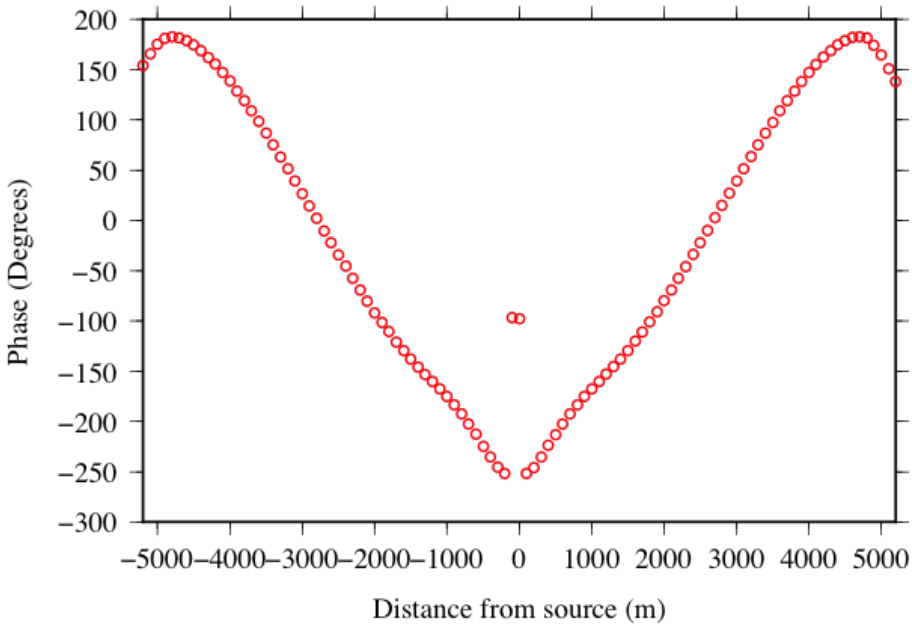

(b)

Figure B.16: Panel (a) electric field amplitude and panel (b) phase results of the *2000 m Disk Depth* scenario (Figure B.15).

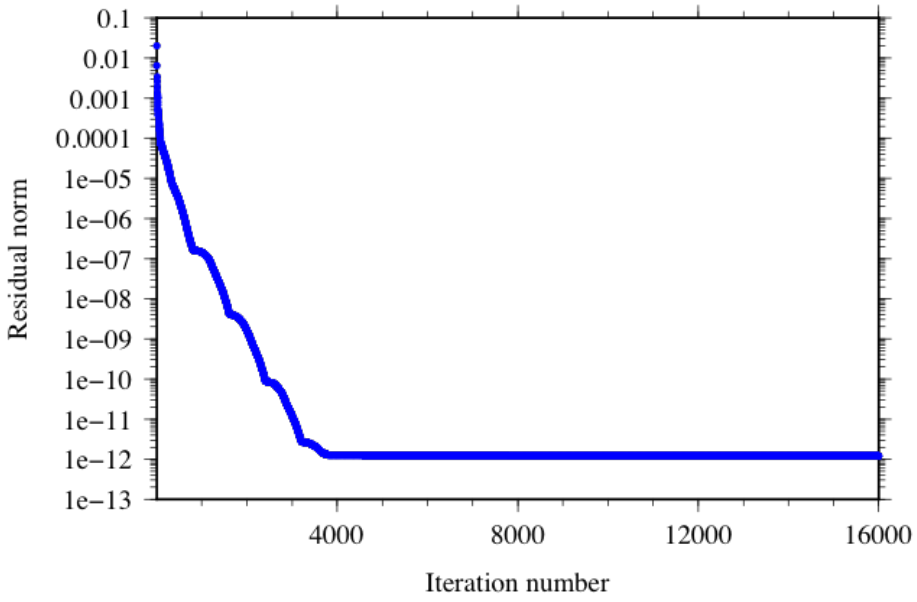

Figure B.17: Convergence curve of the(*2000 m Disk Depth* scenario (Figure B.15).

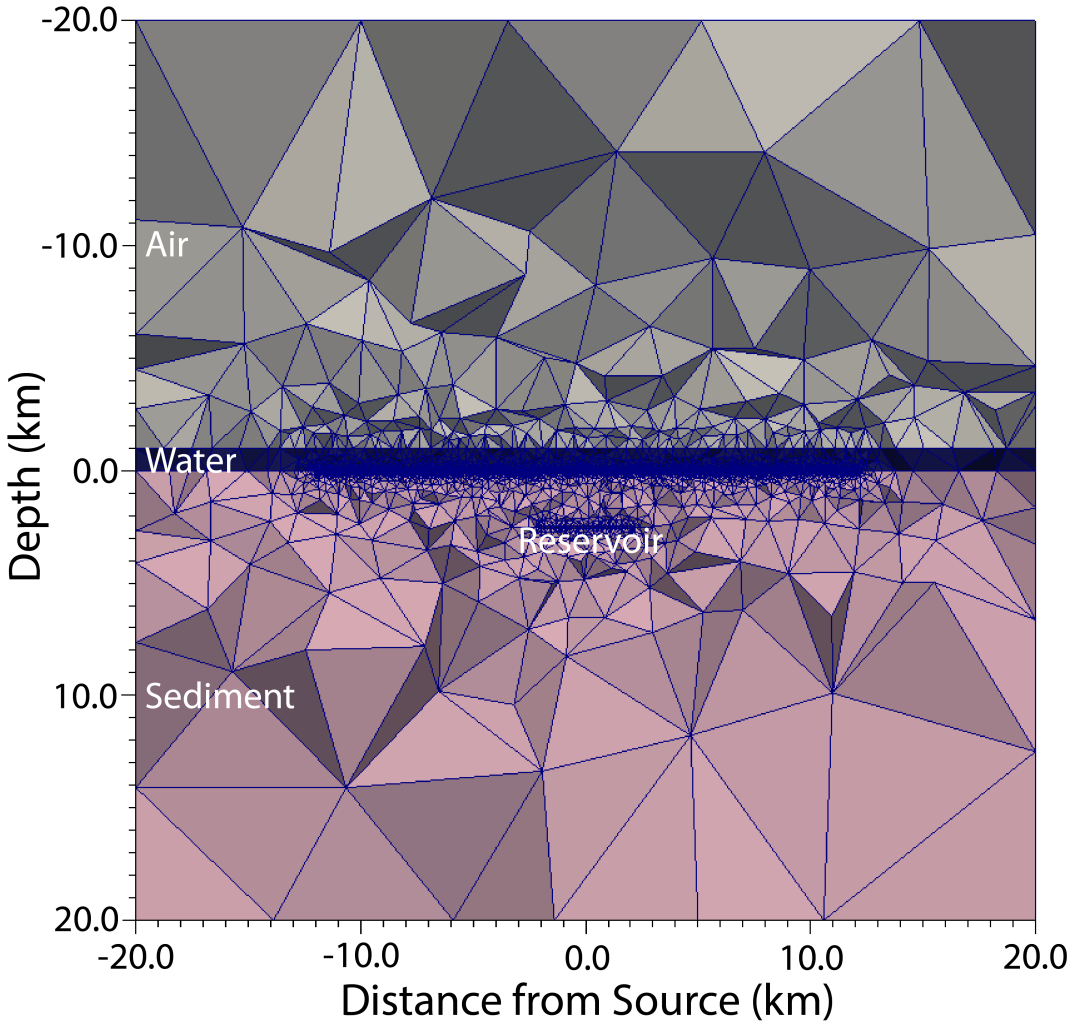

(a)

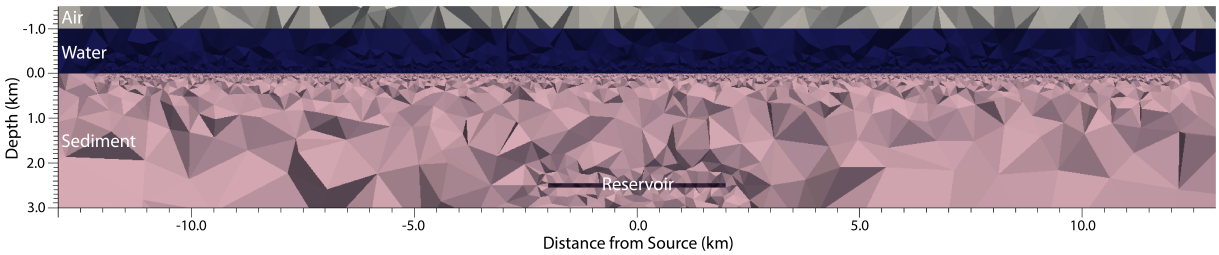

(b)

Figure B.18: Cross-sections centered at $y = 0$ m of the disk model at *2500 m Depth* and 100 m thickness. Panel (a) full view; panel (b) enhanced view of the reservoir.

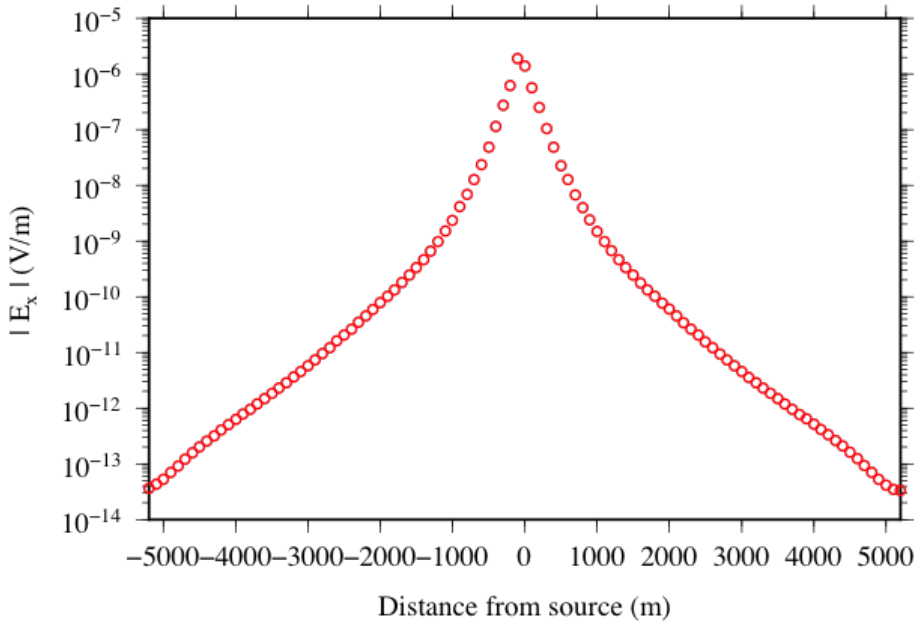

(a)

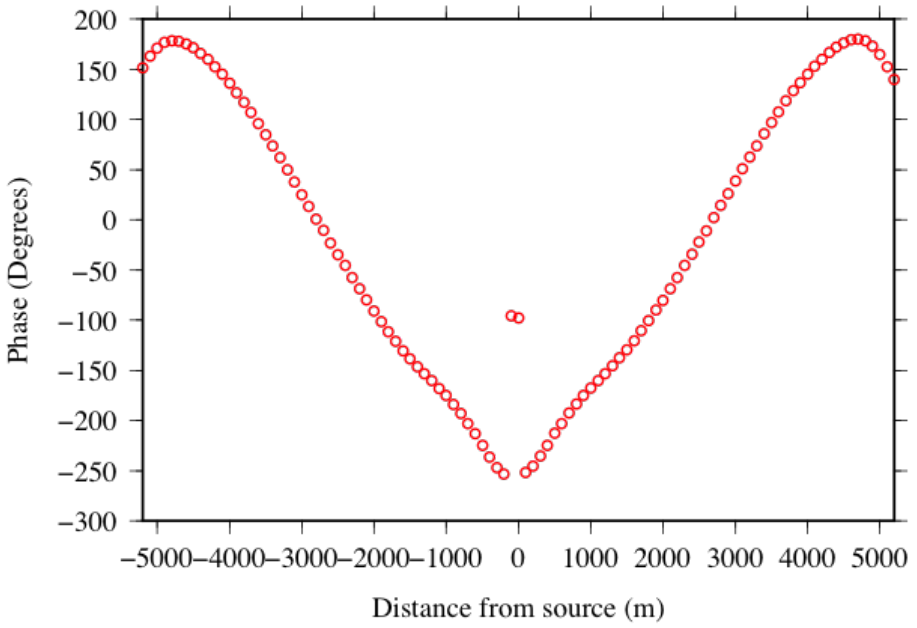

(b)

Figure B.19: Panel (a) electric field amplitude and panel (b) phase results of the *2500 m Disk Depth* scenario (Figure B.18).

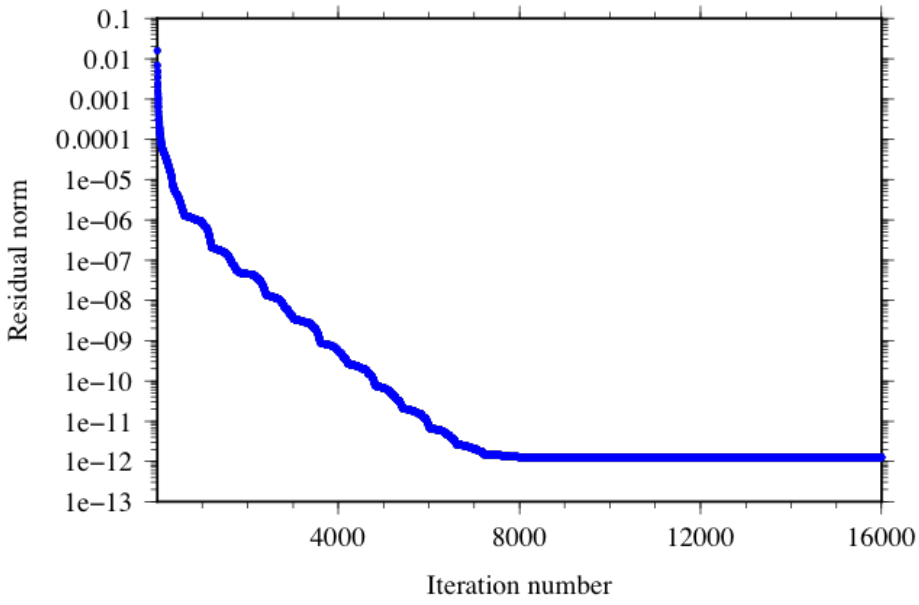

Figure B.20: Convergence curve of the *2500 m Disk Depth* scenario (Figure B.18).

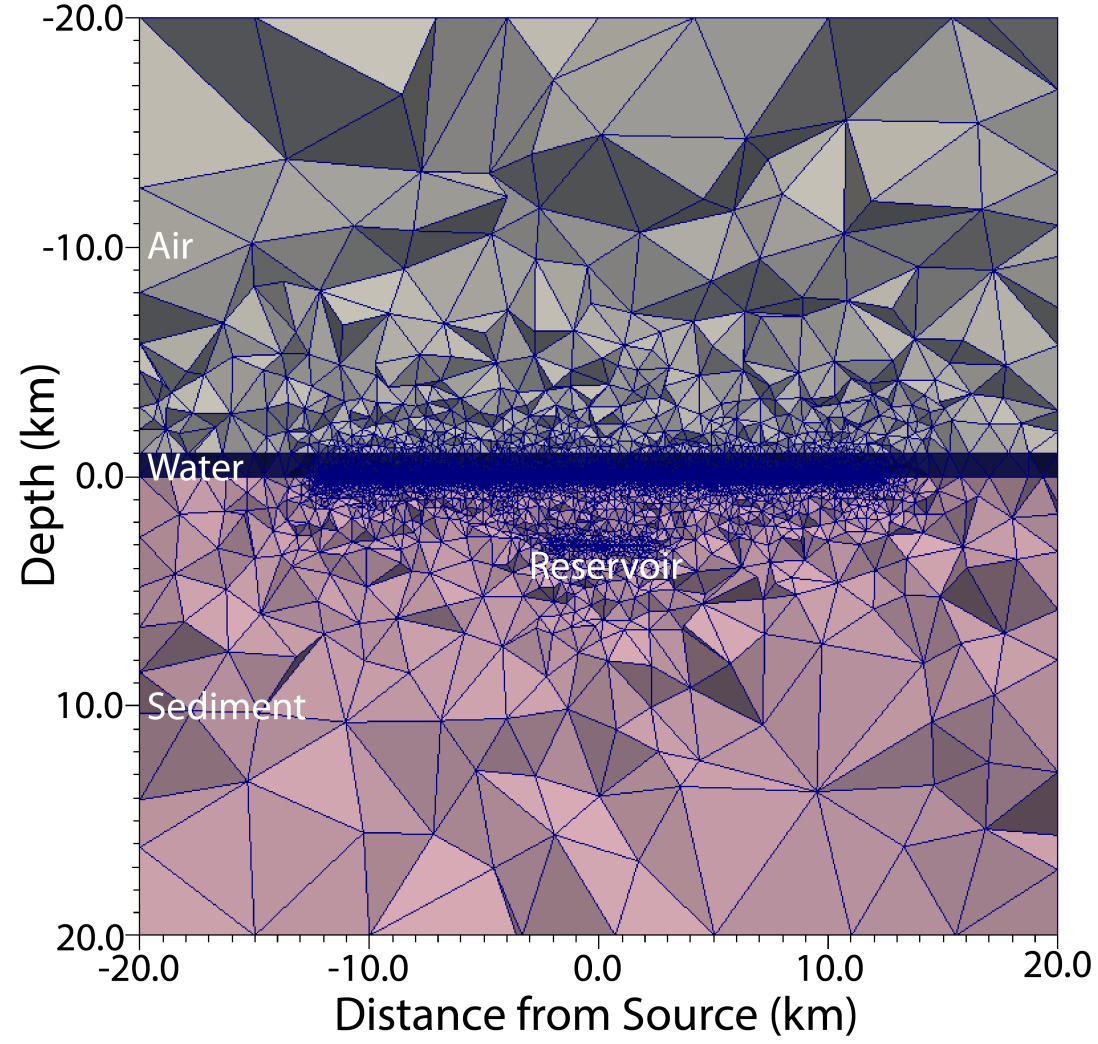

(a)

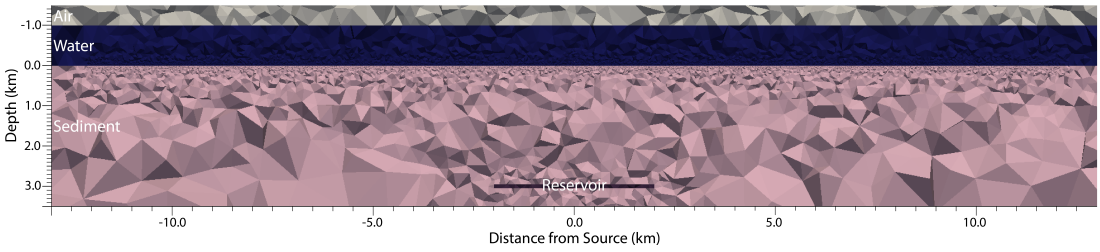

(b)

Figure B.21: Cross-sections centered at $y = 0$ m of the disk model at *3000 m Depth* and 100 m thickness. Panel (a) full view; panel (b) enhanced view of the reservoir.

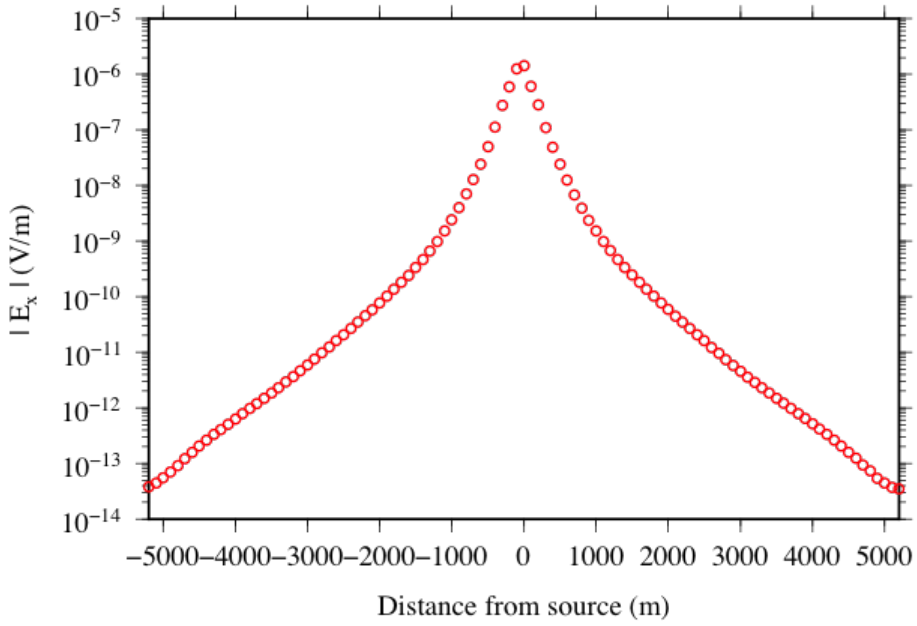

(a)

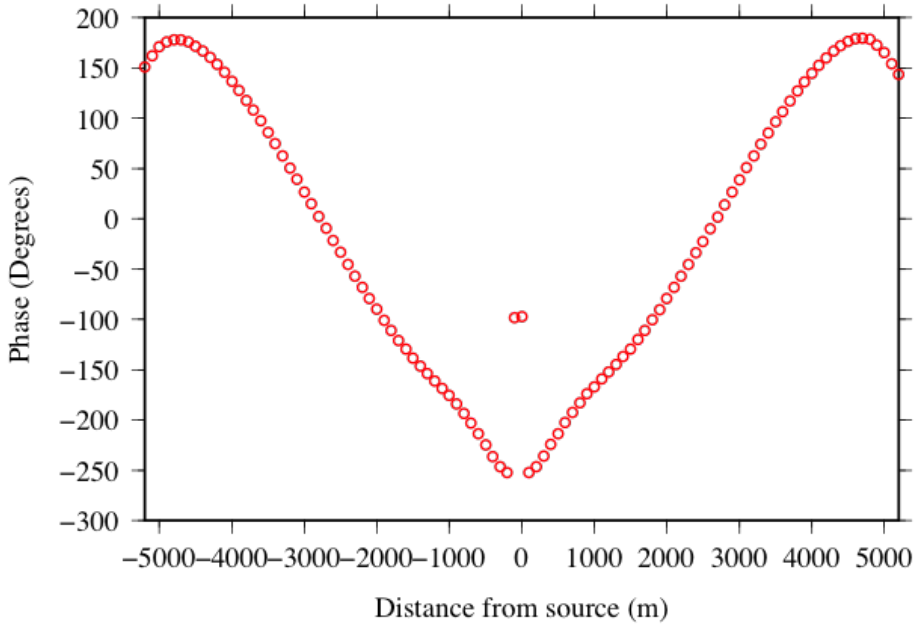

(b)

Figure B.22: Panel (a) electric field amplitude and panel (b) phase results of the *3000 m Disk Depth* scenario (Figure B.21) .

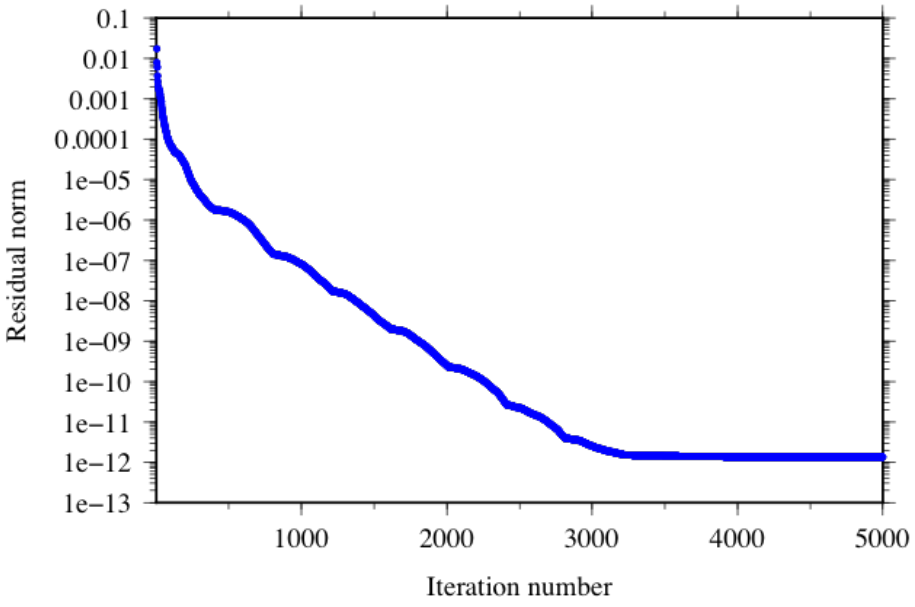

Figure B.23: Convergence curve of the *3000 m Disk Depth* scenario (Figure B.21).

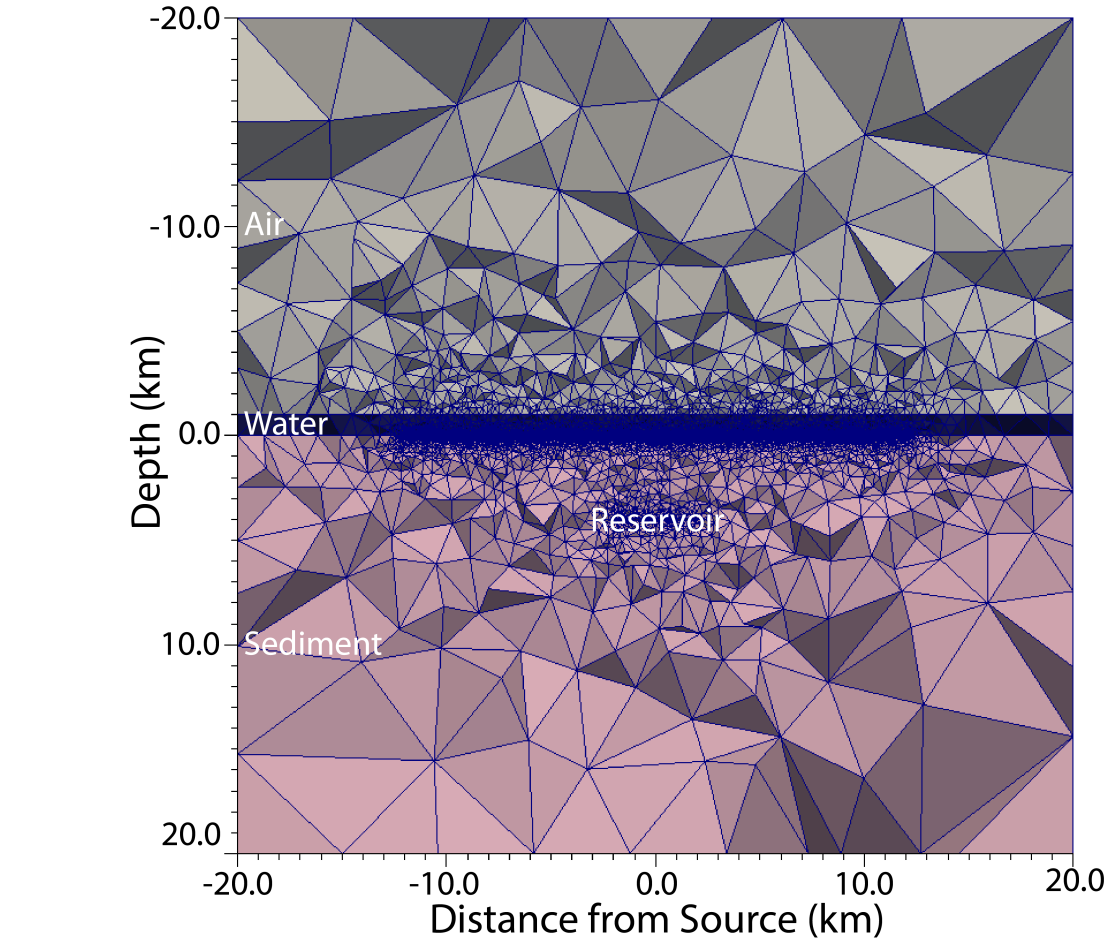

(a)

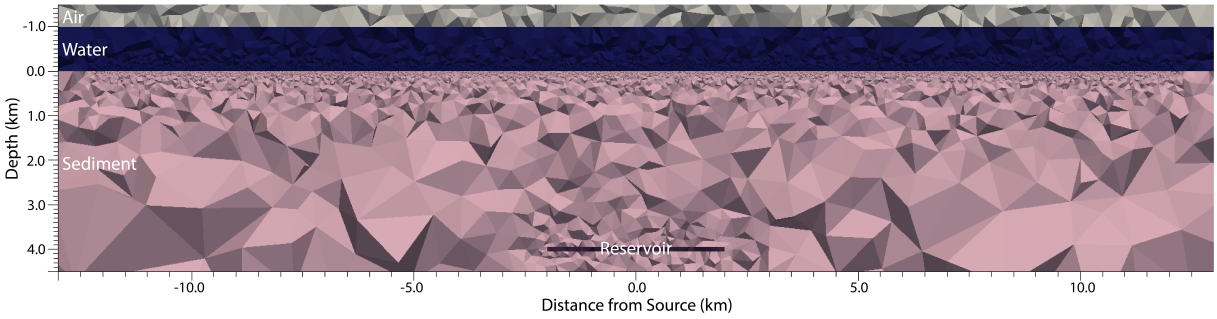

(b)

Figure B.24: Cross-sections centered at $y = 0$ m of the disk model at *4000 m Depth* and 100 m thickness. Panel (a) full view; panel (b) enhanced view of the reservoir.

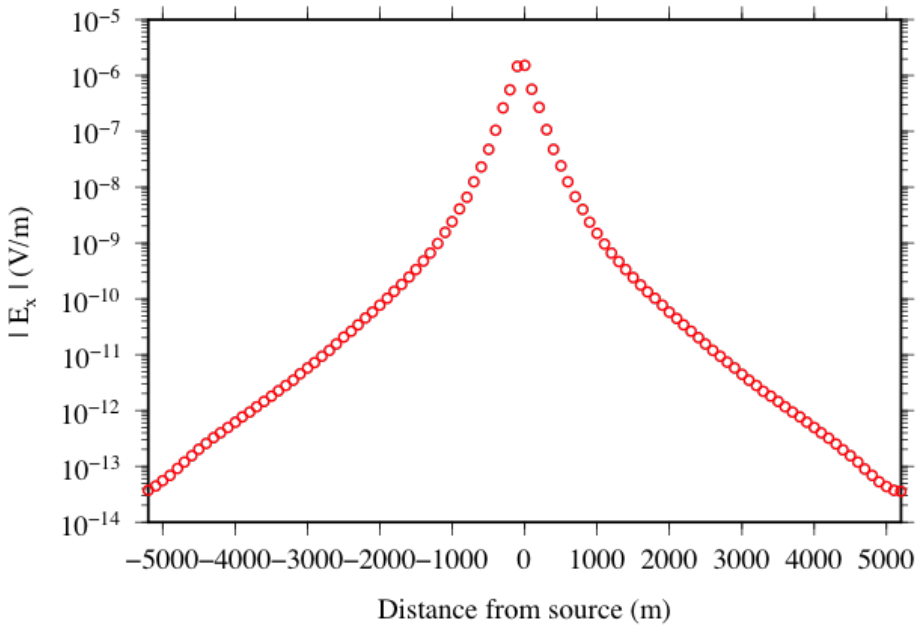

(a)

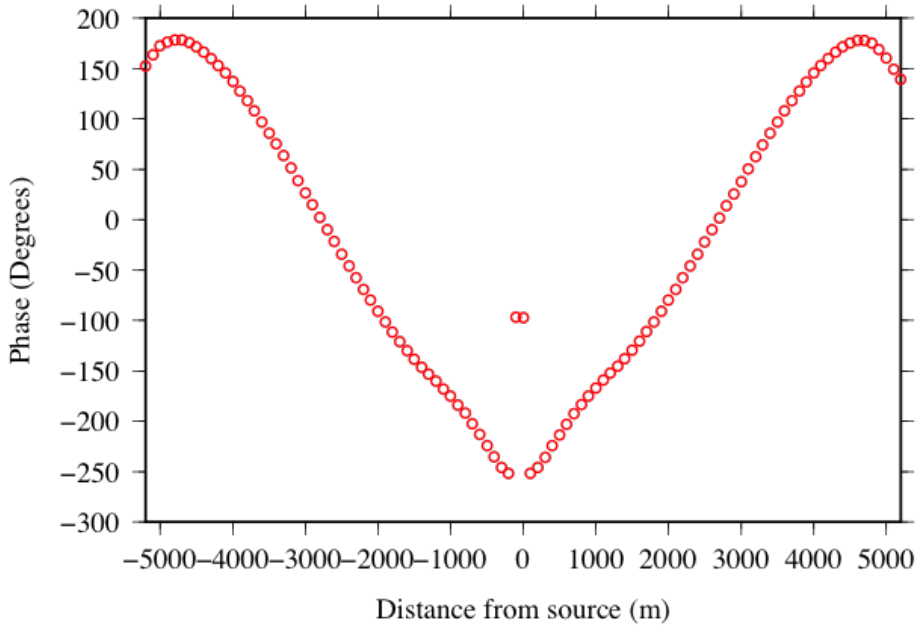

(b)

Figure B.25: Panel (a) electric field amplitude and panel (b) phase results of the *4000 m Disk Depth* scenario (Figure B.24).

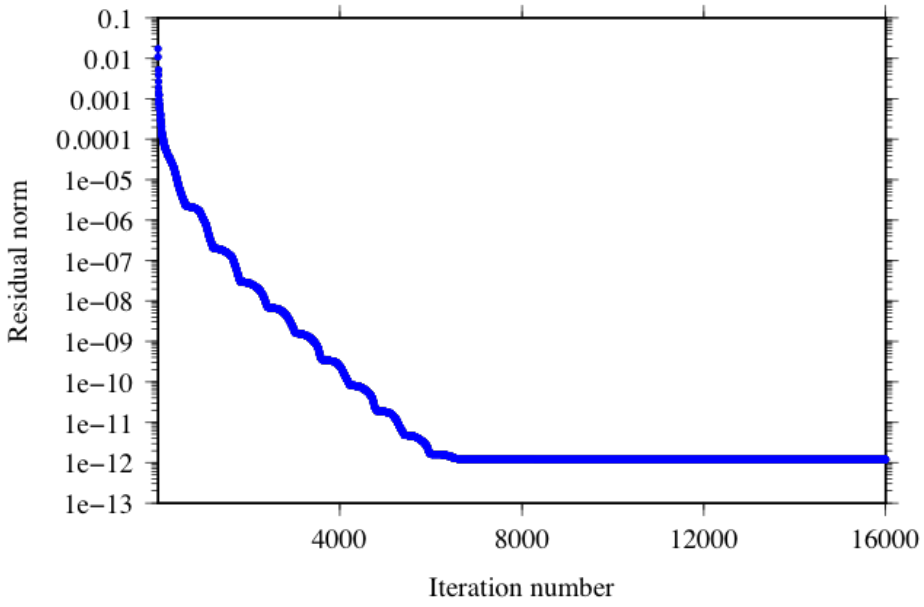

Figure B.26: Phase results of the *4000 m Disk Depth* scenario (Figure B.24).

Appendix C

Additional Reservoir Models

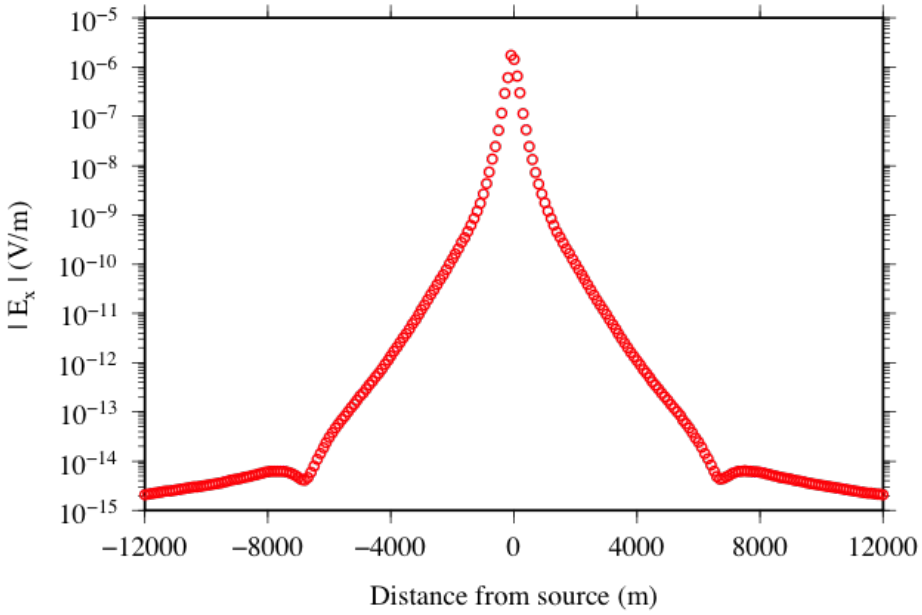

(a)

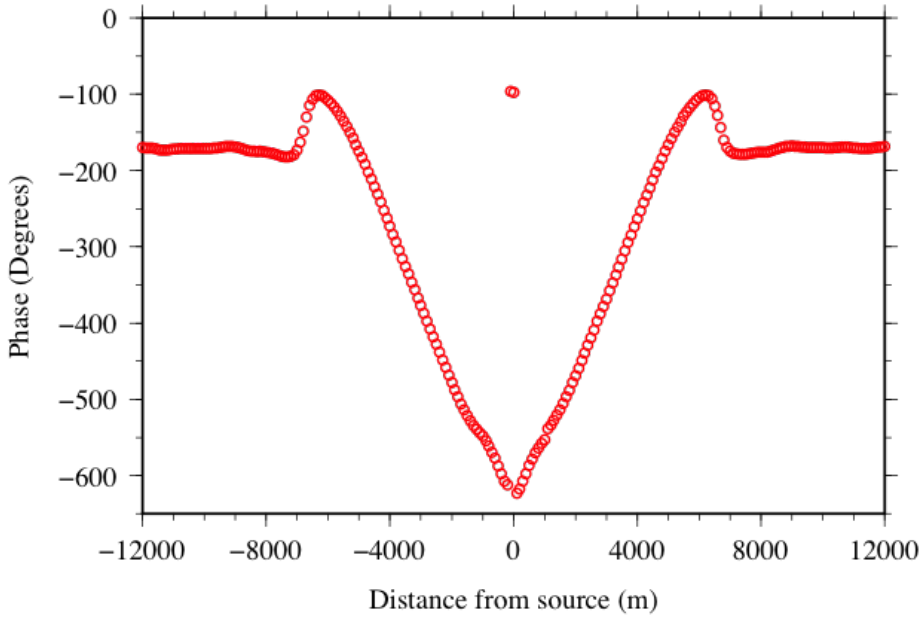

(b)

Figure C.1: Panel (a) electric field amplitude and panel (b) phase results for the model and mesh in Figure 3.26 (*Two Infinite Layers*).

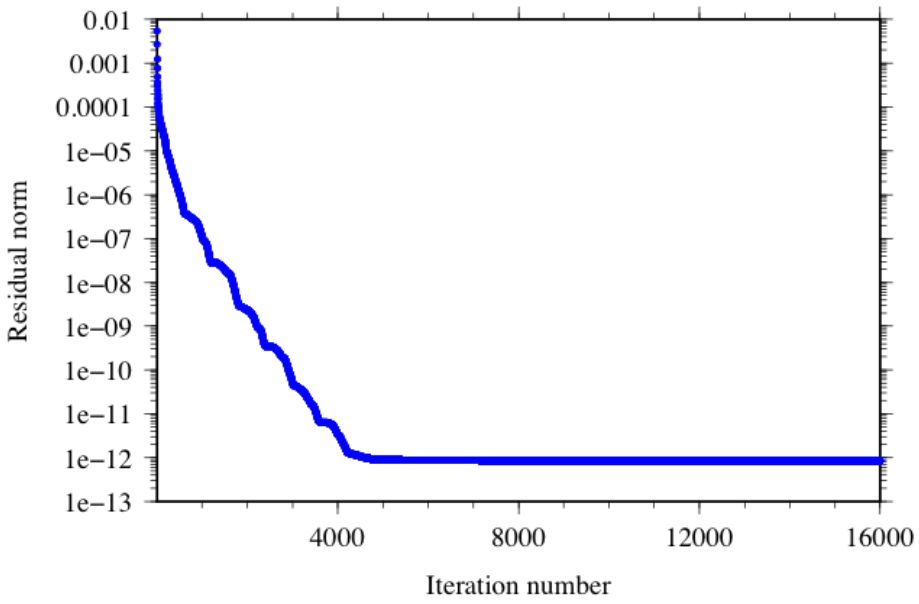

Figure C.2: Convergence curve for the model and mesh in Figure 3.26 (*Two Infinite Layers*).

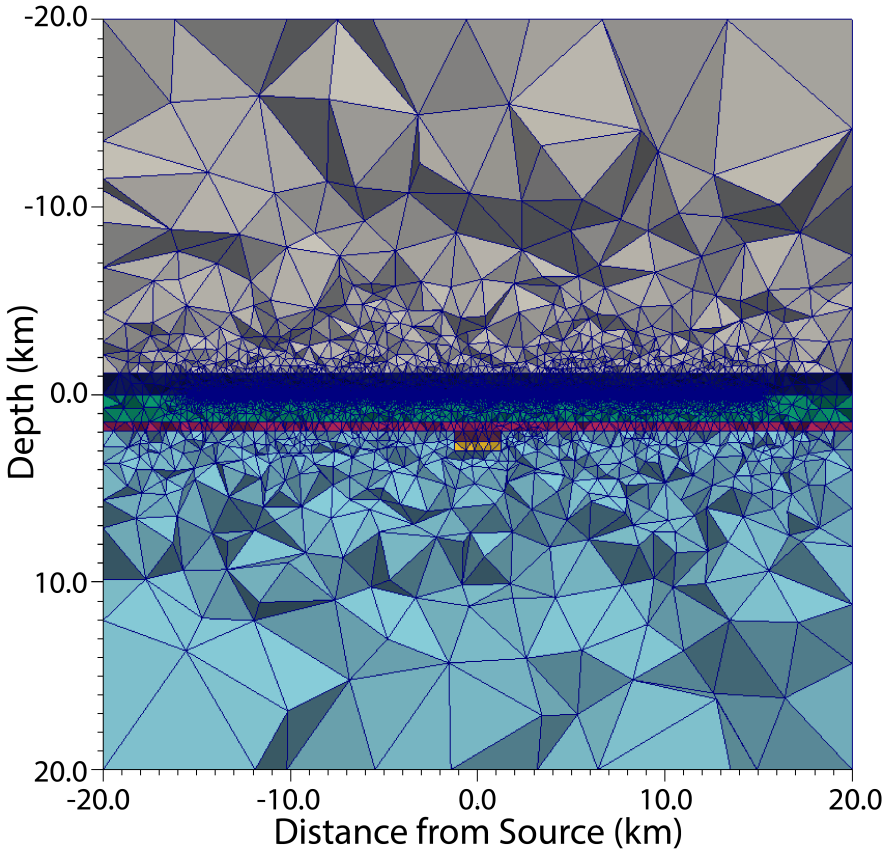

(a)

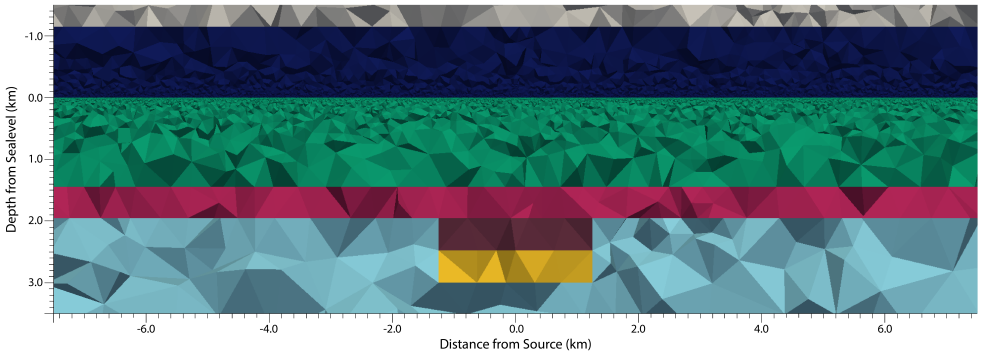

(b)

Figure C.3: Cross-section centered at $y = 0$ m of the simple Flemish Pass Basin model with two infinite subsurface layers and a 2500 m reservoir section composed of a shale upper layer (0.111 S/m) and sand reservoir lower layer (0.01 S/m). The first (green) infinite layer has a conductivity of 0.769 S/m and second (magenta) infinite layer has a conductivity of 0.467 S/m.

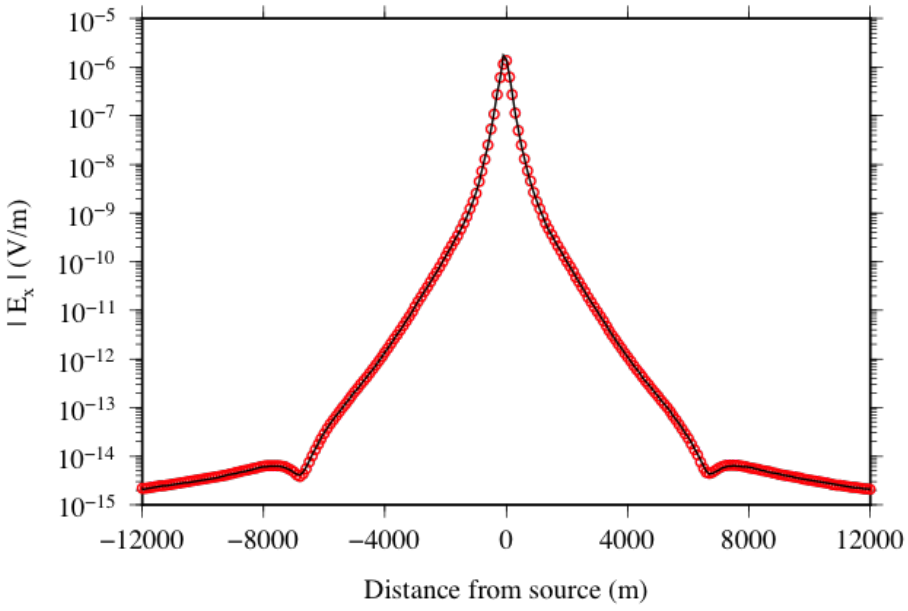

(a)

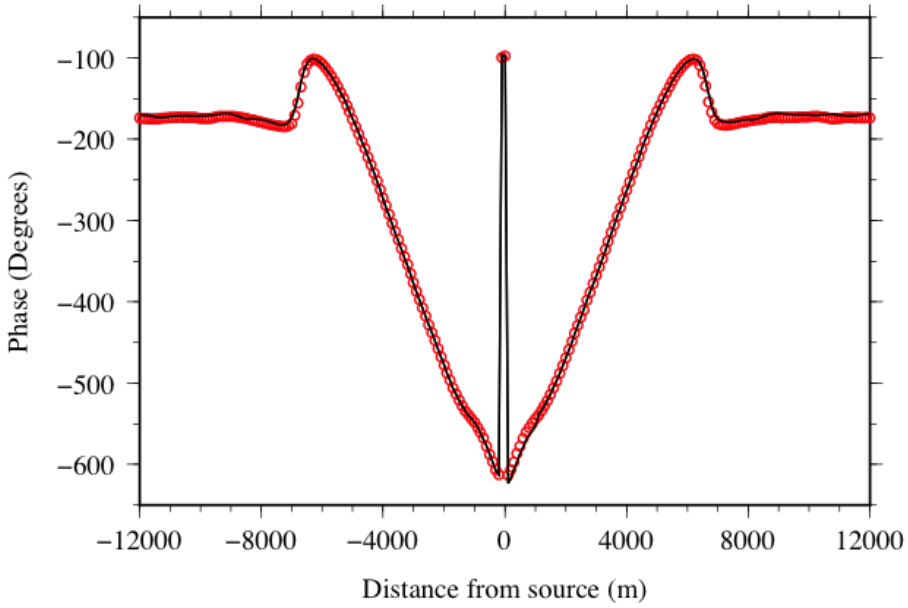

(b)

Figure C.4: Panel (a) electric field amplitude and panel (b) phase results for the model and mesh in Figure C.3. Red circles represent the results of the 2500 m reservoir model and black lines represents the results with no reservoir as seen in Figure C.1.

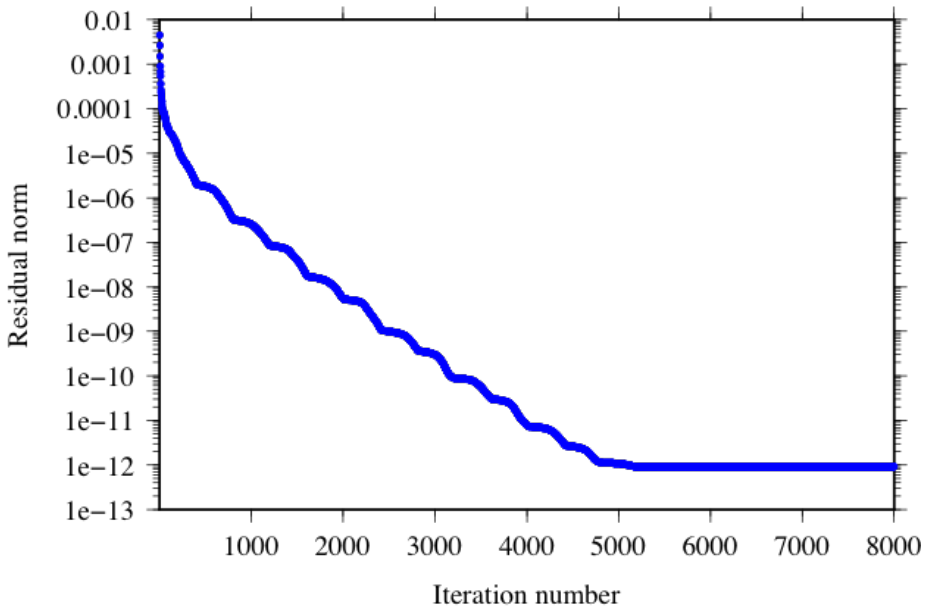

Figure C.5: Convergence curve for the model and mesh in Figure C.3.

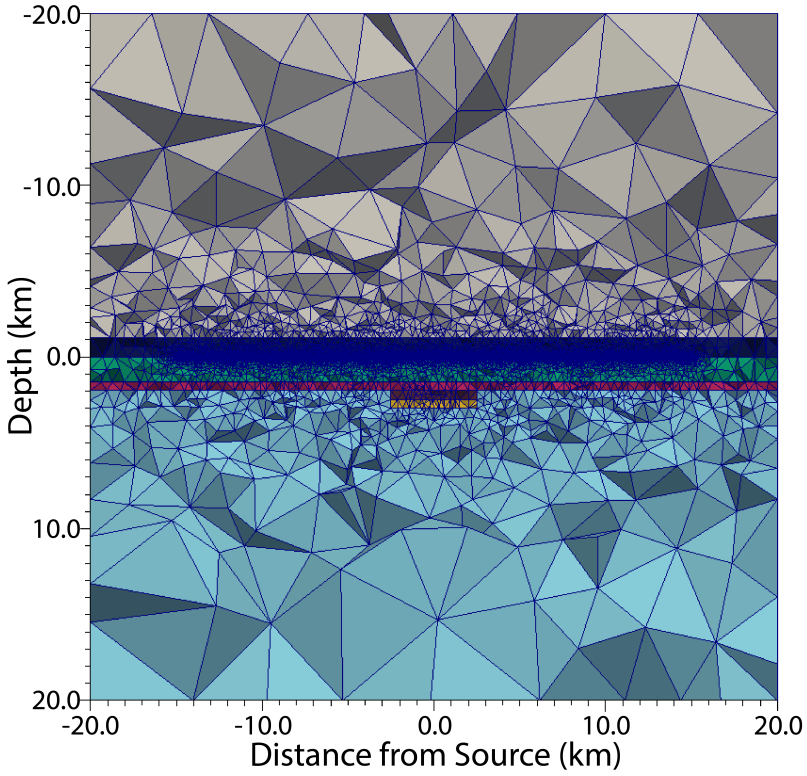

(a)

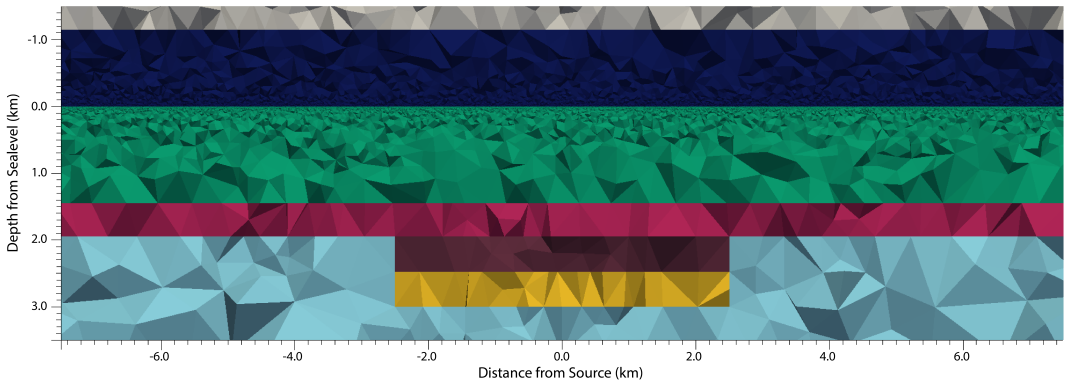

(b)

Figure C.6: Cross-section centered at $y = 0$ m of the simple Flemish Pass Basin model with two infinite subsurface layers and a 5000 m reservoir section composed of a shale upper layer (conductivity of 0.111 S/m) and sand reservoir lower layer (conductivity of 0.01 S/m). The first (green) infinite layer has a conductivity of 0.769 S/m and second (magenta) infinite layer has a conductivity of 0.467 S/m.

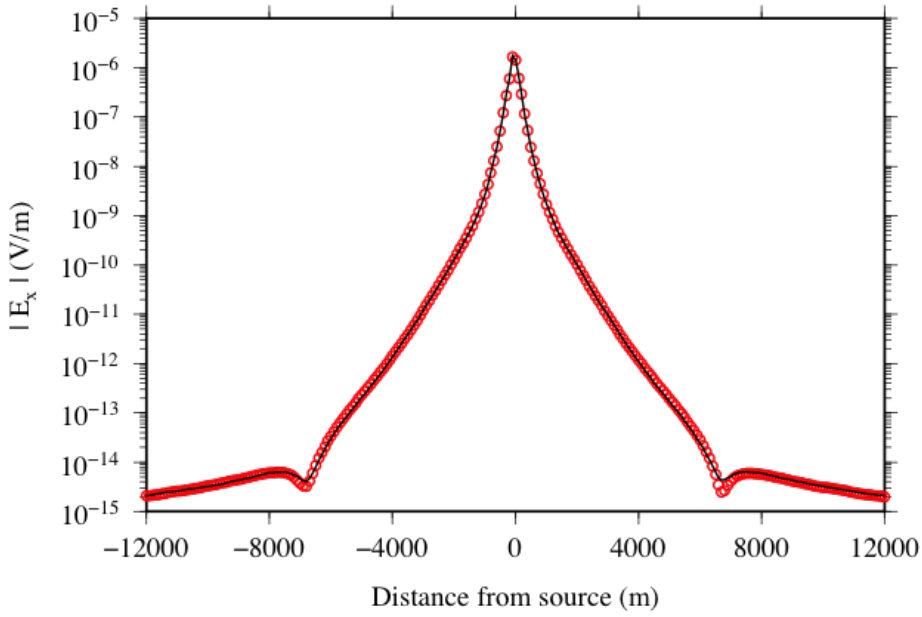

(a)

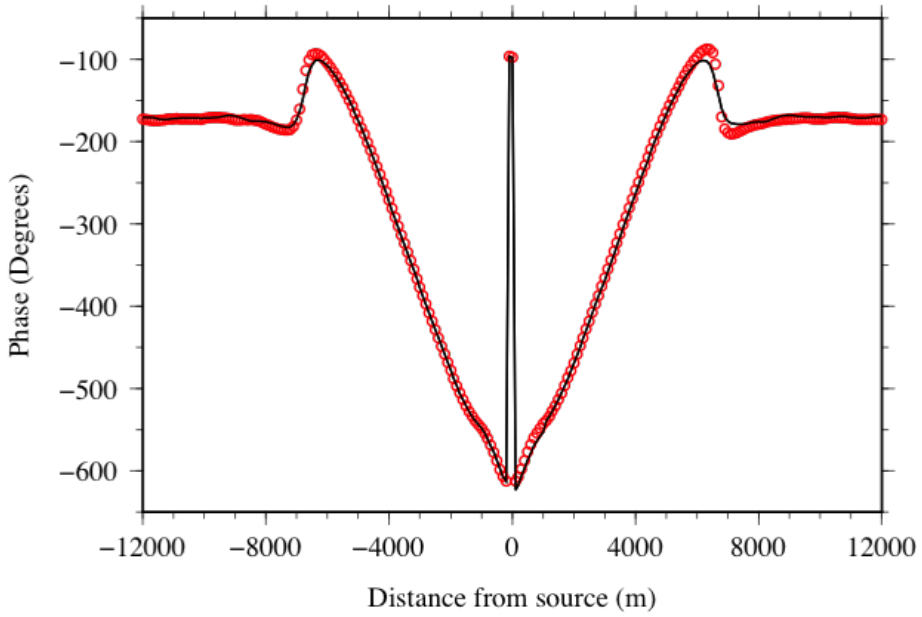

(b)

Figure C.7: Panel (a) electric field amplitude and panel (b) phase results for the model and mesh in Figure C.6. Red circles represent the results of the 5000 m reservoir model and black lines represents the results with no reservoir as seen in Figure C.1.

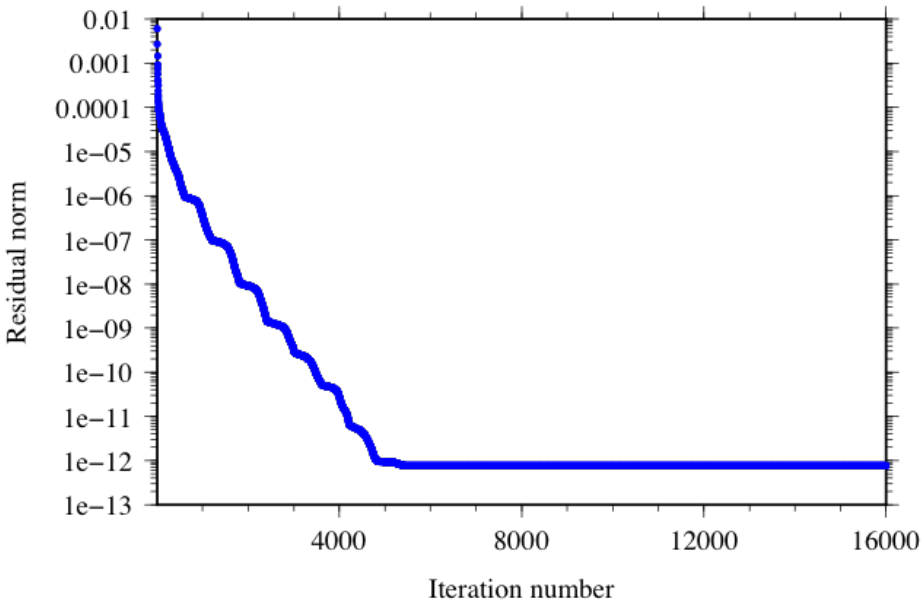

Figure C.8: Convergence curve for the model and mesh in Figure C.6.

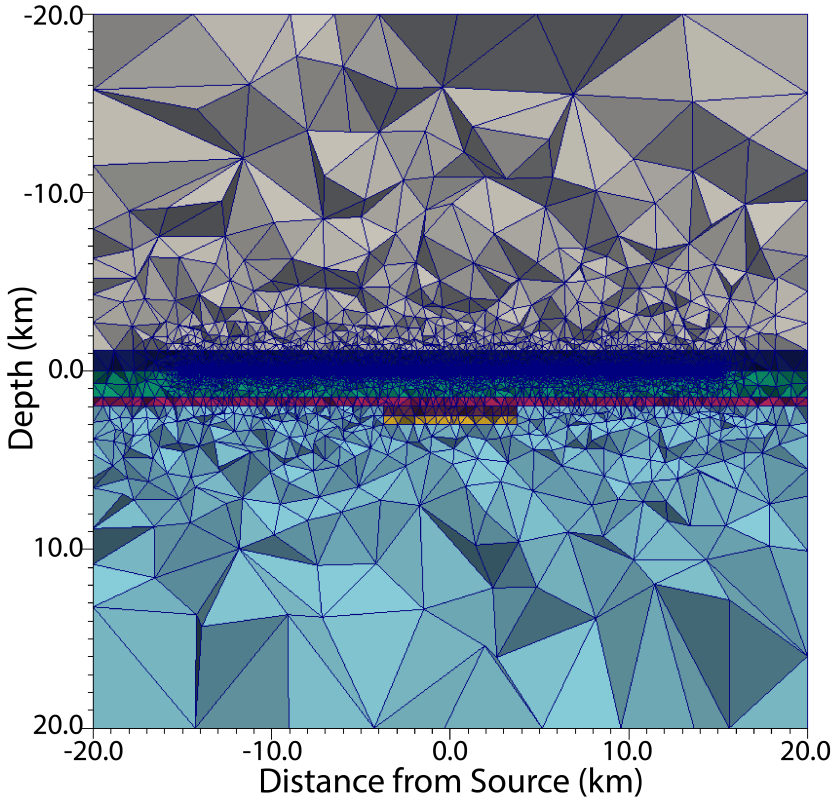

(a)

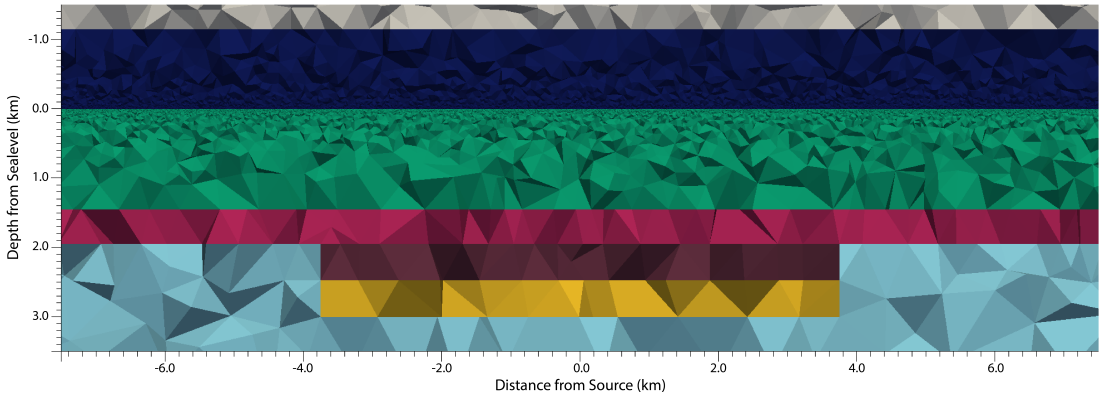

(b)

Figure C.9: Cross-section centered at $y = 0$ m of the simple Flemish Pass Basin model with two infinite subsurface layers and a 7500 m reservoir section composed of a shale upper layer (0.111 S/m) and sand reservoir lower layer (0.01 S/m). The first (green) infinite layer has a conductivity of 0.769 S/m and second (magenta) infinite layer has a conductivity of 0.467 S/m.

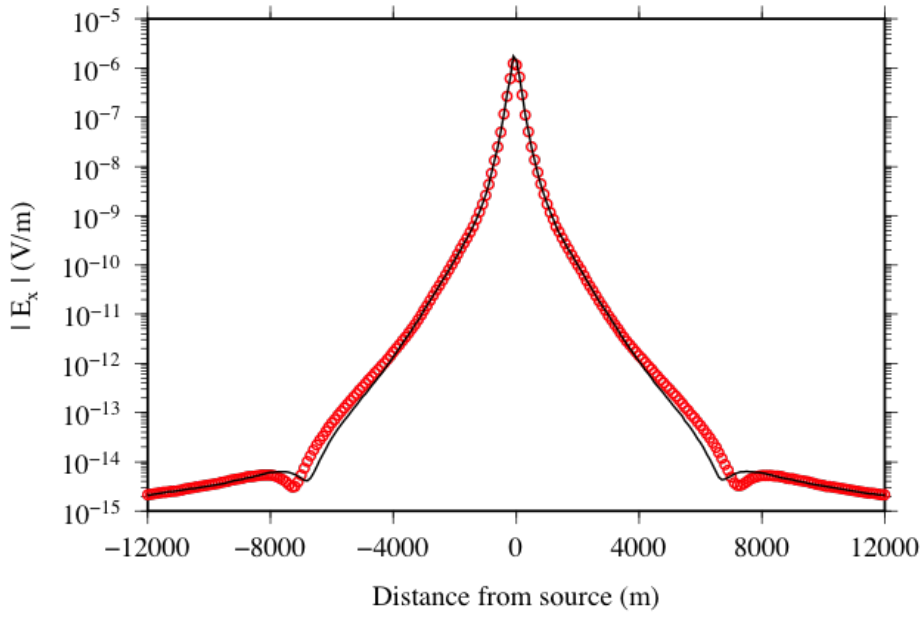

(a)

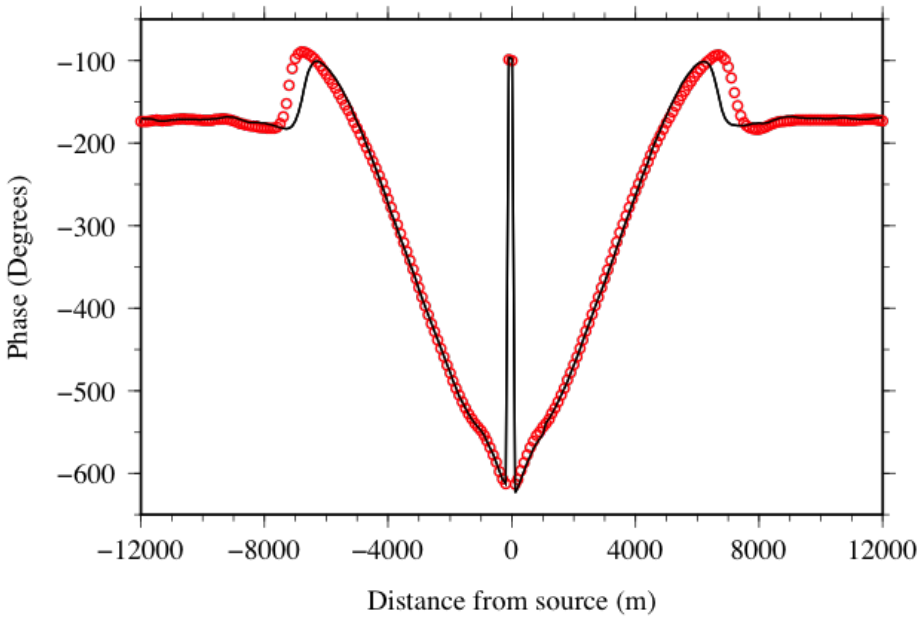

(b)

Figure C.10: Panel (a) electric field amplitude and panel (b) phase results for the model and mesh in Figure C.9. Red circles represent the results of the 7500 m reservoir model and black lines represents the results with no reservoir as seen in Figure C.1.

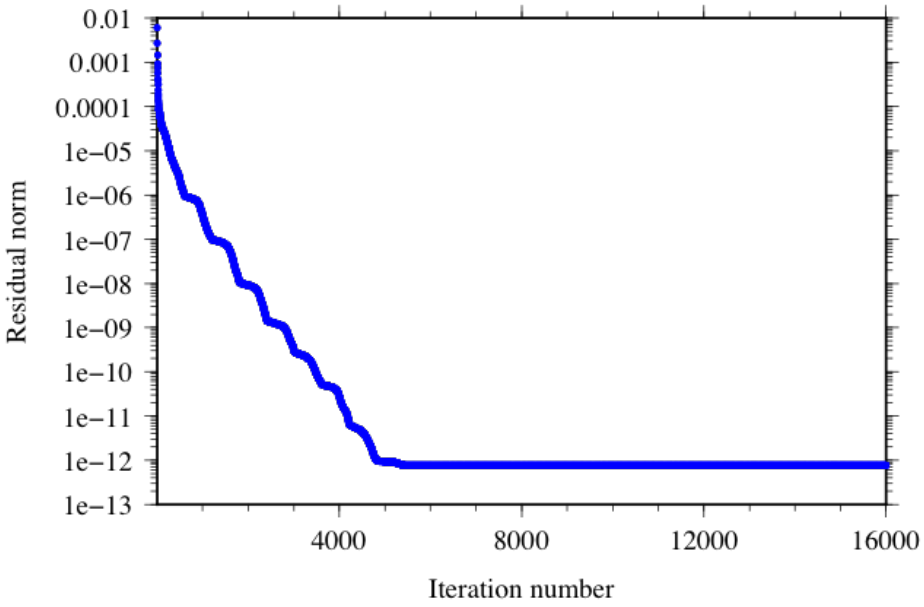

Figure C.11: Convergence curve for the model and mesh in Figure C.9.

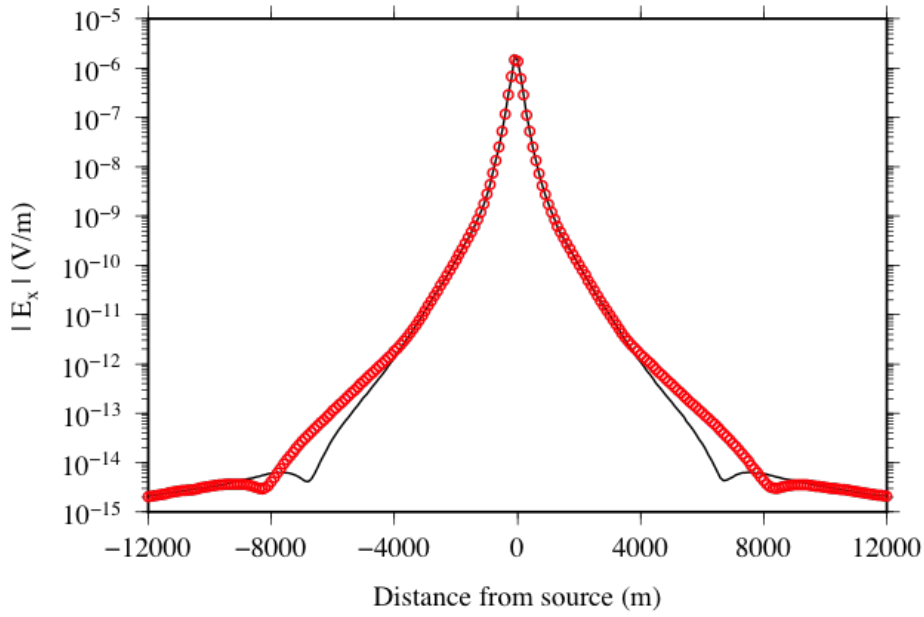

(a)

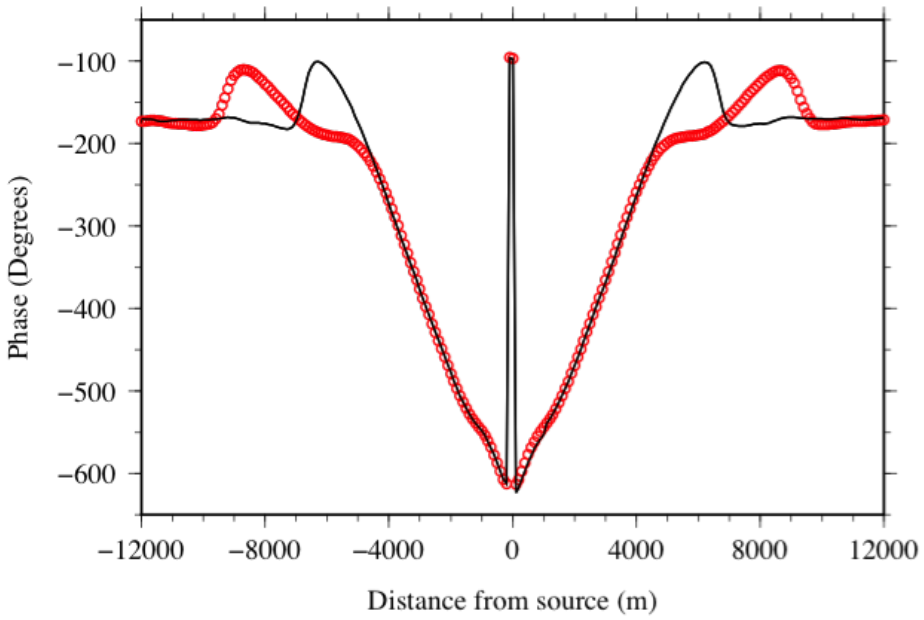

(b)

Figure C.12: Panel (a) electric field amplitude and panel (b) phase results for the model and mesh in Figure 3.27 (*10000 m Reservoir*). Red circles represent the results of the 10000 m reservoir model and black lines represents the results with no reservoir as seen in Figure C.1.

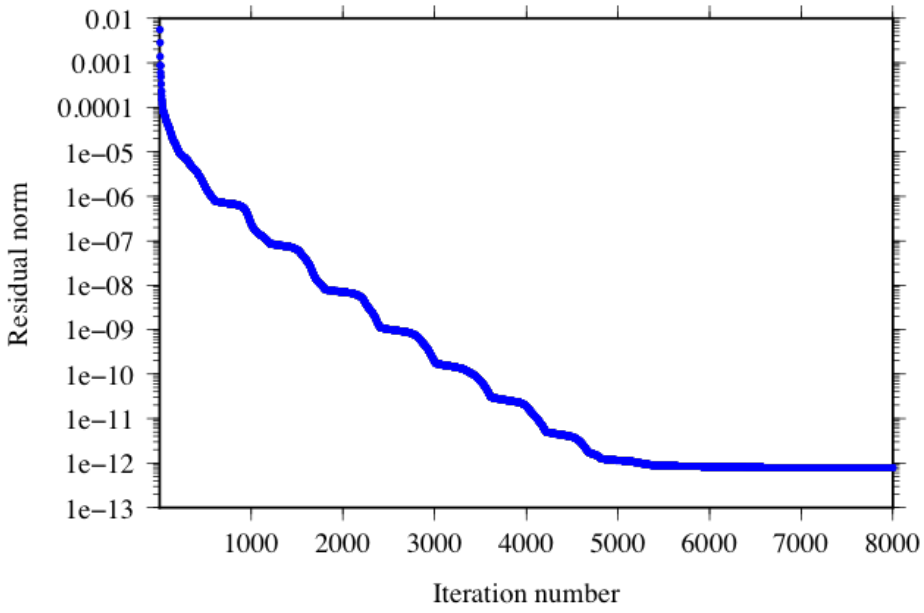

Figure C.13: Convergence curve for the model and mesh in Figure 3.27 (*10000 m Reservoir Model*).

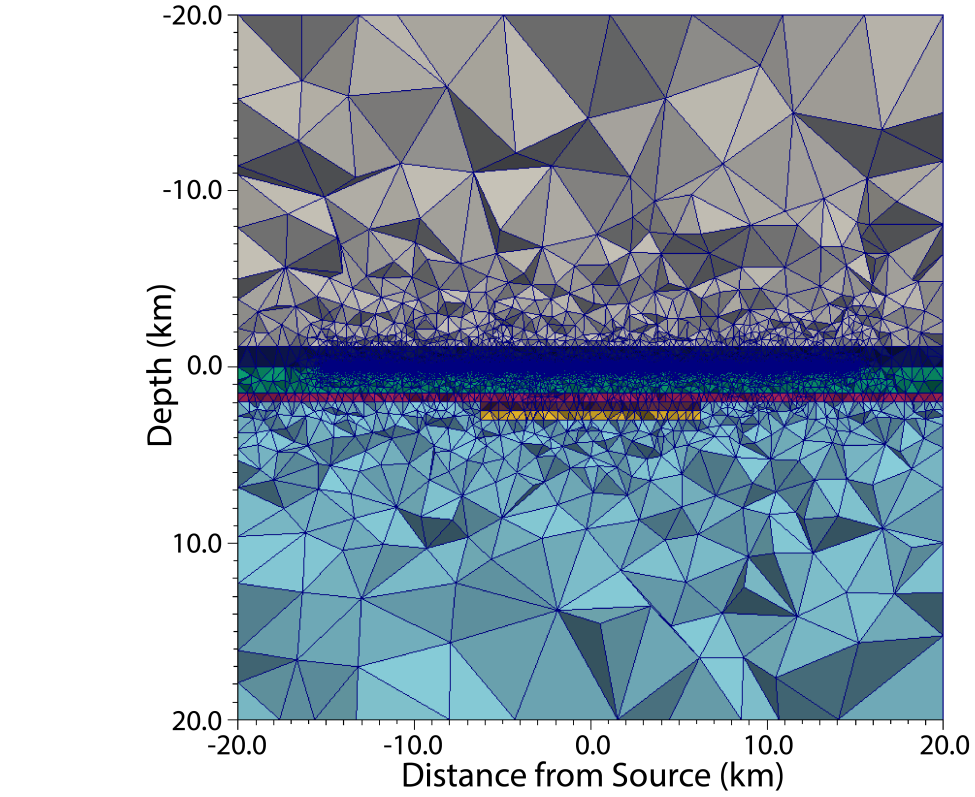

(a)

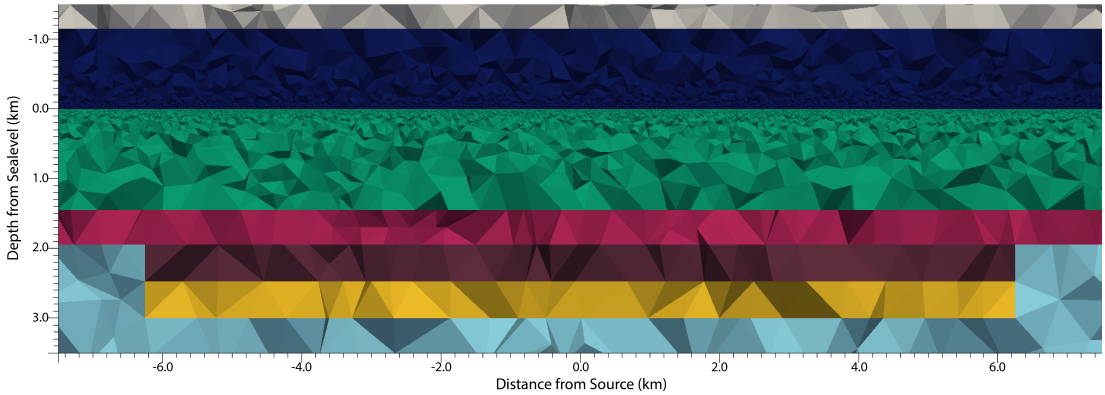

(b)

Figure C.14: Cross-section centered at $y = 0$ m of the simple Flemish Pass Basin model with two infinite subsurface layers and a 12500 m reservoir section composed of a shale upper layer (0.111 S/m) and sand reservoir lower layer (0.01 S/m). The first (green) infinite layer has a conductivity of 0.769 S/m and second (magenta) infinite layer has a conductivity of 0.467 S/m.

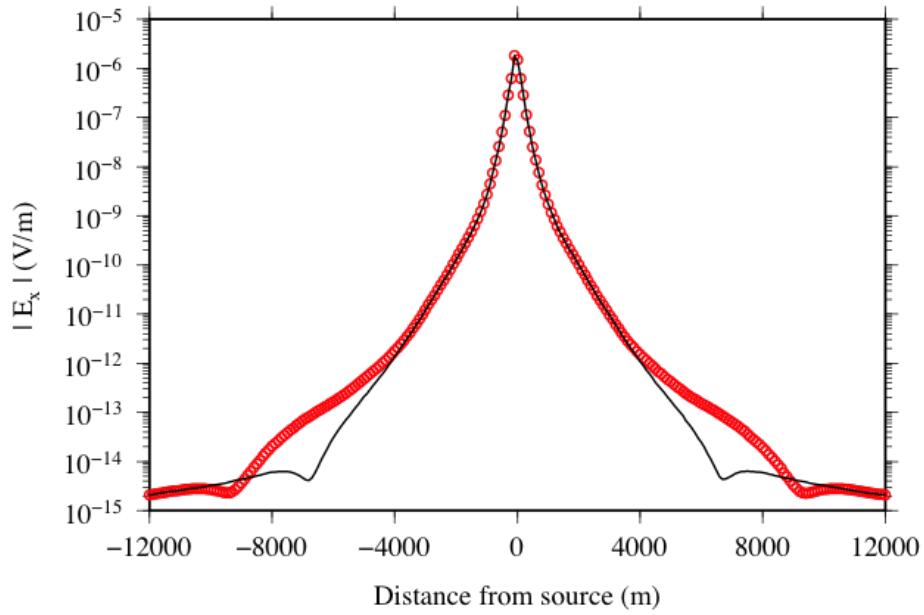

(a)

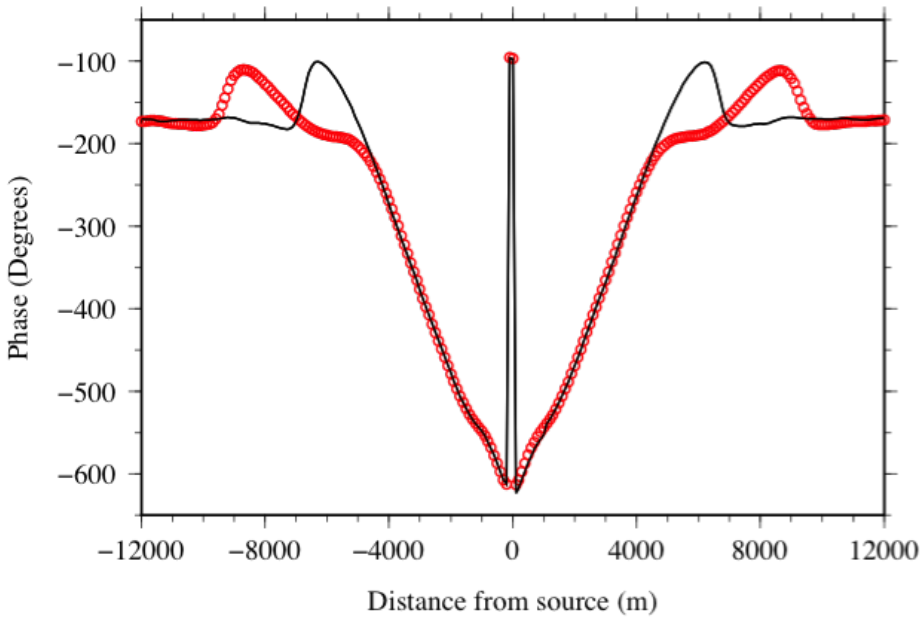

(b)

Figure C.15: Panel (a) electric field amplitude and panel (b) phase results for the model and mesh in Figure C.14. Red circles represent the results of the 12500 m reservoir model and black lines represents the results with no reservoir as seen in Figure C.1.

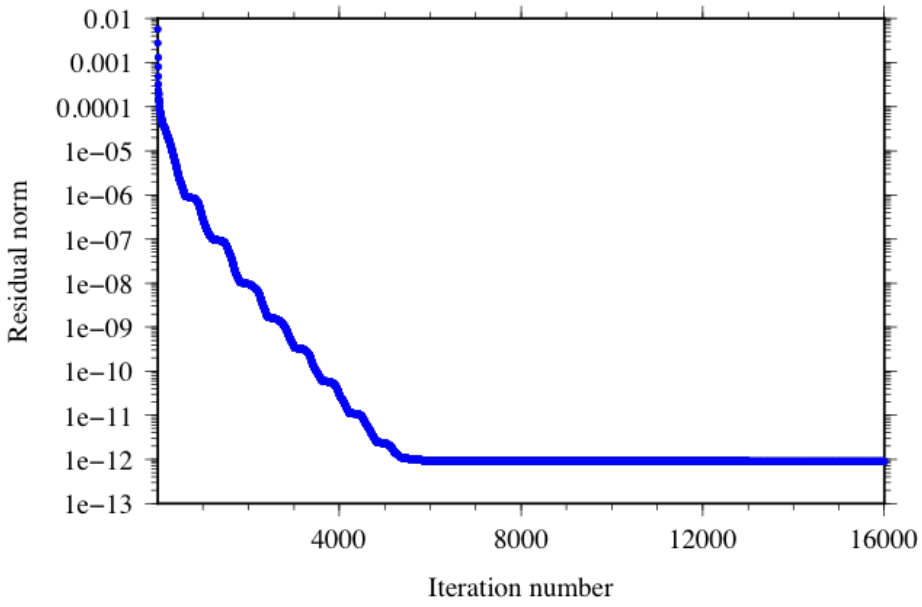

Figure C.16: Convergence curve for the model and mesh in Figure C.14.

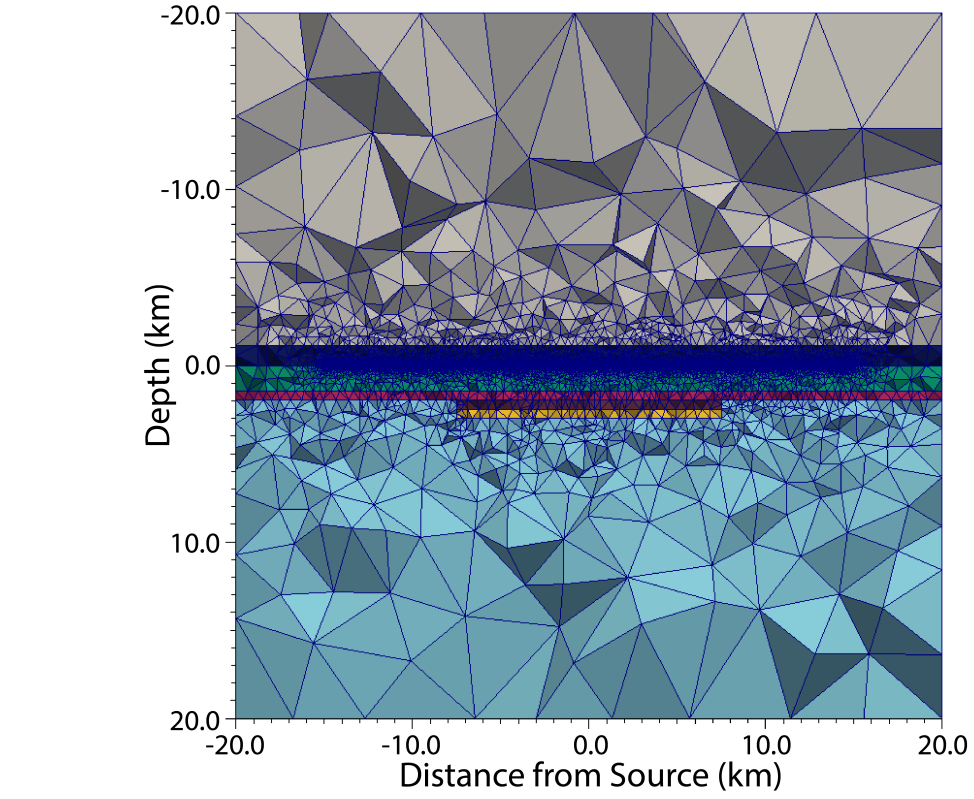

(a)

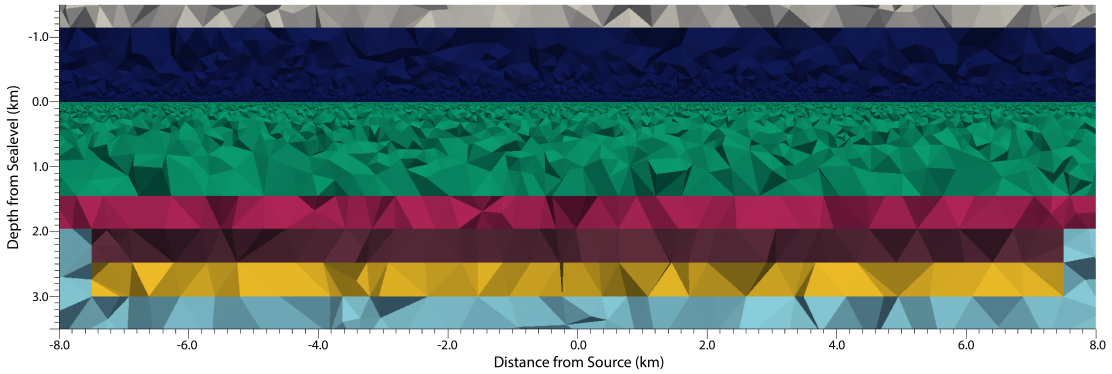

(b)

Figure C.17: Cross-section centered at $y = 0$ m of the simple Flemish Pass Basin model with two infinite subsurface layers and a 15000 m reservoir section composed of a shale upper layer (0.111 S/m) and sand reservoir lower layer (0.01 S/m). The first (green) infinite layer has a conductivity of 0.769 S/m and second (magenta) infinite layer has a conductivity of 0.467 S/m.

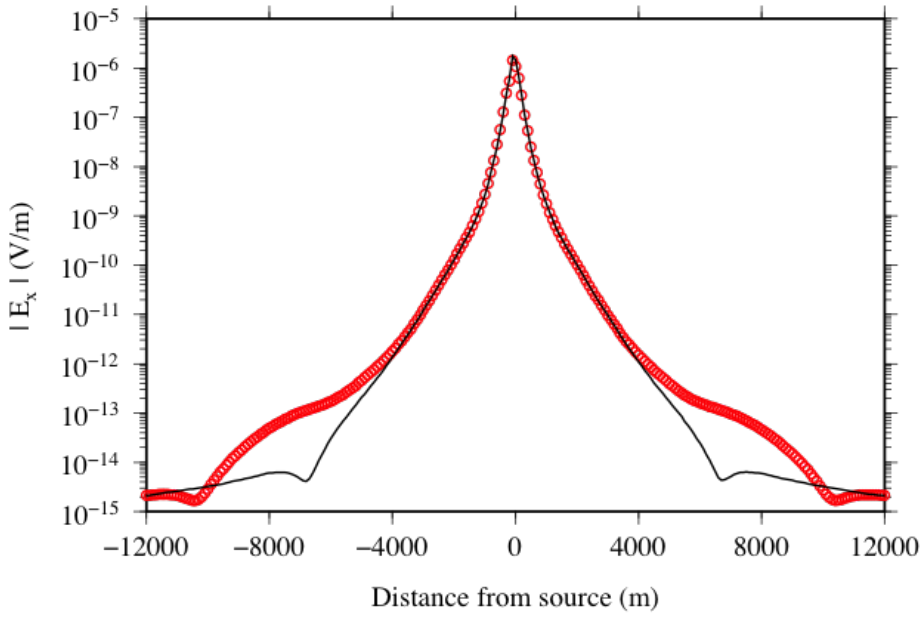

(a)

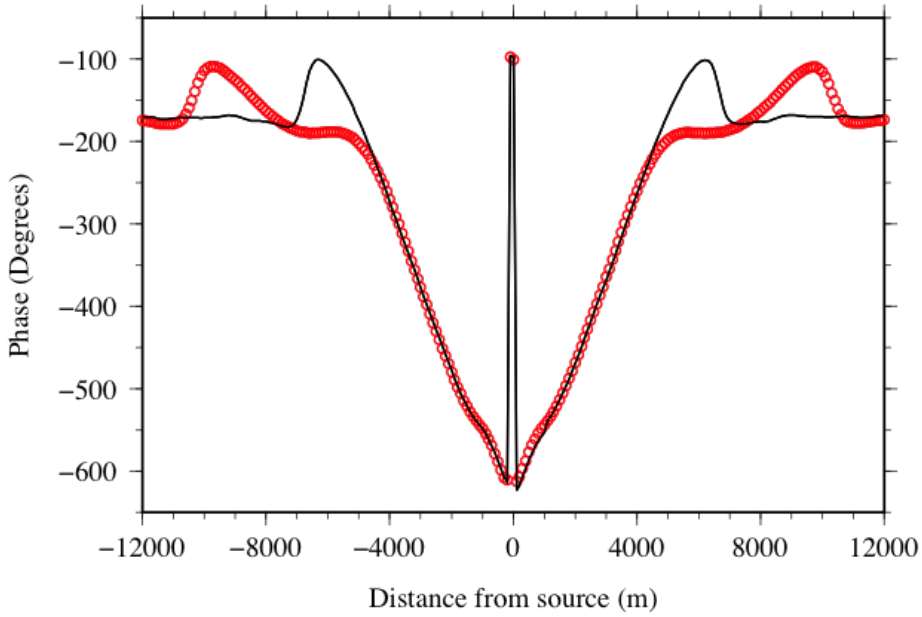

(b)

Figure C.18: Panel (a) electric field amplitude and panel (b) phase results for the model and mesh in Figure C.17. Red circles represent the results of the 15000 m reservoir model and black lines represents the results with no reservoir as seen in Figure C.1.

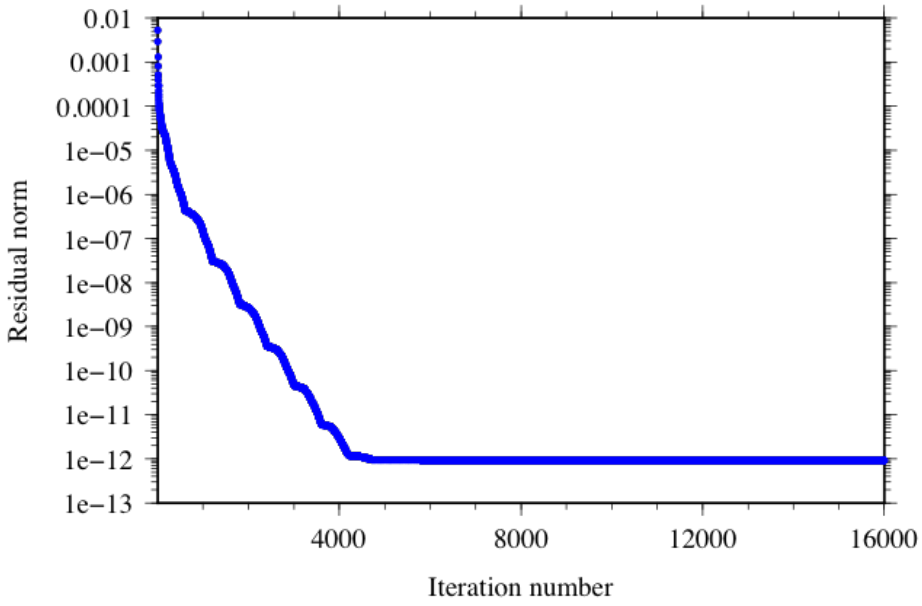

Figure C.19: Convergence curve for the model and mesh in Figure C.17.

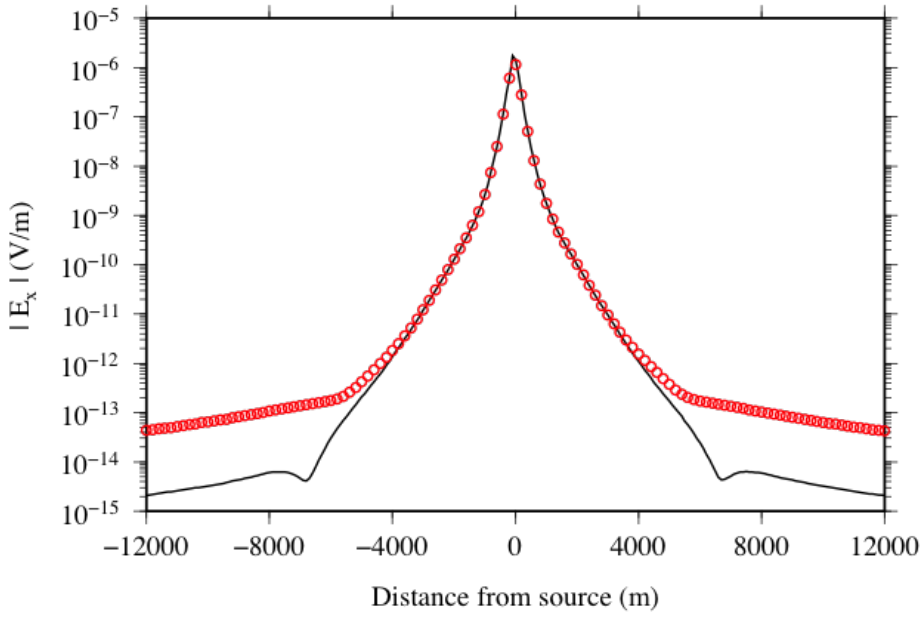

(a)

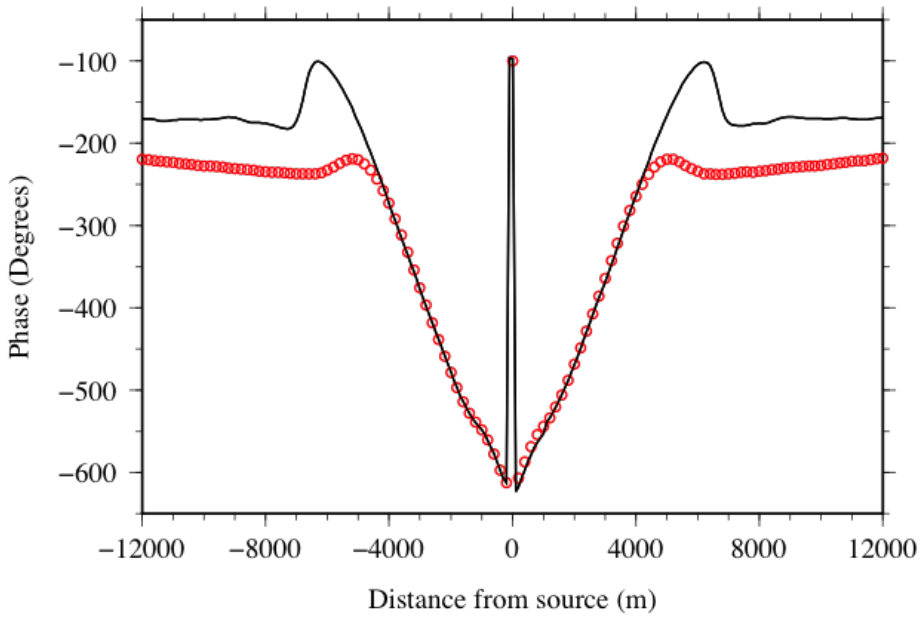

(b)

Figure C.20: Panel (a) electric field amplitude and panel (b) phase results for the model and mesh in Figure 3.28 (*Infinite Reservoir Model*). Red circles represent the results of the infinite reservoir model and black lines represents the results with no reservoir as seen in Figure C.1.

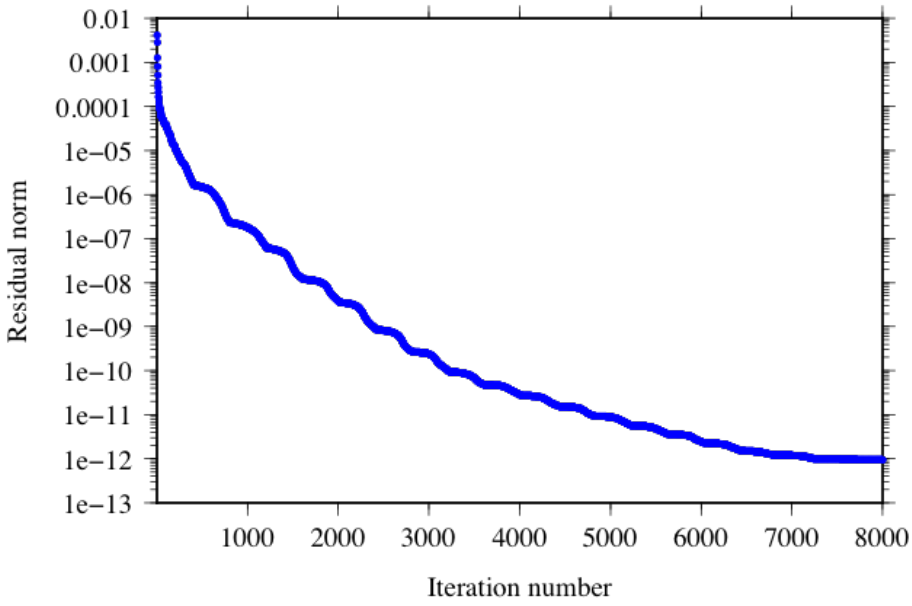

Figure C.21: Convergence curve for the model and mesh in Figure 3.28 (*Infinite Reservoir Model*).

Appendix D

Extended Reservoir Geometries

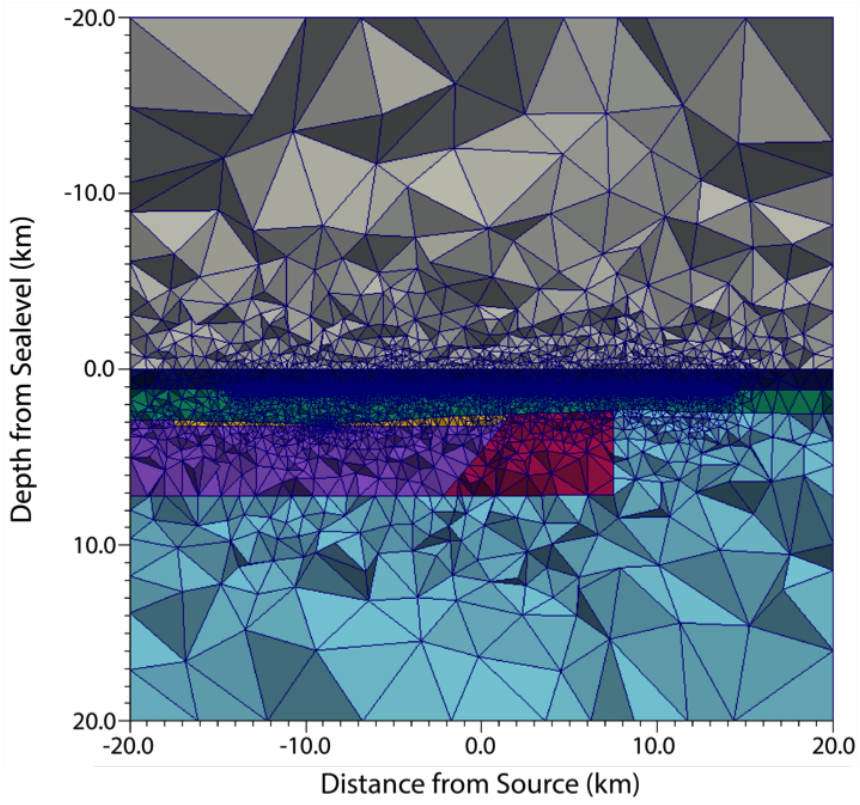

(a)

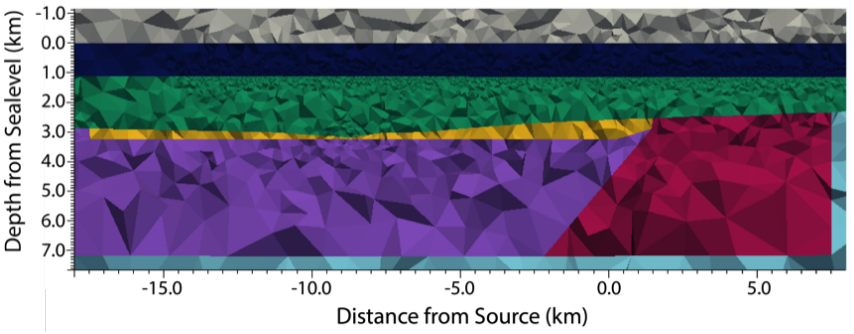

(b)

Figure D.1: Cross-sections centered at $y = 0$ m of the multiple fault block system used in *Model 4*. Panel (a) full view; panel (b) enhanced view of the reservoir geometry.

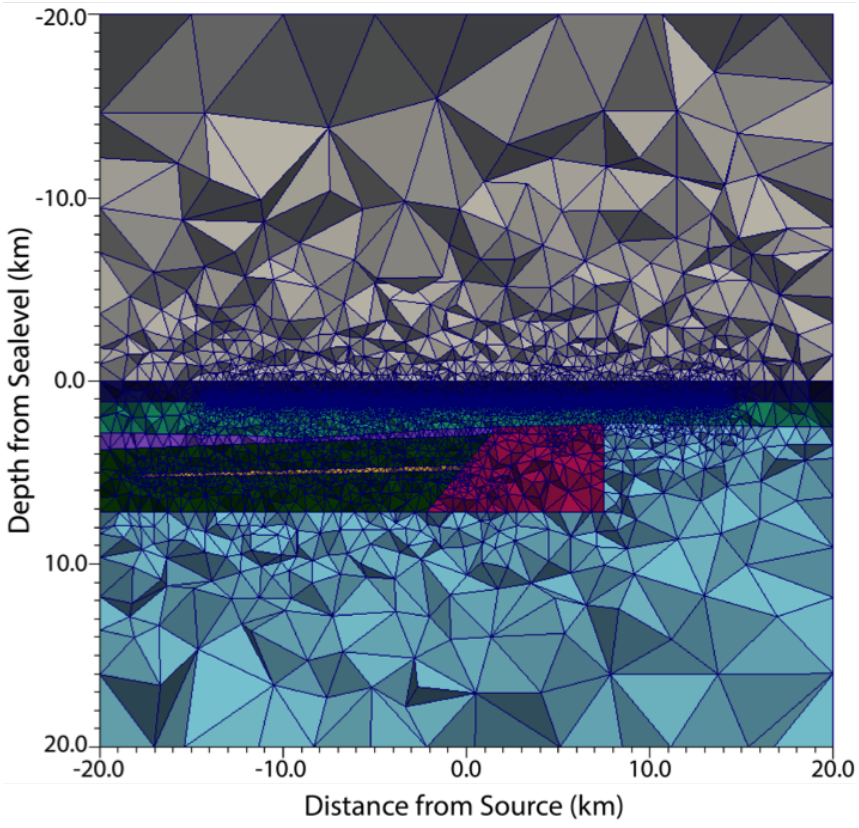

(a)

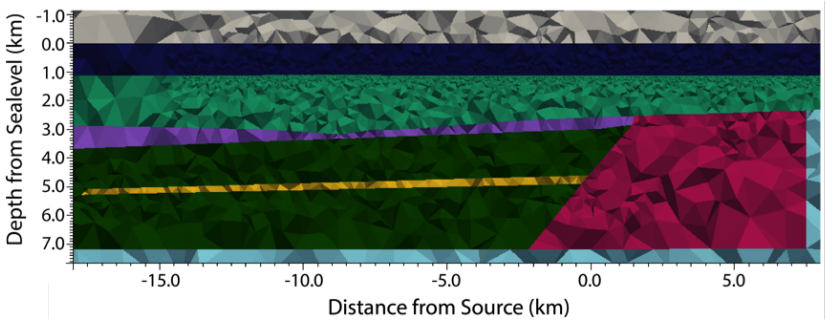

(b)

Figure D.2: Cross-sections centered at $y = 0$ m of the multiple fault block system used in *Model 5*. Panel (a) full view; panel (b) enhanced view of the reservoir geometry.